



HAL
open science

Enriched elasto-plastic beam model

Grégoire Corre

► **To cite this version:**

Grégoire Corre. Enriched elasto-plastic beam model. Structural mechanics [physics.class-ph]. Université Paris-Est, 2018. English. NNT : 2018PESC1031 . tel-02166942

HAL Id: tel-02166942

<https://pastel.hal.science/tel-02166942>

Submitted on 27 Jun 2019

HAL is a multi-disciplinary open access archive for the deposit and dissemination of scientific research documents, whether they are published or not. The documents may come from teaching and research institutions in France or abroad, or from public or private research centers.

L'archive ouverte pluridisciplinaire **HAL**, est destinée au dépôt et à la diffusion de documents scientifiques de niveau recherche, publiés ou non, émanant des établissements d'enseignement et de recherche français ou étrangers, des laboratoires publics ou privés.

UNIVERSITÉ —
— PARIS-EST

Ecole Doctorale SIE

THÈSE

présentée pour l'obtention du grade de

DOCTEUR

de l'université Paris-Est

Spécialité: Structures et Matériaux

par

Grégoire CORRE

intitulée

Higher-order elastoplastic beam models

à soutenir le 19 avril 2018, devant le jury composé de:

Patrice CARTRAUD	Rapporteur	École Centrale de Nantes
David RYCKELYNCK	Rapporteur	École des Mines ParisTech
Bernadette MIARA	Examineur	Université Paris-Est
Xavier CESPEDES	Examineur	STRAINS
Mohammed-Khalil FERRADI	Examineur	STRAINS
Arthur LEBÉE	Examineur	École des Ponts ParisTech
Karam SAB	Directeur de thèse	IFSTTAR

Remerciements

Abstract

This thesis work is presented in the framework of a scientific partnership between Laboratoire Navier and the french start-up STRAINS. Believing in the need for new methodologies in structural analysis, STRAINS is developing a new software dedicated to the structural analysis of bridges. In this context, this work suggests new tools for the analysis of slender structures.

The higher-order elastic beam element developed by Ferradi et al. [2016] is first extended to the case of eigenstrains, enabling the model to deal with various physical phenomena such as creep, prestress or thermal loads. An enriched kinematics is used to capture the local response of the structure. Different examples highlight the local accuracy of the model and its fast computational performances.

The model is also extended to plasticity in small perturbations. Considering the plastic strains developing in the structure as eigenstrains, the previous works are used to derive a higher-order elastoplastic kinematics.

Finally, a new elastoplastic beam element for reinforced concrete is suggested. The concrete material is described by using the elastoplastic beam model developed previously while steel rebars are modeled by one dimensional bar elements. This method enables a fine local description of the concrete behavior and an accurate representation of the reinforcement. The validity of computations is assessed thanks to energy considerations.

Keywords: Beam model; Reduced model; Higher-order kinematics; Eigenstrains; Plasticity; Reinforced concrete

Résumé

Ce travail s'inscrit dans le cadre d'un partenariat scientifique entre le Laboratoire Navier et la société STRAINS. Convaincue du besoin de renouveler les méthodes actuelles de calcul de structures, STRAINS développe un nouveau logiciel dédié à l'analyse des ouvrages d'art. Dans ce contexte, cette thèse propose de nouveaux outils pour l'analyse des structures élancées.

Le modèle élastique de poutre d'ordre supérieur développé par Ferradi et al. [2016] est d'abord adapté au cas des déformations imposées, permettant ainsi au modèle de représenter un grand nombre de phénomènes physiques tels que le fluage, la précontrainte ou les chargements thermiques. Différents exemples viennent souligner la précision numérique du modèle ainsi que ses performances en temps de calcul.

Le modèle est également étendu au cadre de la théorie de la plasticité. Considérant les déformations plastiques comme des déformations imposées, les résultats précédemment obtenus sont utilisés pour développer une nouvelle cinématique d'ordre supérieur.

Enfin, un nouvel élément de poutre élastoplastique pour le béton armé est proposé. Le béton est décrit grâce au modèle élastoplastique et les ferrailages sont modélisés par des éléments barres à une dimension. Cette méthode permet une description précise du comportement du béton et une représentation fidèle des renforcements. La validité des calculs est évaluée par des considérations de dissipation énergétique.

Mots-clés Modèle de poutre; Cinématique d'ordre supérieur; Plasticité; Modèle réduit; Béton armé

Contents

Manuscript layout	1
1 Introduction	3
1.1 Industrial context	5
1.1.1 STRAINS: Structural Analysis & Innovative Softwares	5
1.1.2 Qantara: a new software dedicated to bridge analysis	7
1.2 Beam models in linear elasticity	9
1.2.1 The Euler-Bernoulli beam model	9
1.2.2 Shear force in a beam: The Timoshenko beam model	13
1.2.3 Torsion in a beam: the Vlasov beam theory	15
1.2.4 Non-uniform torsion in a beam: the Bescoter beam model	20
1.2.5 Higher-order beam models	22
1.3 Beam models in elastoplasticity	25
1.3.1 Introduction of elastoplasticity in beam models	25
1.3.2 Beam models based on a 1D macroscopic yield criterion	26
1.3.3 Beam models based on a local yield criterion	30
1.4 Beam models for reinforced concrete	37
1.4.1 Description of a reinforced concrete beam model	37
1.4.2 Concrete constitutive behavior	38
1.4.3 Definition of the beam model	42
2 Higher-order elastic beam model with eigenstrains	47
2.1 Introduction	48
2.2 Kinematic enrichment based on the formal asymptotic expansion	51
2.2.1 The 3D problem and the asymptotic expansion method	51
2.2.2 Cascade resolution	55
2.2.3 Families of kinematic enrichment	62
2.2.4 Numerical approximation of the higher-order beam model	62
2.3 Applications	66
2.3.1 Application to a thermal load	67
2.3.2 Application to a prestressed beam	76
2.4 Conclusion	79
3 Higher-order elastoplastic beam model	83
3.1 Introduction	84
3.2 Standard 3D plasticity	87

3.2.1	The elasto-plastic boundary value problem	87
3.2.2	J_2 flow theory with isotropic hardening	88
3.2.3	Standard 3D plasticity algorithm	89
3.3	From a 3D model to a higher order beam model	93
3.3.1	Reduction of the 3D model	94
3.3.2	The higher-order beam model	95
3.4	The elastoplastic beam model	99
3.4.1	Adaptation of the <i>AELD</i> -beam model to the elasto-plastic behavior	99
3.4.2	Numerical approximation of the higher order beam model	100
3.4.3	Formulation of the beam element	101
3.4.4	The elasto-plastic algorithm	102
3.5	Application to a cantilever beam	105
3.5.1	Study of alternative Newton-Raphson's methods	105
3.5.2	Cantilever beam loaded at its free extremity	109
3.5.3	Parametric studies	116
3.6	Conclusion	120
4	Higher-order elastoplastic beam model for reinforced concrete	123
4.1	Introduction	124
4.2	Definition of an elastoplastic reinforced concrete model	127
4.2.1	General framework and methodology	127
4.2.2	A new model for concrete materials	130
4.2.3	Modeling of steel rebars	135
4.2.4	Kinematic relation between rebars and concrete	137
4.3	Definition of a beam element	140
4.3.1	The <i>AELD</i> beam model	140
4.3.2	Description of the beam kinematics	141
4.3.3	Numerical approximation	142
4.3.4	Local integration of the equilibrium equations	142
4.4	Validation of the model	142
4.4.1	Reinforced T-beam in elasticity	143
4.4.2	Reinforced T-beam in elastoplasticity	148
4.4.3	Reinforced beam with the new concrete model	154
4.4.4	Validity of the elastoplastic model	158
4.4.5	Mesh sensitivity	161
4.5	Conclusion	165
	Conclusion and outlook	167
	A Proof of the symmetry of the beam constitutive equation	173
	Bibliography	175

Manuscript layout

After the second world war, the need for reconstruction and the cheap cost of materials have led to an important growth of the construction industry. In that context, structural engineering was mainly based on linear elastic computations and provided wide safety margins and conservative recommendations. The situation observed nowadays is different. Developed countries have reached high level of facilities and infrastructures and the main issue is to provide accurate expertise on existing structures. The french start-up STRAINS therefore ambitions to provide a new set of numerical tools for structural analysis.

This work is part of the development of a new software dedicated to the analysis of bridges called *Qantara*. It aims at developing new beam finite elements for the analysis of slender structures. This report is based on three articles produced during the time of this PhD and respectively constituting **Chapter 2**, **Chapter 3** and **Chapter 4**. An additional **Chapter 1** has been joined in order to introduce the subsequent chapters.

In **Chapter 1**, after setting the industrial context that initiated this work, a review of the elastic beam models is first depicted. Based on very simple assumptions and used in basic load cases, the first beam models have quickly proved to be insufficient for dealing with higher-order effects. The improvement of beam theories have resulted in an incremental extension of the beam kinematics. A chronological description of the beam models, from the simplest assumptions to the most complex kinematics is presented. This chapter is an introduction to the elastic beam element presented in **Chapter 2**. In a second time, a classification of elastoplastic beam models is suggested. The integration of the elastoplastic behavior can be addressed by macroscopic or local constitutive behaviors, and this introductory chapter of **Chapter 3** aims at distinguishing the main categories of elastoplastic models. Finally, an overview of the beam models for reinforced concrete is presented. This last chapter is an introduction to **Chapter 4**.

The software *Qantara* is mainly based on the higher-order beam element developed by [Ferradi et al. \[2016\]](#). Considering the need in civil engineering applications to account for many physical phenomena such as creep, thermal load or phasing construction, we aim in **Chapter 2** at developing a new beam element submitted to eigenstrains. Using the same theoretical procedure for the model reduction, a new beam element especially derived for the case of eigenstrains is presented. A couple of applications is suggested to illustrate the numerical performance of the model.

We believe that the framework of linear elasticity is too restrictive for accurate structural analysis and that nonlinear computations have become essential. Therefore we develop in **Chapter 3** an extension of the previous beam element to the framework of plasticity. We provide a new finite element combining the numerical accuracy of higher-order models and the time-efficiency of beam elements. This model is actually based on the beam element submitted to eigenstrains introduced in **Chapter 2** by considering the plastic strain as an eigenstrain imposed on the structure. After setting the standard 3D plasticity framework, reducing the 3D problem and describing the derivation of a kinematics accounting for nonlinear

and inelastic displacements, the model is illustrated by a case study highlighting its strong numerical abilities.

Considering the elastoplastic beam element presented in **Chapter 3**, we saw an opportunity to develop a new beam model for reinforced concrete. Using the simple and well-known framework of plasticity, **Chapter 4** defines a new model combining the simplicity and robustness of the theory of plasticity and the numerical accuracy and performance of the elastoplastic beam element previously derived. A 3D Rankine criterion is formulated for concrete and a closed-form expression of the local integration of the equilibrium equations is formulated. The integration of the steel rebars as bar elements embedded into the concrete volume is then described, and their kinematic connection to the concrete degrees of freedom is defined. Given that no 3D Rankine's yield criterion has been found in commercial softwares for a numerical evaluation of our model, a multistep procedure validation is finally presented.

* *
*

Chapter 1

Introduction

Abstract: *This chapter first sets the industrial context of the work presented in this report. The company STRAINS in which the PhD has been carried out is presented. The subsequent sections of this chapter are introductions to chapters 2, 3 and 4 respectively dealing with beam model in linear elasticity, beam models in elastoplasticity and beam models for reinforced concrete.*

Contents

1.1 Industrial context	5
1.1.1 STRAINS: Structural Analysis & Innovative Softwares	5
1.1.2 Qantara: a new software dedicated to bridge analysis	7
1.2 Beam models in linear elasticity	9
1.2.1 The Euler-Bernoulli beam model	9
1.2.2 Shear force in a beam: The Timoshenko beam model	13
1.2.3 Torsion in a beam: the Vlasov beam theory	15
1.2.4 Non-uniform torsion in a beam: the Benscoter beam model	20
1.2.5 Higher-order beam models	22
1.3 Beam models in elastoplasticity	25
1.3.1 Introduction of elastoplasticity in beam models	25
1.3.2 Beam models based on a 1D macroscopic yield criterion	26
1.3.3 Beam models based on a local yield criterion	30
1.4 Beam models for reinforced concrete	37
1.4.1 Description of a reinforced concrete beam model	37
1.4.2 Concrete constitutive behavior	38
1.4.3 Definition of the beam model	42

Notations

In this section are defined notations used in the whole manuscript.

- All latin indices take values between 1 and 3 and all greek indices take values between 1 and 2
- Implicit Einstein's summation is used here: given $\mathbf{a} = (a_1, a_2)$ and $\mathbf{b} = (b_1, b_2)$ two vectors, $a_\alpha b_\alpha = a_1 b_1 + a_2 b_2$
- Given a function $a(x_i)$, the following notation is used for the derivatives :

$$a_{,i} = \frac{da}{dx_i} \quad (1.1)$$

- According to the previous item, the following notation can be adopted for partial derivatives:

$$\partial_{x_i} = \frac{\partial}{\partial x_i}, \quad \partial_\sigma = \frac{\partial}{\partial \sigma} \quad (1.2)$$

- The in-plane Laplace operator is $\Delta_x = \partial_{x_1}^2 + \partial_{x_2}^2$
- The in-plane gradient operator is $\nabla_x = (\partial_{x_1}, \partial_{x_2})$
- ∇_x^s is the symmetric gradient operator
- The coefficient of Lamé are expressed in terms of the Young modulus E and the Poisson's ratio ν :

$$\mu = \frac{E}{2(1 + \nu)}, \quad \lambda = \frac{\nu E}{(1 + \nu)(1 - 2\nu)} \quad (1.3)$$

1.1. Industrial context

1.1 Industrial context

The objective of this section is to introduce the industrial context of this thesis. Born in 2014 in the minds of a handful of structural engineers, STRAINS aims at changing the current paradigm of structural analysis. As part of the development of the software program Qantara dedicated to the analysis of bridges, this work suggests new tools for the numerical analysis of structures.

1.1.1 STRAINS: Structural Analysis & Innovative Softwares

1.1.1.1 Historical context

Structural engineers have historically been concerned by two main issues: the mechanical expertise of existing structures and the design of new constructions. These two activities do not require the same skills. The first implies intuition and understanding of physical concepts while the second involves rigor and project management.

The construction industry has experienced an unprecedented growth in France since the end of the second world war: two third of buildings are post 1948. This effervescence has encouraged the production of studies for new constructions at the expense of the competences in structural expertise. In this context, the low cost of materials has stimulated aesthetic and functional considerations. Builders and designers were seeking for reliability of new complex structures rather than savings of materials or structural optimisation. This period of growth was long enough to strongly influence the structural engineering methods. The need for computer softwares has quickly become a clear evidence. Material consumption being not an issue, it has led to the development of fast computational methods ensuring large dimensioning margins that were not really assessed. Software publishers have designed time-efficient softwares able to provide studies for complex structures in the framlework of elasticity. But this assumption is no longer valid in the case of important loads. The elastic computations are usually followed by the automatic verification of norms and standards. It therefore guarantees the safety of structures at the cost of important margins.

Softwares for structural design and analysis are now able to span the whole production process, from general design of structures to construction drawings. Developments have been mainly brought to preprocessors for numerical modeling and to postprocessors for normative verifications. Such softwares aim to provide all the necessary tools to engineers to produce entire production studies. But they are based on ancient methods of mechanics and use low order finite element models in elasticity.

Given the current level of facilities and infrastructures, a decrease of the number of new constructions is predictable in developed countries. As a result, the need for structural expertise

for existing structures will become more and more important. The structural reliability of old infrastructures must be assessed and decisions must be taken about the necessity to strengthen or repair them. This issue already concerns nuclear industry and will soon encompass all the construction industry. It is therefore necessary to switch from a safe design with important but not assessed margins to a fine evaluation of these safety margins. Physical phenomena must be accurately understood and described. On the other hand, new buildings must now cope with an increase of the material cost. The design of new infrastructures must therefore be carried out with structural optimisation and material savings.

1.1.1.2 Structural analysis softwares

In order to assess the structural capacities of infrastructures, the linear elastic framework of classic design must be discarded. However, current nonlinear methods are time-consuming, and their numerical implementation and use require specific skills and knowledge. It is therefore necessary to look for new effective techniques to access to the post-elastic behavior of structures without a systematic use of complex nonlinear methods.

It is necessary for structural engineers to have a fast and global access to the weak points of a structure design. Bridges for example are mostly modeled and designed by using beam models with very simple kinematics. Those models cannot provide accurate information about the design weaknesses. Costly volumic computations are therefore postprocessed locally to validate the structure. But these computations are numerically too heavy to be carried out at a first step. An intermediate solution must therefore be found.

New softwares must be designed for experts rather than for production. The aim is not to provide a tool for systematic analysis, but for an accurate understanding of the physical phenomena at stake. Softwares must be easy to use and deliver clear results. They are addressed to experienced engineers and must avoid the "black box syndrom" by expliciting the numerical methods used and providing an efficient control of the computations to users. STRAINS develops a set of leading-edge softwares responding to these guidelines.

1.1.1.3 STRAINS

The start-up STRAINS is answering to the issues mentioned before by providing innovative software programs dedicated to the structural analysis of existing and future buildings and infrastructures. These programs are gathered into the numerical platform *Digital-Structure*.

A first aspect of *Digital-Structure* is dedicated to the analysis of ultimate capacity of structures as illustrated on Figure 1.1. The ultimate load is evaluated and framed on 3D meshes thanks to limit analysis. This very effective method avoids the use of incremental elastoplastic process. An error estimator is inherent to the method and automatic remeshing reduces the

1.1. Industrial context

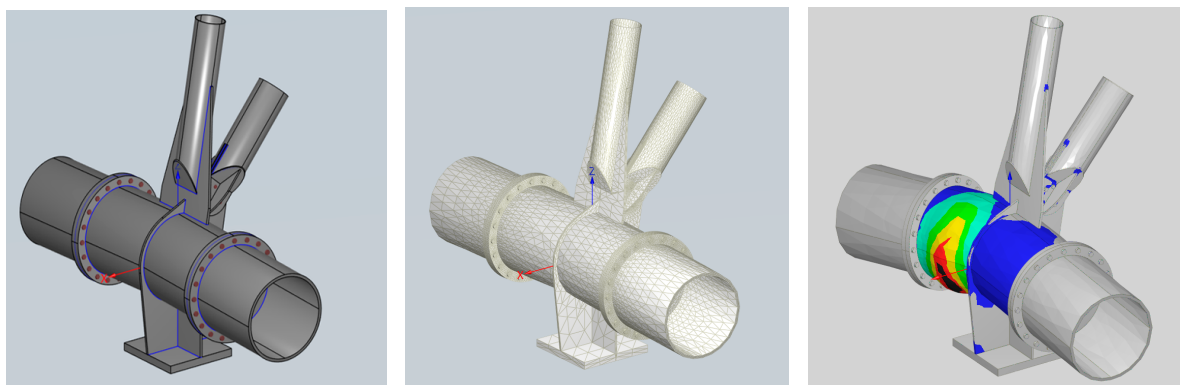


Figure 1.1 – Limit analysis of a connection on *Digital-Structure* (geometry, mesh and displacement)

discretization error. Modern optimisation techniques are used to this end such as the interior point method or second order conic programming [Bleyer, 2015]. A first program dedicated to the analysis of steel connection called *DS-Steel* is already achieved and sold. A new program called *DS-Concrete* for the analysis of reinforced concrete structures will soon be released.

Developments are also concentrated on the design of an innovative software program for the structural analysis of bridges called *Qantara*. Based on the seminal works of Ferradi [Ferradi et al., 2013; Ferradi and Cespedes, 2014; Ferradi et al., 2016] on the development of higher-order beam models, *Qantara* aims to provide a full modeling of the structure and yields local accurate results. Thanks to this model, postprocessings with volumic or shell discretization can be discarded. This program is expected to become a full structural analysis program including static and dynamic computations and accounting for a wide range of physical phenomena such as creep, phasing construction or prestress. *Qantara* is more precisely depicted in Section 1.1.2.

All the developments of STRAINS are based on modern computing techniques and embed cutting-edge numerical components. Programs are designed on the basis of a client-server model SAAS (Software As A Service), meaning that the computations are processed on-line on remote powerful servers. The client can therefore carry out computations from any numerical device with a web connection without any software installation. Results are stored on a cloud and can be downloaded locally by the client.

1.1.2 Qantara: a new software dedicated to bridge analysis

1.1.2.1 Softwares for bridge analysis: a state of the art

Many softwares for the structural analysis of bridges are available today on the market. Moreover, some of these softwares are not limited to the study of bridges but are developed for

a more general structural analysis framework. Examples of these are *Sofistik* (Germany), *Midas* (South Korea), *SAP2000* (USA), *RM Bridge* (Austria), *PCP* or *Pythagore* (France). However, the sector of bridge softwares has remained relatively undeveloped in France, inducing a switch towards foreign softwares. This is in contrast with the presence of strong french publishers in the sector of softwares dedicated to the building industry such as *Graitec* or *Robot* (now par of *AutoDesk*).

Software publishers concentrate their developments on two main topics. The first is the communication between computing programs and drawing programs such as *Revit* or *Autocad*. Second is the automatic check of the construction guidelines (Eurocodes, British Standard, Aashto). In this context, numerical fields such as stress, strains or displacement are considered as intermediate results not always accessible for the user. Softwares are therefore designed as "black box" in which the numerical models and data are not easy to access. Numerical methods are rarely explicated and a critical assessment of the numerical results is therefore not possible. The use of systematic procedures and automated softwares is a natural evolution for the sector of building construction where studies are very repetitive. But the opposite situation is observed in civil engineering construction where unique infrastructures are mostly considered.

Programs for civil engineering structures are mostly developed with beam finite elements. They are used to model important structures including bridge decks, piers and towers. But macroscopic models only deal with a fraction of the problem: longitudinal bending, which is assumed to be constant on the entire width of the structure. Moreover, bridge decks are now wider and wider in new bridge designs thus involving strong cross-sectional bending effects. These global models are in practice completed by local shell or volumic computations dedicated to the study of specific parts of the structure. This process is time-consuming and complex.

1.1.2.2 Conception and design of a new ambitious software

In the context mentioned in the previous section, STRAINS aims to provide innovative and modern tools for the structural analysis of bridges with the scientific support of Laboratoire Navier. The main objectives of the software are the following: a comprehensive model, the simplicity of use and a full set of analysis tools.

The main ingredient of this software is the new higher-order beam model developed by **Ferradi et al. [2016]**. Thanks to an enriched kinematics, the beam element enables the description of the cross-sectional behavior of the structures and various effects due to warping. In this context, the systematic use of complex shell or volumic computations is no longer necessary. By increasing the complexity of a standard beam model by a factor of 10 or 20 the model can provide results similar to the one usually obtained by local computations representing a complexity factor of 1000 or 10000. Above all, the iterative and repetitive switch between

1.2. Beam models in linear elasticity

global and local computations is avoided. To our knowledge and as explained in Section 1.2 and 1.3, many developments are carried out on this kind of beam element but no one has been implemented in a full structural analysis software so far.

In the short and medium term, the software should position as a full software encompassing the concepts of civil engineering. Nonlinear constitutive laws of construction materials like steel and reinforced concrete must especially be implemented. Error estimators will be integrated in the long run as well as automatic optimisation procedures.

The work presented in this report falls within the framework of the development of *Qantara*. First, the higher-order elastic beam element has been adapted to the case of eigenstrains (**Chapter 2**), enabling the model to account for phenomenological effects such as creep, prestress or thermal loads. Then, the beam model has been extended to the framework of elastoplasticity (**Chapter 3**). Finally, it has been used for the development of an elastoplastic beam model for reinforced concrete (**Chapter 4**). All these developments are presented in the subsequent sections.

1.2 Beam models in linear elasticity

This section presents a chronological review of the beam theories in linear elasticity. Starting from the Euler-Bernoulli beam theory, the main beam models are successively introduced and their beam equations are derived. The section is ended by a presentation of the more recent higher-order beam models and particularly models using the asymptotic expansion method.

1.2.1 The Euler-Bernoulli beam model

1.2.1.1 Local description

The beam model of Euler-Bernoulli may be the first beam model to be formulated. It is based on two simple kinematic assumptions, that are:

1. a cross-section is rigid in its own plane
2. a cross-section remains normal to the neutral axis of the beam

These assumptions can be translated into the following kinematics:

$$u_\alpha(\mathbf{x}) = U_\alpha(x_3), \quad u_3(\mathbf{x}) = U_3(x_3) - x_\alpha U_{\alpha,3}(x_3), \quad (1.4)$$

where $U_{\alpha,3}$ is actually the inclination of the section relative to the axis $O\mathbf{x}_\alpha$. This kinematics is represented on Figure 1.2.

The first hypothesis imply that no warping or transversal deformation can occur. As a

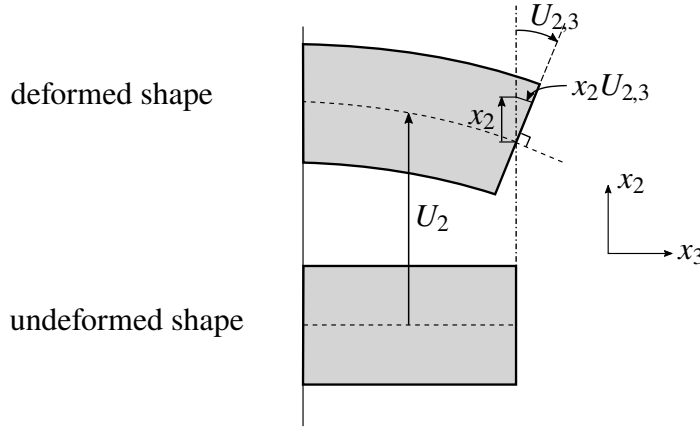


Figure 1.2 – Kinematics of the Euler-Bernoulli model

consequence, the Poisson's effect cannot be accounted for. The fact that the inclination of the section relative to Ox_α equals $U_{\alpha,3}$ is a result of the second hypothesis.

The strain tensor is defined by $\boldsymbol{\varepsilon} = \nabla_{\mathbf{x}}^s(\mathbf{u})$. As a result of Equations (1.4):

$$\varepsilon_{33}(\mathbf{x}) = U_{3,3}(x_3) - x_\alpha U_{\alpha,33}(x_3), \quad \varepsilon_{i\alpha} = \varepsilon_{\alpha i} = 0. \quad (1.5)$$

The Euler-Bernoulli beam model is formulated with the ad hoc assumption of pure traction in direction 3 and the components of $\boldsymbol{\sigma}$ are expressed:

$$\sigma_{33} = E (U_{3,3} - x_\alpha U_{\alpha,33}), \quad \sigma_{i\alpha} = \sigma_{\alpha i} = 0. \quad (1.6)$$

This expression is in clear contradiction with the constitutive law, that is:

$$\boldsymbol{\sigma} = 2\mu\boldsymbol{\varepsilon} + \lambda\text{tr}(\boldsymbol{\varepsilon}). \quad (1.7)$$

This incompatibility suggests that pure traction and pure axial strain cannot be simultaneously achieved with a non-zero Poisson's ratio. In order to fulfil the constitutive law, pure traction is considered and a new expression of $\boldsymbol{\varepsilon}$ is given in accordance with Equation (1.7):

$$\varepsilon_{\beta\beta} = -\nu (U_{3,3} - x_\alpha U_{\alpha,33}), \quad \varepsilon_{33} = U_{3,3} - x_\alpha U_{\alpha,33}, \quad \varepsilon_{ij} = \varepsilon_{ji} = 0 \text{ for } i \neq j. \quad (1.8)$$

The kinematic compatibility of strains is therefore discarded. Indeed, in the case of a non-zero Poisson's ratio, $\varepsilon_{11} = \varepsilon_{22} \neq 0$ and cross-sectional displacements occur. However the slenderness of the beam makes this displacement negligible in comparison with the other rigid motions so that it doesn't come into conflict with the initial assumption of rigid cross-sections.

1.2.1.2 Beam equations

The macroscopic beam equations are obtained by using the principle of virtual work. Considering a beam represented by the domain Ω , the internal work is expressed by:

$$\delta W^{\text{int}} = \int_{\Omega} \boldsymbol{\sigma} : \delta \boldsymbol{\varepsilon} dV. \quad (1.9)$$

1.2. Beam models in linear elasticity

According to Equations (1.8) and (1.6), δW^{int} expands in:

$$\delta W^{\text{int}} = \int_{\Omega} \sigma_{33} (\delta U_{3,3} - x_{\alpha} \delta U_{\alpha,33}) dV. \quad (1.10)$$

Equation (1.10) is integrated over the cross-section, yielding:

$$\delta W^{\text{int}} = \int_0^L (N \delta U_{3,3} + M_{\alpha} \delta U_{\alpha,33}) dx_3, \quad (1.11)$$

with L the length of the beam, N and M_{α} the normal force and the bending moments defined by:

$$N = \int_S \sigma_{33} dA, \quad M_{\alpha} = \int_S -x_{\alpha} \sigma_{33} dA \quad (1.12)$$

The integration by parts of Equation (1.11) is formulated as follows:

$$\delta W^{\text{int}} = \int_0^L (-N_{,3} \delta U_3 + M_{\alpha,33} \delta U_{\alpha}) dx_3 + [N \delta U_3 + M_{\alpha} \delta U_{\alpha,3} - M_{\alpha,3} \delta U_{\alpha}]_0^L. \quad (1.13)$$

The second term of the sum is identified as the external work δW^{ext} . The principle of virtual work ensuring that $\delta W^{\text{int}} = \delta W^{\text{ext}}$, Equation (1.13) leads to the relation:

$$\int_0^L (-N_{,3} \delta U_3 + M_{\alpha,33} \delta U_{\alpha}) dx_3 = 0 \quad (1.14)$$

Since any virtual displacement δU satisfies Equation (1.14), one finally gets the three static beam equations:

$$N_{,3} = 0, \quad M_{\alpha,33} = 0. \quad (1.15)$$

Macroscopic equilibrium is verified with three stress-resultants equations, which is consistent with the fact that three unknowns have been introduced in the kinematics (U_1, U_2 and U_3).

Remark It is considered in all what follows that the cross-sectional coordinate system is placed at the center of gravity of the cross-section, meaning that for a homogeneous section:

$$\int_S x_{\alpha} dA = 0, \quad \int_S x_1 x_2 dA = 0 \quad (1.16)$$

Thus, the bending moments can be expressed in terms of the transversal displacements:

$$M_{\alpha}(x_3) = EI_{\alpha} U_{\alpha,33}(x_3), \quad \text{with} \quad I_{\alpha} = \int_S x_{\alpha}^2 dA \quad (1.17)$$

Thanks to Equation (1.16), injecting the expression of the stress components into Equation (1.15) yields the local direct equations, that are:

$$u_{3,33} = 0, \quad u_{\alpha,3333} = 0 \quad (1.18)$$

1.2.1.3 Shear stress recovery

The Euler-Bernoulli model is a suitable theory for slender beams where the shear deflection can be neglected. But in practice engineers need to estimate the shear distribution in the cross-section. Shear force Q_α is first computed as the derivative of the bending moment:

$$Q_\alpha = M_{\alpha,3} \quad (1.19)$$

The distribution of the average shear stress τ_α at position h_α is then recovered in the cross-section thanks to the Jouravsky formula [Jouravskii, 1856]:

$$\tau_\alpha(h_\alpha) = \frac{Q_\alpha}{I_\alpha e(h_\alpha)} m_\alpha(h_\alpha), \quad (1.20)$$

where I_α is the bending moment, $e(h_\alpha)$ is the width of the beam at h_α and $m_\alpha(h_\alpha)$ is the static moment defined by:

$$m_\alpha(h_\alpha) = \int_{S_\alpha(h_\alpha)} x_\alpha dA. \quad (1.21)$$

$S_\alpha(h_\alpha)$ denotes the surface of the cross-section defined by $x_\alpha > h_\alpha$ as represented on Figure 1.3.

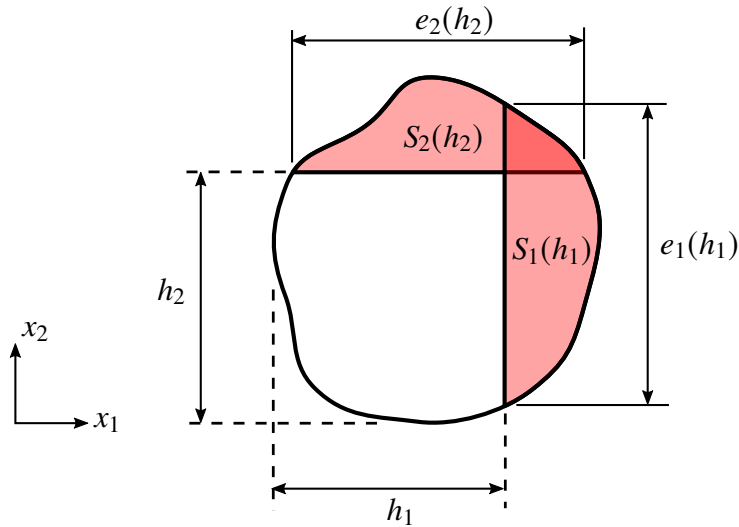


Figure 1.3 – Definition of a cross-section

1.2.1.4 Relevance of the model

The Euler-Bernoulli theory provides a very simple and convenient beam model with only three kinematic unknowns. The longitudinal variable x_3 is separated from the cross-sectional variables x_α in Equation (1.4). Pure longitudinal traction is assumed, leading to a strain kinematically incompatible but satisfying the constitutive law. As defined in Equation (1.8)

1.2. Beam models in linear elasticity

this model does not account for shear energy. This kinematics is therefore relevant for slender beams where shear effects are negligible. For shorter beams, shear effects are no longer negligible and must be taken into account, otherwise computations may lead to wrong estimates of the response of the beam. The Timoshenko model alleviates this problem.

1.2.2 Shear force in a beam: The Timoshenko beam model

1.2.2.1 Local description

The Timoshenko beam model keeps the assumption of rigid cross-section, but releases the normality of the cross-section to the neutral axis of the beam [Timoshenko, 1922]. This means that the inclination of the section relative to Ox_α is no longer equal to the longitudinal derivative of the transversal displacement $U_{\alpha,3}$. The kinematics of the model is given in Equation (1.22) and represented on Figure 1.4.

$$u_\alpha(\mathbf{x}) = U_\alpha(x_3), \quad u_3(\mathbf{x}) = U_3(x_3) - x_\alpha \theta_\alpha(x_3), \quad (1.22)$$

By relaxing the two inclinations θ_1 and θ_2 , the model accounts for shear strains. Indeed, the

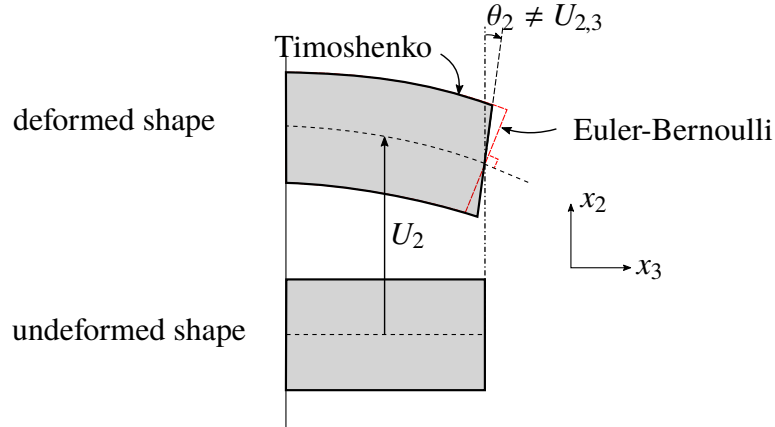


Figure 1.4 – Kinematics of the Timoshenko model

strain tensor $\boldsymbol{\varepsilon} = \nabla_{\mathbf{x}}^s(\mathbf{u})$ is expressed by;

$$\varepsilon_{\alpha\beta} = 0, \quad 2\varepsilon_{\alpha 3} = U_{\alpha,3} - \theta_\alpha, \quad \varepsilon_{33} = U_{3,3} - x_\alpha \theta_{\alpha,3}. \quad (1.23)$$

The Timoshenko beam model is also formulated by considering the in-plane stresses to be zero. The components of $\boldsymbol{\sigma}$ are expressed:

$$\sigma_{\alpha\beta} = 0, \quad \sigma_{\alpha 3} = \mu (U_{\alpha,3} - \theta_\alpha), \quad \sigma_{33} = E (U_{\alpha,3} - x_\alpha \theta_{\alpha,3}) \quad (1.24)$$

As for the Euler-Bernoulli, this expression is in contradiction with the constitutive law of Equation (1.7). $\varepsilon_{\alpha\beta} = 0$ and $\sigma_{\alpha\beta} = 0$ cannot be reached simultaneously with a non-zero

Poisson's ratio. In order to fulfill the compatibility, the considered strain is expressed by:

$$\boldsymbol{\varepsilon} = \begin{pmatrix} -\nu (U_{3,3} - x_\alpha \theta_{\alpha,3}) & 0 & \frac{1}{2} (U_{1,3} - \theta_1) \\ 0 & -\nu (U_{3,3} - x_\alpha \theta_{\alpha,3}) & \frac{1}{2} (U_{2,3} - \theta_2) \\ \frac{1}{2} (U_{1,3} - \theta_1) & \frac{1}{2} (U_{2,3} - \theta_2) & U_{3,3} - x_\alpha \theta_{\alpha,3} \end{pmatrix} \quad (1.25)$$

The model therefore accounts for a shear stress, that is:

$$\sigma_{\alpha 3}(\mathbf{x}) = \mu (U_{\alpha,3}(x_3) - \theta_\alpha(x_3)) \quad (1.26)$$

Given that $\sigma_{\alpha 3}$ only depends on the longitudinal coordinate, the shear stress is constant in the cross-section. However, the boundary conditions on the free edges of the cross-section impose the relation:

$$\sigma_{\alpha 3} n_\alpha = 0, \quad (1.27)$$

where n_α is the in-plane normal to edge of the cross-section. Consequently, because $\sigma_{\alpha 3} \neq 0$, the free boundary conditions cannot be enforced.

1.2.2.2 Beam equations

The principle of virtual works of Equation (1.10) is expressed as follows:

$$\delta W^{\text{int}} = \int_{\Omega} [\sigma_{13} (\delta U_{1,3} - \delta \theta_1) + \sigma_{23} (\delta U_{2,3} - \delta \theta_2) + \sigma_{33} (\delta U_{3,3} - x_\alpha \delta \theta_{\alpha,3})] dV. \quad (1.28)$$

By integrating over the cross-section and proceeding to an integration by parts, the following static beam equations are obtained:

$$Q_{\alpha,3} = 0, \quad -Q_\alpha + M_{\alpha,3} = 0, \quad N_{,3} = 0, \quad (1.29)$$

where the shear forces Q_α are the integration of the shear stresses over the cross-section:

$$Q_\alpha = \int_S \sigma_{\alpha 3} dA \quad (1.30)$$

Thus the macroscopic stress-resultants can be expressed in terms of the kinematic unknowns:

$$N = ESU_{3,3}, \quad Q_\alpha = \mu S (U_{\alpha,3} - \theta_\alpha), \quad M_\alpha = EI_\alpha \theta_{\alpha,3} \quad (1.31)$$

Thanks to Equation (1.16), injecting the expression of the stress components into Equation (1.29) yields the following local equilibrium equations:

$$u_{3,33} = 0, \quad u_{\alpha,33} - \theta_{\alpha,3} = 0, \quad \theta_{\alpha,333} = 0 \quad (1.32)$$

1.2. Beam models in linear elasticity

1.2.2.3 Relevance of the model

By accounting for a shear stress in its kinematics, the Timoshenko beam model improves the Euler-Bernoulli model and is therefore widely used in the engineering community. Its main limitation lies in the non-compliance with the free boundary conditions on the edges of the cross-sections. In practice, a correction factor k_{corr} is often used for the shear stress which then writes:

$$\sigma_{\alpha 3} = k_{\text{corr}} \mu (U_{\alpha,3} - \theta_{\alpha}). \quad (1.33)$$

As a result, the shear stiffness μS is modified into μS_{corr} , yielding a better estimation of the shear forces.

1.2.3 Torsion in a beam: the Vlasov beam theory

The Vlasov beam model is the first theory explicitly formulated to account for torsion. In the present section, the historical works on beams submitted to torsion are first depicted, including the crucial works of Saint-Venant. The solution of a beam submitted to a uniform torsion is then computed and the Vlasov beam model and its related beam equations are finally described.

1.2.3.1 Historical background

Torsion in bars has historically focused the attention of many great scientists, among whom Navier, Poisson, Cauchy and Saint-Venant. Coulomb was the first to establish in 1784 the relation between the torque M_3 and twist angle θ_3 in circular bars, that is:

$$M_3 = \mu J_{\text{circ}} \theta_{3,3}, \quad (1.34)$$

Indeed, in the particular case of circular bars submitted to torsion, cross-sections remain plane and the torsion constant J_{circ} is equal to the polar moment of inertia, which analytical expression is given by:

$$J_{\text{circ}} = \int_{\Omega} (x_1^2 + x_2^2) dV \quad (1.35)$$

Among other conclusions, he found that the shear stress was maximum at points furthest from the center of the circular bar.

In the beginning of the nineteenth century, Navier and Cauchy successively investigated the torsion of non-circular prismatic bars trying to establish the equation equivalent to Equation (1.34). In 1853, Saint-Venant was the first to correctly formulate the solutions of elliptic and rectangular bars submitted to torsion [[de Saint Venant, 1855](#)]. Based on the experimental data of Savart, torsion tests of Duleau and his own tests, he notably established that non-circular cross-sections do not remain plane when torsion is applied, that the shear stress was zero in

the corners of a rectangular cross-section and that the maximum shear stress was observed in the middle of the shorter edges [Saeed, 1962].

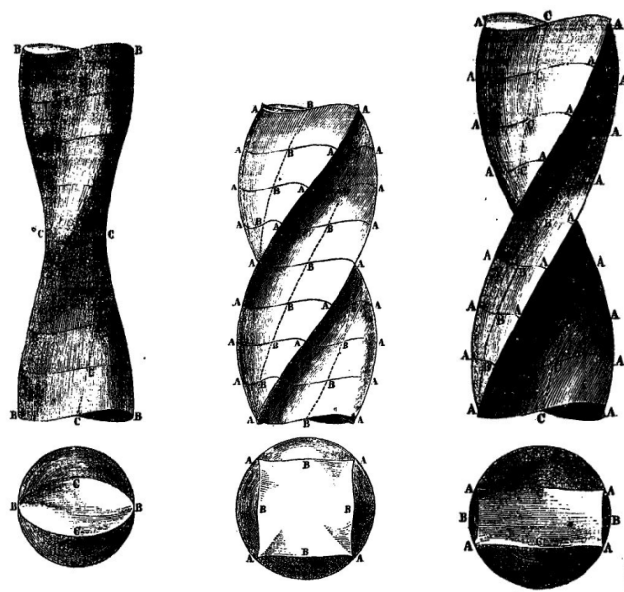


Figure 1.5 – Pure torsion of bars with elliptic, square and rectangular cross-sections: original drawings from A. Barré De Saint-Venant [de Saint Venant, 1855]

In 1871, Boussinesq analytically solved the problem of torsion in a beam by using an analogy with the corresponding hydrodynamic problem. Defining the shear stress by the equation:

$$\sigma_{13} = -\partial_{x_2} F, \quad \sigma_{23} = \partial_{x_1} F \quad (1.36)$$

where $F(x_1, x_2)$ satisfies $\Delta_x F = -2\mu\theta_{3,3}$, he figured out that solving the expression of F was equivalent to find the expression of the velocity of a fluid flowing along the axis of a tube with the same cross-section. In this context, he obtained the following expression of the torque:

$$M_3 = 2 \int_S F dA = \mu J \theta_{3,3}, \quad (1.37)$$

Most of the subsequent works on torsion were devoted to obtain the values of the torsional constant J for particular shapes of the cross-section.

Based on the previous works of Saint-Venant and Boussinesq, Vlasov suggested in 1961 a beam theory with torsional warping. This beam model is described in the present section.

1.2.3.2 Uniform torsion in a prismatic bar

We establish here the solution of a prismatic bar only submitted to uniform torsion, the cross-section being not necessarily circular. The uniform torsion in a bar is expressed by:

$$\theta_{3,33} = 0. \quad (1.38)$$

1.2. Beam models in linear elasticity

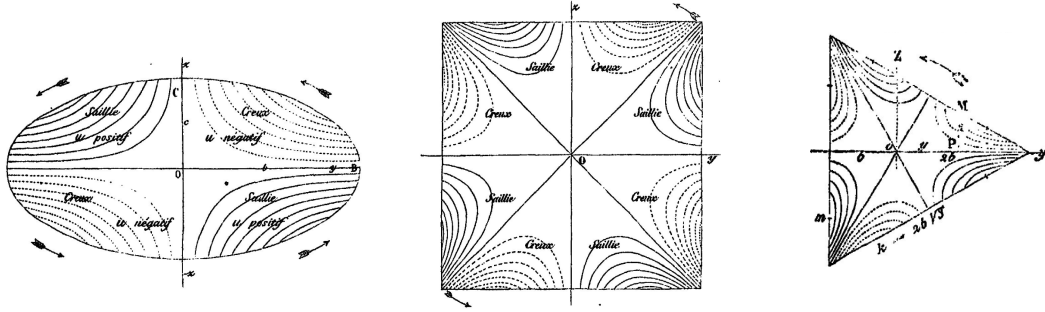


Figure 1.6 – Torsional warping for elliptic, square and triangular cross-sections: original drawings from A. Barré De Saint-Venant [de Saint Venant, 1855]

The kinematics of the solution writes:

$$\mathbf{u} = \begin{pmatrix} -x_2\theta_3 \\ x_1\theta_3 \\ \Psi(\mathbf{x}) \end{pmatrix}, \quad (1.39)$$

where $\Psi(\mathbf{x})$ is the torsion warping. The expression of Ψ is so far unknown. The strain $\boldsymbol{\varepsilon} = \nabla_{\mathbf{x}}^s \mathbf{u}$ takes the following expression:

$$2\varepsilon_{13} = -x_2\theta_{3,3} + \Psi_{,1}, \quad 2\varepsilon_{23} = x_1\theta_{3,3} + \Psi_{,2}, \quad \varepsilon_{\alpha\beta} = \varepsilon_{33} = 0, \quad (1.40)$$

and the stress writes:

$$\sigma_{13} = \mu(-x_2\theta_{3,3} + \Psi_{,1}), \quad \sigma_{23} = \mu(x_1\theta_{3,3} + \Psi_{,2}), \quad \sigma_{\alpha\beta} = \sigma_{33} = 0. \quad (1.41)$$

The local equilibrium is given by the relation:

$$\operatorname{div}(\boldsymbol{\sigma}) = \mathbf{0}. \quad (1.42)$$

We consider the third equation of (1.42), that is:

$$\sigma_{3i,i} = 0. \quad (1.43)$$

Injecting Equation (1.41) into (1.43) yields the simple relation:

$$\Delta_{\mathbf{x}}\Psi = 0, \quad (1.44)$$

where $\Delta_{\mathbf{x}} = \partial_{x_1}^2 + \partial_{x_2}^2$ is the cross-sectional Laplace operator. The free boundary conditions on the edges of the cross-section is expressed by:

$$\sigma_{\alpha 3}n_{\alpha} = 0, \quad (1.45)$$

which then yields, thanks to Equation (1.41):

$$\nabla_{\mathbf{x}}\Psi \cdot \mathbf{n} = \theta_{3,3}(x_1n_2 - x_2n_1), \quad (1.46)$$

where $\nabla_x = (\partial_{x_1}, \partial_{x_2})$ and $\mathbf{n} = (n_1, n_2)$. Denoting by ∂S the boundary of the cross-section S , the torsion warping function Ψ is defined within a constant by the following partial differential problem:

$$\begin{cases} \Delta_x \Psi = 0 & \text{on } S \\ \nabla_x \Psi \cdot \mathbf{n} = \theta_{3,3} (x_1 n_2 - x_2 n_1) & \text{on } \partial S \end{cases} \quad (1.47)$$

The resolution of Equation (1.47) cannot be carried out analytically, except for the special case of circular sections where $\Psi = 0$. It therefore requires numerical methods such as the finite element method. The torsional warping for elliptic, square and triangular cross-sections was early represented by Saint-Venant (see Figure 1.6).

1.2.3.3 The Vlasov kinematics

Vlasov included in his model the solution of Equation (1.47) as a new static degree of freedom [Vlasov, 1961]. The torsional kinematics of the Vlasov beam model therefore writes:

$$\mathbf{u}(\mathbf{x}) = \begin{pmatrix} -x_2 \theta_3(x_3) \\ x_1 \theta_3(x_3) \\ \psi(x_\alpha) \theta_{3,3}(x_3) \end{pmatrix} \quad (1.48)$$

According to Equation (1.48), and within the framework of plane stress, the stress is given by:

$$\boldsymbol{\sigma} = \begin{pmatrix} 0 & 0 & \mu (\psi_{,1} - x_2) \theta_{3,3} \\ 0 & 0 & \mu (\psi_{,2} + x_1) \theta_{3,3} \\ \mu (\psi_{,1} - x_2) \theta_{3,3} & \mu (\psi_{,2} + x_1) \theta_{3,3} & E \psi \theta_{3,3} \end{pmatrix}. \quad (1.49)$$

The constitutive law then yields the expression of the compatible strain:

$$\boldsymbol{\varepsilon} = \begin{pmatrix} -\nu \psi \theta_{3,3} & 0 & \frac{1}{2} (\psi_{,1} - x_2) \theta_{3,3} \\ 0 & -\nu \psi \theta_{3,3} & \frac{1}{2} (\psi_{,2} + x_1) \theta_{3,3} \\ \frac{1}{2} (\psi_{,1} - x_2) \theta_{3,3} & \frac{1}{2} (\psi_{,2} + x_1) \theta_{3,3} & \psi \theta_{3,3} \end{pmatrix} \quad (1.50)$$

1.2.3.4 Beam equations

The principle of virtual works of Equation (1.10) is expressed according to Equations (1.49) and (1.50):

$$\delta W^{\text{int}} = \int_{\Omega} [\sigma_{13} (\psi_{,1} - x_2) \theta_{3,3} + \sigma_{23} (\psi_{,2} + x_1) \theta_{3,3} + \sigma_{33} \psi \theta_{3,3}] dV \quad (1.51)$$

Integrating over the cross-section leads to the following expression of δW^{int} :

$$\delta W^{\text{int}} = \int_0^L [(M_3 + \phi) \delta \theta_{3,3} + B \delta \theta_{3,3}] dV, \quad (1.52)$$

1.2. Beam models in linear elasticity

with the stress-resultants M_3 , ϕ and B are defined by:

$$M_3 = \int_S (x_1 \sigma_{23} - x_2 \sigma_{13}) dA, \quad \phi = \int_S \sigma_{\alpha 3} \psi_{,\alpha} dA, \quad B = \int_S \sigma_{33} \psi dA \quad (1.53)$$

The stress-resultants are expressed in terms of the kinematic unknowns by injecting the expression of the stress components of Equation (1.50) into Equation (1.53):

$$M_3 = \mu J \theta_{3,3}, \quad \phi = \mu P \theta_{3,3}, \quad B = EK \theta_{3,33}, \quad (1.54)$$

where

$$J = \int_S u_{\alpha}^{\text{tor}} (\psi_{,\alpha} + u_{\alpha}^{\text{tor}}) dA, \quad P = \int_S \psi_{,\alpha} (u_{\alpha}^{\text{tor}} + \psi_{,\alpha}) dA, \quad K = \int_S \psi^2 dA, \quad (1.55)$$

with $\mathbf{u}^{\text{tor}} = (-x_2, x_1)$ the in-plane rotation of the section. The first equation of (1.54) is the same equation as the one formulated by Coulomb in 1784 for circular beams. The expression of the torsion constant J which is equal to the polar moment of inertia for circular sections, is given in Equation 1.55 for general cross-sections. The bi-moment B appears for nonuniform torsion. An simple example involving the bi-moment is a clamped thin-walled beam submitted to torsion at its free end: the boundary condition prevents the section from rotating and generates a kinematic frustration that propagates longitudinally. K is called the warping constant. The constant P is actually equals to zero. Indeed, integrating by part the expression of P in Equation (1.55) yields:

$$P = \int_S \psi (\text{div}_{\mathbf{x}} \mathbf{u}^{\text{tor}} + \Delta_{\mathbf{x}} \psi) dA + \int_{\partial S} \psi (\nabla_{\mathbf{x}} \psi + \mathbf{u}^{\text{tor}}) \cdot \mathbf{n} dl \quad (1.56)$$

According to Equation (1.47), $\Delta_{\mathbf{x}} \psi = 0$ and using Equation (1.48) yields $\nabla_{\mathbf{x}} \psi \cdot \mathbf{n} = -\mathbf{u}^{\text{tor}} \cdot \mathbf{n}$ on ∂S . Given that $\text{div}_{\mathbf{x}} \mathbf{u}^{\text{tor}} = 0$, we finally get $P = 0$.

By integrating by part Equation (1.52), the virtual work δW^{int} can be expressed as follows:

$$\delta W^{\text{int}} = \int_0^L (B_{,33} - M_{3,3}) \delta \theta_3 dx_3 + [(M_3 - B_{,3}) \delta \theta_3 + B \delta \theta_{3,3}]_0^L \quad (1.57)$$

The second member of Equation (1.57) is the external work δW^{ext} , yielding the following equation:

$$\int_0^L (B_{,33} - M_{3,3}) \delta \theta_3 dx_3 = 0. \quad (1.58)$$

Equation (1.58) being satisfied for any virtual displacement, the static beam equations are:

$$B_{,33} - M_{3,3} = 0 \quad (1.59)$$

The local equilibrium equation is obtained by injecting the expression of the stress components of Equation (1.50) into Equation (1.60):

$$\theta_{3,3333} - \omega^2 \theta_{3,33} = 0 \quad (1.60)$$

where $\omega^2 = \frac{\mu J}{EK}$. The solution of Equation (1.60) is given by:

$$\theta_3(x_3) = ae^{\omega x_3} + be^{-\omega x_3} + cx_3 + d, \quad (1.61)$$

where the constants a , b , c and d are determined by the boundary conditions on the rotation and the warping of the two extremities.

1.2.3.5 Relevance of the model

The theory developed by Vlasov for the torsion of beams enlarges the possible deformations described by a beam model. In Equation (1.48), the longitudinal variable x_3 is still separated from the cross-sectional variables x_α . The Vlasov beam model becomes particularly relevant for short cantilever beams submitted to torsion where the bi-moment is non negligible and the torsional warping becomes important. The torsional warping mode and its associated degree of freedom have been computed for uniform torsion in prismatic bars. Consequently the model becomes less relevant when it comes to non-uniform torsion. The Bencoter beam model described in the coming section mitigates this problem.

1.2.4 Non-uniform torsion in a beam: the Bencoter beam model

1.2.4.1 The Bencoter kinematics

Based on the beam model developed by Vlasov, Bencoter suggested to relax the kinematic variable associated to the new torsional warping mode [Bencoter, 1954]. The computation of the warping mode ψ is unchanged and solved according to Equation (1.47), but its associated variable is not equal to the unit angle of torsion $\theta_{3,3}$. This kinematic enrichment enables a better description of the non-uniform torsion. The kinematics of the Bencoter model therefore writes:

$$\mathbf{u}(\mathbf{x}) = \begin{pmatrix} -x_2\theta_3(x_3) \\ x_1\theta_3(x_3) \\ \psi(x_\alpha)\xi(x_3) \end{pmatrix}, \quad (1.62)$$

$\xi(x_3)$ being the new degree of freedom associated to the warping mode $\psi(x_\alpha)$.

1.2.4.2 Beam equations

The strain and stress are expressed according to Equation (1.62). The principle of virtual works then yields:

$$\delta W^{\text{int}} = \int_{\Omega} [\sigma_{13} (\psi_{,1}\xi - x_2\theta_{3,3}) + \sigma_{23} (\psi_{,2}\xi + x_1\theta_{3,3}) + \sigma_{33}\psi\xi_{,3}] dV \quad (1.63)$$

1.2. Beam models in linear elasticity

After an integration by part, the following static beam equations are obtained:

$$B_{,3} - \phi = 0 \quad M_{3,3} = 0 \quad (1.64)$$

where the stress-resultants are expressed according to Equation (1.53). They can be written in terms of the kinematic unknowns by using the stress components expressions:

$$M_3 = \mu (L\xi + I_0\theta_{3,3}), \quad \phi = \mu (Q\xi + L\theta_{3,3}), \quad B = EK\xi_{,3}, \quad (1.65)$$

where L , I_0 , Q are defined by:

$$L = \int_S (\mathbf{u}^{\text{tor}} \cdot \nabla_x \psi) dA, \quad I_0 = \int_S \mathbf{u}^{\text{tor}} \cdot \mathbf{u}^{\text{tor}} dA, \quad Q = \int_S \nabla_x \psi \cdot \nabla_x \psi dA. \quad (1.66)$$

K is expressed according to Equation (1.55). The beam equations can be expressed under the following matrix form:

$$\begin{pmatrix} M_3 \\ \phi \\ B \end{pmatrix} = \begin{pmatrix} \mu I_0 & \mu L & 0 \\ \mu L & \mu Q & 0 \\ 0 & 0 & Ek \end{pmatrix} \begin{pmatrix} \theta_{3,3} \\ \xi \\ \xi_{,3} \end{pmatrix} \quad (1.67)$$

Injecting Equation (1.66) into Equation (1.64) leads to the local equilibrium equation:

$$\theta_{3,33} = -\frac{L}{I_0} \xi_{,3} \quad \xi_{,333} - \omega^2 \xi_{,3} = 0, \quad \text{with } \omega^2 = \mu \frac{QI_0 - L^2}{EKI_0} \quad (1.68)$$

One can notice that:

$$\mu \int_S \left[\begin{pmatrix} \mathbf{u}^{\text{tor}} \\ \nabla_x \psi \\ \sqrt{E/\mu} \psi \end{pmatrix} \left(\mathbf{u}^{\text{tor}} \quad \nabla_x \psi \quad \sqrt{E/\mu} \psi \right) \right] dA = \begin{pmatrix} \mu I_0 & \mu L & X \\ \mu L & \mu Q & Y \\ X & Y & EK \end{pmatrix}. \quad (1.69)$$

The second member of Equation (1.69) is therefore a positive semi-definite matrix, and consequently the relation $QI_0 - L^2 \geq 0$ is satisfied, ensuring that $\omega^2 \geq 0$. The solution of Equation (1.68) is given by:

$$\theta_3 = -\frac{L}{I_0\omega} (ae^{\omega x_3} - be^{-\omega x_3}) + dx_3 + e, \quad \xi = ae^{\omega x_3} + be^{-\omega x_3} + c. \quad (1.70)$$

The constants are determined by the boundary conditions on the rotation and the warping of the two extremities.

1.2.4.3 Relevance of the model

The adjustment brought by Benscoter to the Vlasov model can be compared to the one operated by Timoshenko on the Euler-Bernoulli model: a kinematic variable associated to a new displacement mode is relaxed by creating a new degree of freedom. The relaxation of the torsional warping enables a better description of the non-uniform torsion. This new degree of freedom is especially useful in the case of a clamped boundary where a kinematic frustration propagates from the extremity along the longitudinal axis.

1.2.5 Higher-order beam models

The beam theories presented so far have been introduced in a chronological sequence, and therefore from the simplest kinematics to the richest. Many models with further kinematic refinements have since been suggested in order to overcome the limitations of the previous theories, resulting in the development of higher-order beam models. After a brief description of the works of Saint-Venant, partially mentioned in Section 1.2.3 for the study of torsion, some of these models considered both significant and relevant for the present document are presented in this section.

1.2.5.1 The Saint-Venant solution

As illustrated by the models presented so far, the common method used to improve a beam solution is to enlarge the kinematics of its displacement solution and to relax the associated degree of freedom if needed.

The Timoshenko beam model represents an enhancement of the Euler-Bernoulli model by accounting for shear effects. However it cannot satisfy the free boundary conditions as mentioned in Section 1.2.2. This issue has been actually solved by Saint-Venant in the XIXth century. He first considered an homogeneous isotropic beam loaded at its end in a weak sense. Starting from 3D considerations, a full 3D solution was obtained where the 6 classical generalized stress evolve linearly along the beam and where the cross-section can deform in its own-plane and out of its plane. In this context, the displacement solution was found to be a linear combination of the 6 rigid motions of the cross-section and of new displacements he computed. The free boundary conditions are satisfied with these additional displacements and a better approximation of the 3D stress solution is obtained. Furthermore, the traction, bending moments, torsion moment and shear forces are correctly evaluated. The kinematics associated to this solution is commonly known as the Saint-Venant solution.

In order to further improve the accuracy of beam solutions, many refined models have been developed. Because of their enlarged kinematics they are called higher-order beam models. Some of them are presented in this section.

1.2.5.2 The Iesan beam model

Iesan suggested an extension of the Saint-Venant solution to the case of heterogeneous and anisotropic cross-sections [Iesan, 1976], the elasticity tensor being considered as a function of the in-plane coordinates $C_{ijkl} = C_{ijkl}(x_1, x_2)$. Assuming that the displacement vector is also a function of the only in-plane coordinates $u_i = u_i(x_1, x_2)$, the local equilibrium equations are expressed on the cross-section. The solutions of the local equilibrium equations are the 6 rigid motions of the cross-section and 4 additional displacement solutions.

1.2. Beam models in linear elasticity

In the case of an homogeneous and isotropic material, the 4 additional solutions are exactly the additional displacements previously identified by Saint-Venant. Their closed-form expressions are:

$$\mathbf{u}^{(1)} = \frac{\nu}{2} \begin{pmatrix} x_2^2 - x_1^2 \\ -2x_1x_2 \\ 0 \end{pmatrix}, \quad \mathbf{u}^{(2)} = \frac{\nu}{2} \begin{pmatrix} -2x_1x_2 \\ x_1^2 - x_2^2 \\ 0 \end{pmatrix}, \quad \mathbf{u}^{(3)} = \nu \begin{pmatrix} -x_1 \\ -x_2 \\ 0 \end{pmatrix}, \quad \mathbf{u}^{(4)} = \begin{pmatrix} 0 \\ 0 \\ \psi(x_1, x_2) \end{pmatrix}. \quad (1.71)$$

The function ψ is the torsional warping already introduced in the Vlasov beam model. The 10 identified solutions of the cross-sectional equilibrium equations compose the kinematics of the model. According to Equation (1.71), 3 transversal displacement and 1 warping displacement are added to the 3 rigid translations and 3 rigid rotations of the cross-section. $\mathbf{u}^{(1)}$ and $\mathbf{u}^{(2)}$ are higher-order displacements associated to the bending of the beam, whereas $\mathbf{u}^{(3)}$ is associated to its extension. These 3 displacements are considered only for a non-zero Poisson's ratio.

Based on this kinematics, the beam model is then formulated. The body forces and surface tractions considered are assumed to be polynomial functions of the longitudinal coordinate:

$$\mathbf{f} = \sum_{p=1}^m \tilde{\mathbf{f}}_p(x_1, x_2)x_3^p \quad (1.72)$$

$$\mathbf{t} = \sum_{p=1}^m \tilde{\mathbf{t}}_p(x_1, x_2)x_3^p, \quad (1.73)$$

where $\tilde{\mathbf{f}}_p$ and $\tilde{\mathbf{t}}_p$ are functions of the in-plane coordinates and belong to C^∞ . The solution is then computed thanks to a cascade resolution: assuming that the solution of the problem loaded by the body force $\mathbf{f}^n = \tilde{\mathbf{f}}_n(x_1, x_2)x_3^n$ and the surface traction $\mathbf{t}^n = \tilde{\mathbf{t}}_n(x_1, x_2)x_3^n$ is known, the problem loaded by \mathbf{f}^{n+1} and \mathbf{t}^{n+1} is formulated and solved. This way, the global problem is solved order by order and the corresponding solutions are added to form the global solution.

Iesan successfully extended the Saint-Venant solution to the case of inhomogeneous and anisotropic beams. A limitation of the model presented here is the high regularity required for the loads. Indeed, concentrated loads commonly used in practice cannot be described by Equations (1.72) or (1.73).

1.2.5.3 The asymptotic expansion models

The asymptotic expansion method Originated by the works of Lions [1973], the asymptotic expansion method has been widely used for the development of beam models. The concept of this method is to express the variables of the 3D problem as power series of a small parameter. In the case of beams it is the ratio between the typical size of the cross-section and the length of the beam. Let consider for example a variable of the 3D problem \mathbf{a} , a beam of length L and with a typical dimension of its cross-section h . The scaling ratio $\eta = h/L$ is formed and \mathbf{a} is

expanded as follows:

$$\mathbf{a}(\mathbf{x}) = \sum_{k=0} \eta^k a_k(\mathbf{x}), \quad (1.74)$$

where $a_k(\mathbf{x})$ is the k^{th} -order term of the asymptotic expansion of \mathbf{a} . By introducing into the rescaled problem the asymptotic expansions of each variable, the 3D problem can be expressed as a power series of auxiliary problems. This collection of auxiliary problems are then solved by induction. The first problems correspond to the leading orders of the problem ($k = 0, 1, 2, \dots$), while the higher-orders effects of the global response of the structure are described by higher-order auxiliary problems.

The asymptotic expansion method for beam models Thanks to the asymptotic expansion method, [Trabucho and Viaño \[1987\]](#) derived the beam theories previously developed, offering by the way a new mathematical justification and insight to these models. The Euler-Bernoulli theory is obtained in the first order of the asymptotic expansion. Going further in the expansion, they derived the Timoshenko beam model [[Trabucho and Viaño, 1990](#)], the Saint-Venant solution [[Trabucho and Viano, 1988](#)] and developed models higher-order kinematics [[Trabucho and Viano, 1989](#)].

The resolution on the cross-section of the auxiliray problems previously introduced yields a collection of in-plane and warping displacements $\tilde{\mathbf{u}}^i = \tilde{\mathbf{u}}^i(x_1, x_2)$ here called displacement modes. These displacements modes are added to the kinematics of the model. The 3D displacement \mathbf{u} therefore writes:

$$\mathbf{u} = \sum_{k=1}^n \tilde{\mathbf{u}}^i(x_1, x_2) X_i(x_3), \quad (1.75)$$

where n is the size of the collection. The asymptotic expansion method is used for the computation of the displacement modes but not for the resolution of the element. Considering the modes $\tilde{\mathbf{u}}^i$ as kinematic enrichment carried by the independent generalized beam displacements $X_i = X_i(x_3)$ overcomes the problem of regularity conditions identified in the model of Iesan but also present if the asymptotic expansion formalism is considered for the resolution of the element. Indeed, the application of the minimum of the potential energy on this kinematics results in low regularity restrictions on the load applied. The formal mathematical framework of this method also called the Galerkin spectral approximation has been depicted in [[Miara and Trabucho, 1992](#)].

As a result, the asymptotic expansion method provides a systematic method to enrich the kinematics of a beam model. The expansion order can be arbitrarily fixed, and the collection of displacement modes is optimal for a given order n in terms of approximation error far from the extremities. The limitation of the asymptotic method lies in the description of the reponse of the structure close to the boundary conditions. Indeed, the displacement modes being computed for cross-section far from the extremities, the influence of the boundary conditions

1.3. Beam models in elastoplasticity

on the response of the structure is not explicitly captured by the kinematic enrichment. This issue, not presented in this report, has been solved by STRAINS by computing additional displacement modes specific to the boundary conditions.

Remark The expression of the displacement used in Equation (1.75) is a very general notation for beam models and is not limited to the scope of asymptotic expansion models. For example, the Euler-Bernoulli model can be expressed according to this formalism by writing:

$$\tilde{\mathbf{u}}^1 = \begin{pmatrix} 1 \\ 0 \\ 0 \end{pmatrix}, \quad \tilde{\mathbf{u}}^2 = \begin{pmatrix} 0 \\ 1 \\ 0 \end{pmatrix}, \quad \tilde{\mathbf{u}}^3 = \begin{pmatrix} 0 \\ 0 \\ 1 \end{pmatrix}, \quad \tilde{\mathbf{u}}^4 = \begin{pmatrix} 0 \\ 0 \\ x_1 \end{pmatrix}, \quad \tilde{\mathbf{u}}^5 = \begin{pmatrix} 0 \\ 0 \\ x_2 \end{pmatrix}, \quad (1.76)$$

each mode being respectively associated with the following kinematic variables:

$$X_1 = U_1, \quad X_2 = U_2, \quad X_3 = U_3, \quad X_4 = -U_{1,3}, \quad X_5 = -U_{2,3} \quad (1.77)$$

The improvement brought by the Timoshenko beam theory simply consists in relaxing the kinematic variables X_4 and X_5 , meaning that the same 5 displacement modes are considered, but are associated with the following kinematic variables:

$$X_1 = U_1, \quad X_2 = U_2, \quad X_3 = U_3, \quad X_4 = -\theta_1, \quad X_5 = -\theta_2 \quad (1.78)$$

The higher-order models presented in this section then introduce additional displacement modes and kinematic variables.

The development of richer kinematics has led to higher-order beam models able to describe a wide range of phenomena in linear elasticity. The introduction of elastoplasticity addressed in the next section is much more complex and the development of higher-order kinematics for the description of elastoplastic behaviors is not straightforward.

1.3 Beam models in elastoplasticity

This section suggests a classification of the elastoplastic beam models. Two main categories of models can be distinguished. First, the models based on a yield criterion expressed in terms of one or several stress-resultants. These models are based on a macroscopic criterion providing fast computational performance but poor local results. Second, the models using a yield criterion expressed in terms of the stress-components. These models are locally accurate, but are computationally more demanding.

1.3.1 Introduction of elastoplasticity in beam models

Elastoplasticity deals with the formation of irreversible strains in the structure and their nonlinear effects on the global response of the beam.

At the cross-section scale, plastic strains $\boldsymbol{\varepsilon}^p$ appear when the material is stressed beyond its elastic limit. The total strain is therefore the sum of an elastic strain and a plastic strain:

$$\boldsymbol{\varepsilon} = \boldsymbol{\varepsilon}^e + \boldsymbol{\varepsilon}^p. \quad (1.79)$$

The nonlinear behavior of the beam is expressed through the stress-strain relationship. The total strain being kinematically compatible and because of the apparition of plastic strain, stress cannot be computed as a linear function of the displacement \boldsymbol{u} anymore:

$$\boldsymbol{\sigma} = \boldsymbol{C} : (\nabla^s \boldsymbol{u} - \boldsymbol{\varepsilon}^p), \quad (1.80)$$

with \boldsymbol{C} the stiffness tensor.

At the beam scale, the nonlinear behaviour of the structure is given by the relationship between generalized stress and kinematic variables, as illustrated by the static beam equations given in Equations (1.15), (1.29), (1.54) or (1.64). It is a macroscopic consequence of the local nonlinear behaviour defined in Equation (1.80).

The state of the structure can therefore be defined either by the macroscopic stress-resultants or by the local stresses. In each case, the elastic or plastic state of the beam is determined through the use of a yield criterion. As a result the integration of the elastoplastic behavior in a beam model might be adressed by two approaches.

The first approach consists in accounting for plasticity by using a yield criterion expressed in terms of the stress-resultants. The local stresses are computed with an elastic assumption, then integrated to form the generalized stresses. The latter are then corrected in case of a plastic evolution according to the yield criterion. This method requires a preliminary formulation of the yield surface for the corresponding stress-resultants. These nonlinear relations must be established by 2D or 3D computations and should account for stress-resultants interactions.

The second approach is based on a local yield criterion expressed in terms of the local stress $\boldsymbol{\sigma}$. A 3D beam kinematics is considered and the elastoplastic behavior is locally integrated. The two different approaches are described in Figure 1.7.

A review of the two approaches is presented in Section 1.3.2 for the models using a 1D elastoplastic beam models and in Section 1.3.3 for the 3D elastoplastic beam models.

1.3.2 Beam models based on a 1D macroscopic yield criterion

1.3.2.1 An illustrative 1D elastoplastic Timoshenko beam model

Based on the simple model introduced in [Owen and Hinton, 1980], the 1D approach is first illustrated with an elastoplastic model based on the Timoshenko kinematics. The Timoshenko beam kinematics has been described in Section 1.2.2.

1.3. Beam models in elastoplasticity

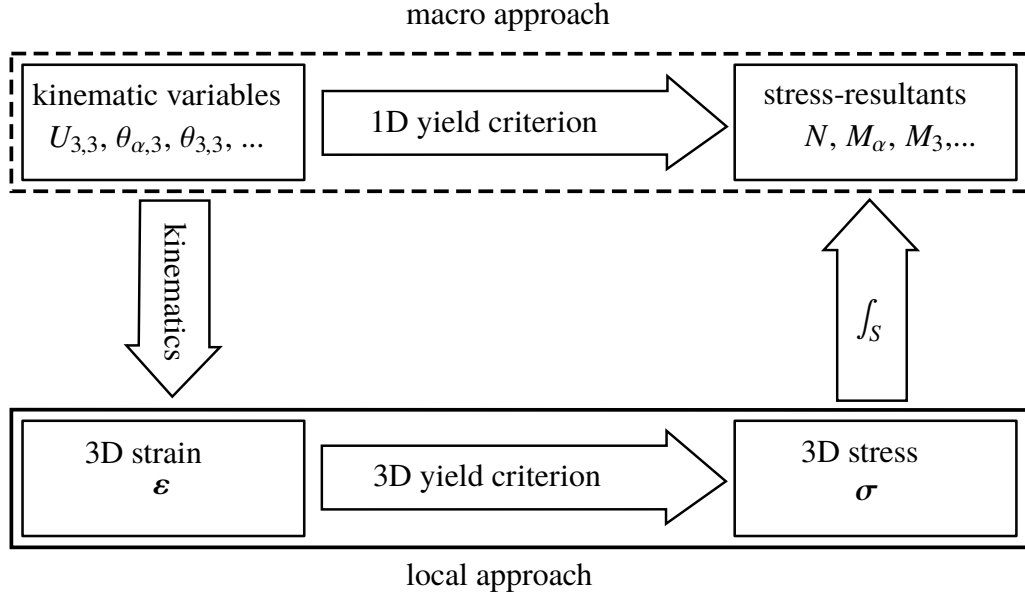


Figure 1.7 – Illustration of the macroscopic and microscopic elastoplastic integration schemes

We consider a rectangular beam of cross-sectional dimensions $b \times h$ submitted to bending around the axis Ox_1 . The first step in the definition of the elastoplastic model consists in defining the yield criterion. The normal stress of the Timoshenko model is given by $\sigma_{33} = E (U_{\alpha,3} - x_{\alpha}\theta_{\alpha,3})$. The distribution of stress is therefore linear through the cross-section with maximum and minimum stress reached at the top and bottom fibers of the section. During bending, σ_{33} increases until it reaches a maximal plastic value σ_y as described on Figure 1.8.

Once σ_y is reached, plastification propagates through the thickness of the section as described in state (3), until the fully plastic state (4) is reached. The bending moments corresponding to each situation are:

$$M_2^{(1)} = E \frac{bh^3}{12} \theta_{2,3}, \quad M_2^{(2)} = \frac{\sigma_y bh^2}{6}, \quad M_2^{(3)} = \sigma_y b \left(\frac{h^2}{4} - \frac{x_y^2}{3} \right), \quad M_2^{(4)} = \frac{\sigma_y bh^2}{4} \quad (1.81)$$

$M_2^{(3)}$ is a function of the local variable x_y describing the propagation of the plastic zone through the thickness of the section. Since we aim to express a elastoplastic equation expressing the bending moment M_2 as function of the curvature $\theta_{2,3}$, the intermediate state (3) is discarded and we consider that the first plastification of the element corresponds to the full plastification of state (4). The yield moment is therefore defined by:

$$M_y = \frac{\sigma_y bh^2}{6}, \quad (1.82)$$

and the 1D yield criterion has the simple following expression:

$$M_2(x_3) - M_y \leq 0, \quad (1.83)$$

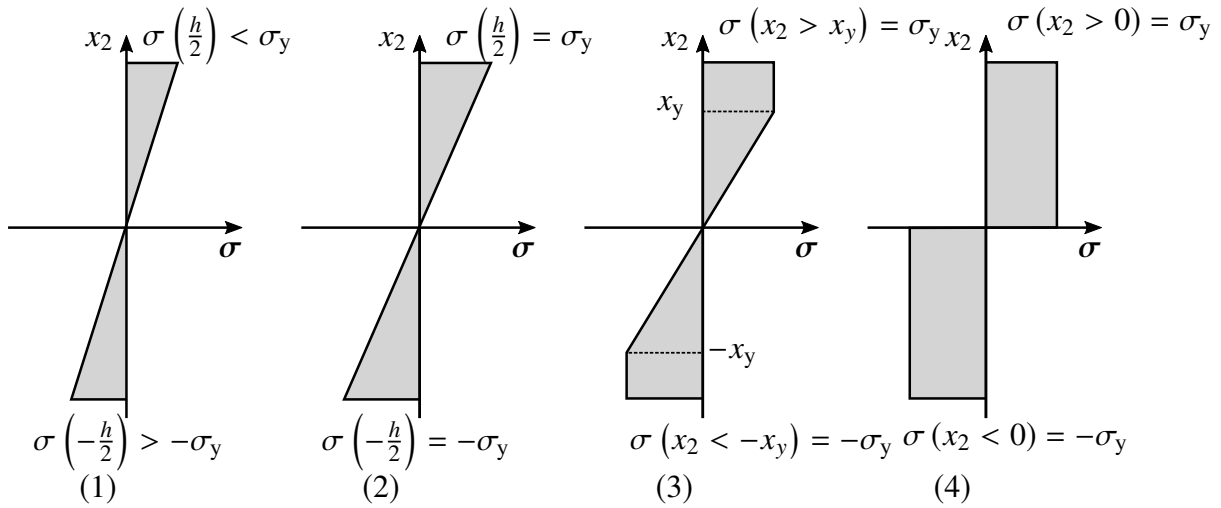


Figure 1.8 – Evolution of normal stress during bending

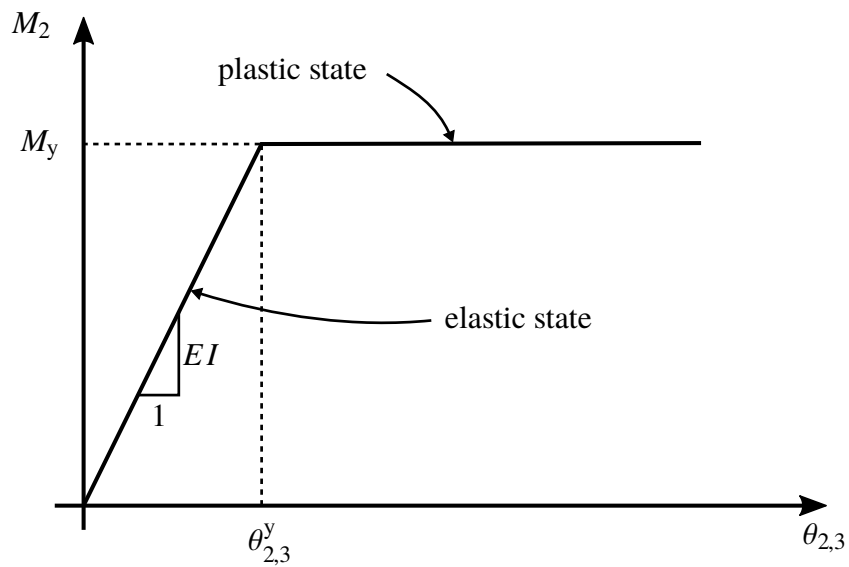


Figure 1.9 – Moment-curvature relationship with the macro yield criterion

1.3. Beam models in elastoplasticity

The moment-curvature law is represented on Figure 1.9.

The preliminary step is completed: the elastoplastic beam element is now defined by the 1D constitutive moment-curvature relationship represented on Figure 1.9 and by the yield criterion expressed in Equation (1.82). The example studied here is very simple and accounts only for one stress-resultant. If a second stress-resultant like the normal stress N or the second bending moment M_1 is introduced, the yield criterion must be redefined and must consider the potential interactions between the resultants. The yield criterion becomes a function of several parameters, motivating the name of yield surface.

1.3.2.2 Computation of the stress-resultants yield criterion

Yield criterion with one stress-resultant As illustrated by the previous Timoshenko-based model, the main challenge in the 1D approach lies in the definition of the yield surface. Many closed-form solutions have been historically proposed for simple cross-section geometry and loadings.

In particular, the problem of prismatic bars submitted to torsion has been historically investigated since the seminal works of Saint-Venant. Based on the membrane analogy of Prandtl [Prandtl, 1903], Nadai demonstrated in 1923 that the shear stress and the torque in a solid bar submitted to torsion could be estimated by pouring dry sand on a tray whose shape is similar to that of the cross-section of the bar [Nadai, 1923] (first published in German, his works were then translated in English in [Nadai, 1931]). He established that the maximum torque that could be withstood by the bar was proportional to the volume of sand on the tray and that the stress distribution was given by the surface of the heap. This sand-heap analogy was first formulated for solid bars but then extended to the case of hollow sections [Sadowsky, 1941] with a numerical application given by [Shaw, 1944]. Following the work done by Nadai, many models were developed with closed-form yield criterion for beams submitted to torsion with common cross-section: solutions for the torsion of I-beams [Christopherson, 1940], oval cross-sections [Sokolovsky, 1946] or rectangular sections [Smith and Sidebottom, 1965] were successively formulated.

Combined stress-resultants yield criterion The formulation of the yield surface is more complicated when it comes to combined generalized stress since their interaction must be taken into account. The yield surface of thin-walled beams submitted to both twisting and torsion has been analytically expressed by Hill and Siebel [1951]. The formulation of a closed-form solution was made possible by assuming constant distribution of stress through the thickness of the wall. However, they found that the yield surface of solid bars could not be exactly solved [Hill and Siebel, 1953].

The description of the yield surface becomes more complex as we consider more stress-resultants and their potential interactions. The yield surface presented on Figure 1.10 has been

numerically computed for a L-shaped reinforced concrete beam [Bleyer and de Buhan, 2013]. Its complex shape illustrates the difficulty to find analytical solutions for such cases. Bleyer and de Buhan therefore suggested a numerical approximation of the yield surface by facets and ellipsoids.

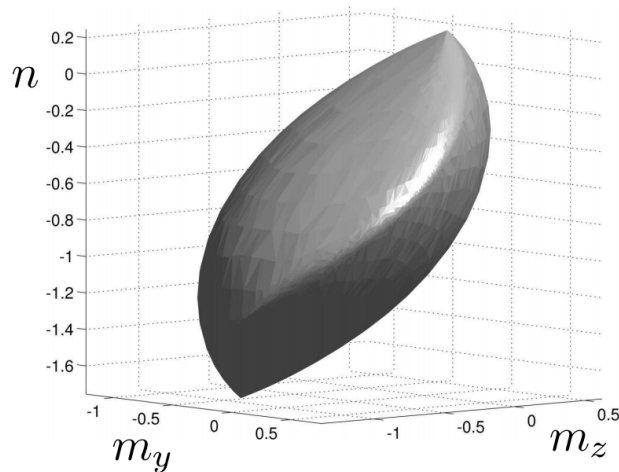


Figure 1.10 – Yield surface expressed in terms of bending moments and normal stress [Bleyer and de Buhan, 2013]

Once the yield surface is described, the beam element can be formulated and solved. The main advantage of this approach is the simplicity and computational performance of a 1D resolution since the yield criterion is only checked at the longitudinal nodes of the beam. The price of this computational efficiency is a potential local inaccuracy. As illustrated by the elastoplastic Timoshenko beam model in the previous section, plastification is considered only when the full plastic state has been reached, therefore discarded the stage of plastic propagation through the thickness of the section. Beam models with local yield criteria expressed in terms of the three-dimensional stress states are developed in order to mitigate this lack of local accuracy.

1.3.3 Beam models based on a local yield criterion

In order to improve the local accuracy of the beam model, the natural approach consists in using a local yield criterion. Two solutions might be considered.

The first approach is to discretize the cross-section into layers (for 2D description) or fibers (for 3D description), each one being associated with a beam kinematics. This is the spirit of the example presented in Section 1.3.3.1 and the method used in multifibers models. This method can be performed with simple kinematics for each layer or fiber but their multiplication comes with a higher computation time.

The second approach is to enhance the kinematics of the beam element. One single beam

1.3. Beam models in elastoplasticity

element is used but with a 3D kinematics able to describe the nonlinear behavior of the local variables. The kinematics may be computed a priori or may evolve during the computation. This second approach is presented in Section 1.3.3.2.

1.3.3.1 An illustrative elastoplastic Timoshenko beam model

We consider the beam introduced in Section 1.3.2.1. The beam is still submitted to bending around axis Ox_1 . By contrast with the stress-resultants approach adopted previously, a local criterion is used now. To that purpose, the cross-section of the beam is discretized into m horizontal layers of respective thickness t_l as represented on Figure 1.11.

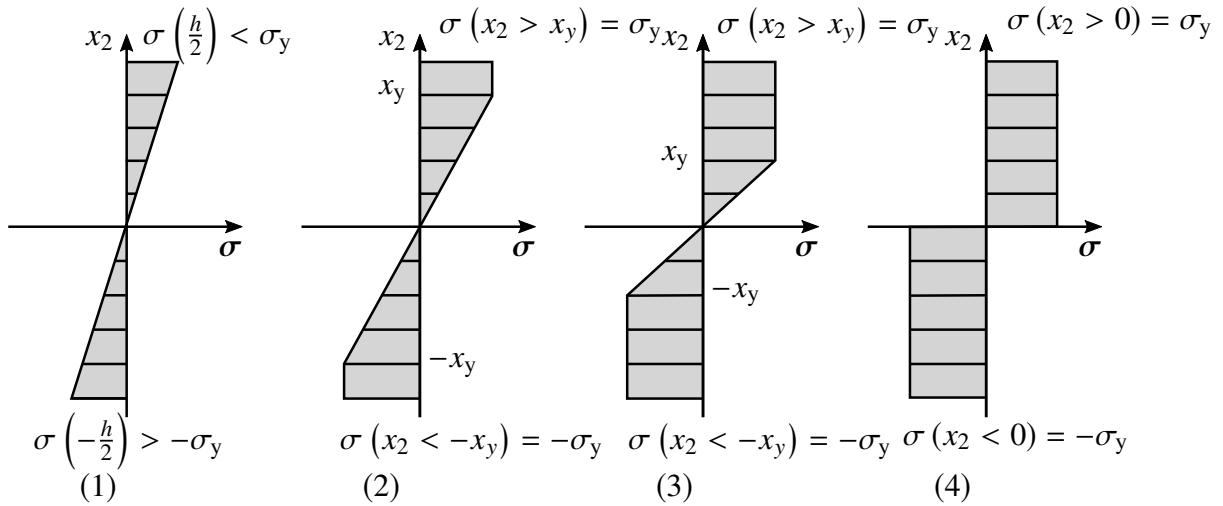


Figure 1.11 – Evolution of normal stress during bending

Remark A discretization along Ox_2 into layers is suitable for the present 2D description of the beam and the study of bending around Ox_1 . As indicated previously, a discretization along both cross-sectional axes with fibers could have been used as well for a finer 3D description of the local response and for loads involving a nonuniform response of the section. This is the method used in multifibers models.

Thanks to the discretization along Ox_2 , the spreading of yielding through the thickness of the beam can be better described. Four intermediate states can be notably represented before full plastic state is reached. Each layer is associated with the following local yield criterion:

$$|\sigma_{33}(\mathbf{x})| - \sigma_y \leq 0, \quad (1.84)$$

Based on the stress components, this approach yields much better local results. The bending moment can be computed at the different stages of the plastification. As long as the evolution

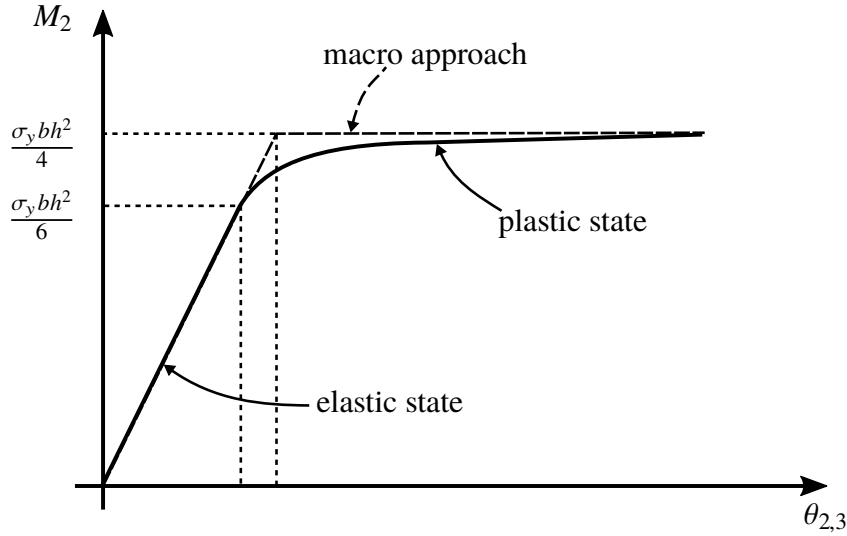


Figure 1.12 – Moment-curvature relationship with the local yield criterion

is elastic, $\sigma_{33}(\mathbf{x}) = -x_2\theta_{2,3}(x_3)$, and the discretized bending moment is given by:

$$M_2^{(1)} = -2b \left(\sum_{l=1}^{m/2} E_l t_l x_l^2 \right) \theta_{2,3}, \quad \text{with} \quad x_l = \frac{(2l-1)h}{2m} \quad (1.85)$$

where E_l is the Young modulus of each layer and x_l the vertical position of the center of each layer. This is the discrete form of the macroscopic relation $M_2^{(1)} = -EI\theta_{2,3}$. Once yielding starts spreading from the outer fibers to the center, the bending moment becomes:

$$M_2^{(2,3)} = 2b\sigma_y \left(\sum_{l=1}^j \frac{x_l^2}{x_y} t_l + \sum_{l=j+1}^{m/2} x_l t_l \right), \quad (1.86)$$

where j is the number of the last plastified layer ($x_j > 0$). Finally, the bending moment of the full plastic state is given by:

$$M_2^{(4)} = \frac{\sigma_y b h^2}{4}. \quad (1.87)$$

For $j = 0$, Equation (1.86) consistently yields $M_2^{(2,3)} = M_2^{(4)}$. The moment-curvature relationship is represented on Figure 1.12. Contrary to the stress-resultants approach, plastification starts as soon as the absolute value of the normal stress of the outer layers is greater than the elastic yield σ_y . Therefore the nonlinear relation between moment and curvature starts from $M_2 = (\sigma_y b h^2) / 6$ and not $M_2 = (\sigma_y b h^2) / 4$.

By expressing the yield criterion locally, no preliminary computation is needed. The local yield criterion is applied on each local integration point of each cross-section. This method provides more accurate global and local results, but is computationally more demanding as shown by the study of [Gendy and Saleeb \[1993\]](#).

1.3. Beam models in elastoplasticity

As indicated in the introduction of Section 1.3.3, an alternative local approach could have been used: instead of improving the beam response by discretizing the beam element into several beam element represented by layers, the model could have been improved by considering a single beam element but with an enhanced kinematics. In the first case the number of degrees of freedom is increased by increasing the number of sub-elements, in the second case the number of degrees of freedom is increased by increasing the numbers of displacement modes. The description of the latter case is presented in Section 1.3.3.2.

1.3.3.2 Higher-order models

Section 1.2 shows that the search of accuracy and performance in the development of elastic beam models leads to the definition of higher-order kinematics. The same approach can be adopted in order to develop elastoplastic beam models. However the task is more complicated: elastoplastic computations are mostly incremental and plasticity evolves during the computation. The nonlinear deformations involved are more complex to capture and the number of displacement modes required to satisfactorily represent the beam response might be very important.

Two methods are distinguished: models with kinematics defined before the nonlinear computation called *a posteriori* models, and models with kinematics computed and evolving during the computation called *a priori* models.

***A posteriori* models** Most of the time, the kinematics used to describe the elastic evolution of a beam element is not suitable for describing its elastoplastic behaviour since not compatible plastic strains of displacement and stress cannot be properly captured. New displacement modes must therefore be added into the kinematics of the element. *A posteriori* models define a kinematics for the element before its incremental resolution. It is assumed that this kinematics is accurate enough to describe the whole elastoplastic evolution of the element.

The definition of additional displacement modes can be an educated guess based on the knowledge of the load applied and on the geometry of the cross-section considered. For instance, [Bathe and Chaudhary \[1982\]](#) studied the elastoplastic evolution of a rectangular beam submitted to torsion. To that purpose, they defined the following displacement modes in the kinematics of the element:

$$\tilde{\mathbf{u}}_1 = \begin{pmatrix} -x_2 \\ x_1 \\ 0 \end{pmatrix}, \quad \tilde{\mathbf{u}}_2 = \begin{pmatrix} 0 \\ 0 \\ x_1 x_2 \end{pmatrix}, \quad \tilde{\mathbf{u}}_3 = \begin{pmatrix} 0 \\ 0 \\ x_1 x_2 (x_1^2 - x_2^2) \end{pmatrix}, \quad (1.88)$$

each mode being associated with an independent kinematic variable. The first mode $\tilde{\mathbf{u}}_1$ is the classical in-plane rotation of the cross-section, usually associated with the rotation angle θ_3 . The modes $\tilde{\mathbf{u}}_2$ and $\tilde{\mathbf{u}}_3$ are warping mode added for the description of the elastoplastic

evolution of the section. In the particular case of rectangular beams submitted to torsion, this kinematics yields satisfactory results.

Many developments have been carried out in the field of thin-walled beams. The nonlinear evolution of these elements is governed by a competition between plasticity and instabilities, making of the description of their behavior a complex issue. [Abambres et al. \[2014\]](#) developed a higher-order elastoplastic element for thin-walled beams. The kinematics is extended with a large number of displacement modes (up to 137), thus covering the potential displacement occurring during the elastoplastic evolution of the element. The methodology used for the computation of the displacement modes is described in [[Gonçalves et al., 2010](#)]. The shape of the cross-section is first discretized with nodes. Then "basic" modes are created by considering the displacement of one node along one of the three directions. These basic modes are then considered as imposed displacements in order to compute their higher-order related modes. A great amount of modes is therefore created. Based on their relevance for the problem studied, about half of them is then discarded. The method adopted here consists in creating an exhaustive kinematics that encompass all the potential cross-sectional displacement of the beam.

A similar approach is used by [[Carrera and Giunta, 2010](#)]: the kinematics is extended by using displacement modes computed thanks to polynomials interpolated on a 2D discretization of the cross-section.

The method adopted in [[Abambres et al., 2014](#)] and [[Carrera and Giunta, 2010](#)] aims to compute a wide range of additional displacement modes in order to capture the nonlinearities of the beam response. However the relevance of these modes is first assumed and confirmed *a posteriori* by the results of the computations. The Proper Orthogonal Decomposition (POD) enables to compute more empiric kinematics [[Chatterjee, 2000](#)]. This approach suggests to extract a reduced basis from a set of displacement fields obtained by preliminary numerical computations or experimental data. The reduced basis is created by proceeding to an orthogonalisation on the collection of displacement fields. This procedure is also known as the Karhunen-Loeve decomposition or the single value decomposition. It aims to extract the salient feature of the response of the structure. The accuracy of the model depends on the truncation chosen in the creation of the reduced basis and on the similarity between the displacement fields yielded by the preliminary computations and the displacement produced by the situations studied *a posteriori* with the reduced model.

In the Nonuniform Transformation Field Analysis (NTFA), [Michel and Suquet \[2003\]](#); [Roussette et al. \[2009\]](#) suggested to study the elastoplastic behavior of composite materials with a POD-like model. This model is not built by expressing the total displacement but with a kinematics expressed for the plastic strains. Preliminary 3D computations are processed on the sample material with elementary loadings (extension, compression, etc). A reduced basis is then extracted from the set of plastic strains obtained from the elementary computations. This method can be very effective when the scope of potential deformations is previously

1.3. Beam models in elastoplasticity

identified and encompassed by the preliminary computations.

A posteriori models offer the great advantage to compute a single kinematics for the whole nonlinear computation. The kinematics is created once and for all before the resolution of the beam element. However two drawbacks are inherent to this kind of models. First, it can be a complex task to identify all the potential displacements for an elastoplastic beam submitted to general loads (shear and normal force, bending moment or torque). Second, as a result of the first remark the number of displacement modes required to obtain satisfactory results may be very large. The numerical efficiency of the model can be consequently affected. The *a priori* models mitigate this issue by computing *ad hoc* kinematics computed during the incremental elastoplastic procedure.

***A priori* models** In order to define a kinematics more adapted to the current elastoplastic state of the structure, *a priori* models update the kinematics during the incremental resolution of the element. The kinematics therefore evolves according to the progression of plastic strain in the structure. **Baba and Kajita [1982]** studied the classical problem of a prismatic bar submitted to torsion. The kinematics adopted is the following:

$$\tilde{\mathbf{u}}_1 = \begin{pmatrix} -x_2 \\ x_1 \\ 0 \end{pmatrix}, \quad \tilde{\mathbf{u}}_2 = \begin{pmatrix} 0 \\ 0 \\ \psi \end{pmatrix}, \quad (1.89)$$

the first mode being associated with the in-plane rotation θ_3 and the second mode with its longitudinal derivative $\theta_{3,3}$. It is suggested by the Vlasov beam model in Equation (1.48), the difference being that the warping function ψ is now computed according to elastoplastic state of the cross-section. The section is discretized into square elements on which the local elastoplastic equilibrium equations are expressed. The local value of the warping function ψ_e is computed on each element of the beam section and their assembly yields the overall warping function ψ . This way, the function ψ is computed as a function of the incremental rotations and of the incremental plastic strain in the cross-section. Given the longitudinal variation of the plastic state along the beam, the computation of a single plastic warping function for the whole length is not a relevant choice. Therefore the beam is discretized into fine beam elements on which a different warping function is computed and assumed constant. This method yields results consistent with experimental data and closed-form solutions [**Smith and Sidebottom, 1965**]. Moreover, this model is effective for any shape of the cross-section without distinction between solid, thick-walled or thin-walled section. The comparison between the *a priori* model of [**Bathe and Chaudhary, 1982**] introduced previously and the model of [**Baba and Kajita, 1982**] highlights the main differences between the two approaches. While the first model is based on an assumed kinematics but is only valid for rectangular beams, the second is effective for any shape of the cross-section, the price being the computation of the warping function at each increment.

A generalization of the POD introduced previously has been widely developed and used in the past years. This method, called the Proper Generalized Decomposition (PGD) also

assumed a variables separation [Chinesta et al., 2011]. By contrast with the POD, the PGD does not need *a priori* knowledge on the solution. This method was first devised and used in the nonlinear and non-incremental Large Time Increment (LATIN) method developed by Ladeveze [1999] and was initially called the radial time-space approximation. The LATIN method is a method of resolution for nonlinear problems global in time and space which consists in solving successive global and local linear problems. The PGD is one of the main tool of this technique. A separation of the time and space coordinates is assumed and the displacement is expressed as follows:

$$\mathbf{u} = \sum_i S_i(\mathbf{x})T_i(t). \quad (1.90)$$

Equation (1.90) is injected into the weak formulation of the equilibrium problem and the time space functions T_i are computed for fixed space functions S_i . The space functions can then be updated according to a residual. Thanks to its non-incremental approach, this method enables very fast computations for reasonable number of degrees of freedom (usually a few tens). However the time computation can become large as the number of internal variables is high, a space-time solver being applied for each couple $S_i(\mathbf{x})T_i(t)$. An example of a PGD technique applied to a composite beam model can be found in [Vidal et al., 2012].

By computing displacement modes or reduced basis during the nonlinear resolution, *a priori* models provides relevant kinematics without costly preliminary computations. By considering only the kinematics relevant for the current iteration or increment, it solves the problem of the accumulation of modes required by the *a posteriori* methods.

A classification of the elastoplastic beam models presented in Section 1.3 is suggested in Figure 1.13. Models using a macroscopic yield criterion expressed in terms of the generalized stress have first been described in Section 1.3.2. The yield surface is computed for a single stress-resultant or by considering the combination of several stress-resultants and their interaction. Models adopting a local yield criterion expressed in terms of the stress components have been presented in a second time in Section 1.3.3. These models use two strategies in order to improve their local accuracy. Some are discretized in the cross-sectional directions into layers or fibers. Each subelement is associated with a beam kinematics which is usually a Euler-Bernoulli or Timoshenko model. The second approach consists in improving the kinematics of the element with displacement modes able to capture the nonlinearities due to the local yielding of the structure. Here again, two types of models can be distinguished. A first category of models completely define the beam kinematics before the resolution of the element. This kinematics is fixed during the whole elastoplastic computation. The second category updates the kinematics during the elastoplastic resolution process, thus considering an evolving shorter and relevant kinematics for the model. The new elastoplastic beam model presented in Chapter 3 falls within this last category of elastoplastic models.

1.4. Beam models for reinforced concrete

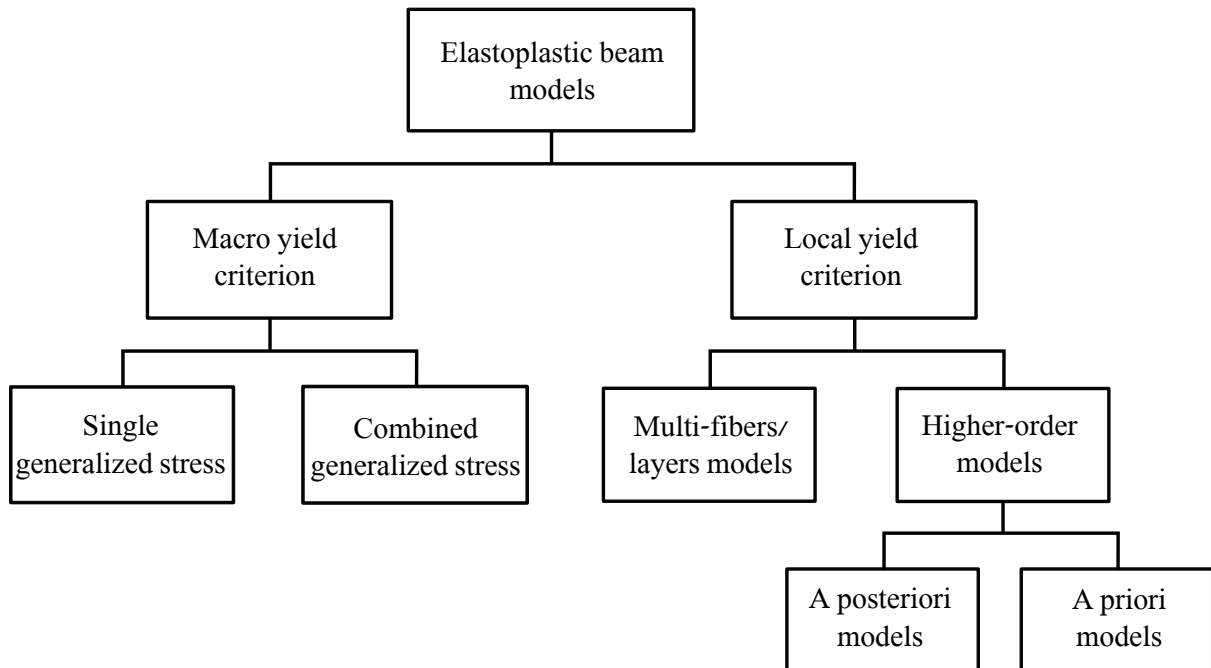


Figure 1.13 – Classification of the elastoplastic beam models presented in Section 1.3

1.4 Beam models for reinforced concrete

This section identifies the existing categories of beam models for reinforced concrete. Three main steps are considered for the definition of a beam model for reinforced concrete. First, the constitutive behavior of materials must be defined. Many models of various complexity have been suggested for concrete while the theory of plasticity is mostly used for steel. Second, the beam model and its kinematics must be defined. Finally, the structural connection between steel and concrete must be numerically expressed. This third issue can be closely linked to the choice of the beam model.

1.4.1 Description of a reinforced concrete beam model

The vast majority of today's building and infrastructures use reinforced concrete for structural material, naturally focusing the attention of the computational mechanics community on the development of numerical models. In this context, the high slenderness of many structural elements like beams or bridge decks stimulates the development of beam models.

The development of a beam model for reinforced concrete involves complex material and structural issues. Three steps can be identified for the definition of a reinforced concrete beam model.

The first step is the constitutive modelling of steel and concrete. Steel is mostly described with elastoplastic behavior associated to a Von-Mises criterion. This simple yield criterion is indeed suitable for most metals. By contrast, concrete is a complex material both on the local and the global scale. Its inherent inhomogeneity makes it a tough material to describe and model. Section 1.4.2 is dedicated to the description of the main categories of constitutive models suggested for concrete.

The second step is the definition of a beam model. The model must meet two major requirements. First it must be able to describe the material heterogeneity of a reinforced concrete element. Reinforced concrete is a composite material made of a concrete matrix and strengthened by steel rebars. We therefore expect the beam model to take the local description of each material into account. Second, the model must exhibit a sufficiently refined kinematics in order to provide accurate local results. The description of the main beam models used for the definition of reinforced concrete is presented in Section 1.4.3.

The third step is the numerical modelling of the structural connection between steel and concrete. Indeed, steel rebars are patterned in order to ensure a better bond with concrete. Interlocking of rebars and concrete aggregates prevents from bond-slip problems. This structural contact must find its counterpart in the definition of the beam model. It is actually closely linked to the definition of the beam model. This issue will be addressed at the end of Section 1.4.3.

1.4.2 Concrete constitutive behavior

1.4.2.1 Material description of concrete

Concrete is a material which may sustain high compressive loads. Usual concrete shows linear elastic behavior up to a yield limit f_c ranging from 20 MPa to 40 MPa. In contrast, it exhibits a low tension strength and cannot support tensile stress higher than a value f_t usually between 0 MPa and 5 MPa. Important stresses generate cracks in both tension ($\sigma > 0$) and compression ($\sigma < 0$) which result in a decrease of the stress as the deformation still gets larger. This phenomenon, called softening can be seen as a negative hardening. The uniaxial strain-stress behavior of concrete is represented on Figure 1.14. The softening stage quickly leads to a total loss of strength in tension. A short positive hardening stage can be observed before softening in compression.

The elastic range represented on Figure 1.14 is likely to evolve in case of cyclic loadings. In 3D structures, the elastic range depends on the 3D stress state. As observed by [Kupfer et al. \[1969\]](#), the elastic domain of concrete is not a perfect square under biaxial stress. As shown on Figure 1.15, the elastic limit in bi-compression is about 16% higher. It is known that concrete can support stresses much more important than f_c under hydrostatic stress state.

1.4. Beam models for reinforced concrete

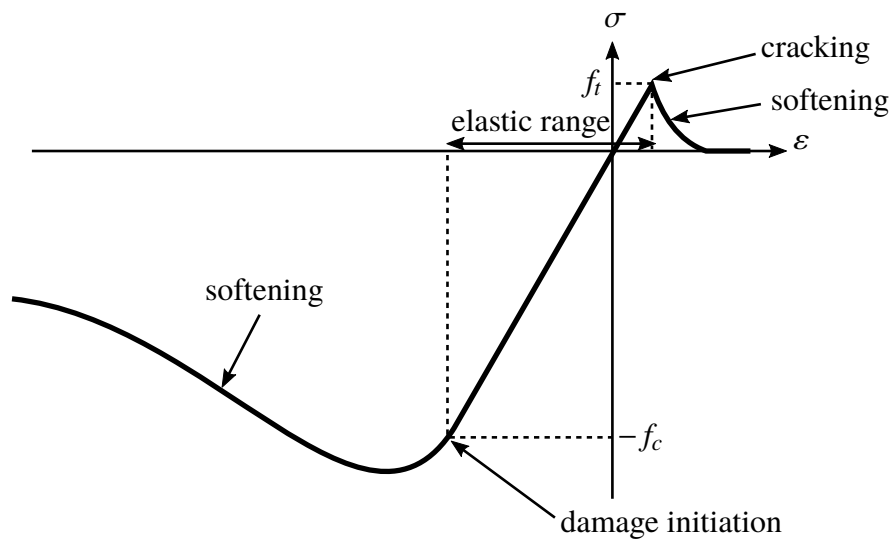


Figure 1.14 – Strain-stress concrete relationship

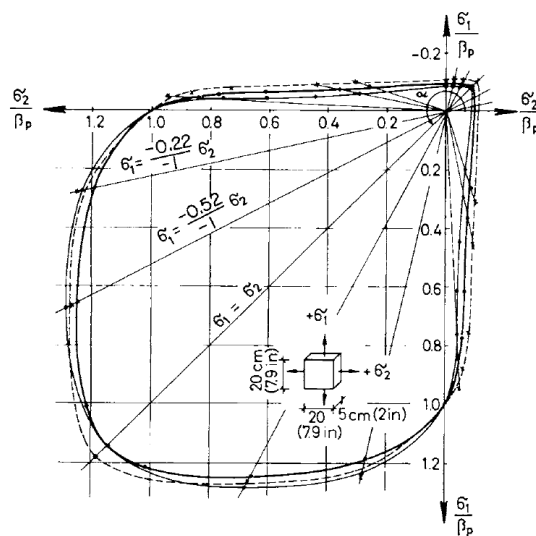


Figure 1.15 – Küpfer biaxial stress tests for three types of concrete [Kupfer et al., 1969]

Softening comes with a decrease of the local stiffness of the material called damage. Like plasticity, damage is usually described with a damage-variable that can only increase and takes value between 0 for a sound material and 1 for a material without strength.

Three different categories of concrete descriptions can be distinguished among the large amount of existing models. First, damage-models only use a damage description of the concrete behavior in tension and compression. Second, plastic-models are based on the well-known theory of plasticity. Finally, most of models uses a combined plastic-damage approach to

benefit from the advantages of both descriptions. The three different categories are presented in the coming sections.

1.4.2.2 Damage models

The nonlinear phenomena occurring out of the elastic domain is described with a damage approach. Once the yield stress is reached in tension or compression, the softening and the decrease of the material stiffness are described thanks to a damage variable. Denoting this variable by D , a natural and common approach consists in weighting the local stiffness by the factor $(1 - D)$, D ranging from 0 to 1 [Mazars, 1986; de Vree et al., 1995]. The stress-strain relation then reads:

$$\boldsymbol{\sigma} = (1 - D) \mathbf{C} : \boldsymbol{\varepsilon}. \quad (1.91)$$

This simple constitutive relation accounting for damage stands for an isotropic behavior. The damage variable is governed by an equivalent strain which expression varies with the models. A simple improvement of this model is brought by La Borderie by considering two independent damage variables D_c and D_t for describing the respective behavior of concrete in compression and tension [La Borderie, 1991].

The damage phenomenon is due to the apparition of small cracks which open orthogonally to the applied load. This inherent anisotropic behavior of damage is not taken into account by the previous models. It has motivated the development of more complex damage models. A common method to model the anisotropy of damage is to consider a second or fourth order tensor \mathbf{D} . However the development of such models must cope with two main difficulties. First the damage constitutive law described by \mathbf{D} must be defined and characterized. Then the numerical implementation of these models is generally a complex task [Govindjee et al., 1995; Leroux, 2012].

1.4.2.3 Plastic models

Due to the complexity of damage models, the well-known theory of plasticity is sometimes preferred for the description of the nonlinear behavior of concrete. In addition, plasticity is a more suitable framework for the description of irreversible strains or dilatancy. Plastic models are the combination of a yield surface and hardening and softening laws.

The yield surface, defined by a yield criterion, defines the elastic domain in stress space. The most used yield criterion for concrete include among others the common Mohr-Coulomb, Drucker-Prager and the Rankine criteria, and more advanced criteria such that the criteria suggested by [Willam and Warnke, 1974], Ottosen [Ottosen, 1977],[Hsieh et al., 1988] or the more recent unified strength criterion suggested by [Du et al., 2010]. The latter three account for complex features like the effect of hydrostatic pressure or the smoothness and convexity of the yield surface. By introducing additional parameters for the definition of their criterion,

1.4. Beam models for reinforced concrete

they try to best fit with the experimental data notably provided by Küpfer [Kupfer et al., 1969].

The hardening and softening laws define the plastic evolution once the yield surface is reached. They are usually governed by scalar hardening or softening parameters. [Grassl et al., 2002] suggested a hardening law using the trace of the plastic tensor as governing parameter for the study of concrete under triaxial compression. Using a non-associated flow rule, their model succeeded in accounting for the effect of triaxial stresses on the deformation of concrete. Based on the yield surface suggested in [Bigoni and Piccolroaz, 2004], [Poltronieri et al., 2014] developed a simple and robust elastoplastic model for concrete. They kept the essential elements of a concrete model: smoothness and convexity of the yield surface and a hardening law. Hardening is governed by a single parameter, and cannot describe softening. The choice of directness and simplicity is intentional, therefore providing an efficient tool for the study of concrete under triaxial stresses. In order to enlarge the applicability of plastic models for concrete, they can be combined with fracture criteria [Park and Kim, 2005].

1.4.2.4 Plastic-damage models

Advanced models describe accurately the complexity of the local behavior of concrete by combining damage and plasticity. The use of both theories enables to represent the stiffness degradation, the local damage, the softening and hardening evolution of stress or the propagation of cracks. Plastic-damage models are usually the combination of isotropic hardening and isotropic or anisotropic damage.

In that context, the coupling between damage and plasticity can be addressed by different approaches. A first category of plastic-damage models explicitly expressed the coupling between plasticity and damage. Some models define the plastic relations in the effective (undamaged) stress-space [Wu et al., 2006; Cicekli et al., 2007]. The coupling is thus described by a damage variable in the plastic flow rule and damage is computed independently from plastic strain. Other models express the plastic relations in the actual (damaged) stress space [Brüning and Ricci, 2005]. However this second method has proved to be numerically less stable [Al-Rub and Voyiadjis, 2004].

As mentioned before, damage is related to a local anisotropic opening of cracks. A better description of concrete damage should therefore couple plasticity with anisotropic damage law. However, the development of anisotropic laws for damage and their numerical implementation is not straightforward [Hansen et al., 2000; Carol et al., 2001; Cicekli et al., 2007], justifying why isotropic models are often preferred [Salari et al., 2004; Grassl and Jirásek, 2006; de Sciarra, 2012].

Three categories of elastoplastic models have been described in this section. Damage models are suitable for capturing the stiffness degradation and microscopic phenomena such as micro-

cracks or softening. However, damage cannot account for important effects such as irreversible strains or inelastic volumetric expansion in compression. These phenomena can be described by plastic models. Plasticity has the great advantage to be a simple and numerically robust theory offering a large scope of possible phenomenological descriptions: strong nonlinearities, softening or irreversible strains can be considered in plasticity. However it is not sufficient to take stiffness degradation into account. It has motivated the development of combined plastic-damage models. These models offer accurate local description of concrete behavior but must face with some difficulties: definition of the coupling between plasticity and damage, the mathematical ill-posed nature of damage description and the complexity of the numerical implementation inherited from damage definition.

1.4.3 Definition of the beam model

The definition of the beam element is the second step for the definition of beam model for reinforced concrete. The same categories of models can be distinguished as the ones presented in Section 1.3 and depicted in Figure 1.13. First, some elastoplastic model for reinforced concrete based on stress-resultant approaches are described. Then, we present more locally accurate models using local yield criterion and more specifically multi-fibers models since they are the currently most developed beam models for the study of slender reinforced concrete structures.

1.4.3.1 Stress-resultant based models

The steps for the definition of an elastoplastic beam model for reinforced concrete based on a stress-resultant yield-criterion are the same as exposed in Section 1.3.2. A preliminary description of the yield surface must be computed. To that end, the cross-section may be discretized with 1D or 2D elements in order to compute the relationship between the stress-resultants considered and their associated kinematic variables. In the case of reinforced concrete, the modeling of steel rebars must be considered. Then the 1D beam element can then be formulated. The elastoplastic behavior is consequently integrated on the 1D discretization of the element which prevents from costly local integrations on a discretization of the cross-section and provides fast computations. The philosophy of the stress-resultants beam models is well described in [Anthoine et al., 1997].

The combination of several stress-resultants should theoretically lead to the computation of a multi-dimensional yield surface accounting for the interaction between the different stress-resultants considered. However, the combined interaction of stress-resultants is often discarded because of the complexity it implies. [Pham et al., 2012] suggested a model for reinforced concrete frames submitted to axial deformation, shear and bending. While the bending moment is given an elastoplastic constitutive law according to curvature, axial deformation and shear are supposed to remain elastic. Similarly, [Bui et al., 2014] developed a beam

1.4. Beam models for reinforced concrete

element for reinforced concrete beams submitted to bending and shear without considering their interaction in the yield criterion. Instead, the interaction of bending and shear can be approximated by dividing the beam into two elements.

The main advantage of stress-resultant model is the fast numerical computations they offer. By contrast, they are not suitable for a fine description of the local behavior of reinforced concrete structures. Based on a macroscopic yield criterion, the yield computed by the model may not represent the actual microscopic state of the structure. This point has notably been highlighted in Section 1.3 by the comparison of the two Timoshenko elastoplastic beam models. This is especially true as steel rebars are now considered in the structure.

1.4.3.2 Multi-fibers models

The use of a local yield criterion mitigates the issue of local accuracy observed in the stress-resultant models. In this context, multi-fibers models are widely used for the study of reinforced concrete beams. The cross-section is discretized into layers (for 2D problems) or in fibers (for 3D problems). Each subelement (layer or fiber) is associated with a beam kinematics. This method is particularly suitable for the description of inhomogeneous structures such as reinforced concrete. Indeed, while some fibers are associated with the characteristics and the local behavior of concrete, others can be used for the description of steel rebars. Longitudinal rebars can therefore be easily and locally described. This approach is less convenient for the representation of frame rebars. They can however be taken into account by modifying the characteristics of concrete core, thus representing the effect of confinement. A multi-fibers beam formulation is illustrated on Figure 1.16. A reinforced concrete structure composed of longitudinal rebars and transversal frames is modeled by a multi-fibers element. The 3D volume is discretized into 1D beam elements. According to its position each element is associated with either the material characteristics of steel (in black), either with the characteristics of plain concrete (in gray), or with the characteristics of confined concrete (in white). A longitudinal 1D discretization of the beam element is considered for the local integration of the elastoplastic equilibrium equations.

The kinematics used for the fibers is usually based on simple beam theory. A classic approach consists in associating each fiber with the Euler Bernoulli beam model (see Section 1.2.1). This model is convenient as long as shear effects can be neglected [Spacone et al., 1996; Spacone and Limkatanyu, 2000]. Due to the inability of such models to account for shear forces, the Timoshenko beam model is more commonly used in multi-fibers models (see Section 1.2.2). By considering a uniform shear stress distribution in the cross-section, the Timoshenko model can describe more accurately local fields [Mazars et al., 2006] and can represent shear failure mechanisms [Bui et al., 2014; Jukić et al., 2014]. However, the Timoshenko model cannot satisfy the free boundary conditions on the cross-section as mentioned in Section 1.2.2.

An interesting review of multi-fibers beam models for reinforced concrete can be found in

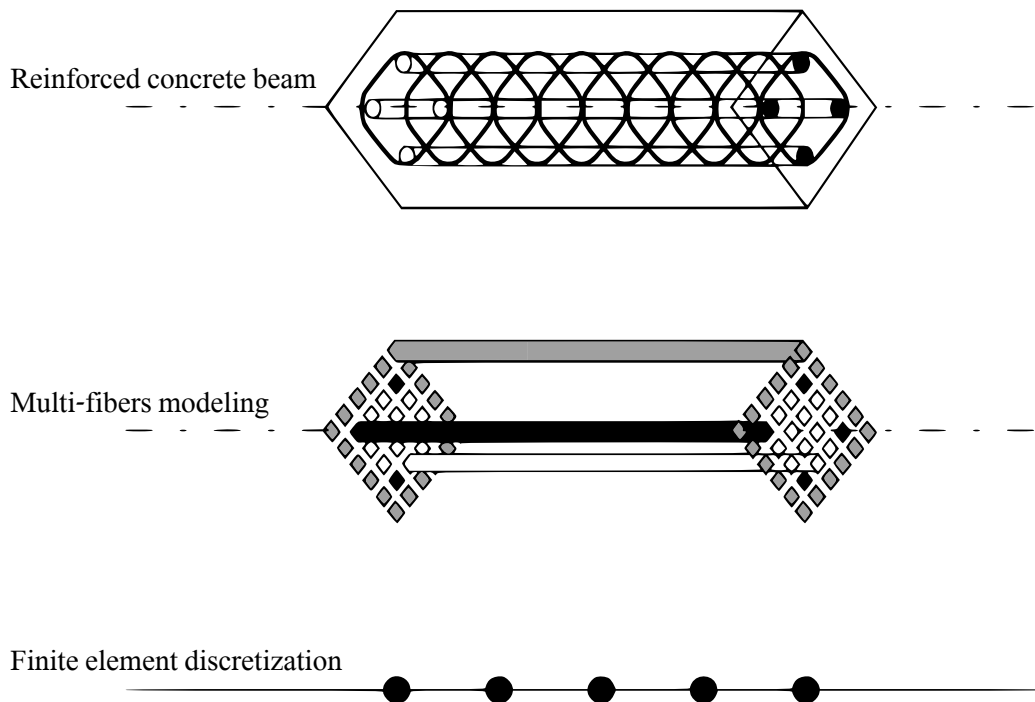


Figure 1.16 – Model reduction of a reinforced concrete beam to a multi-fibers beam element

[Ceresa et al., 2007].

1.4.3.3 Numerical description of the structural connection between steel and concrete

The third step in the definition of an elastoplastic beam model for reinforced concrete is the modeling of the rebars. Rebars are additional structural elements fully embedded in a concrete matrix. Aggregates interlocking and rebar's surface patterns must ensure a strong bonding between steel and concrete. The numerical modeling of the rebars must describe this structural connection.

For stress-resultants models, this issue is only considered during the preliminary computation of the yield surface. Once the yield criterion is defined, the 1D beam element is solved without consideration about the inhomogeneous nature of reinforced concrete, thus underlining the weakness of these models to provide accurate local results.

Multi-fibers models are convenient for the local description of longitudinal rebars. Without specific methods for representing bond-slip effects, the structural connection is ensured by the displacement continuity between steel fibers and concrete fibers. However, this approach does not enable an accurate description of non-longitudinal rebars. As shown on Figure 1.16, non-longitudinal rebars are taken into account with an homogenization approach.

1.4. Beam models for reinforced concrete

A finer discretization is adopted for steel reinforcement in the reinforced concrete model presented in Chapter 4. Concrete is represented by an elastoplastic beam element and rebars are considered as 1D bar elements embedded into the 3D volume of the beam. They can therefore be oriented and localized freely in the 3D volume of concrete, thus enabling an accurate representation of complex reinforcements.

The complexity arising in the definition of a beam model for reinforced concrete has been highlighted in this section. The first issue lies in the constitutive modelling of the material. Complex constitutive laws providing an accurate description of damage and softening have been suggested. But these models are often difficult to manipulate and implement in numerical codes. The choice of the beam model is the second issue. The choice of a stress-resultants based model often offers time-efficient numerical models, but fails in providing an accurate description of the local behavior. To this end, a local approach like multi-fibers models is more adapted. Finally, it has been shown that the modelling of rebars and their kinematic relation with concrete are often linked to the definition of the beam model.

* *
*

Chapter 2

Higher-order elastic beam model with eigenstrains: theory and illustrations

Abstract: *This chapter introduces a new higher-order elastic beam model accounting for eigenstrains. Based on the higher-order elastic beam model developed by Ferradi et al. [2016], the extension suggested here enables the model to deal with a wide range of phenomena such as creep, prestress or thermal loads. The beam model is first presented and then illustrated by two applications: a table submitted to a thermal load and a cantilever beam prestressed by a steel cable.*

Contents

2.1	Introduction	48
2.2	Kinematic enrichment based on the formal asymptotic expansion	51
2.2.1	The 3D problem and the asymptotic expansion method	51
2.2.2	Cascade resolution	55
2.2.3	Families of kinematic enrichment	62
2.2.4	Numerical approximation of the higher-order beam model	62
2.3	Applications	66
2.3.1	Application to a thermal load	67
2.3.2	Application to a prestressed beam	76
2.4	Conclusion	79

2.1 Introduction

Structural analysis must take into account eigenstrains such as thermal load, prestress or weakly coupled swelling phenomena. Furthermore, beam models are certainly the most widely used models by structural engineers because of their simplicity. This motivates the introduction of these prescribed strains into beam models. However, the kinematics of beam models is often based on very simple assumptions which are often unable to describe precisely local effects induced by these strains prescribed arbitrarily in the section. In the absence of richer kinematics, shell models or full 3D computations are necessary. Those computations being time-consuming, the simplicity and the great time efficiency of beam models motivates the development of adequately refined higher-order beam models.

Beam models have a long history and a vast variety of contributions may be found in the literature. The first beam models were based on *ad-hoc* assumptions on the 3D fields which motivated the denomination *axiomatic*. Most of the time axiomatic models rely on an educated guess on the 3D displacement field in a separated form between the longitudinal coordinate and the in-section coordinates. Then, straightforward application of the minimum of potential energy leads to 1D boundary value problems corresponding to the beam model. The Euler-Bernoulli beam model was the first suggestion. In this model, it is assumed that the cross-section of the beam is rigid in its own plane and that it remains orthogonal to the neutral axis of the beam. Hence, this model neglects the transverse shear strain and suffers from a kinematic contradiction: since the section is not allowed to deform in its plane, transverse Poisson's effect is precluded. The Timoshenko beam model allows an independent rotation of the section with respect to the neutral axis in order to take the transverse shear strain into account [Timoshenko, 1922]. However, since the section rotates rigidly, the shear strain is uniform in the section which does not satisfy the free lateral boundary. Furthermore, the transverse Poisson's effect is still restrained. These contradictions, suggested to push further the kinematic enrichment in a polynomial form as illustrated in [Carrera et al., 2011; Giunta et al., 2016]. However, having a correct approximation requires a high number of kinematic degrees of freedom and raises the question of the sparsity of the approximation as will be recalled below.

It turns out that, at leading order in the slenderness, these kinematic contradictions were resolved quite early thanks to Saint Venant solution [de Saint Venant, 1855]. Indeed, this solution was originally derived for an elastic beam with a homogeneous and isotropic section loaded at the extremities in a weak sense. Starting from static considerations, a full 3D solution was obtained where the 6 classical generalized stress vary linearly along the beam and the section is free to deform in its plane as well as out of its plane. More precisely, the 3D displacement field appears as the superposition of the classical rigid motion of the section and of additional displacements related to the generalized stress which correct the over-constrained rigid motion of the section. As consequence, the 3D stress is better approximated than in the preceding approaches and the traction, bending, torsional and shear force stiffnesses

2.1. Introduction

are correctly evaluated.

Whereas this solution is perfectly relevant for rather compact and homogeneous sections, the Saint Venant solution is not accurate enough when considering more general sections such as anisotropic or heterogeneous materials, open and closed thin-walled sections. A classical illustration involves torsion warping. Indeed, the latter is assumed uniform along the beam in the Saint Venant solution. Hence, clamped boundary conditions may not be strongly satisfied. In practical situations, clamping a thin-walled beam generates a kinematic frustration which propagates far from the extremity and needs correct estimation. A first successful extension of Saint Venant solution was made by Vlasov [Vlasov, 1961] who included the torsional warping as an independent static degree of freedom (so called bi-moment) followed by Benscoter [Benscoter, 1954] who further assumed that the corresponding kinematic degree of freedom is also independent. Both works rely on the torsional warping correction included in the Saint Venant solution.

The efficiency of these models to capture end effects encouraged further refinement in more general configurations. A noticeable contribution is from Iesan [Iesan, 1976] who extended the Saint Venant solution to the case of fully anisotropic and heterogeneous section. In addition the beam was loaded with body forces and surface tractions in a separated form between in-section coordinates and the longitudinal coordinate. The longitudinal variation of the loads was assumed polynomial of a fixed order and the corresponding solutions for each order is obtained by a recursive process.

Almost identical results were obtained from the formal asymptotic expansion. Indeed, this method is based on a scaling of the original 3D problem so that it depends explicitly on a small parameter. In the case of beams, it is the ratio between the typical size of the cross section and the length of the beam. Then the solution is assumed following an asymptotic expansion with respect to the small parameter and inserted in the 3D equations. A collection of embedded in-section and longitudinal problems is obtained which is solved by induction. The monograph from Trabucho & Viano [Trabucho and Viaño, 1996] presents the method and links the lowest orders of the asymptotic expansion with the Saint Venant solution as well as Vlasov beam model. Most of recent contributions questions the correct derivation of boundary conditions especially at higher order [Buannic and Cartraud, 2001a,b; Kim et al., 2008; Kim and Wang, 2011]. Another family of enriched beam model was derived following the so-called “Variational Asymptotic Method” [Yu et al., 2002; Yu and Hodges, 2004; Yu et al., 2012; Hodges, 2006]. This approach is very similar to formal asymptotic expansion and most of its developments were made assuming large displacements and rotations of the section which makes higher-order developments much more involved.

In addition to the difficulties regarding boundary conditions, the main limitations of the asymptotic expansion approach are the very high regularity of the applied load which is required when going higher order and the embedded structure of the sequence of 1D problems to be solved. This makes the classical approach impractical for engineering applications. Remarka-

bly, the same difficulty arises with the extended Saint Venant solution from Iesan [Iesan, 1976] since only polynomial loadings are solution. For instance, concentrated loads commonly used in practice do not satisfy such regularity.

A solution to overcome this difficulty is to consider the whole family of in-section displacements or “modes” generated from formal asymptotic expansion as kinematic enrichment carried by independent generalized beam displacements. Indeed, the application of the minimum of the potential energy does not restrict severely the regularity of the longitudinal distribution of the applied load. The very first illustration of this approach is the model from Benscoter [Benscoter, 1954] which treats the torsional warping as an independent degree of freedom. In the case of a homogeneous and isotropic beam this idea was fully generalized by Miara & Trabucho [Miara and Trabucho, 1992] (also detailed in [Trabucho and Viaño, 1996]) and so called “Galerkin spectral approximation”. This work is based on the seminal idea from Vogelius & Babuska [Vogelius and Babuska, 1981a,b] which also originated the family of “hierarchical models” for plates and shells [Actis et al., 1999]. Two noticeable observations were made. First, the formal asymptotic expansion delivers a free family of kinematic enrichment which is dense in the space of the 3D solution. This means that going sufficiently high in the expansion allows arbitrary refinement of the 3D solution. Second, the truncation of this family ensures that the corresponding beam model is asymptotically consistent except at the boundary. This means that the kinematic enrichment delivered by the formal asymptotic expansion is optimal in terms of approximation error far from the extremities of the beam.

Practical implementation of this concept were suggested by El Fatmi [El Fatmi, 2016] Lahmar et al. [Lahmar et al., 2017] and Ferradi et al. [Ferradi et al., 2016]. In [El Fatmi, 2016], the enrichment was limited to the contribution of the Saint Venant modes and transverse loadings which are uniform in the longitudinal direction. However, longitudinal or higher-order enrichments were discarded and there remained an educated guess for enriching further the beam model. This approach was also extended to uniform thermal loads in [Lahmar et al., 2017]. In [Ferradi et al., 2016], the enrichment related to any kind of load was introduced up to an arbitrary order. A closed-form solution of the higher-order beam model was derived and comparisons with full 3D calculations were performed. Even for a concentrated load arbitrarily located in the section, the approximated solution yielded surprisingly good results.

In the present paper, the same approach is applied to eigenstrains and illustrated with two cases study. Furthermore, the higher order beam model is implemented with NURBS finite elements in order to allow longitudinal variations of the applied load. There are fewer contributions related to applied eigenstrain in beam theories. In addition to those previously mentioned, the general case of periodic beams as well as thin walled beam was investigated by Kolpakov [Kolpakov, 1993, 1998, 2012]. However, the formal asymptotic expansion was not carried out up to an arbitrary order.

This paper is also an opportunity to redevelop the formal asymptotic expansion procedure and emphasize its close link with Saint Venant solution as well as the extension from Iesan [Iesan,

2.2. Kinematic enrichment based on the formal asymptotic expansion

1976]. It is organized as follows. First the formal asymptotic expansion procedure is applied to a beam with a prescribed eigenstrain and the higher-order beam theory is derived and solved numerically with NURBS finite elements in Section 2.2. Then, two elementary cases study are investigated. A bridge submitted to a local elevation of temperature in Section 2.3.1 and a prestressed beam in Section 2.3.2

2.2 Kinematic enrichment based on the formal asymptotic expansion

This section is dedicated to the extension of the higher-order elastic beam element developed by Ferradi [Ferradi et al., 2016] to the case of eigenstrains. The 3D problem is first formulated and the asymptotic expansion method is applied. The cascade resolution of the resulting auxiliary problems yields a collection of displacement modes thus constituting the kinematics of the element. The cross-section of the beam is numerically approximated for the computation of the displacement modes and the element is longitudinally approximated. A locking study is carried out on the longitudinal interpolation functions.

2.2.1 The 3D problem and the asymptotic expansion method

2.2.1.1 The 3D problem

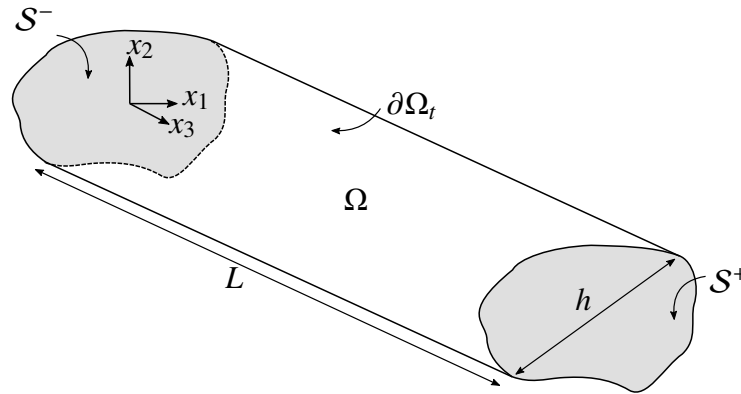


Figure 2.1 – The beam configuration

We consider a beam occupying the prismatic domain Ω (Figure 3.1) with a length L and a cross-sectional typical size h . The boundary $\partial\Omega$ is the union of the lateral (free) surface $\partial\Omega_t$ and the two end sections S^\pm (clamped). The longitudinal coordinate is x_3 and the section coordinates are x_1 and x_2 denoted as x_α ¹, the corresponding reference frame is denoted $(O, \mathbf{e}_1, \mathbf{e}_2, \mathbf{e}_3)$ where O is an arbitrary point of the plane $x_3 = 0$.

1. In the following, Greek indices $\alpha, \beta, \gamma = 1, 2$ denote in-section dimensions and Latin indices $i, j, k, l =$

The constitutive material of the beam is only function of the section coordinates x_α and invariant in the longitudinal direction. For convenience and without limitation, the corresponding fourth order stiffness tensor $\mathbf{C}(x_\alpha)$ is assumed monoclinic with respect to a plane of normal \mathbf{e}_3 :

$$C_{\alpha\beta\gamma 3} = C_{333\alpha} = 0. \quad (2.1)$$

The beam is only subjected to eigenstrains ε_{ij}^* . The corresponding 3D linear boundary value problem writes as:

$$\begin{cases} \operatorname{div}_x \boldsymbol{\sigma} = 0 & \text{on } \Omega, \\ \boldsymbol{\sigma} = \mathbf{C} : (\boldsymbol{\varepsilon} - \boldsymbol{\varepsilon}^*) & \text{on } \Omega, \\ \boldsymbol{\varepsilon} = \nabla_x^s \mathbf{u} & \text{on } \Omega, \\ \boldsymbol{\sigma} \cdot \mathbf{n} = 0 & \text{on } \partial\Omega_t, \\ \mathbf{u} = 0 & \text{on } S^\pm, \end{cases} \quad (2.2)$$

where \mathbf{n} is the outer normal to $\partial\Omega_t$, ∇_x^s is the symmetric part of the 3D gradient operator and div_x is the 3D divergence operator. Casting the weak form of this boundary value problem reveals that, in addition to the classical regularity of \mathbf{u} , the eigenstrain load needs to be square integrable.

Note that another way to introduce eigenstrains would be to turn it into a body force $\mathbf{f}^* = -\operatorname{div}_x(\mathbf{C} : \boldsymbol{\varepsilon}^*)$ and a force per unit surface $\mathbf{T}^* = (\mathbf{C} : \boldsymbol{\varepsilon}^*) \cdot \mathbf{n}$ on $\partial\Omega_t$. Then it would be possible to use the method presented in [Ferradi et al., 2016]. This remark shows that, without considering fields regularity, the optimality result presented in [Miara and Trabucho, 1992] may be adapted to the present situation. However, this approach involves the preliminary computation of the divergence $\operatorname{div}_x(\mathbf{C} : \boldsymbol{\varepsilon}^*)$, which may be a source of numerical imprecision, especially with heterogeneous sections or eigenstrains with low regularity. This motivates the present direct formulation of the higher-order beam theory.

2.2.1.2 Scaling and variable separation

A new set of coordinates y_i is defined from the global coordinates,

$$(x_1, x_2, x_3) = (hy_1, hy_2, Ly_3), \quad (2.3)$$

which rewrites the derivation operator as:

$$\nabla_x = \frac{1}{L} \left(\nabla_{y_3} + \frac{1}{\eta} \nabla_{y_\alpha} \right), \quad (2.4)$$

as well as the integration over the domain Ω as:

$$\int_{\Omega} d\Omega = \int_0^L \int_S dx_\alpha dx_3 = L^3 \eta^2 \int_0^1 \int_{S^0} dy_\alpha dy_3 = L^3 \eta^2 \int_0^1 \langle \rangle dy_3, \quad (2.5)$$

1, 2, 3, all three dimensions. Einstein summation convention on repeated indices is used.

2.2. Kinematic enrichment based on the formal asymptotic expansion

where $\eta = \frac{h}{L}$ is the small parameter related to the slenderness of the beam, \mathcal{S}^0 is the scaled cross-section, independent from η and $\langle \cdot \rangle$ denotes integration on the scaled cross-section.

The eigenstrain is assumed to have the following separated form:

$$\varepsilon_{ij}^* = \eta \tilde{d}_{ij}(y_\alpha) T(y_3), \quad (2.6)$$

where $\tilde{d}_{ij}(y_\alpha)$ is the eigenstrain distribution in the section and $T(y_3)$ is its longitudinal variation. In this section, capital letters denote functions of only the y_3 coordinate (except for \mathbf{C}) and $\tilde{\bullet}$ denotes functions of only in-section coordinates y_α .

2.2.1.3 Expansion

The asymptotic expansion method is a formal procedure in which all fields are assumed sufficiently smooth. It yields a cascade of in-section and longitudinal boundary value problems which are classically solved recursively. In the present case, only the in-section problems are of interest in order to derive a collection of displacement modes.

The displacement, strain and stress variables are expanded as power series of the small parameter as follows [Sanchez-Palencia, 1980; Trabucho and Viaño, 1996; Buannic and Cartraud, 2001a; Zhao et al., 2015]:

$$\mathbf{u} = L (U_\alpha^0(y_3) \mathbf{e}_\alpha + \eta \mathbf{u}^1 + \eta^2 \mathbf{u}^2 + \dots), \quad (2.7)$$

$$\boldsymbol{\varepsilon} = \boldsymbol{\varepsilon}^0 + \eta \boldsymbol{\varepsilon}^1 + \eta^2 \boldsymbol{\varepsilon}^2 + \dots, \quad (2.8)$$

$$\boldsymbol{\sigma} = \boldsymbol{\sigma}^0 + \eta \boldsymbol{\sigma}^1 + \eta^2 \boldsymbol{\sigma}^2 + \dots \quad (2.9)$$

and introduced in the equations of the 3D boundary value problem (3.3) where each power p of η is identified. The problem being linear, the choice of the starting order has no incidence on the final formulation in terms of physical variable. Here the starting order is chosen so that the leading order of the displacement field is 0. The starting order of the other fields is chosen accordingly. This motivates the scaling of the eigenstrain in Equation (2.6).

For $p \in \mathbb{N}$, each compatibility equations, boundary conditions and constitutive equations for p and equilibrium equations for $p - 1$ yield an auxiliary problem on the cross-section which splits in two uncoupled boundary value problems.

Transverse displacement First, the in-section displacement problems (transverse mode) \mathcal{T}^{p+1} are gathered for $p \geq 0$:

$$\mathcal{T}^{p+1} : \begin{cases} \sigma_{\alpha\beta,\beta}^p + \sigma_{\alpha 3,3}^{p-1} = 0 & \text{on } \mathcal{S}^0, & (2.10a) \\ \sigma_{\alpha\beta}^p = C_{\alpha\beta\gamma\delta} \left(\varepsilon_{\delta\gamma}^p - \delta_{p1} \tilde{d}_{\delta\gamma} T \right) + C_{\alpha\beta 33} \left(\varepsilon_{33}^p - \delta_{p1} \tilde{d}_{33} T \right) & \text{on } \mathcal{S}^0, & (2.10b) \\ \sigma_{33}^p = C_{33\alpha\beta} \left(\varepsilon_{\beta\alpha}^p - \delta_{p1} \tilde{d}_{\beta\alpha} T \right) + C_{3333} \left(\varepsilon_{33}^p - \delta_{p1} \tilde{d}_{33} T \right) & \text{on } \mathcal{S}^0, & (2.10c) \\ \varepsilon_{\alpha\beta}^p = u_{(\alpha,\beta)}^{p+1}, \quad \varepsilon_{33}^p = u_{3,3}^p & \text{on } \mathcal{S}^0, & (2.10d) \\ \sigma_{\alpha\beta}^p n_\beta = 0 & \text{on } \partial\mathcal{S}^0. & (2.10e) \end{cases}$$

where $\sigma^{-1} = 0$ and $\delta_{1p} = 1$ if $p = 1$ and $\delta_{1p} = 0$ else. Transposing the results from [Ciarlet and Ciarlet, 2004; Amrouche et al., 2006], for a simply connected cross-section and regular enough \mathbf{C} and loadings, this boundary value problem on the displacement u_α^{p+1} is a pure traction problem which is well-posed provided that the applied load is globally self-equilibrating for in-section translations and rotation:

$$\left\langle \sigma_{\alpha 3,3}^{p-1} \right\rangle = 0 \quad \text{and} \quad \left\langle y_\beta \varepsilon_{\beta\alpha} \sigma_{\alpha 3,3}^{p-1} \right\rangle = 0, \quad (2.11)$$

where $\varepsilon_{\alpha\beta}$ is the permutation operator: $\varepsilon_{11} = \varepsilon_{22} = 0$, $\varepsilon_{12} = +1$, $\varepsilon_{21} = -1$. Then, under condition (2.11), the solution is uniquely defined up to the following rigid motion of the section in its plane:

$$u_\alpha^{R,p+1} = U_\alpha^{p+1}(y_3) + y_\beta \varepsilon_{\beta\alpha} \Theta^{p+1}(y_3). \quad (2.12)$$

where U_α^{p+1} is a transverse displacement and Θ^{p+1} a twist rotation.

Longitudinal displacement Second, the longitudinal displacement problems (warping mode) \mathcal{W}^p are obtained for $p \geq 0$:

$$\mathcal{W}^{p+1} : \begin{cases} \sigma_{3\alpha,\alpha}^p + \sigma_{33,3}^{p-1} = 0 & \text{on } \mathcal{S}^0, & (2.13a) \\ \sigma_{\alpha 3}^p = C_{\alpha 3\beta 3} 2 \left(\varepsilon_{\beta 3}^p - \delta_{p1} \tilde{d}_{\beta 3} T \right) & \text{on } \mathcal{S}^0, & (2.13b) \\ 2\varepsilon_{\alpha 3}^p = u_{3,\alpha}^{p+1} + u_{\alpha,3}^p & \text{on } \mathcal{S}^0, & (2.13c) \\ \sigma_{\alpha 3}^p n_\alpha = 0 & \text{on } \partial\mathcal{S}^0. & (2.13d) \end{cases}$$

Again, for a simply connected cross-section and regular enough \mathbf{C} and loadings, this boundary value problem on the displacement u_3^{p+1} is well-posed if the applied load is globally self-equilibrating for the longitudinal translation:

$$\left\langle \sigma_{33,3}^{p-1} \right\rangle = 0. \quad (2.14)$$

In this case, the solution is uniquely defined up to a uniform longitudinal displacement:

$$u_3^{R,p+1} = U_3^{p+1}(y_3). \quad (2.15)$$

2.2. Kinematic enrichment based on the formal asymptotic expansion

Resultants and macroscopic equilibrium equations The rigid motion of the section suggests the following definition of the beam resultants at each order $p \geq 0$:

$$N_3^p = \langle \sigma_{33}^p \rangle, \quad M_\alpha^p = \langle y_\alpha \sigma_{33}^p \rangle, \quad M_3^p = \langle y_\beta \epsilon_{\beta\alpha} \sigma_{\alpha 3}^p \rangle \quad \text{and} \quad V_\alpha^p = \langle \sigma_{\alpha 3}^p \rangle, \quad (2.16)$$

where N_3^p is the normal traction, M_α^p are the bending moments ², M_3^p is the moment of torsion and V_α^p are the shear forces.

These resultants must comply with the following beam equilibrium equations for each $p \geq 0$:

$$\begin{cases} N_{3,3}^p = 0, & (2.17a) \\ M_{\alpha,3}^p = V_\alpha^{p+1}, & (2.17b) \\ M_{3,3}^p = 0, & (2.17c) \\ V_{\alpha,3}^p = 0. & (2.17d) \end{cases}$$

Indeed, from the in-section equilibrium equations (2.10a) and (2.13a):

$$\begin{aligned} \langle \sigma_{3\alpha,\alpha}^{p+1} + \sigma_{33,3}^p \rangle &= \int_{\partial S^0} \sigma_{\alpha 3}^{p+1} n_\alpha dl + N_{3,3}^p = 0, \\ \langle y_\beta (\sigma_{3\alpha,\alpha}^{p+1} + \sigma_{33,3}^p) \rangle &= -V_\beta^{p+1} + \int_{\partial S^0} y_\beta \sigma_{\alpha 3}^{p+1} n_\alpha dl + M_{\beta,3}^p = 0, \\ \langle y_\gamma \epsilon_{\gamma\alpha} (\sigma_{\alpha\beta,\beta}^{p+1} + \sigma_{\alpha 3,3}^p) \rangle &= \langle -y_{\gamma,\beta} \epsilon_{\gamma\alpha} \sigma_{\alpha\beta}^{p+1} \rangle + \int_{\partial S^0} y_\gamma \epsilon_{\gamma\alpha} \sigma_{\alpha\beta}^{p+1} n_\beta dl + M_{3,3}^p = 0, \\ \langle \sigma_{\alpha\beta,\beta}^{p+1} + \sigma_{\alpha 3,3}^p \rangle &= \int_{\partial S^0} \sigma_{\alpha\beta}^{p+1} n_\beta dl + V_{\alpha,3}^p = 0. \end{aligned} \quad (2.18)$$

Note that equilibrium equations (2.17a-c-d) are identical to conditions (2.11,2.14). Hence, satisfying beam equilibrium equations ensures that \mathcal{T}^p and \mathcal{W}^p have a unique solution up to the rigid motions (2.12,2.15).

2.2.2 Cascade resolution

The series of problems are now solved order by order.

2.2.2.1 First-order problems

Transverse displacement The problem \mathcal{T}^1 is not loaded. Consequently, the transverse displacement u_α^1 is a rigid motion and the corresponding stress is null:

$$u_\alpha^1 = U_\alpha^1(y_3) + y_\beta \epsilon_{\beta\alpha} \Theta^1(y_3) \quad \text{and} \quad \sigma_{\alpha\beta}^0 = 0, \quad \sigma_{33}^0 = 0. \quad (2.19)$$

Here, Θ^1 appears as the leading order angle of twist and U_α^1 as the next order macroscopic transverse displacement.

2. It will appear that M_α^p is the working conjugate to the curvature $U_{\alpha,33}^p$ and not the conventional bending moment. Indeed, the classical definition is $m_\alpha^p = \langle \epsilon_{\alpha\beta} y_\beta \sigma_{33}^p \rangle = \epsilon_{\alpha\beta} M_\beta^p$. This choice is made for convenience.

Longitudinal displacement The longitudinal displacement problem (warping mode) \mathcal{W}^1 writes as:

$$\mathcal{W}^1 : \begin{cases} \sigma_{3\alpha,\alpha}^0 = 0 & \text{on } \mathcal{S}^0, & (2.20a) \\ \sigma_{\alpha 3}^0 = C_{\alpha 3\beta 3} 2\varepsilon_{\beta 3}^0 & \text{on } \mathcal{S}^0, & (2.20b) \\ 2\varepsilon_{\alpha 3}^0 = u_{3,\alpha}^1 + U_{\alpha,3}^0 & \text{on } \mathcal{S}^0, & (2.20c) \\ \sigma_{\alpha 3}^0 n_\alpha = 0 & \text{on } \partial\mathcal{S}^0. & (2.20d) \end{cases}$$

The applied load is self-equilibrating and the solution of this boundary value problem writes as:

$$u_3^1 = U_3^1 + y_\alpha U_{\alpha,3}^0 \quad \text{and} \quad \sigma_{\alpha 3}^0 = 0, \quad (2.21)$$

where $U_{\alpha,3}^0$ appears as the bending rotation and U_3^1 as the leading order longitudinal displacement.

2.2.2.2 Second-order problems

Transverse displacement The transverse displacement u_α^2 is derived through:

$$\mathcal{T}^2 : \begin{cases} \sigma_{\alpha\beta,\beta}^1 = 0 & \text{on } \mathcal{S}^0, & (2.22a) \\ \sigma_{\alpha\beta}^1 = C_{\alpha\beta\gamma\delta} (\varepsilon_{\delta\gamma}^1 - \tilde{d}_{\delta\gamma} T) + C_{\alpha\beta 33} (\varepsilon_{33}^1 - \tilde{d}_{33} T), & \text{on } \mathcal{S}^0, & (2.22b) \\ \sigma_{33}^1 = C_{33\alpha\beta} (\varepsilon_{\beta\alpha}^1 - \tilde{d}_{\beta\alpha} T) + C_{3333} (\varepsilon_{33}^1 - \tilde{d}_{33} T) & \text{on } \mathcal{S}^0, & (2.22c) \\ \varepsilon_{\alpha\beta}^1 = u_{(\alpha,\beta)}^2, \quad \varepsilon_{33}^1 = U_{3,3}^1 + y_\alpha U_{\alpha,33}^0 & \text{on } \mathcal{S}^0, & (2.22d) \\ \sigma_{\alpha\beta}^1 n_\beta = 0 & \text{on } \partial\mathcal{S}^0. & (2.22e) \end{cases}$$

Again, the applied load is globally self-equilibrating. The solution of this boundary value problem parametrized by the elongation $U_{3,3}^1$, the curvatures $U_{\alpha,33}^0$ and the eigenstrain T writes as the linear superposition of each contribution:

$$u_\alpha^2 = \tilde{u}_\alpha^{\varepsilon^3} U_{3,3}^1 + \tilde{u}_\alpha^{\chi^1} U_{1,33}^0 + \tilde{u}_\alpha^{\chi^2} U_{2,33}^0 + \tilde{u}_\alpha^T T + U_\alpha^2 + y_\beta \varepsilon_{\beta\alpha} \Theta^2, \quad (2.23)$$

where $\tilde{u}_\alpha^{\varepsilon^3}$, $\tilde{u}_\alpha^{\chi^1}$, $\tilde{u}_\alpha^{\chi^2}$ are in-section displacements related to transverse Poisson's effect under pure traction and pure curvatures which are illustrated for a square section in Figure 2.2. When the section is homogeneous, these correctors have a closed-form expression which is detailed in [Zhao et al., 2015] for instance. Finally, \tilde{u}_α^T is a transverse Poisson's effect related to the eigenstrain. In order to be uniquely defined, the following constraints are applied to all these in-section displacements:

$$\langle \tilde{u}_\alpha \rangle = 0 \quad \text{and} \quad \langle y_\beta \varepsilon_{\beta\alpha} \tilde{u}_\alpha \rangle = 0. \quad (2.24)$$

2.2. Kinematic enrichment based on the formal asymptotic expansion

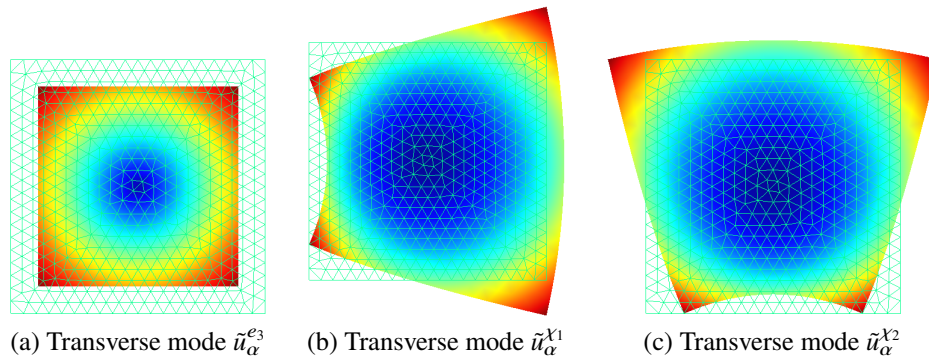


Figure 2.2 – Transverse modes related to pure traction and pure curvatures for a homogeneous square section with an isotropic material

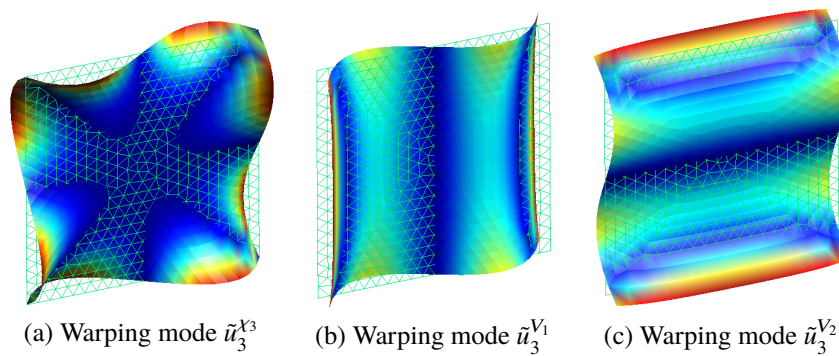


Figure 2.3 – Warping modes related to pure torsion and pure shear forces for a homogeneous square section with an isotropic material

Longitudinal displacement The longitudinal displacement u_3^2 complies with:

$$\mathcal{W}^2 : \begin{cases} \sigma_{3\alpha,\alpha}^1 = 0 & \text{on } \mathcal{S}^0, & (2.25a) \\ \sigma_{\alpha 3}^1 = C_{\alpha 3\beta 3} 2 \left(\varepsilon_{\beta 3}^1 - \tilde{d}_{\beta 3} T \right) & \text{on } \mathcal{S}^0, & (2.25b) \\ 2\varepsilon_{\alpha 3}^1 = u_{3,\alpha}^2 + y_\beta \varepsilon_{\beta\alpha} \Theta_{,3}^1 + U_{\alpha,3}^1 & \text{on } \mathcal{S}^0, & (2.25c) \\ \sigma_{\alpha 3}^1 n_\alpha = 0 & \text{on } \partial\mathcal{S}^0. & (2.25d) \end{cases}$$

The applied load is globally self-equilibrating. The solution of this boundary value problem parametrized by $\Theta_{,3}^1$, $U_{\alpha,3}^1$ and T writes as the linear superposition of each contribution:

$$u_3^2 = \tilde{u}_3^{\chi_3} \Theta_{,3}^1 + \tilde{u}_3^T T + U_3^2 + y_\alpha U_{\alpha,3}^1, \quad (2.26)$$

where $\tilde{u}_3^{\chi_3}$ is the torsion warping illustrated in Figure 2.3a and \tilde{u}_3^T a warping related to the eigenstrain. Indeed, the displacement $\tilde{u}_3^{\chi_3}$ is exactly the solution of the Neumann problem for Saint Venant's torsion. Again, these warpings are constrained as follows:

$$\langle \tilde{u}_3 \rangle = 0. \quad (2.27)$$

Macroscopic constitutive equations From the solution of second order problems, the first order stress may be written as:

$$\begin{cases} \sigma_{\alpha\beta}^1 = \tilde{\sigma}_{\alpha\beta}^{\varepsilon_3} U_{3,3}^1 + \tilde{\sigma}_{\alpha\beta}^{\chi_1} U_{1,33}^0 + \tilde{\sigma}_{\alpha\beta}^{\chi_2} U_{2,33}^0 + \tilde{\sigma}_{\alpha\beta}^T T, & (2.28a) \\ \sigma_{\alpha 3}^1 = \tilde{\sigma}_{\alpha 3}^{\chi_3} \Theta_{,3}^1 + \tilde{\sigma}_{\alpha 3}^T T, & (2.28b) \\ \sigma_{33}^1 = \tilde{\sigma}_{33}^{\varepsilon_3} U_{3,3}^1 + \tilde{\sigma}_{33}^{\chi_1} U_{1,33}^0 + \tilde{\sigma}_{33}^{\chi_2} U_{2,33}^0 + \tilde{\sigma}_{33}^T T. & (2.28c) \end{cases}$$

Expressing the traction and bending moments leads to the following constitutive equations:

$$\begin{cases} N_3^1 = A_3 U_{3,3}^1 + S_1 U_{1,33}^0 + S_2 U_{2,33}^0 + N_3^T T, & (2.29a) \\ M_1^1 = S_1^* U_{3,3}^1 + D_1 U_{1,33}^0 + D_{12} U_{2,33}^0 + M_1^T T, & (2.29b) \\ M_2^1 = S_2^* U_{3,3}^1 + D_{12}^* U_{1,33}^0 + D_2 U_{2,33}^0 + M_2^T T, & (2.29c) \end{cases}$$

where:

$$\begin{cases} A_3 = \langle \tilde{\sigma}_{33}^{\varepsilon_3} \rangle, & S_1 = \langle \tilde{\sigma}_{33}^{\chi_1} \rangle, & S_2 = \langle \tilde{\sigma}_{33}^{\chi_2} \rangle, & N_3^T = \langle \tilde{\sigma}_{33}^T \rangle, \\ S_1^* = \langle y_1 \tilde{\sigma}_{33}^{\varepsilon_3} \rangle, & D_1 = \langle y_1 \tilde{\sigma}_{33}^{\chi_1} \rangle, & D_{12} = \langle y_1 \tilde{\sigma}_{33}^{\chi_2} \rangle, & M_1^T = \langle y_1 \tilde{\sigma}_{33}^T \rangle, \\ S_2^* = \langle y_2 \tilde{\sigma}_{33}^{\varepsilon_3} \rangle, & D_{12}^* = \langle y_2 \tilde{\sigma}_{33}^{\chi_1} \rangle, & D_2 = \langle y_2 \tilde{\sigma}_{33}^{\chi_2} \rangle, & M_2^T = \langle y_2 \tilde{\sigma}_{33}^T \rangle. \end{cases} \quad (2.30)$$

The modulus A_3 is the traction stiffness, D_1 and D_2 are the bending stiffnesses. The moduli N_3^T , M_1^T and M_2^T are the traction and bending moments induced by the eigenstrain. It is proved in Appendix (A) that $S_1^* = S_1$, $S_2^* = S_2$ and $D_{12}^* = D_{12}$. The stiffnesses S_1 and S_2 are related to

2.2. Kinematic enrichment based on the formal asymptotic expansion

the first moments of inertia. Furthermore, there is a position for O , the origin of the reference frame, such that $S_1 = S_2 = 0$ and rotating the reference frame with respect to e_3 , there is an angle such that $D_{12} = 0$. When the section is homogeneous, this choice of reference frame corresponds to the centroid of the section oriented along one of the principal axis of the second moments of inertia. This is assumed in the following:

$$\begin{cases} N_3^1 = A_3 U_{3,3}^1 + N_3^T T, & (2.31a) \\ M_1^1 = D_1 U_{1,33}^0 + M_1^T T, & (2.31b) \\ M_2^1 = D_2 U_{2,33}^0 + M_2^T T. & (2.31c) \end{cases}$$

Similarly the torsion is expressed as function of the macroscopic displacements and the eigenstrain:

$$M_3^1 = D_3 \Theta_{,3}^1 + M_3^T T. \quad (2.32)$$

where the torsion stiffness and the torsion induced by the eigenstrain are:

$$D_3 = \langle y_\gamma \epsilon_{\gamma\alpha} \tilde{\sigma}_{\alpha 3}^{\chi^3} \rangle \quad \text{and} \quad M_3^T = \langle y_\gamma \epsilon_{\gamma\alpha} \tilde{\sigma}_{\alpha 3}^T \rangle. \quad (2.33)$$

Whereas the uncoupling between traction and bending moments may always be satisfied with a proper choice of the reference frame, the uncoupling between torsion is obtained here because of the symmetry assumption (2.1). This assumption may be released without limiting the approach presented here. Indeed, constitutive equations (2.31) and (2.32) would be simply coupled in such a case.

2.2.2.3 Third-order problems

Transverse displacement The transverse displacement u_α^3 is derived through \mathcal{T}^3 and loaded by $\Theta_{,33}^1$, $T_{,3}$, $U_{3,3}^2$ and $U_{\alpha,33}^1$. The applied load is self-equilibrating in translation. Indeed:

$$\langle \sigma_{\alpha 3}^1 \rangle = V_\alpha^1 = M_{\alpha,3}^0 = 0. \quad (2.34)$$

Furthermore, from the macroscopic equilibrium in torsion (2.17c) and the constitutive equation (2.32), it is possible to express $\Theta_{,33}^1$ as function of $T_{,3}$:

$$M_{3,3}^1 = D_3 \Theta_{,33}^1 + M_3^T T_{,3} = 0. \quad (2.35)$$

Substituting this relation in \mathcal{T}^3 ensures that it is equilibrated in rotation and leads to:

$$\mathcal{T}^3 : \begin{cases} \sigma_{\alpha\beta,\beta}^2 + \left(\tilde{\sigma}_{\alpha 3}^T - \frac{M_3^T}{D_3} \tilde{\sigma}_{\alpha 3}^{\chi^3} \right) T_{,3} = 0 & \text{on } \mathcal{S}^0, & (2.36a) \\ \sigma_{\alpha\beta}^2 = C_{\alpha\beta\gamma\delta} \varepsilon_{\delta\gamma}^2 + C_{\alpha\beta 33} \varepsilon_{33}^2, & \text{on } \mathcal{S}^0, & (2.36b) \\ \sigma_{33}^2 = C_{33\alpha\beta} \varepsilon_{\beta\alpha}^2 + C_{3333} \varepsilon_{33}^2 & \text{on } \mathcal{S}^0, & (2.36c) \\ \varepsilon_{\alpha\beta}^2 = u_{(\alpha,\beta)}^3, \quad \varepsilon_{33}^2 = \left(\tilde{u}_3^T - \frac{M_3^T}{D_3} \tilde{u}_3^{\chi^3} \right) T_{,3} + U_{3,3}^2 + y_\alpha U_{\alpha,33}^1 & \text{on } \mathcal{S}^0, & (2.36d) \\ \sigma_{\alpha\beta}^2 n_\beta = 0 & \text{on } \partial\mathcal{S}^0. & (2.36e) \end{cases}$$

The solution of this boundary value problem writes as:

$$u_\alpha^3 = \tilde{u}_\alpha^{T\nabla} T_{,3} + \tilde{u}_\alpha^{e_3} U_{3,3}^2 + \tilde{u}_\alpha^{\chi_1} U_{1,33}^1 + \tilde{u}_\alpha^{\chi_2} U_{2,33}^1 + U_\alpha^3 + y_\beta \epsilon_{\beta\alpha} \Theta^3 \quad \text{with} \quad \langle \tilde{u}_\alpha^{T\nabla} \rangle = 0 \quad \text{and} \quad \langle y_\beta \epsilon_{\beta\alpha} \tilde{u}_\alpha^{T\nabla} \rangle = 0 \quad (2.37)$$

and yields only one new transverse displacement localization related to the first-order variations of T .

Longitudinal displacement The longitudinal displacement u_3^3 complies with \mathcal{W}^3 and is loaded by $\Theta_{,3}^2$, $T_{,3}$, $U_{3,33}^1$ and $U_{\alpha,333}^0$. The applied load is not globally self-equilibrating for each individual loading. From the constitutive equation (2.31a) and the equilibrium equation (2.17a) with $p = 1$ it is deduced that :

$$U_{3,33}^1 = -\frac{N_3^T}{A_3} T_{,3}. \quad (2.38)$$

Substituting this in \mathcal{W}^3 ensures it is well-posed. Furthermore, it is also convenient to ensure that the load is also self-equilibrating in bending. This is obtained, from the constitutive equations (2.31b) and (2.31c) and the equilibrium equation (2.17b) for $p = 1$:

$$U_{1,333}^0 = \frac{V_1^2 - M_1^T T_{,3}}{D_1} \quad \text{and} \quad U_{2,333}^0 = \frac{V_2^2 - M_2^T T_{,3}}{D_2}. \quad (2.39)$$

Inserting these relations in problem \mathcal{W}^3 leads to:

$$\left\{ \begin{array}{l} \sigma_{3\alpha,\alpha}^2 + \tilde{\sigma}_{33}^{\chi_1} \frac{V_1^2}{D_1} + \tilde{\sigma}_{33}^{\chi_2} \frac{V_2^2}{D_2} + \left(\tilde{\sigma}_{33}^T - \frac{N_3^T}{A_3} \tilde{\sigma}_{33}^{e_3} - \frac{M_1^T}{D_1} \tilde{\sigma}_{33}^{\chi_1} - \frac{M_2^T}{D_2} \tilde{\sigma}_{33}^{\chi_2} \right) T_{,3} = 0, \quad (2.40a) \\ \sigma_{\alpha 3}^2 = C_{\alpha 3\beta 3} 2\varepsilon_{\beta 3}^2, \quad (2.40b) \\ 2\varepsilon_{\alpha 3}^2 = u_{3,\alpha}^3 + \tilde{u}_\alpha^{\chi_1} \frac{V_1^2}{D_1} + \tilde{u}_\alpha^{\chi_2} \frac{V_2^2}{D_2} + \left(\tilde{u}_\alpha^T - \frac{N_3^T}{A_3} \tilde{u}_\alpha^{e_3} - \frac{M_1^T}{D_1} \tilde{u}_\alpha^{\chi_1} - \frac{M_2^T}{D_2} \tilde{u}_\alpha^{\chi_2} \right) T_{,3} + y_\beta \epsilon_{\beta\alpha} \Theta_{,3}^2 + U_{\alpha,3}^2, \quad (2.40c) \\ \sigma_{\alpha 3}^2 n_\alpha = 0. \quad (2.40d) \end{array} \right.$$

Equations (2.40a) to (2.40c) are applied on \mathcal{S}_0 and Equation (2.40d) is applied on $\partial\mathcal{S}_0$. The solution is parametrized by the shear forces V_α^2 the first-order variations of the eigenstrain $T_{,3}$ and higher-order displacements. It writes as the linear superposition of each contributions:

$$u_3^3 = \tilde{u}_3^{V_1} V_1^2 + \tilde{u}_3^{V_2} V_2^2 + \tilde{u}_3^{T\nabla} T_{,3} + \tilde{u}_3^{\chi_3} \Theta_{,3}^2 + y_\alpha U_{\alpha,3}^2 + U_3^3. \quad \text{with} \quad \langle \tilde{u}_3 \rangle = 0 \quad (2.41)$$

The longitudinal displacements $\tilde{u}_3^{V_1}$ and $\tilde{u}_3^{V_2}$ are warpings related to shear forces illustrated in Figure (2.3b) and (2.3c). Indeed, considering the whole problem \mathcal{W}^3 loaded exclusively with shear forces, one can identify the corresponding Neumann problems in Saint Venant's beam theory. Furthermore, the equilibrium equation (2.40a) considered with only the shear forces loading and integrated on a partial section is actually Jouravskii's Formula [Jouravskii, 1856] which gives a fair estimate of shear stress in beams.

2.2. Kinematic enrichment based on the formal asymptotic expansion

Macroscopic constitutive equations From the solution of third order problems, the second-order stress may be written as:

$$\begin{cases} \sigma_{\alpha\beta}^2 = \tilde{\sigma}_{\alpha\beta}^{\epsilon_3} U_{3,3}^2 + \tilde{\sigma}_{\alpha\beta}^{\chi_1} U_{1,33}^1 + \tilde{\sigma}_{\alpha\beta}^{\chi_2} U_{2,33}^1 + \tilde{\sigma}_{\alpha\beta}^{T\nabla} T_{,3}, & (2.42a) \\ \sigma_{\alpha 3}^2 = \tilde{\sigma}_{\alpha 3}^{V_1} V_1^2 + \tilde{\sigma}_{\alpha 3}^{V_2} V_2^2 + \tilde{\sigma}_{\alpha 3}^{T\nabla} T_{,3} + \tilde{\sigma}_{\alpha 3}^{\chi_3} \Theta_{,3}^2, & (2.42b) \\ \sigma_{33}^2 = \tilde{\sigma}_{33}^{\epsilon_3} U_{3,3}^2 + \tilde{\sigma}_{33}^{\chi_1} U_{1,33}^1 + \tilde{\sigma}_{33}^{\chi_2} U_{2,33}^1 + \tilde{\sigma}_{33}^{T\nabla} T_{,3}. & (2.42c) \end{cases}$$

Expressing the second-order traction and bending moments leads to:

$$\begin{cases} N_3^2 = A_3 U_{3,3}^2 + N_3^{T\nabla} T_{,3}, & (2.43a) \\ M_1^2 = D_1 U_{1,33}^1 + M_1^{T\nabla} T_{,3}, & (2.43b) \\ M_2^2 = D_2 U_{2,33}^1 + M_2^{T\nabla} T_{,3}, & (2.43c) \end{cases}$$

where $N_3^{T\nabla} = \langle \tilde{\sigma}_{33}^{T\nabla} \rangle$, $M_1^{T\nabla} = \langle y_1 \tilde{\sigma}_{33}^{T\nabla} \rangle$ and $M_2^{T\nabla} = \langle y_2 \tilde{\sigma}_{33}^{T\nabla} \rangle$ are the traction and bending moments induced by the longitudinal variations of the eigenstrain T . Similarly the second-order torsion is expressed as function of the macroscopic displacements and the eigenstrain:

$$M_3^2 = D_3 \Theta_{,3}^2 + y_\alpha^S \epsilon_{\alpha\beta} V_\beta^2 + M_3^{T\nabla} T_{,3}, \quad (2.44)$$

where the torsion induced by the variations of eigenstrains is $M_3^{T\nabla} = \langle y_\gamma \epsilon_{\gamma\alpha} \tilde{\sigma}_{\alpha 3}^{T\nabla} \rangle$ and the shear center of the beam is defined as:

$$y_1^S = - \langle y_\alpha \epsilon_{\alpha\beta} \tilde{\sigma}_{\beta 3}^{V_2} \rangle \quad \text{and} \quad y_2^S = \langle y_\alpha \epsilon_{\alpha\beta} \tilde{\sigma}_{\beta 3}^{V_1} \rangle. \quad (2.45)$$

When the section presents two axis of symmetry, the shear center is in O but this is not always true.

2.2.2.4 Fourth-order and higher-order problems

The induction process may be pursued any higher order. Indeed, noticing that $V_{\alpha,3}^p = 0$ and following the same procedure as for \mathcal{T}^3 and \mathcal{W}^3 it appears that \mathcal{T}^4 and \mathcal{W}^4 are formally identical to \mathcal{T}^3 and \mathcal{W}^3 , incrementing the orders and depending on the second derivative of T . Hence, going higher order leads to the derivation of displacement localizations related to higher derivatives of T relevant for faster variations of T .

The use of the asymptotic expansion method is based on the scaling in equation (2.3). Hence the rescaled coordinates y_i have been used in the expression of the auxiliary problems \mathcal{T}^p and \mathcal{W}^p . However, the distinction between the two sets of coordinates is no longer necessary in practice once the section modes are computed. The use of the coordinates y_i is therefore dropped in all what follows and replaced by the use of the coordinates x_i .

2.2.3 Families of kinematic enrichment

In the asymptotic expansion procedure, three families of kinematic enrichment emerged. First, the rigid motion of the section was carried by the six macroscopic variables U_i^p , $U_{\alpha,3}^p$ and Θ_3^p . They are respectively related to the following displacement modes:

$$\tilde{\mathbf{u}}^{U_1} = \begin{pmatrix} 1 \\ 0 \\ 0 \end{pmatrix}, \quad \tilde{\mathbf{u}}^{U_2} = \begin{pmatrix} 0 \\ 1 \\ 0 \end{pmatrix}, \quad \tilde{\mathbf{u}}^{U_3} = \begin{pmatrix} 0 \\ 0 \\ 1 \end{pmatrix}, \quad \tilde{\mathbf{u}}^{\Theta_2} = \begin{pmatrix} 0 \\ 0 \\ -x_1 \end{pmatrix}, \quad \tilde{\mathbf{u}}^{\Theta_1} = \begin{pmatrix} 0 \\ 0 \\ x_2 \end{pmatrix}, \quad \tilde{\mathbf{u}}^{\Theta_3} = \begin{pmatrix} -x_2 \\ x_1 \\ 0 \end{pmatrix}. \quad (2.46)$$

Second, the six correctors related to the six beam resultants³ were derived: $\tilde{u}_\alpha^{e_3}$, $\tilde{u}_\alpha^{X_1}$, $\tilde{u}_\alpha^{X_2}$, $\tilde{u}_3^{X_3}$, $\tilde{u}_3^{V_1}$, $\tilde{u}_3^{V_2}$. They are also referred to as Saint Venant's modes [Iesan, 1976; El Fatmi, 2016]. Note that $\tilde{u}_3^{X_3}$ is the warping used by Benscoter [Benscoter, 1954]. Third, exactly as in [Ferradi et al., 2016], a family of modes related to the eigenstrain loading and its longitudinal variations was obtained: $\tilde{\mathbf{u}}^T, \tilde{\mathbf{u}}^{T^N}, \tilde{\mathbf{u}}^{T^{N^2}} \dots$

Finally, this suggests gathering all these modes in the following approximation for the 3D displacement:

$$\mathbf{u} = \sum_{i=1}^n \tilde{\mathbf{u}}^i(x_\alpha) X_i(x_3) \quad (2.47)$$

where n is the number of modes and $X_k(x_3)$ are longitudinal unknown fields. It is demonstrated in [Miara and Trabucho, 1992] that the modes generated are linearly independent. But in the eventuality where the components of the eigenstrains would be described respectively with different longitudinal functions ($T^1, T^2 \dots$), redundancies may occur. In this case it is necessary to orthogonalize the basis of modes.

2.2.4 Numerical approximation of the higher-order beam model

The discretization of the section used for the resolution of the auxiliary problems is presented. The discretization of the longitudinal beam element and the numerical approximation of the total displacement are then exposed. This approximated expression of the displacement is used to formulate the expression of the minimum of potential energy, leading to the 1D boundary value problem.

2.2.4.1 Numerical resolution of the auxiliary problems

For each order p , the weak forms of \mathcal{T}^p and \mathcal{W}^p are expressed. The resolution of the formulations obtained yields the displacement modes. The numerical resolution is operated by

3. From the traction, bending and torsion constitutive equations (2.31) and (2.32), $\tilde{u}_\alpha^{e_3}$, $\tilde{u}_\alpha^{X_\beta}$ and $\tilde{u}_3^{X_3}$ may directly be expressed as function of N_3 , M_β and M_3 .

2.2. Kinematic enrichment based on the formal asymptotic expansion

a discretization of the section with finite elements. The elements chosen here are triangles, the interpolation being quadratic. More precisely, the isoparametric expressions of the interpolation functions are:

$$\begin{aligned} N_1(a_1, a_2) &= a_1(2a_1 - 1) \quad , \quad N_2(a_1, a_2) = a_2(2a_2 - 1) \quad , \quad N_3(a_1, a_2) = (1 - a_1 - a_2)(1 - 2a_1 - 2a_2) \\ N_4(a_1, a_2) &= 4a_1a_2 \quad , \quad N_5(a_1, a_2) = 4a_2(1 - a_1 - a_2) \quad , \quad N_6(a_1, a_2) = 4a_1(1 - a_1 - a_2). \end{aligned} \quad (2.48)$$

But there is no limitation in the choice of the type of finite elements. Stress and strain are computed at the three Gauss points of each element while displacement is computed at the nodes of the sectional mesh. Note that \mathcal{T}^p and \mathcal{W}^p are also loaded with eigenstrains which must be expressed at the Gauss points (in Equation (2.40c) for instance). Hence, for the resolution of \mathcal{T}^p and \mathcal{W}^p , the displacement loading the auxiliary problems must be interpolated at the Gauss points thanks to the interpolation functions.

2.2.4.2 Numerical approximation of the beam element

To solve the higher-order beam model, the one-dimensional longitudinal problem needs to be formulated. The kinematic variables X_i are expressed with interpolation functions:

$$X_i(x_3) = \sum_{k=1}^m N_k(x_3) \tilde{U}^{i,k}, \quad (2.49)$$

with m the number of interpolation functions. $\tilde{U}^{i,k}$ is the generalized displacement associated to the mode i and the interpolation function k .

We use NURBS (Non-Uniform Rational B-Splines). NURBS are a generalization of B-Splines and Bézier curves). NURBS basis functions are defined by a degree p and a non-uniform knot vector $\Xi = \{\xi_1, \xi_2, \dots, \xi_l\}$ with l the number of knots. This domain partition allows the definition of basis functions, defined recursively by the Cox-de Boor's formulas. 0th order functions are piecewise constants:

$$N_{k,0}(\xi) = \begin{cases} 1 & \text{if } \xi_k \leq \xi < \xi_{k+1}, \\ 0 & \text{otherwise.} \end{cases} \quad (2.50)$$

Higher-order basis functions ($p > 0$) are then defined by

$$N_{k+1,p}(\xi) = \frac{\xi - \xi_k}{\xi_{k+p} - \xi_k} N_{k,p-1}(\xi) + \frac{\xi_{k+p+1} - \xi}{\xi_{k+p+1} - \xi_{k+1}} N_{k+1,p-1}(\xi). \quad (2.51)$$

It defines $m = l + p - 1$ NURBS basis functions for the order p , each function being C^{p-1} . It can be noticed that NURBS basis functions form a partition of unity:

$$\sum_{k=1}^m N_{k,p}(\xi) = 1. \quad (2.52)$$

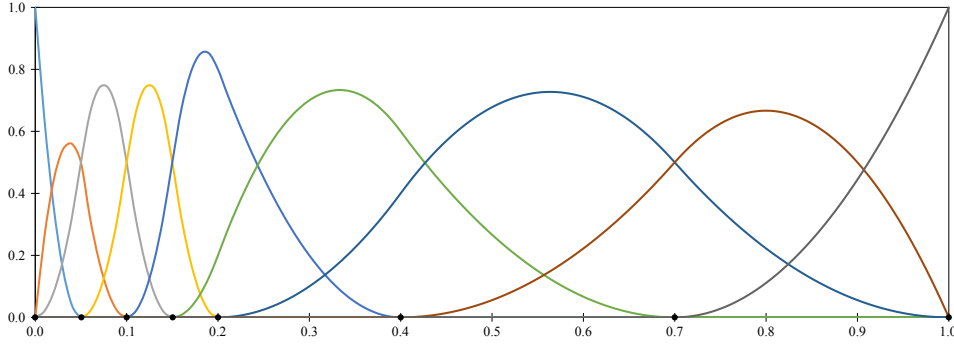


Figure 2.4 – 2nd-order NURBS basis functions for the knot vector $\{0, 0.05, 0.1, 0.15, 0.2, 0.4, 0.7, 1\}$

Moreover the basis functions are in general not interpolatory except at the ends of the beam. This motivates distinction between knots and "nodes".

Each basis function is a polynomial with a compact support contained in the interval $[\xi_k, \xi_{k+p+1}]$. Their use is therefore convenient to describe very fast variations of a field: refining the mesh defines more basis functions with short supports and affords a better localization of the field. This is an important advantage of NURBS over Lagrange polynomials: the support of a Lagrange polynomial is the whole domain $[\xi_0, \xi_l]$, and a Lagrange polynomial can show important oscillations on this interval in certain cases, a situation often called the Runge's phenomenon. The number of interpolation functions m depends on the refinement of the mesh and the chosen polynomial degree. In practice, in order to better describe fast variations of a mechanical field, the degree of the NURBS shouldn't be too high, since the higher the degree is, the larger the supports of the functions are. An illustration of NURBS basis functions with a variable refinement of the mesh is presented in Figure 2.4.

2.2.4.3 Formulation of the beam problem

For a fixed degree p of NURBS interpolation, the total displacement can now be approximated as:

$$\hat{\mathbf{u}} = \sum_{i=1}^n \tilde{\mathbf{u}}^i(\mathbf{x}) \sum_{k=1}^m N_{k,p}(x_3) \tilde{U}^{i,k}. \quad (2.53)$$

The stationarity of the minimum of the potential energy based on equations (3.3) requires:

$$\text{Find } \mathbf{u} \in \mathcal{K}, \quad \int_{\Omega} \boldsymbol{\varepsilon}(\mathbf{u}) : \mathbf{C} : \boldsymbol{\varepsilon}(\hat{\mathbf{u}}) d\Omega = \int_{\Omega} \boldsymbol{\varepsilon}^* : \mathbf{C} : \boldsymbol{\varepsilon}(\hat{\mathbf{u}}) d\Omega, \quad \forall \hat{\mathbf{u}} \in \mathcal{K}, \quad (2.54)$$

where $\mathcal{K} = \{\text{regular enough } \mathbf{u} \mid \mathbf{u} = \mathbf{0} \text{ on } \mathcal{S}^{\pm}\}$ is the set of kinematically compatible fields. The injection of the approximation $\hat{\mathbf{u}}$ (3.52) into equation (2.54) leads to the classical linear system:

$$\mathbf{K} \tilde{\mathbf{U}} = \mathbf{F}^{\text{th}}, \quad (2.55)$$

2.2. Kinematic enrichment based on the formal asymptotic expansion

where $\tilde{U} = \{\tilde{U}^{i,k}\}$ with $1 \leq i \leq n$ and $1 \leq k \leq m$. The resolution of (2.55) yields the value of all the kinematic unknowns. Equation (3.52) then gives the total displacement.

2.2.4.4 Locking study

NURBS offers many advantages but they are not yet free from locking [Echter and Bischoff, 2010]. A cantilever beam has been studied in order to investigate this phenomenon and define the range of applicability of the present discretization. The beam has a constant square section of $S = 1 \times 1 \text{ m}^2$, is clamped for $x_3 = 0$ and is loaded for $x_3 = L$ by a vertical force $F(L) = F^0/L^3$. The young's modulus and the Poisson's ratio are $E = 35 \text{ GPa}$ and $\nu = 0$. The kinematics of the beam comprises the rigid and Saint Venant's modes, and also up to three modes associated to the load applied and its gradients as described in [Ferradi et al., 2016] and so called force modes. This means that there are only 15 kinematic DOF per section. The beam element is interpolated with NURBS of various degrees, defined by 11 knots evenly distributed in $[0, L]$, with $\xi_1 = 0$ and $\xi_{11} = L$. Hence the total number of DOF is the same for all calculations.

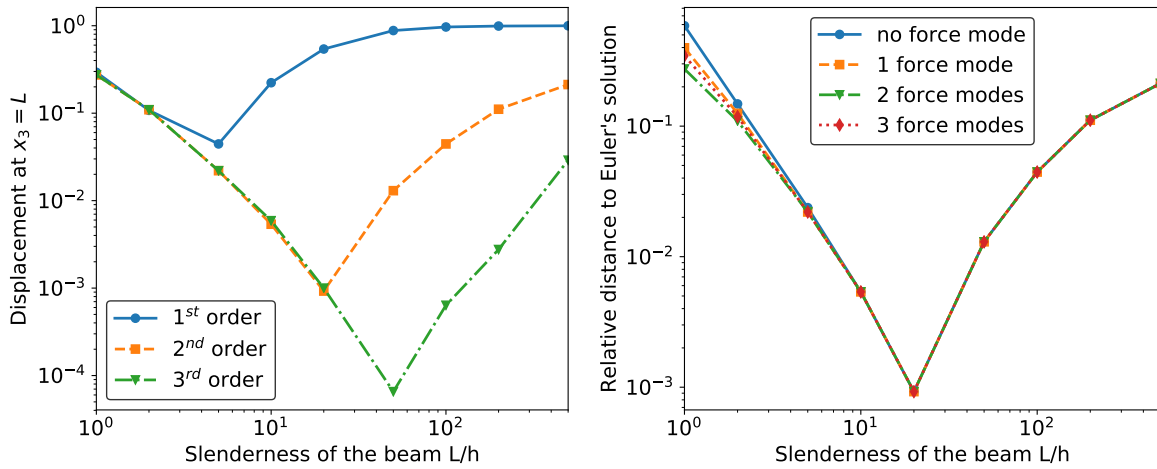
The analytical expression of the vertical displacement at $x_3 = L$ for Euler's model is well-known. Hence, the following relative error between Euler's model and the higher-order beam model is defined:

$$e^{\text{Euler}} = \left| \frac{u_2^{\text{beam}} - u_2^{\text{Euler}}}{u_2^{\text{Euler}}} \right|, \quad \text{with} \quad u_2^{\text{Euler}} = \frac{FL^3}{3EI}, \quad \text{and} \quad u_2^{\text{beam}} = \frac{1}{S} \langle u_2(x_1, x_2, L) \rangle, \quad (2.56)$$

where S is the area of the section. The Euler solution delivers a good indication on the numerical behavior of the present finite element when the slenderness increases since it is known to be the limit model for large slenderness.

First, the influence of the order of the NURBS on the locking phenomenon is investigated for an enrichment limited to 2 force modes (the applied load and its first gradient). Figure 2.5a shows the relative error as function of the slenderness of the beam for several NURBS orders. For low slenderness, all relative errors are high. Indeed, for such slenderness, it is the Euler model which is not valid. When increasing the slenderness, all beam models are expected to converge towards the Euler solution. This is not the case when locking occurs. The first order NURBS basis functions are identical to the Lagrange polynomials classically used. Therefore the same locking phenomenon is observed and e^{Euler} goes to 1 for high slenderness. The second order NURBS also suffers from locking after $L/h = 20$. Third order NURBS tends to the Euler's solution with a best match for $L/h = 50$ and $e^{\text{Euler}} < 1.10^{-4}$. Locking appears from $L/h = 100$. However, distance to Euler's solution remains only about 1% for $L/h = 500$.

Second, the influence of the number of force modes is investigated with second order NURBS. Figure 2.5b shows the relative error as function of the slenderness of the beam for several



(a) Various degree of interpolation, 2 force modes (b) Various numbers of force modes, 2nd order interpolation

Figure 2.5 – Study of locking on a cantilever beam loaded at its end, NURBS interpolation

number of force modes. It shows that increasing the number of force modes does not influence the slenderness above which locking occurs.

Therefore, for common situations with $L/h < 100$, second-order or third order NURBS can be considered as adapted for the interpolation of the beam element. In case of higher slenderness, increasing the number of longitudinal knots will mitigate locking.

2.3 Applications

This section presents two case studies using the beam element derived in the previous chapter. A table submitted to a thermal load is first considered. The beam is clamped at both ends and the load shows longitudinal and horizontal discontinuities in its application. The model is then illustrated by a cantilever beam prestressed by a steel cable. Both case studies are computed with the higher-order beam model and a volumic reference solution. The comparison highlights the numerical accuracy of the beam solution and its computational performances.

2.3. Applications

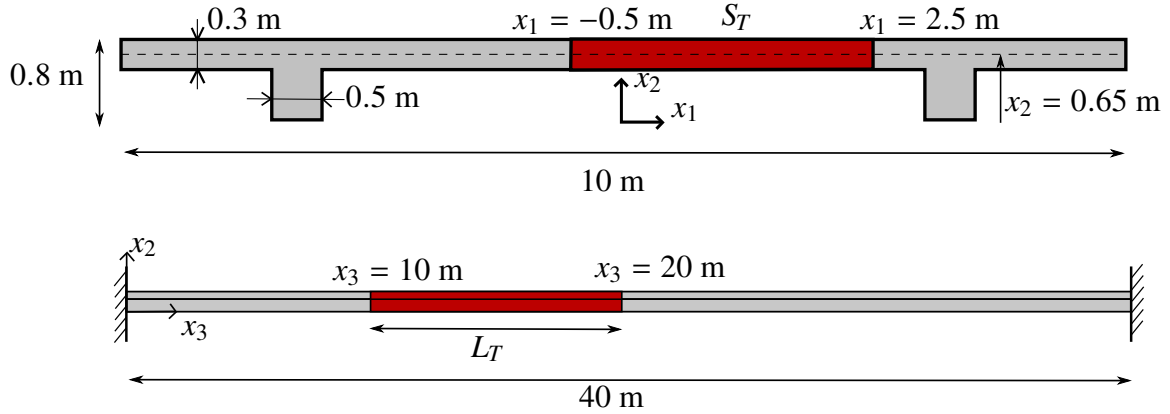


Figure 2.6 – Geometry of the beam and domain Ω_T submitted to thermal load

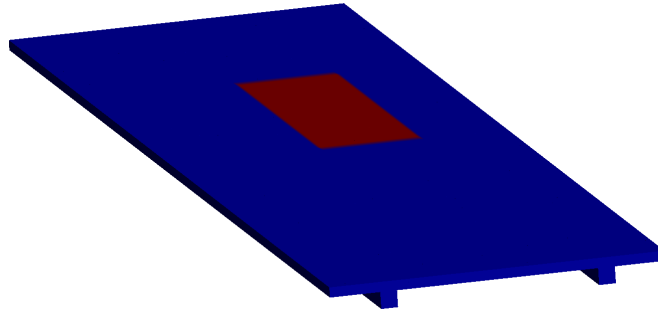


Figure 2.7 – Position of the thermal load area Ω_T

2.3.1 Application to a thermal load

2.3.1.1 Thermal load on a clamped beam

To illustrate the method, we consider a beam clamped at both ends, and loaded with a thermal load. The section of the beam is represented in Figure 2.6. The beam is 40 m long. The volume of the beam is denoted by Ω . A thermal load is applied on the volume $\Omega_T = S_T \times L_T$ described in Figures 2.6 and 2.7. The thermal load generates an isotropic strain on Ω_T :

$$\boldsymbol{\varepsilon}_{ij}^* = \alpha (T - T^{\text{ref}}) \delta_{ij} \quad (2.57)$$

where α is the dilatation coefficient, here fixed at $12 \cdot 10^{-6}$, and T^{ref} is the reference temperature

$$T - T^{\text{ref}} = \begin{cases} T^{\text{max}} - T^{\text{ref}} = 40^\circ\text{C} & \text{on } \Omega_T \\ 0^\circ\text{C} & \text{on } \Omega \setminus \Omega_T \end{cases} \quad (2.58)$$

Higher-order elastic beam model with eigenstrains

mesh	1	2	3	4
elements in slab's thickness	2	3	6	6
elements in slab's width	40	100	100	200
total number of elements	18492	140000	280000	560000
total time	320 s	1577 s	8505 s	27753 s

Table 2.1 – Refinement of the meshes

The material considered is homogeneous and isotropic. We consider the following values of the Young's modulus and the Poisson's ratio: $E = 210$ GPa and $\nu = 0.3$.

2.3.1.2 Reference solution

A 3D model computed with *Code_Aster* is taken as a reference solution for our study. A convergence study related to the refinement of the mesh is first carried out. 4 meshes are investigated. Each mesh is made of hexahedric elements, each element being quadratic. The refinements of the 4 meshes are described in Table 2.1.

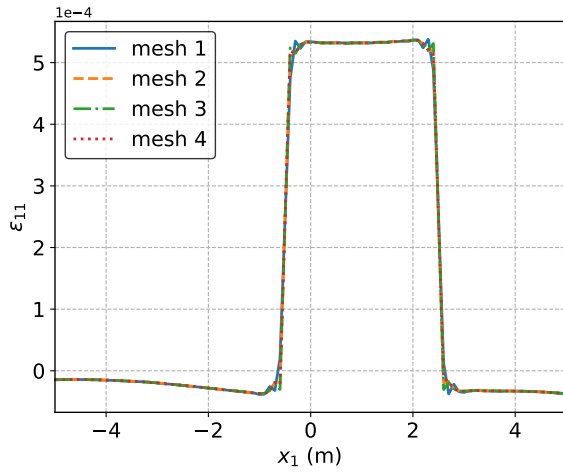
In order to assess the convergence of the different computations, the values of the strains are observed in the middle of the eigenstrain area ($x_3 = 15$ m) and close to the strain discontinuity ($x_3 = 9, 90$ m). The results are extracted at the center of the slab's thickness ($x_2 = 0.65$ m) and presented in Figure 2.8.

The results quickly converge. The Figure 2.8f representing the strain ε_{33} at $x_3 = 9, 90$ m shows a slower convergence. Figure 2.8f shows that convergence is reached for mesh 3, since the curves of mesh 3 and mesh 4 are almost overlapping. Results obtained with mesh 2 shows a gap with the converged values about 5%. Mesh 4 is chosen as the reference solution. In order to compare the results of the solutions presented in Figures 2.8a-2.8f we define the following L_2 -estimator for a given x_3 and for $x_2 = 0.65$ m:

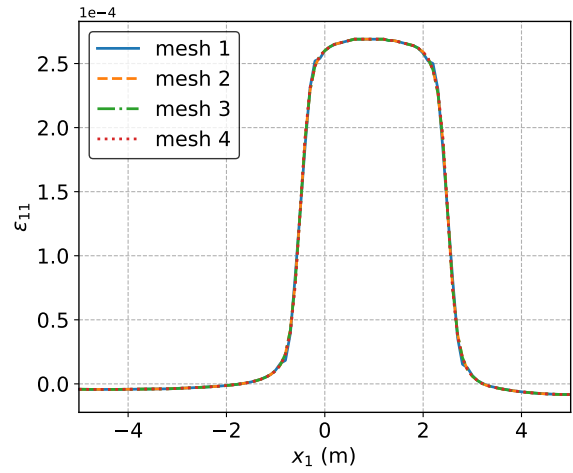
$$e_{L_2}(\varepsilon_{ij}) = \frac{\left[\int_{L_1} \left(\varepsilon_{ij}(x_1) - \varepsilon_{ij}^{(4)}(x_1) \right)^2 dx_1 \right]^{1/2}}{\left[\int_{L_1} \left(\varepsilon_{ij}^{(4)}(x_1) \right)^2 dx_1 \right]^{1/2}} \quad (2.59)$$

where $L_1 = [-5, 5]$ is the width of the considered section. The relative errors between meshes 1, 2 and 3 and mesh 4 are gathered in Table 2.2. The maximum relative errors of each solution give an estimate of the accuracy of the reference solution and will be compared to the error of the higher-order beam approximation.

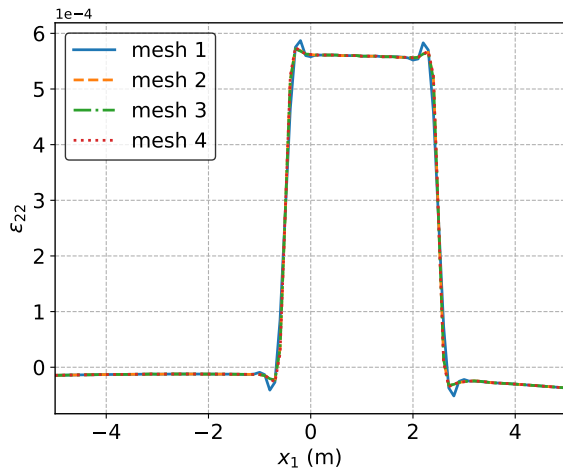
2.3. Applications



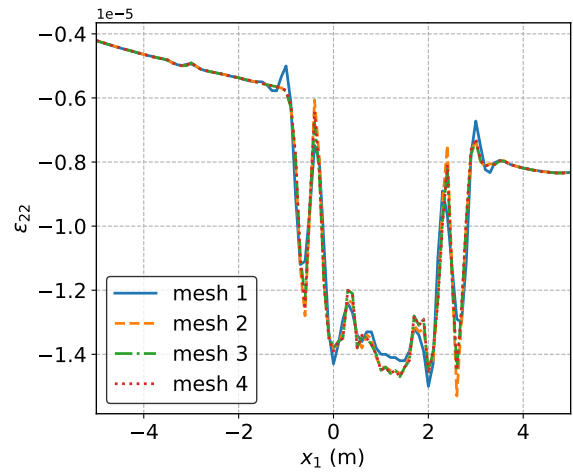
(a) Strain ε_{11} , $x_3 = 15$ m



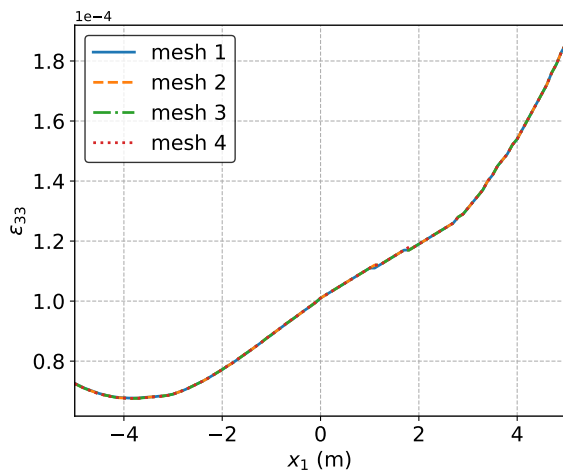
(d) Strain ε_{11} , $x_3 = 9,90$ m



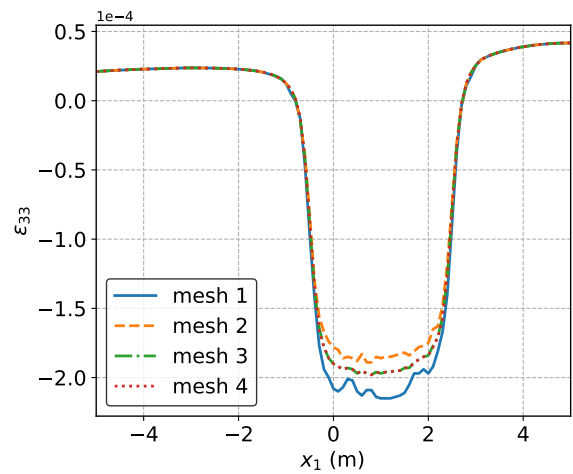
(b) Strain ε_{22} , $x_3 = 15$ m



(e) Strain ε_{22} , $x_3 = 9,90$ m



(c) Strain ε_{33} , $x_3 = 15$ m



(f) Strain ε_{33} , $x_3 = 9,90$ m

Figure 2.8 – Axial strains in the heated area and close to the temperature discontinuity for the 3D solution

Higher-order elastic beam model with eigenstrains

	$x_3 = 15 \text{ m}$			$x_3 = 9,90 \text{ m}$		
	ε_{11}	ε_{22}	ε_{33}	ε_{11}	ε_{22}	ε_{33}
mesh 1	2,81	4,38	7,21	1,34	5,15	7,53
mesh 2	0,40	0,49	0,02	0,46	1,85	5,32
mesh 3	0,98	0,55	0,01	0,41	0,63	0,56

Table 2.2 – Strain relative errors e_{L_2} in percentage of meshes 1, 2 and 3 compared to mesh 4

2.3.1.3 Higher-order beam solution

For the computation of the present method, the section is meshed with 712 triangle elements, as shown in Figure 2.9. Each element is quadratic. The longitudinal and transverse components of the eigenstrain are assumed to vary accordingly to two different longitudinal functions T_1 and T_2 :

$$\begin{aligned}
 \varepsilon_{\alpha 3}^* &= 0 \\
 \varepsilon_{\alpha\beta}^* &= d(x_\gamma)T_1(x_3)\delta_{\alpha\beta} \\
 \varepsilon_{33}^* &= d(x_\gamma)T_2(x_3)
 \end{aligned} \tag{2.60}$$

where $d(x_\alpha)$ is defined as:

$$d(x_\gamma) = \begin{cases} \alpha(T^{\max} - T^{\text{ref}}) & \text{if } x_\gamma \in S_T \\ 0 & \text{if } x_\gamma \notin S_T \end{cases} \tag{2.61}$$

The use of two different functions T_1 and T_2 is an arbitrary choice based on experience. Since the components of the eigenstrain follow two different longitudinal functions, the 2D computation yields twice as many eigenstrain modes, which represents a kinematics richer than if a single function had been used. The first orthonormalized eigenstrain modes computed up to the second gradients of T_1 and T_2 are given in Figure 2.9.

The longitudinal mesh is composed of 42 knots: 41 knots are evenly distributed between 0 and L and an additional knot is placed at $x_3 = 9,90$. This last knot is added in order to better compute displacements and strains close to the eigenstrain discontinuity. This longitudinal mesh is less refined than the one of the reference model which has 400 elements along its longitudinal axis.

The model is first computed without eigenstrain modes. Thus the only modes considered are rigid and Saint Venant's modes as presented in Section 2.2.3. We call this solution S_0 with 12 kinematic DOF per section. The model is then computed up to the second gradient of the eigenstrain $\mathbf{u}^{\nabla T_i^2}$, $i = 1, 2$. This should yield a maximum of 6 modes (\mathbf{u}^{T_1} , \mathbf{u}^{T_2} , $\mathbf{u}^{\nabla T_1}$, $\mathbf{u}^{\nabla T_2}$, $\mathbf{u}^{\nabla T_1^2}$ and $\mathbf{u}^{\nabla T_2^2}$). In our case of study $\mathbf{u}^{T_1} = \mathbf{u}^{T_2}$. We therefore get only 5 additional eigenstrain modes which are presented in Figure 2.9. It can be noticed that $\mathbf{u}^{T_1} = \mathbf{u}^{T_2}$ does not imply $\mathbf{u}^{T_1\nabla} = \mathbf{u}^{T_2\nabla}$, since the recursive definition of transversal problems \mathcal{T}^{p+1} and warping problems \mathcal{W}^{p+1} is second order: they imply loading terms as function of displacements of the order $p - 1$ and p .

2.3. Applications

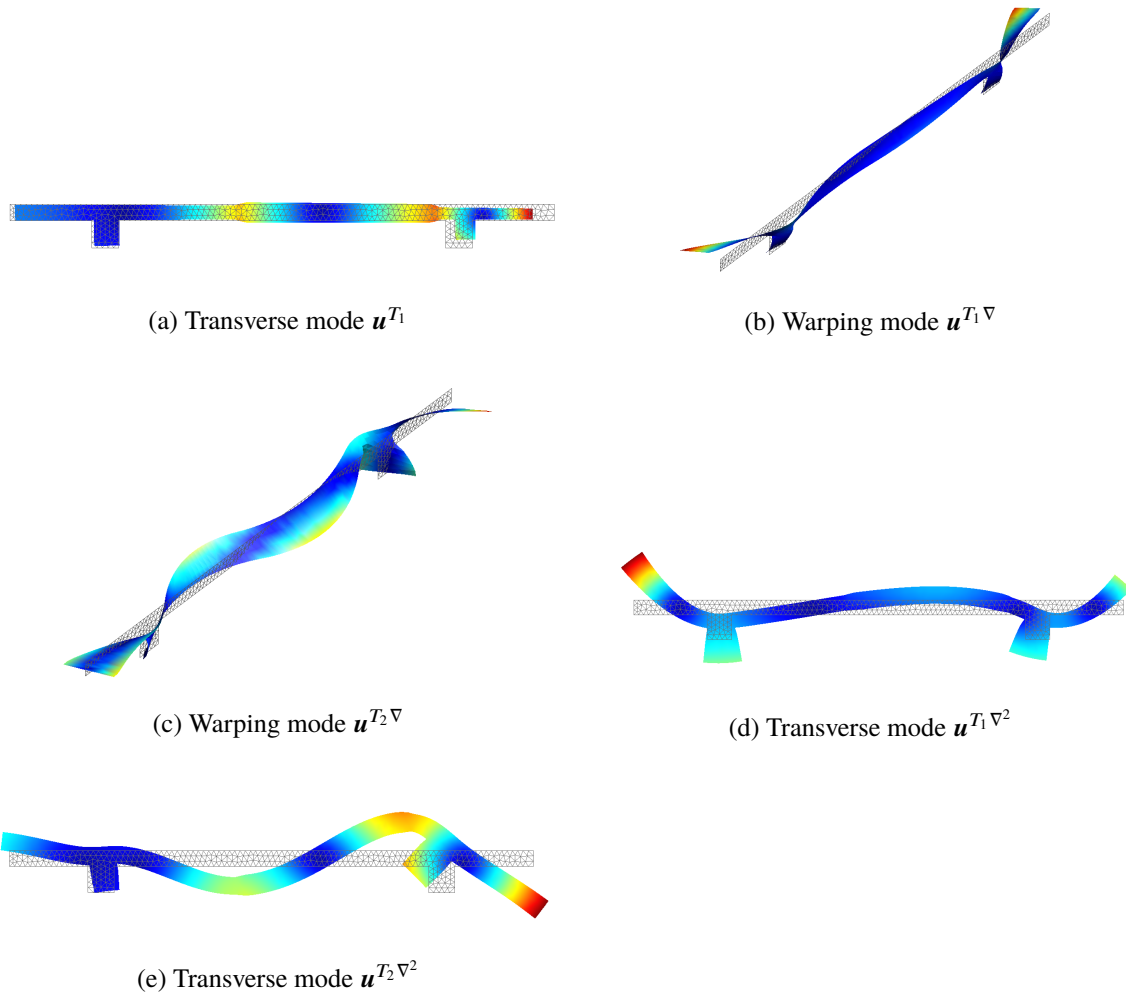


Figure 2.9 – The 5 eigenstrain modes related to the heated area in the cross-section for case study 1.

Higher-order elastic beam model with eigenstrains

	reference model	higher-order beam model
type of elements	20-node hexahedron	6-node triangle + 42-knot beam
number of elements	560000	712 + 1
CPU computation time	27753 s	11 s

Table 2.3 – Comparison of the solutions

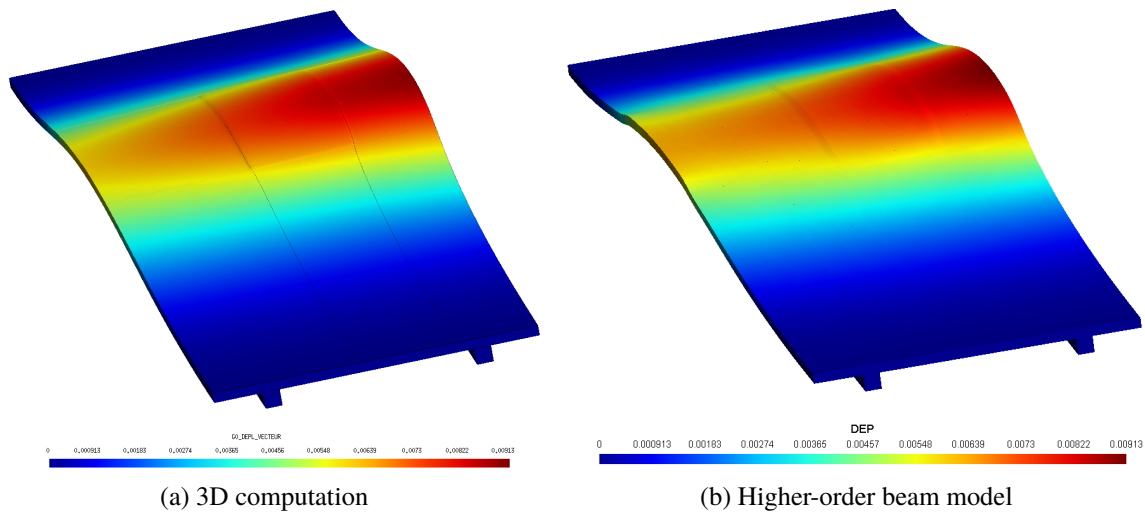


Figure 2.10 – Deformed structure under thermal load (amplification factor = 200)

We call this second solution S with 17 kinematic DOF per section. The comparison between S and S_0 highlights the contribution of the eigenstrain modes to the global response. The main features of the 3D solution and the solution S are presented in Table 3.2.

2.3.1.4 Comparison of the solutions

The deformed structure obtained with the 3D computation and with the higher-order beam model are presented in Figure 2.10 (the same scale is used for both figures). The color map shows the norm of the 3D displacement. Figure 2.10 illustrates the ability of the higher-order beam model to capture the cross-sectional displacements. The higher-order beam model can also satisfactorily capture the discontinuities of loads: the heated area is easily identifiable in Figure 2.10b.

A finer comparison of the present beam model to the reference model is now performed. Like with the reference solution, the results presented hereafter are all extracted at the mid surface of the slab ($x_2 = 0.65$ m), as defined in Figure 2.6. In order to compare the different solutions

2.3. Applications

we define as previously the following L_2 -estimators:

$$e_{L_2}(u_i) = \frac{\left[\int_{L_1} (u_i(x_1) - u_i^{3D}(x_1))^2 dx_1 \right]^{1/2}}{\left[\int_{L_1} (u_i^{3D}(x_1))^2 dx_1 \right]^{1/2}}, \quad e_{L_2}(\varepsilon_{ij}) = \frac{\left[\int_{L_1} (\varepsilon_{ij}(x_1) - \varepsilon_{ij}^{3D}(x_1))^2 dx_1 \right]^{1/2}}{\left[\int_{L_1} (\varepsilon_{ij}^{3D}(x_1))^2 dx_1 \right]^{1/2}} \quad (2.62)$$

Results in the heated area The first results presented are computed in the middle of the heated area at $x_3 = 15$ m. Displacement and strain are shown in Figures 2.11. Shear strains being less significant are not presented here.

The displacement u_1 matches well with the 3D solution, since $e_{L_2}(u_1(x_3 = 15 \text{ m})) = 1,69 \cdot 10^{-2}$. The discontinuity of the eigenstrain clearly appears in Figure 2.11a. Displacement obtained with S_0 shows that the beam modes are not sufficient to describe the global response to this specific load. The vertical displacement u_2 matches with the 3D model with an error $e_{L_2}(u_2(x_3 = 15 \text{ m})) = 2,33 \cdot 10^{-2}$, but a higher expansion order would bring even more satisfying results. Looking at the longitudinal displacement, the 3D solution is more rigid than the beam solution, and $e_{L_2}(u_3(x_3 = 15 \text{ m})) = 4,00 \cdot 10^{-2}$. The accuracy of the solution could be improved by refining the longitudinal mesh. According to Figures 2.11d to 2.11f, the axial strains computation shows very satisfying prediction. The strain ε_{33} shows a little difference with the reference model $e_{L_2}(\varepsilon_{33}(x_3 = 15 \text{ m})) = 2,45 \cdot 10^{-2}$. This error can still be lowered by increasing the number of modes or by refining the longitudinal mesh. As presented in Table 3.2, the computation of this method is fast, and it provides satisfying results.

Discontinuity and boundary conditions It is now interesting to compare the response provided by both models close to the strain discontinuity and close to one clamped end. The displacements computed at $x_3 = 9,90$ m and $x_3 = 1$ m are shown in Figure 2.12.

Close to the discontinuity, the prediction of solution S is still satisfying. The cross-sectional displacements matches with the 3D model: $e_{L_2}(u_1(x_3 = 9,90 \text{ m})) = 1,42 \cdot 10^{-2}$ and $e_{L_2}(u_2(x_3 = 9,90 \text{ m})) = 1,50 \cdot 10^{-2}$. Even if the longitudinal displacement is less satisfying with a L_2 -error $e_{L_2}(u_3(x_3 = 9,90 \text{ m})) = 6,94 \cdot 10^{-2}$, it appears that the model has no real difficulty in capturing the discontinuities. If needed, the results of u_3 could be improved by increasing the number of longitudinal knots.

The effect of the boundaries on the displacements appears in Figures 2.12d to 2.12f ($x_3 = 1$ m). Solution S matches well on the 3D model for the longitudinal displacement u_3 ($e_{L_2}(u_3(x_3 = 1 \text{ m})) = 2,52 \cdot 10^{-2}$), but the cross-sectional displacements u_1 and u_2 are not so close to the reference solution: $e_{L_2}(u_1(x_3 = 1 \text{ m})) = 3,57 \cdot 10^{-1}$ and $e_{L_2}(u_2(x_3 = 1 \text{ m})) = 1,39 \cdot 10^{-1}$). Yet the estimation is suitable for engineering practice. It is consistent to find less accurate results

Higher-order elastic beam model with eigenstrains

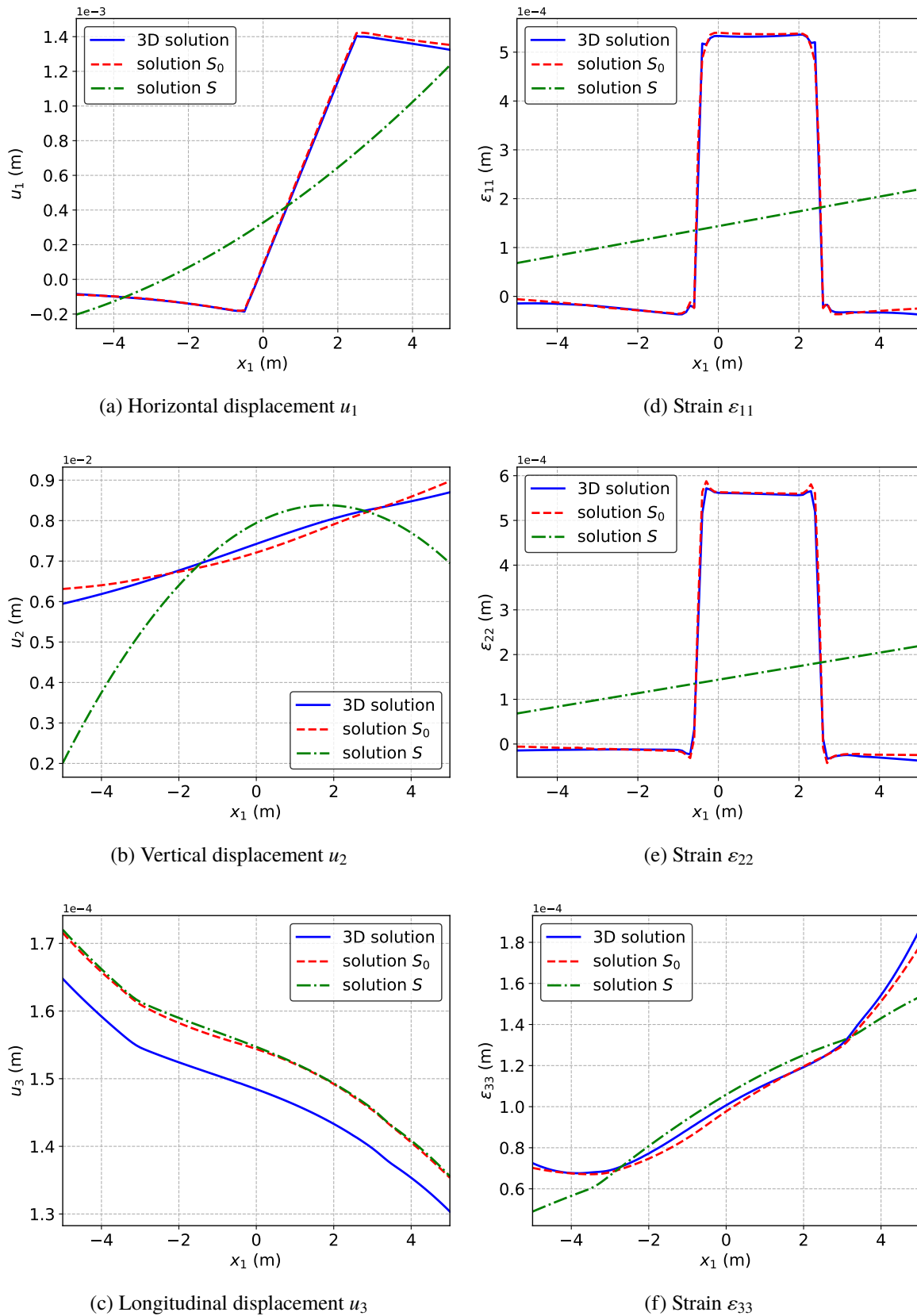
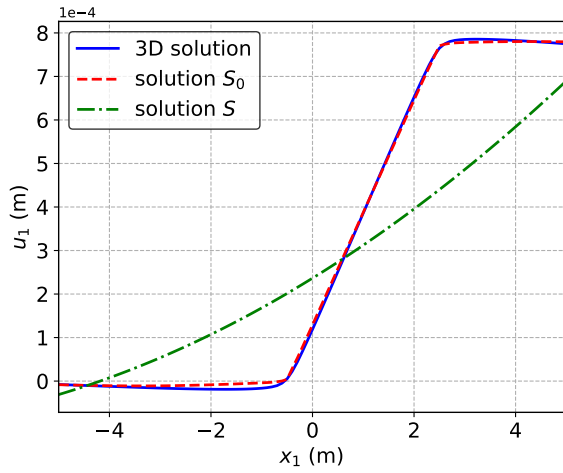
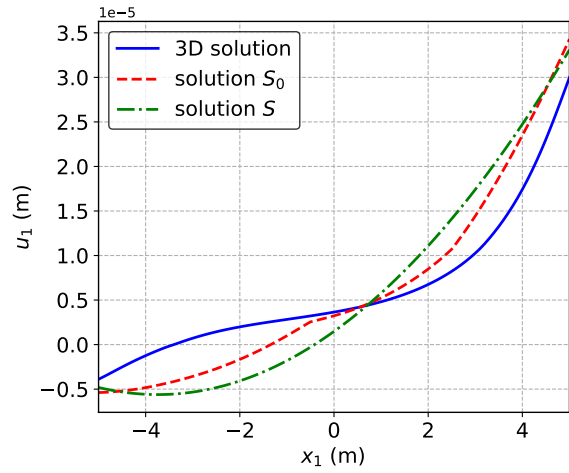


Figure 2.11 – Comparison of displacements and strains of the slab in the heated zone, $x_3 = 15$ m

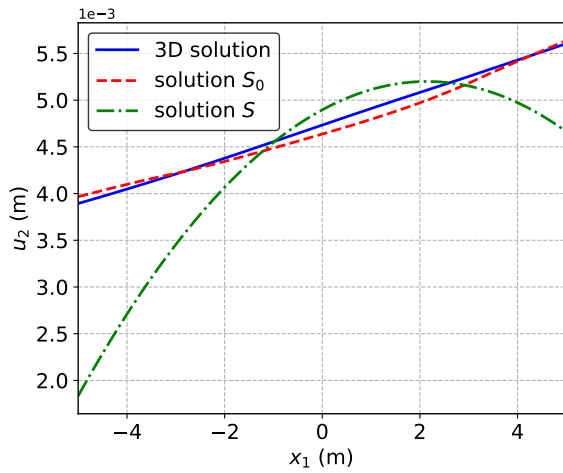
2.3. Applications



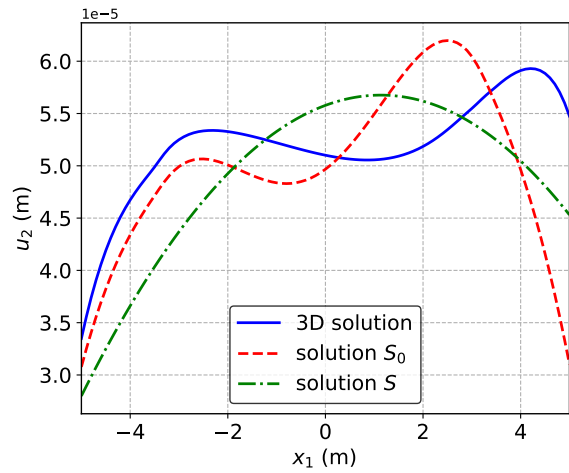
(a) Horizontal displacement u_1



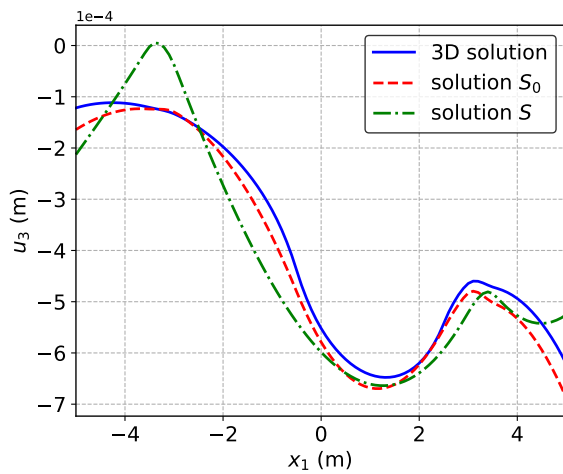
(d) Horizontal displacement u_1



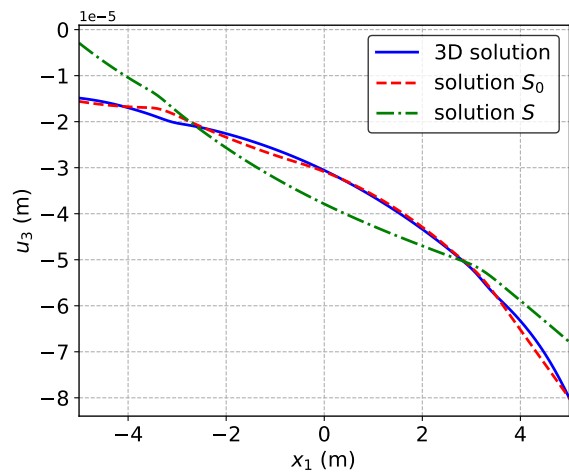
(b) Vertical displacement u_2



(e) Vertical displacement u_2



(c) Longitudinal displacement u_3



(f) Longitudinal displacement u_3

Figure 2.12 – Displacement of the heated slab close to the temperature discontinuity $x_3 = 9,90$ m (a), (b), (c) and close to supports $x_3 = 1$ m (d), (e), (f)

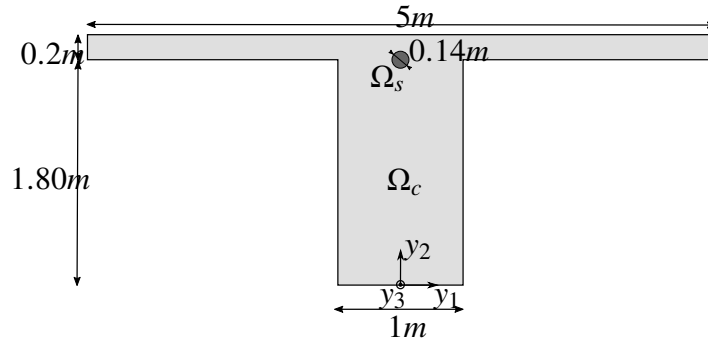


Figure 2.13 – Section of the prestressed beam

close to the boundaries since the boundary conditions are not considered in the computation of the modes. The boundaries requires particular strains that could be captured by adding modes specifically computed for the boundary conditions under consideration.

2.3.2 Application to a prestressed beam

2.3.2.1 Prestressed cable in a cantilever beam

We further illustrate the present model with a cantilever beam prestressed with a steel cable. The section of the beam is represented in Figure 2.13. The beam is 20 m long. The concrete domain is denoted by Ω_c and the steel domain by Ω_s . A constant eigenstrain $\boldsymbol{\varepsilon}^* = \varepsilon_{33}^* \mathbf{e}_3 \otimes \mathbf{e}_3$ is applied in Ω_s , with $\varepsilon_{33}^* = 7 \cdot 10^{-3}$, corresponding to 23 MN tension in the prestressed cable. Both materials are homogeneous and isotropic with:

- $(E, \nu)_{\text{concrete}} = (35 \text{ GPa}, 0.2)$
- $(E, \nu)_{\text{steel}} = (200 \text{ GPa}, 0.3)$

The beam is 20 m long. Note that, a real concrete beam would require additional reinforcement bars as well as a non-linear constitutive behavior. This simplified example is chosen here to illustrate the ability of eigenstrain modes to capture rather fast variations of the strain in the section.

2.3.2.2 Reference and beam solution

As for the previous example, a convergence study is carried out in order to choose the reference solution. The study is computed with *Code_Aster* with full 3D computations. The mesh of the chosen reference solution is made of 99680 pentahedric elements, each element being quadratic. This mesh has been constructed by meshing the end section with 2492 triangles, and then by extruding this 2D mesh on 40 section evenly distributed from $x_3 = 0$ to $x_3 = L$. For the computation with the higher-order beam model, the section is meshed with 1788 triangle elements. Each element is quadratic. The displacement modes are computed

2.3. Applications

	reference model	higher-order beam model
type of elements	15-node pentahedron	6-node triangle + 41 longitudinal knots
number of elements	99680	1788 + 1
CPU computation time	1805 s	24 s

Table 2.4 – Main features of the 3D solution and solution S

accordingly to this load, using the same decomposition of the eigenstrain as in the previous example. The sectional modes are computed up to the fourth gradient of the eigenstrain. The 5 first orthonormalized modes associated to the eigenstrain \mathbf{u}^T , $\mathbf{u}^{\nabla T}$, $\mathbf{u}^{\nabla T^2}$, $\mathbf{u}^{\nabla T^3}$ and $\mathbf{u}^{\nabla T^4}$ are represented in Figure 2.14. These three cross-sectional modes and two warping modes clearly illustrate the action of the cable on the beam. The shift between purely transversal or purely warping modes at each order comes from the monoclinic symmetry of the constitutive material (2.1) and the absence of shear in the thermal loading of the present case study.

The longitudinal mesh is composed of 41 knots evenly distributed on the length of the beam. The longitudinal mesh used here is the same as the one of the reference model. A first solution only with the rigid and the Saint Venant's modes is computed and called S_0 with 12 kinematic DOF per section. The solution using also the 5 eigenstrain modes is called S and involves 17 kinematics DOF per section. The main features of the 3D model and the solution S are presented in Table 2.4.

2.3.2.3 Comparison of the solutions

The deformed structure obtained with the 3D computation and with the higher-order beam model are presented in Figure 2.15 (the same scale is used for both figures). As expected, the prestressed cable compresses and raises the beam. The higher-order beam model captures cross-sectional displacements such as the lowering of the edges of the table, and warping displacements such as the punching effect of the cable which can be observed at the end of the beam. A finer comparison of the models is presented now. Displacements and strains are computed at mid-span of the beam at $x_3 = 10$ m and close to the clamped end at $x_3 = 0.5$ m. The results presented hereafter are all extracted at the axis of symmetry of the section for $x_1 = 0$ m.

Results at mid-span of the beam The displacements computed at $x_3 = 10$ m are presented in Figure 2.16. Because of the symmetry of the structure and the load, the horizontal displacement at $x_1 = 0$ m is expected to be zero. Very low values are observed in the three computations. However, these results can still be considered like almost zero values in view of the numerical oscillations of the 3D solution. The vertical displacement in Figure 2.16b illustrates the action of the cable close to $x_2 = 1.8$ m. This effect cannot be captured without eigenstrain modes. The L_2 -error is $e_{L_2}(u_2(x_3 = 10 \text{ m})) = 1,27 \cdot 10^{-2}$. The longitudinal displacement is

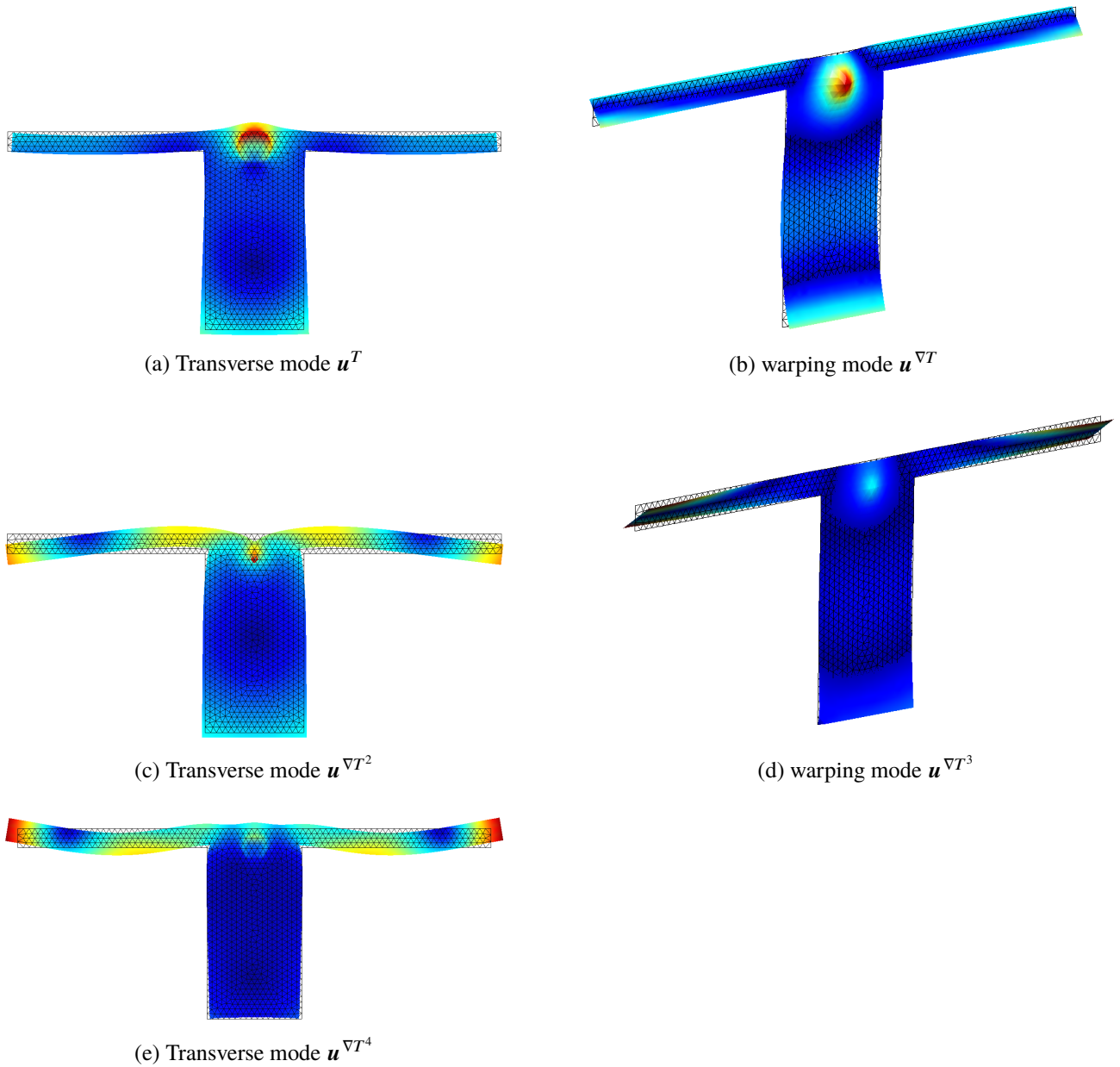


Figure 2.14 – The 5 eigenstrain modes related to the prestress in the steel cable used in case study 2.

2.4. Conclusion

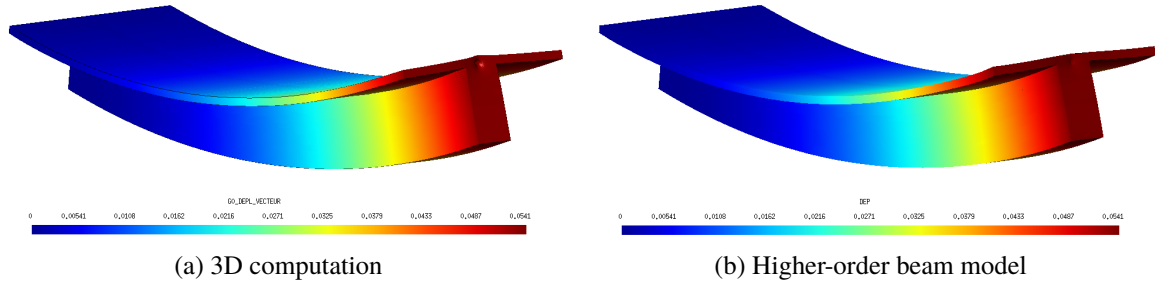


Figure 2.15 – Deformed structure under prestress steel cable (amplification factor = 100)

also well represented by the beam model with $e_{L_2}(u_3(x_3 = 10 \text{ m})) = 2,43 \cdot 10^{-2}$. The strains deriving from these displacements are presented in Figures 2.16d to 2.16f. The shear strains are not presented here because of their very small amplitude. Thanks to the enrichment of its kinematics, the beam model is able to capture the strains locally generated by the cable. However, the strains ε_{11} and ε_{22} of solution S does not perfectly match with the 3D solution in the prestressed area, leading to the errors $e_{L_2}(\varepsilon_{11}(x_3 = 10 \text{ m})) = 7,67 \cdot 10^{-2}$ and $e_{L_2}(\varepsilon_{22}(x_3 = 10 \text{ m})) = 2,69 \cdot 10^{-1}$. The accuracy of these results could be improved by providing a more refined mesh in the prestressed area of the model.

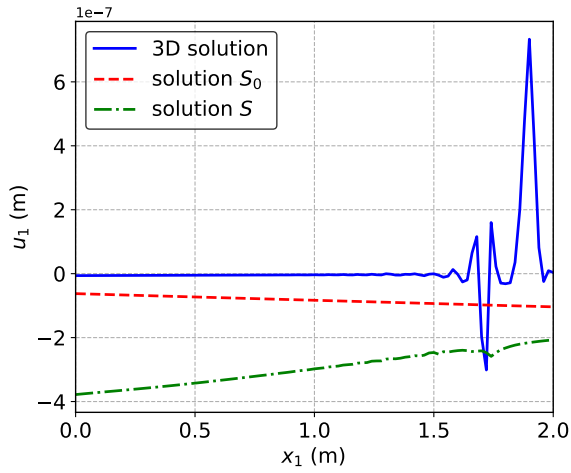
Results close to support The previous example showed that the results were less satisfactory near the boundary conditions. This is confirmed in the present case by the computations at $x_3 = 0,5 \text{ m}$. The beam solution S still correctly matches with the 3D solution, but larger errors are observed: $e_{L_2}(u_2(x_3 = 0,5 \text{ m})) = 2,43 \cdot 10^{-1}$ and $e_{L_2}(u_3(x_3 = 0,5 \text{ m})) = 5,12 \cdot 10^{-2}$. It can be noticed that even if the amplitude of the vertical displacement close to support is globally 1000 times smaller than in the middle of the beam at $x_3 = 10 \text{ m}$, the detailed influence of the cable is still well captured by the beam model.

Regarding strains, the beam model does not perfectly match with the 3D model but remains suitable for engineering practice. The L_2 -error of the axial strains are $e_{L_2}(\varepsilon_{11}(x_3 = 0,5 \text{ m})) = 1,35 \cdot 10^{-1}$, $e_{L_2}(\varepsilon_{22}(x_3 = 0,5 \text{ m})) = 2,48 \cdot 10^{-1}$ and $e_{L_2}(\varepsilon_{33}(x_3 = 0,5 \text{ m})) = 1,56 \cdot 10^{-1}$. Solution S does not describe the variation of ε_{33} around $x_2 = 1,80 \text{ m}$. This is explained by the influence of the boundary conditions on the displacement. This should be solved by the computation and the addition of new modes specific to the boundary conditions.

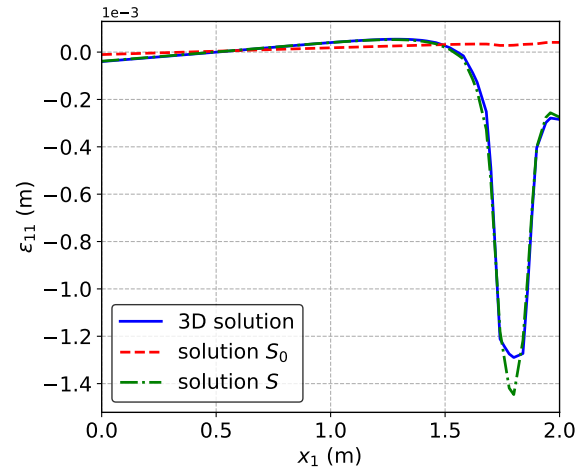
2.4 Conclusion

A numerical method based on the asymptotic expansion method was recently suggested by Ferradi et al. [Ferradi et al., 2016]. The strength of this higher-order model is that the kinematics

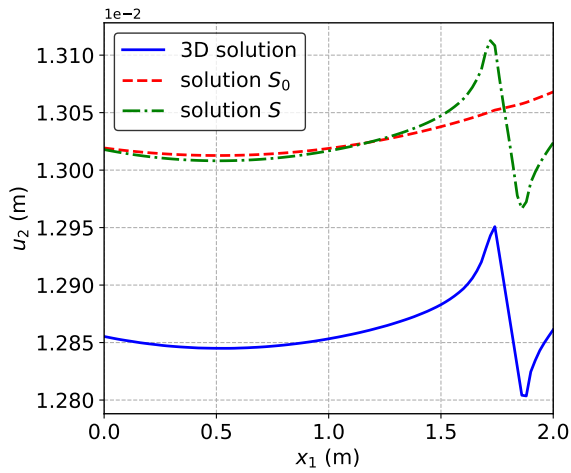
Higher-order elastic beam model with eigenstrains



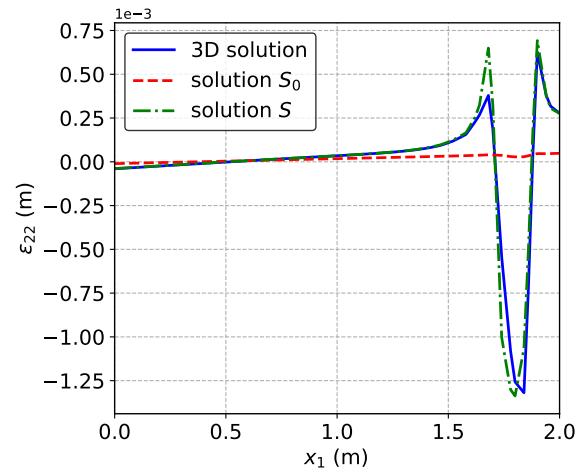
(a) Horizontal displacement u_1



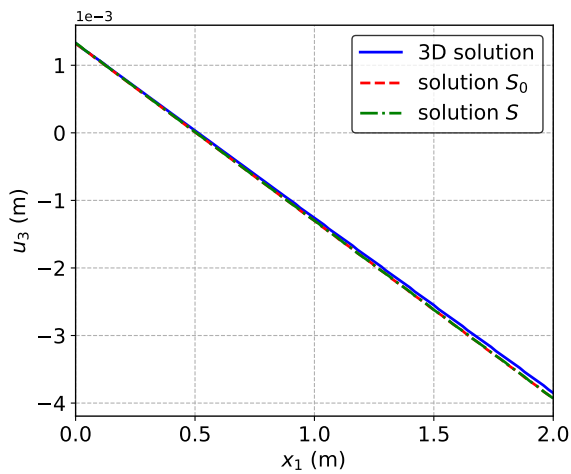
(d) Strain ϵ_{11}



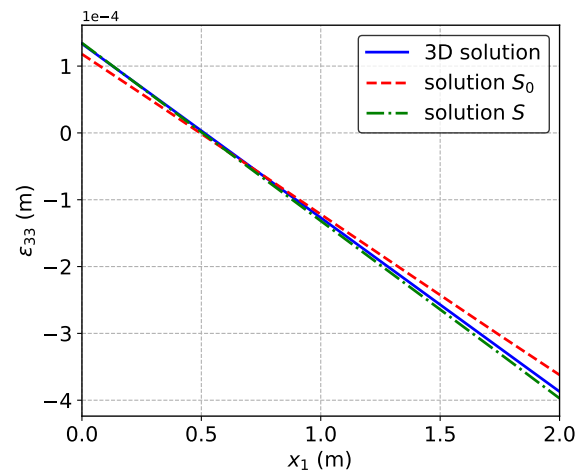
(b) Vertical displacement u_2



(e) Strain ϵ_{22}



(c) Longitudinal displacement u_3



(f) Strain ϵ_{33}

Figure 2.16 – Displacement and strain at mid-length of the beam, $x_3 = 10$ m

2.4. Conclusion

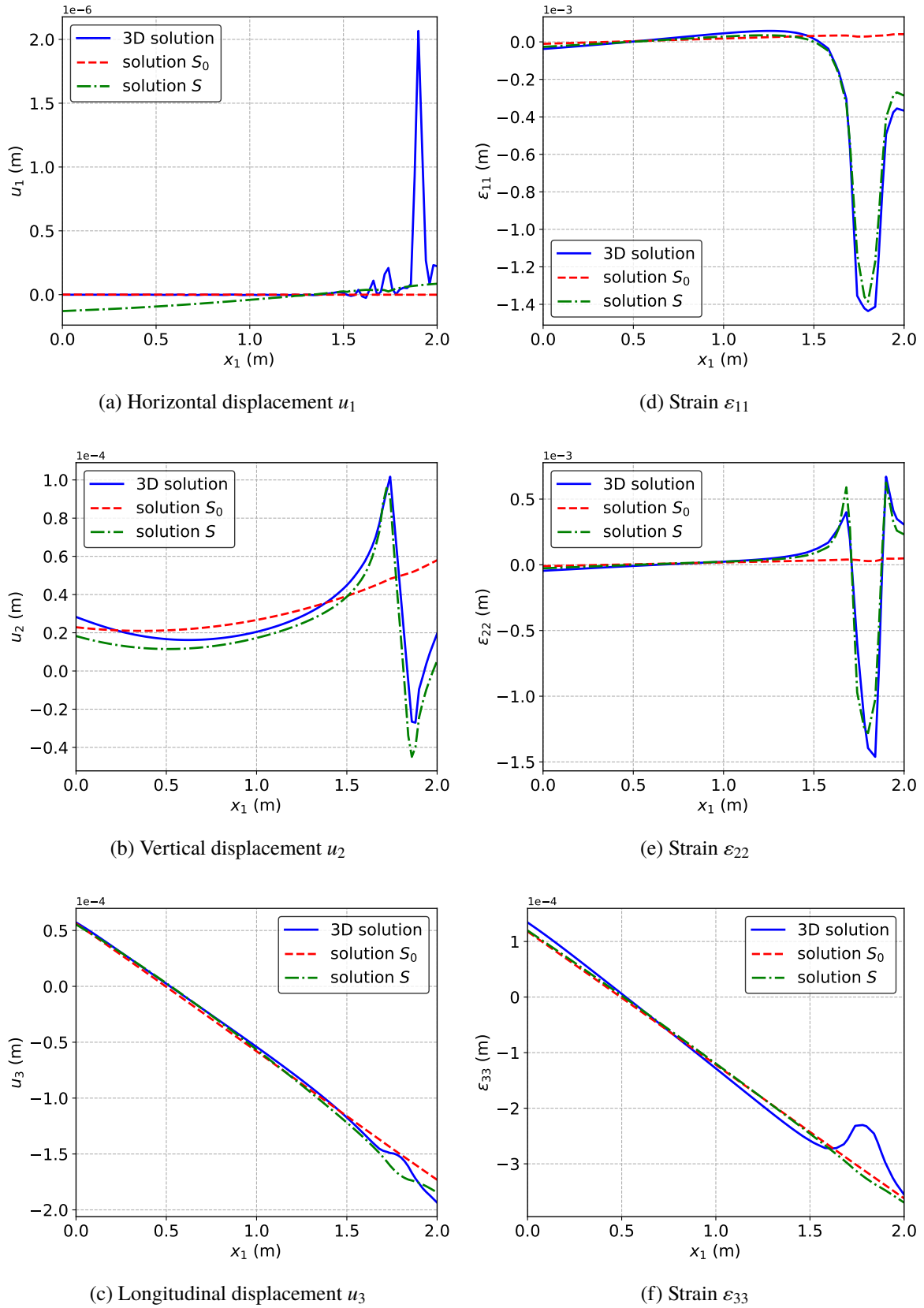


Figure 2.17 – Displacement and strain close to support, $x_3 = 0,5$ m

of the beam is enriched not only with 2D-modes related to the geometry of the section, but also according to the loads applied on the structure. This way, local effects produced by the application of the loads are directly captured by the beam element. Moreover, the extension of the kinematics does not require any *a priori* knowledge on the solution of the problem. Based on the use of the asymptotic expansion method, this model enables the user to enrich the kinematics of the beam until any expansion order n , and to refine the results subsequently.

Because of the presence of many inelastic phenomena in civil engineering applications, the current paper extends this method to the case of eigenstrains. The introduction of eigenstrains in the equilibrium equations leads to the computation of additional modes specific to the strains applied to the structure. These modes are added to the higher-order kinematics of the beam.

When compared to a 3D computation, the model presented here shows very satisfying results with a significantly reduced computational cost. Indeed, only very few additional modes and corresponding beam DOF (3 to 5) were required for capturing fairly well the applied eigenstrains. These time performances can still largely be improved by more advanced numerical techniques. As shown in this article, the model is able to capture strain discontinuities: the thermal discontinuity introduced in the first example is faithfully described in the results computed by the beam model. This example also illustrates the ability of the model to capture both transverse and longitudinal discontinuities. The second example highlights the ability of the model to render local behavior such as the punching of the prestress cable on the end section of the clamped beam. However, the very close vicinity of the boundaries sometimes seems more difficult to compute, as exposed in the first example. In order to better describe the mechanical behavior next to boundary conditions, the introduction of new modes specific to these boundary conditions is already under investigation.

* *
*

Chapter 3

Higher-order elastoplastic beam model

Abstract: *This chapter presents a new higher-order elastoplastic beam model. The elastic beam model introduced in Chapter 2 is extended to the case of plasticity. The standard framework of plasticity is first set. The methodology for reducing a 3D model to a beam model is then described and the higher-order elastoplastic beam model is presented. It is illustrated by the case study of a cantilever beam asymmetrically loaded at its end by a vertical force.*

Contents

3.1	Introduction	84
3.2	Standard 3D plasticity	87
3.2.1	The elasto-plastic boundary value problem	87
3.2.2	J_2 flow theory with isotropic hardening	88
3.2.3	Standard 3D plasticity algorithm	89
3.3	From a 3D model to a higher order beam model	93
3.3.1	Reduction of the 3D model	94
3.3.2	The higher-order beam model	95
3.4	The elastoplastic beam model	99
3.4.1	Adaptation of the <i>AELD</i> -beam model to the elasto-plastic behavior	99
3.4.2	Numerical approximation of the higher order beam model	100
3.4.3	Formulation of the beam element	101
3.4.4	The elasto-plastic algorithm	102
3.5	Application to a cantilever beam	105
3.5.1	Study of alternative Newton-Raphson's methods	105
3.5.2	Cantilever beam loaded at its free extremity	109
3.5.3	Parametric studies	116
3.6	Conclusion	120

3.1 Introduction

Beam elements are among the most used elements in structural analysis. They combine a significant simplicity in the modeling of structures and a strong time efficiency in the computation of the results.

The development of linear elastic beam models has been widely investigated. Since the earliest model of Euler-Bernoulli, a large number of elastic beam models has been suggested. The main issue in elasticity lies in the definition of the kinematics of the model which entirely determines its efficiency. Higher-order beam models offer extended kinematics able to describe more accurately local phenomena in beam structures. There are numerous way to build such kinematics assuming a priori a variable separation between the longitudinal coordinate of the beam and the in-section coordinates. For instance, Proper Orthogonal Decomposition, reduced basis approaches [Miled et al., 2013] or Proper Generalized Decomposition [Ladeveze, 1999; Chinesta et al., 2011; Bognet et al., 2012] may be used depending on the existence of a priori error estimators and the wish to update the kinematics during the computation.

It turns out that the formal asymptotic expansion of the 3D beam problem with respect to the inverse of the slenderness of the beam provides such a basis which may be derived a priori for any given beam cross-section. This approach, suggested early [Miara and Trabucho, 1992], was recently implemented in the case of linear elastic beams submitted to arbitrary loads as well as eigenstrains [Ferradi et al., 2016; Corre et al., 2017a]. Two noticeable observations were made in [Miara and Trabucho, 1992]. First, the formal asymptotic expansion delivers a free family of kinematic enrichment which is dense in the space of the 3D solution. This means that going sufficiently high in the expansion allows arbitrary refinement of the 3D solution. Second, the truncation of this family ensures that the corresponding beam model is asymptotically consistent except at the boundary. This means that the kinematic enrichment delivered by the formal asymptotic expansion is optimal in terms of approximation error far from the extremities of the beam.

Introducing elasto-plastic behavior is more complex. The inherent non-linearity of plasticity and the incremental nature of plastic analysis makes the definition of a relevant kinematics more difficult. Two main approaches are followed when solving an elasto-plastic beam problem: 1D elasto-plastic beam model based on a priori cross-section analysis and 3D elasto-plastic beam models based on a 3D beam kinematics.

The first natural approach is to express the plastic flow in terms of generalized beam variables and to solve an elasto-plastic 1D problem. This requires the elasto-plastic analysis of the cross-section for pure or combined generalized stresses and the derivation of the corresponding yield surface. The cross-section analysis may be incremental or based on yield design but assumes a uniform distribution of generalized stresses in the longitudinal direction: normal force, shear forces, bending moments and torque. In this direction, closed-form solutions were

3.1. Introduction

first devised and numerical approximation of cross-section analysis were implemented later. Indeed, the elastic problem of pure-torsion was early solved by Saint-Venant and the plastic analysis of the torsion of a beam was sketched. [Nadai, 1931] was the first to suggest a solution for the elasto-plastic problem and to calculate a plastic torque thanks to the sand-heap analogy. Then, closed-form solutions of the plastic torque have then been developed for the torsion of beams with common cross-sections: [Christopherson, 1940] solved the torsion of I-beams, [Sokolovsky, 1946] obtained a solution for beams with oval sections and [Smith and Sidebottom, 1965] for prismatic bars with rectangular sections. Closed form solutions have also been obtained for bending analysis. Combined generalized stress state were also investigated [Hill and Siebel, 1953; Boulton, 1962]. A key difficulty is the derivation of a yield surface directly function of the beam generalized stress taking into account correctly their possible interactions as well as hardening. There were recent improvements in this direction, approximating the yield surface with facets or ellipsoids [Bleyer and de Buhan, 2013]. Once the yield surface is defined, there remains to compute the elasto-plastic response of the beam, either with closed form solutions [Štok and Halilović, 2009], yield analysis [Olsen, 1999] or by means of finite element approximations [Argyris et al., 1982; Papadrakakis and Papadopoulos, 1995]. This approach has the advantage to present fast computation time, since only a 1D elasto-plastic problem needs to be solved. However, its accuracy remains limited by the beam theory assumptions. First, it cannot handle local phenomena related to the distribution of the applied load as well as to the boundary conditions. Second, it provides only an averaged description of the actual stress in the beam.

In order to improve the accuracy of the beam model, the second classical approach consists in setting a beam kinematics expressing the 3D displacement field in a separate form between the in-section coordinates and the longitudinal coordinate. This kinematics may be defined a priori or may evolve during the incremental procedure. For a fixed increment of the generalized displacements, the corresponding 3D stress is computed and the yield criterion is expressed locally. A local algorithm such as the radial return is processed on the whole body to compute the local plastic state of the beam. This locally admissible stress state is integrated on each cross-section yielding the corresponding longitudinal distribution of the beam generalized stresses. Finally, the beam global equilibrium is ensured with a classical Newton-Raphson procedure. This approach was compared with purely 1D approach by [Gendy and Saleeb, 1993]. The 3D approach appeared to be much more accurate and closer to the full 3D solution for a reasonably higher computation time than a 1D approach. Many numerical models therefore adopt the continuum-based description in terms of 3D stress components in order to benefit from its accuracy. The main difficulty lies again in the definition of a relevant kinematics able to describe the displacement related to plastic flow.

Most approaches where the kinematics is fixed a priori rely on the ones already used in linear elasticity such as Euler-Bernoulli, Timoshenko kinematics or even Saint-Venant solution, eventually with non-linear geometric corrections. For instance, [Bathe and Chaudhary, 1982] suggested to introduce the Saint-Venant warping function into the kinematics in order to compute the elasto-plastic torsion of a rectangular beam. Once the kinematics is defined,

there remains to choose the number of integration points in the cross-section in order to compute precisely the local plastic flow. Multiplying integration points improves the accuracy of the results at the price of a higher computation time for the cross-sections integrals. This is the spirit of multi-fiber beam models (see for instance [Mazars et al., 2006]).

Another direction is to enrich arbitrarily the section kinematics with degrees of freedom not necessarily related to classical cross-section displacements. An early attempt was made by [Bathe and Wiener, 1983] who performed the elastic-plastic analysis of I-beams in bending and torsion composed of three simple beam elements. This concept was formalized extensively by [Carrera et al., 2011] and co-workers.

Because plastic flow may not be easily known a priori a natural improvement of the preceding methods is to update the beam kinematics during the load increments. This is the direction followed by [Baba and Kajita, 1982] who suggested a method in which a warping mode is determined according to the plastic state of each cross-section and which was recently updated by [Tsiatas and Babouskos, 2017]. However, in this approach, it is necessary to compute a 2D elasto-plastic cross-section problem, which remains computationally costly.

In this paper, the linear higher-order beam model based on the formal asymptotic expansion [Ferradi et al., 2016; Corre et al., 2017a] is extended to elasto-plasticity in the small strains framework. This is achieved as follows. First, a higher-order kinematics is computed a priori for the considered section and applied load. As already mentioned, this kinematics forms an optimal reduced basis far from the extremities of the beam. Second, during the incremental procedure, this basis is updated with few displacement modes related to the plastic flow which occurs in the beam. More precisely, the plastic strain in some chosen cross-sections is considered as an eigenstrain load and used for computing the corresponding section displacement following the formal asymptotic expansion in [Corre et al., 2017a]. Note that, contrary to Nonuniform Transformation Field Analysis [Michel and Suquet, 2003, 2004; Roussette et al., 2009] where a basis of plastic strains is introduced, in the present approach, *displacement* plastic modes are added to the total displacement approximation. This approach presents two major advantages. First, the number of beam degrees of freedom remains very limited (about 20) thanks to the sparsity of the kinematics. Second, the update of the kinematics is not too costly because few cross-sections are used for the update and it does not require additional elasto-plastic computations in the cross-section.

The paper is organized as follows. The first section is dedicated to the description of a standard 3D plasticity model: the J_2 flow theory is described and its local integration as well as the classic Newton-Raphson's procedure are briefly recalled. The formulation of the higher-order elastic beam model presented in [Ferradi et al., 2016; Corre et al., 2017a] is then devised in Section 3.3: the definition of the kinematics thanks to the asymptotic expansion method is briefly recalled. The adaptation of this higher-order beam model to the framework of plasticity is presented in Section 3.4. Section 3.4.4 is dedicated to the description of the iterative-incremental plasticity algorithm. A radial return algorithm is used locally and an

3.2. Standard 3D plasticity

adaptation of the Newton-Raphson's procedure is suggested to satisfy the global equilibrium. An application of the model to a cantilever beam is given in Section 3.5.

3.2 Standard 3D plasticity

This section sets the framework of standard three dimensional plasticity used for the subsequent development of an higher-order elastoplastic beam model. After defining the elasto-plastic boundary value problem, we consider the classic J_2 flow theory with isotropic hardening. The radial return algorithm used for the local integration of the equilibrium equations and the global Newton-Raphson procedure used for the global incremental algorithm are then presented.

3.2.1 The elasto-plastic boundary value problem

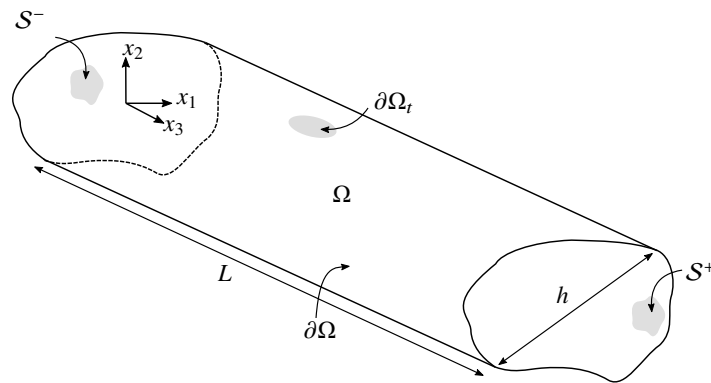


Figure 3.1 – The beam configuration

We consider a beam occupying the prismatic domain Ω (Figure 3.1) with a length L and a cross-sectional typical size h . The boundary $\partial\Omega$ is the union of the lateral surface $\partial\Omega_t$ and the two end sections S^\pm (clamped). The longitudinal coordinate is x_3 and the section coordinates are x_1 and x_2 denoted as x_α ¹, the corresponding reference frame is denoted $(O, \mathbf{e}_1, \mathbf{e}_2, \mathbf{e}_3)$ where O is an arbitrary point of the plane $x_3 = 0$.

The constitutive material of the beam is only function of the section coordinates x_α and invariant in the longitudinal direction. The fourth order elastic stiffness tensor $\mathbf{C}(x_\alpha)$ is assumed isotropic.

Let $[0, T] \subset \mathbb{R}_+$ be the time interval of interest of the problem. The displacement of the beam

1. In the following, Greek indices $\alpha, \beta, \gamma = 1, 2$ denote in-section dimensions and Latin indices $i, j, k, l = 1, 2, 3$, all three dimensions. Einstein summation convention on repeated indices is used.

is defined by the function

$$\mathbf{u} : \Omega \times [0, T] \rightarrow \mathbb{R}^3 \quad (3.1)$$

and the total infinitesimal strain tensor $\boldsymbol{\varepsilon}$ is the symmetric gradient of \mathbf{u} . The total strain splits into an elastic part $\boldsymbol{\varepsilon}^e$ and a plastic part $\boldsymbol{\varepsilon}^p$:

$$\boldsymbol{\varepsilon}(\mathbf{x}, t) = \boldsymbol{\varepsilon}^e(\mathbf{x}, t) + \boldsymbol{\varepsilon}^p(\mathbf{x}, t) \quad (3.2)$$

We consider an external body force $\mathbf{b}(\mathbf{x}, t)$ defined on $\Omega \times]0, T]$, and a surfacic force $\mathbf{t}(\mathbf{x}, t)$ defined on $\partial\Omega_t \times]0, T]$ loading the beam. The evolution is elasto-plastic, quasi-static and under small deformation. The corresponding 3D elasto-plastic boundary value problem writes as:

$$\left. \begin{array}{ll} \operatorname{div}_x \boldsymbol{\sigma} + \mathbf{b} = 0 & \text{on } \Omega \\ \boldsymbol{\sigma} = \mathbf{C} : (\boldsymbol{\varepsilon} - \boldsymbol{\varepsilon}^p) & \text{on } \Omega \\ \boldsymbol{\varepsilon} = \nabla_x^s \mathbf{u} & \text{on } \Omega \\ \boldsymbol{\sigma} \cdot \mathbf{n} = \mathbf{t} & \text{on } \partial\Omega_t \\ \mathbf{u} = 0 & \text{on } \mathcal{S}^\pm \end{array} \right\} \times [0, T], \quad (3.3)$$

where \mathbf{n} is the outer normal to $\partial\Omega_t$, ∇_x^s is the symmetric part of the 3D gradient operator and div_x is the 3D divergence operator. The flow rule is not specified in equations (3.3) but is given in Section 3.2.2.

3.2.2 J_2 flow theory with isotropic hardening

The state of the beam at a time t is defined by the variables $\boldsymbol{\varepsilon}$, $\boldsymbol{\varepsilon}^p$, $\boldsymbol{\sigma}$ and p , where p is an internal variable. In stress-space, the space of plastically compatible states is defined by:

$$\mathbb{E}_\sigma = \{(\boldsymbol{\sigma}, p) \in \mathbb{S} \times \mathbb{R}_+ \mid f(\boldsymbol{\sigma}, p) \leq 0\} \quad (3.4)$$

where \mathbb{S} is the space of statically compatible stresses, and $f : \mathbb{S} \times \mathbb{R}_+ \rightarrow \mathbb{R}$ is the yield criterion function. The state is elastic for any $(\boldsymbol{\sigma}, p) \in \mathbb{S} \times \mathbb{R}_+$ such that $f(\boldsymbol{\sigma}, p) < 0$. The boundary of \mathbb{E}_σ is defined by

$$\partial\mathbb{E}_\sigma = \{(\boldsymbol{\sigma}, p) \in \mathbb{S} \times \mathbb{R}_+ \mid f(\boldsymbol{\sigma}, p) = 0\} \quad (3.5)$$

and is called the yield surface.

We consider an associated flow rule, therefore the plastic strain flow follows the normality flow rule:

$$\dot{\boldsymbol{\varepsilon}}^p = \gamma \frac{\partial f}{\partial \boldsymbol{\sigma}} \quad (3.6)$$

where γ is a non-negative function called the consistency parameter, and $\dot{\bullet} = \partial \bullet / \partial t$. We can then express the Kuhn-Tucker conditions, describing the evolution of $\boldsymbol{\sigma}$ in \mathbb{E}_σ :

$$\gamma \geq 0, \quad f(\boldsymbol{\sigma}, p) \leq 0, \quad \gamma \dot{f}(\boldsymbol{\sigma}, p) = 0 \quad (3.7)$$

3.2. Standard 3D plasticity

The *Huber-Von Mises* [Mises, 1913] or J_2 criterion is defined by the yield function:

$$f(\boldsymbol{\sigma}, p) = \|s\| - R(p) \leq 0 \quad (3.8)$$

where s is the deviatoric part of $\boldsymbol{\sigma}$ and $\|\bullet\| = \sqrt{\bullet : \bullet}$. We consider a linear isotropic hardening R defined by:

$$R(p) = \sqrt{\frac{2}{3}} (\sigma_0 + H \cdot p) \quad (3.9)$$

where σ_0 is the yield stress, H is the plastic modulus and $p : \Omega \times]0, T] \rightarrow \mathbb{R}_+$ is the equivalent plastic strain, expressed by:

$$p(\mathbf{x}, t) = \sqrt{\frac{2}{3}} \int_0^t \|\dot{\boldsymbol{\varepsilon}}^p(\mathbf{x}, \tau)\| d\tau \quad (3.10)$$

Note that $p \geq 0, \forall t \in [0, T]$. The criterion used here ensures the convexity of \mathbb{E}_σ and a smooth boundary $\partial\mathbb{E}_\sigma$. The *Prandtl-Reuss* equations then write as:

$$f(\boldsymbol{\sigma}, p) = \|s\| - R(p) \leq 0, \quad (3.11a)$$

$$\dot{\boldsymbol{\varepsilon}}^p = \gamma \mathbf{n}, \quad \mathbf{n} = \frac{s}{\|s\|}, \quad (3.11b)$$

$$\dot{p} = \gamma \sqrt{\frac{2}{3}}, \quad \dot{p} \geq 0, \quad \dot{p} (\|s\| - R(p)) = 0 \quad (3.11c)$$

Thanks to equation (3.6), the plastic flow is orthogonal to the yield surface since \mathbf{n} is the normal to the yield surface.

Using equations (3.7) and (3.11), the rate of change of $\boldsymbol{\sigma}$ can be expressed in terms of the total strain rate $\dot{\boldsymbol{\varepsilon}}$:

$$\dot{\boldsymbol{\sigma}} = \mathbf{C}^{ep} : \dot{\boldsymbol{\varepsilon}}. \quad (3.12)$$

Here \mathbf{C}^{ep} is the elasto-plastic tangent moduli, given by:

$$\mathbf{C}^{ep} = \kappa \mathbf{1} \otimes \mathbf{1} + 2\mu \left(\mathbf{I} - \frac{1}{3} \mathbf{1} \otimes \mathbf{1} - \frac{\mathbf{n} \otimes \mathbf{n}}{1 + \frac{H}{3\mu}} \right) \quad (3.13)$$

where κ is the bulk modulus, μ is the shear modulus, \mathbf{I} is the fourth-order symmetric unit tensor, and $\mathbf{1}$ is the second-order unit tensor.

3.2.3 Standard 3D plasticity algorithm

Considering the problem introduced in Section 3.2, we recall here the procedure classically used to deal with an elasto-plastic 3D model.

The equations governing the beam evolution are gathered in equations (3.3) and (3.11). We assume that $\mathbf{u}(\mathbf{x}, 0) = \boldsymbol{\varepsilon}(\mathbf{x}, 0) = \boldsymbol{\varepsilon}^p(\mathbf{x}, 0) = \boldsymbol{\sigma}(\mathbf{x}, 0) = \mathbf{f}(\mathbf{x}, 0) = \mathbf{t}(\mathbf{x}, 0) = 0$. The time range $[0, T]$ of the study is uniformly discretized into N time steps: $\{t_0, t_1, \dots, t_N\}$ with $t_0 = 0$ and $t_N = T$. The objective of the plasticity algorithm is to compute the state of the structure $\mathbf{S}_n = \{\mathbf{u}_n, \boldsymbol{\varepsilon}_n, \boldsymbol{\varepsilon}_n^p, \boldsymbol{\sigma}_n, p_n\}$ for each time step $t = t_n$. The state \mathbf{S}_{n+1} is computed from the state of the previous step \mathbf{S}_n and from the input \mathbf{f}_{n+1} and \mathbf{t}_{n+1} . The approach is iterative: the discretized equilibrium equations are solved at a global level, generating an incremental strain $\Delta\boldsymbol{\varepsilon}$. This strain yields new state variables $\{\boldsymbol{\sigma}, \boldsymbol{\varepsilon}^p, p\}$, by integrating the local constitutive equations. The global balance equation is then tested with the new stress. The iteration process is continued until the global balance is satisfied.

3.2.3.1 The radial return algorithm

The local plasticity algorithm exposed in this section is the well-known radial return method. The radial return algorithm was first introduced by [Wilkins, 1964], and was applied to J_2 flow theory. The linear isotropic and kinematic hardening have been considered and introduced into the radial return algorithm by [Krieg and Key, 1976].

We consider the time step $[t_n, t_{n+1}]$, and assume the state \mathbf{S}_n to be known. The algorithm solves the following problem: determine the state variables $\mathbf{C}_{n+1}^{\text{ep}}$, $\boldsymbol{\sigma}_{n+1}$, $\boldsymbol{\varepsilon}_{n+1}^p$ and p_{n+1} at time t_{n+1} with the knowledge of $\boldsymbol{\sigma}_n$, $\boldsymbol{\varepsilon}_n^p$, p_n and the strain increment $\Delta\boldsymbol{\varepsilon}_n$ at time t_n .

The equations (3.3) and (3.11) are discretized and expressed at $t = t_{n+1}$:

$$\begin{cases} \boldsymbol{\sigma}_{n+1} = \boldsymbol{\sigma}_n + \kappa \text{tr}(\Delta\boldsymbol{\varepsilon}_n) \mathbf{1} + 2\mu (\Delta\mathbf{e}_n - \Delta\boldsymbol{\varepsilon}_n^p), \\ \|\mathbf{s}_{n+1}\| - R(p_n + \Delta p_n) \leq 0, \\ \Delta\boldsymbol{\varepsilon}_n^p = \Delta p_n \sqrt{\frac{3}{2}} \mathbf{n}_{n+1}, \\ \Delta p_n \geq 0, \quad \Delta p_n (\|\mathbf{s}_{n+1}\| - R(p_n + \Delta p_n)) = 0 \end{cases} \quad (3.14)$$

where $\Delta\mathbf{e}_n$ is the deviatoric part of $\Delta\boldsymbol{\varepsilon}_n$. The radial return algorithm is a well documented procedure. It is summarized here in Algorithm 1.

The consistent elasto-plastic tangent moduli The consistent elasto-plastic tangent moduli is the discrete counterpart of the continuum elasto-plastic tangent moduli defined in equation (3.13). The notion of consistent tangent moduli was presented in [Simo and Taylor, 1985], and originates in [Hughes and Taylor, 1978]. Its expression is given by:

$$\mathbf{C}_{n+1}^{\text{ep}} = \mathbf{C} - \mathbf{D}_{n+1}. \quad (3.15)$$

Here $\mathbf{D}_{n+1} = 2\mu \frac{\partial \Delta\boldsymbol{\varepsilon}_n^p}{\partial \Delta\boldsymbol{\varepsilon}_n}$ is a plastic correction to the elastic tensor \mathbf{C} . Its expression is established as follows:

$$\mathbf{D}_{n+1} = 2\mu \left[\theta_n \left(\mathbf{I} - \frac{1}{3} \mathbf{1} \otimes \mathbf{1} \right) + \bar{\theta}_n \mathbf{n}_{n+1} \otimes \mathbf{n}_{n+1} \right] \quad (3.16)$$

3.2. Standard 3D plasticity

Algorithm 1 Radial return algorithm

Require: $\Delta\boldsymbol{\varepsilon}_n, \boldsymbol{\sigma}_n, \boldsymbol{\varepsilon}_n^p, p_n$

Ensure: $\boldsymbol{C}_{n+1}^{\text{ep}}, \boldsymbol{\sigma}_{n+1}, \boldsymbol{\varepsilon}_{n+1}^p, p_{n+1}$

- 1: Compute trial elastic stresses $\boldsymbol{s}_{n+1}^{\text{trial}} = \boldsymbol{s}_n + 2\mu\Delta\boldsymbol{e}_n$ and $\boldsymbol{\sigma}_{n+1}^{\text{trial}} = \boldsymbol{\sigma}_n + \kappa\text{tr}(\Delta\boldsymbol{\varepsilon}_n)\mathbf{1} + 2\mu\Delta\boldsymbol{e}_n$
 - 2: Compute $f_{n+1}^{\text{trial}} = \|\boldsymbol{s}_{n+1}^{\text{trial}}\| - R(p_n)$
 - 3: **if** $f_{n+1}^{\text{trial}} < 0$ **then**
 - 4: $\boldsymbol{\sigma}_{n+1} = \boldsymbol{\sigma}_{n+1}^{\text{trial}}, \boldsymbol{\varepsilon}_{n+1}^p = \boldsymbol{\varepsilon}_n^p, p_{n+1} = p_n$
 - 5: **else if** $f_{n+1}^{\text{trial}} > 0$ **then**
 - 6: Compute Δp_n by solving the consistency equation $\sqrt{\frac{3}{2}}\|\boldsymbol{s}_{n+1}^{\text{trial}}\| - 3\mu\Delta p_n - \sqrt{\frac{3}{2}}R(p_n + \Delta p_n) = 0$
 - 7: Compute $\boldsymbol{n}_{n+1} = \boldsymbol{s}_{n+1}^{\text{trial}}/\|\boldsymbol{s}_{n+1}^{\text{trial}}\|$
 - 8: Compute the increment of plastic strain $\Delta\boldsymbol{\varepsilon}_n^p = \Delta p_n\sqrt{\frac{3}{2}}\boldsymbol{n}_{n+1}$
 - 9: Update state variables $\boldsymbol{\sigma}_{n+1} = \boldsymbol{\sigma}_{n+1}^{\text{trial}} - 2\mu\Delta\boldsymbol{\varepsilon}_n^p, \boldsymbol{\varepsilon}_{n+1}^p = \boldsymbol{\varepsilon}_n^p + \Delta\boldsymbol{\varepsilon}_n^p, p_{n+1} = p_n + \Delta p_n$
 - 10: Compute the consistent elasto-plastic tangent moduli $\boldsymbol{C}_{n+1}^{\text{ep}}$
 - 11: **end if**
-

where

$$\theta_n = \sqrt{\frac{2}{3}} \frac{3\mu\Delta p_n}{\|\boldsymbol{s}_{n+1}^{\text{trial}}\|}, \quad \bar{\theta}_n = \frac{3\mu}{3\mu + H} - \theta_n \quad (3.17)$$

3.2.3.2 The global algorithm

The objective of the plasticity algorithm is to yield the state \boldsymbol{S}_{n+1} with the knowledge of the state \boldsymbol{S}_n . The local integration of equations (3.3) and (3.11) ensures that the stress $\boldsymbol{\sigma}_n$ computed with the algorithm 1 is plastically admissible, meaning that $\boldsymbol{\sigma}_n$ is inside the elasto-plastic domain \mathbb{E}_σ . The global algorithm will ensure that $\boldsymbol{\sigma}_n$ is statically admissible, meaning that the global equilibrium is verified. If the evolution is plastic, both conditions are not reached simultaneously, motivating the iterative procedure. The procedure presented here is based on the *Newton-Raphson* algorithm.

Formulation of the balance equations and the Newton-Raphson algorithm The balance equation writes as the weak form of the local equilibrium equations, here expressed as the time step $t = t_{n+1}$:

$$\int_{\Omega} \boldsymbol{\sigma}_{n+1} : \boldsymbol{\varepsilon}[\hat{\boldsymbol{u}}] d\Omega = \int_{\Omega} \boldsymbol{f}_{n+1} \cdot \hat{\boldsymbol{u}} d\Omega + \int_{\partial\Omega_t} \boldsymbol{t}_{n+1} \cdot \hat{\boldsymbol{u}} dS, \quad \forall \hat{\boldsymbol{u}} \in C(\mathcal{S}^\pm, \mathbf{0}). \quad (3.18)$$

where $C(\mathcal{S}^\pm, \mathbf{0})$ is the space of displacements kinematically admissible for a zero displacement imposed on \mathcal{S}^\pm . The local Algorithm 1 is represented by the function \mathcal{L} of the variables $\Delta\boldsymbol{\varepsilon}_n$,

σ_n , $\boldsymbol{\varepsilon}_n^p$ and p_n .

$$\sigma_{n+1} = \mathcal{L}(\Delta\boldsymbol{\varepsilon}, \sigma_n, \boldsymbol{\varepsilon}_n^p, p_n). \quad (3.19)$$

The main input of the algorithm is the strain increment $\Delta\boldsymbol{\varepsilon}_n$. This motivates the choice of the displacement increment $\Delta\mathbf{u}_n$ as the main unknown of the problem. We write:

$$\Delta\boldsymbol{\varepsilon}_n = \boldsymbol{\varepsilon}[\Delta\mathbf{u}_n]. \quad (3.20)$$

For convenience, we only keep the first variable in the expression of stress at time t_{n+1} : $\sigma_{n+1} = \mathcal{L}(\boldsymbol{\varepsilon}[\Delta\mathbf{u}_n])$.

$C(\mathbf{0})$ being the space of displacements kinematically admissible to zero, we must find $\Delta\mathbf{u}_n \in C(\mathbf{0})$ such as the global balance is ensured, meaning that the residual is zero:

$$\mathcal{R}(\Delta\mathbf{u}_n, \hat{\mathbf{u}}) = 0, \quad \forall \hat{\mathbf{u}} \in C(\mathbf{0}), \quad (3.21)$$

where

$$\mathcal{R}(\Delta\mathbf{u}_n, \hat{\mathbf{u}}) = \int_{\Omega} \mathcal{L}(\boldsymbol{\varepsilon}[\Delta\mathbf{u}_n]) : \boldsymbol{\varepsilon}[\hat{\mathbf{u}}] d\Omega - \int_{\Omega} \mathbf{f}_{n+1} \cdot \hat{\mathbf{u}} d\Omega - \int_{\partial\Omega_t} \mathbf{t}_{n+1} \cdot \hat{\mathbf{u}} dS. \quad (3.22)$$

The iterative process consists in finding $\Delta\mathbf{u}_n$ satisfying equation (3.21) by using a Newton-Raphson method: we iteratively correct $\Delta\mathbf{u}_n^{(k)}$ thanks to the linearized equation:

$$\mathcal{R}(\Delta\mathbf{u}_n^{(k)}, \hat{\mathbf{u}}) + \left\langle \mathcal{R}'(\Delta\mathbf{u}_n^{(k)}, \hat{\mathbf{u}}), \delta\mathbf{u}_n^{(k)} \right\rangle = 0, \quad (3.23)$$

where $\delta\mathbf{u}_n^{(k)} = \Delta\mathbf{u}_n^{(k+1)} - \Delta\mathbf{u}_n^{(k)}$ is the correction brought to $\Delta\mathbf{u}_n^{(k)}$. The correction must satisfy $\delta\mathbf{u}_n^{(k)} \in C(\mathbf{0})$. The convergence is reached for k such that:

$$\|\mathcal{R}(\Delta\mathbf{u}_n^{(k)}, \hat{\mathbf{u}})\| < \epsilon \|\mathcal{R}(\mathbf{0}, \hat{\mathbf{u}})\|, \quad (3.24)$$

where ϵ is a scalar setting the convergence tolerance. The increment is then updated $\mathcal{R}(\Delta\mathbf{u}_n, \hat{\mathbf{u}}) = \mathcal{R}(\Delta\mathbf{u}_n^{(k)}, \hat{\mathbf{u}})$. Using equation (3.22), the second member of equation (3.23) can be written as:

$$\left\langle \mathcal{R}'(\Delta\mathbf{u}_n^{(k)}, \hat{\mathbf{u}}), \delta\mathbf{u}_n^{(k)} \right\rangle = \int_{\Omega} \boldsymbol{\varepsilon}[\delta\mathbf{u}_n^{(k)}] : \mathbf{C}_{n+1}^{\text{ep}} : \boldsymbol{\varepsilon}[\hat{\mathbf{u}}] d\Omega. \quad (3.25)$$

The consistent elasto-plastic tangent moduli $\mathbf{C}_{n+1}^{\text{ep}}$ is computed from the strain increment $\Delta\boldsymbol{\varepsilon}_n^{(k)}$ thanks to the radial return algorithm exposed in Algorithm 1.

Approximation of the global procedure Assuming a 3D discretization of the beam, the *Newton-Raphson* procedure is approximated with finite elements. We consider a mesh with N_e elements and G points of Gauss in each element. In all that follows, the finite element

3.3. From a 3D model to a higher order beam model

matrices are denoted with the notation $[\bullet]$, and the finite element vectors are denoted with the notation $\{\bullet\}$. The approximation of equation (3.25) yields

$$\int_{\Omega} \boldsymbol{\varepsilon}[\delta \mathbf{u}_n^{(k)}] : \mathbf{C}_{n+1}^{\text{ep}} : \boldsymbol{\varepsilon}[\hat{\mathbf{u}}] \, d\Omega = \{\hat{\mathbf{u}}\} [\mathbf{K}^{\text{ep}}] \{\delta \mathbf{u}_n^{(k)}\}, \quad (3.26)$$

where $[\mathbf{K}^{\text{ep}}]$ is the global tangent stiffness matrix computed from the local elasto-plastic tangent moduli $\mathbf{C}_{n+1}^{\text{ep}}$. The first member of equation (3.23) is approximated as follows:

$$-\mathcal{R}(\Delta \mathbf{u}_n^{(k)}, \hat{\mathbf{u}}) = \{\hat{\mathbf{u}}\} \{\mathbf{R}\} \quad (3.27)$$

$\{\mathbf{R}\}$ is the residual force, defined as the sum of the external and the internal forces:

$$\{\mathbf{R}\} = \{\mathbf{F}_n^{\text{ext}}\} + \{\mathbf{F}_n^{\text{int},(k)}\} \quad (3.28)$$

This leads to the classical formulation:

$$[\mathbf{K}^{\text{ep}}] \{\delta \mathbf{u}_n^{(k)}\} = \{\mathbf{R}\} \quad (3.29)$$

The resolution of equation (3.29) yields the displacement correction $\{\delta \mathbf{u}_n^{(k)}\}$. The global algorithm is presented in Algorithms 2 and 3.

Algorithm 2 Standard global algorithm

- 1: Initialize state variables: $\mathbf{S}_0 = \{\mathbf{u}_0, \boldsymbol{\varepsilon}_0, \boldsymbol{\varepsilon}_0^{\text{p}}, \boldsymbol{\sigma}_0, p_0\}$
 - 2: **for** $n = 1$ to M **do**
 - 3: Initialize $\mathbf{S}_n = \mathbf{S}_{n-1}$
 - 4: $\{\Delta \mathbf{u}\} = \{\mathbf{0}\}$
 - 5: Assemble the residual $\{\mathbf{R}\} = \{\mathbf{F}^{\text{ext}}\} + \{\mathbf{F}^{\text{int}}\}$, $r^{\text{ref}} = \|\{\mathbf{R}\}\|$, $r = r^{\text{rf}}$
 - 6: $i = 0$
 - 7: **while** $r > r^{\text{ref}}$ **do**
 - 8: Assemble the elasto-plastic stiffness matrix $[\mathbf{K}^{\text{ep}}]$
 - 9: Solve $[\mathbf{K}^{\text{ep}}] \{\delta \mathbf{u}\} = \{\mathbf{R}\}$ and assemble $\{\Delta \mathbf{u}\} = \{\Delta \mathbf{u}\} + \{\delta \mathbf{u}\}$
 - 10: Compute $\{\boldsymbol{\sigma}_n\}$, $\{\Delta \boldsymbol{\varepsilon}_n^{\text{p}}\}$ and $\mathbf{C}^{\text{ep}} \leftarrow$ **Algorithm 3**
 - 11: Compute $\{\mathbf{F}^{\text{int}}\}$
 - 12: Update $\{\mathbf{R}\}$, $r = \|\{\mathbf{R}\}\|$
 - 13: $i = i + 1$
 - 14: **end while**
 - 15: Update $\mathbf{S}_n = \{\mathbf{u}_n, \boldsymbol{\varepsilon}_n, \boldsymbol{\varepsilon}_n^{\text{p}}, \boldsymbol{\sigma}_n, p_n\}$
 - 16: **end for**
-

3.3 From a 3D model to a higher order beam model

This section presents the model reduction methodology. Starting from a three dimensional problem, the model is reduced to a beam problem. The higher-order elastic beam model presented in **Chapter 2** is then recalled.

Algorithm 3 Standard global subalgorithm

Require: $\Delta \mathbf{u}_n, \mathbf{S}_n$

Ensure: $\sigma_n, \Delta \boldsymbol{\varepsilon}_n^p, \Delta p_n, \mathbf{C}^{\text{ep}}(\mathbf{x})$

- 1: **for** $e = 1$ to N_e **do**
 - 2: **for** $g = 1$ to G **do**
 - 3: Compute $\Delta \boldsymbol{\varepsilon}_n(\mathbf{x}^g)$ from $\Delta \tilde{\mathbf{U}}$ and $\mathbb{B}_n^{(k)}$
 - 4: Update $\boldsymbol{\varepsilon}_n(\mathbf{x}^g)$
 - 5: Update $\sigma_n(\mathbf{x}^g), \Delta \boldsymbol{\varepsilon}_n^p(\mathbf{x}^g), \Delta p_n(\mathbf{x}^g)$ and $\mathbf{C}^{\text{ep}}(\mathbf{x}^g) \leftarrow$ **Algorithm 1**
 - 6: **end for**
 - 7: **end for**
-

3.3.1 Reduction of the 3D model

The standard algorithm presented in the previous section works for any 3D model. A 3D mesh of the structure implies a great number of elements. Some steps within an iteration can quickly become very time consuming, especially the assembly of the stiffness matrix and the resolution of the global balance equation $[\mathbf{K}^{\text{ep}}] \{\delta \mathbf{u}\} = \{\mathbf{R}\}$. In the beam presented in Section 3.2.1, the longitudinal dimension is larger than the two other dimensions, characterized by the length h . Therefore, we aim for a more time-efficient model taking this special geometrical feature into account.

Using a separation of the cross-sectional coordinates (x_1, x_2) and the longitudinal coordinate x_3 , the reduction of a 3D model to a beam model leads to the following expression of the displacement:

$$\mathbf{u} = \sum_i \tilde{\mathbf{u}}^i(x_\alpha) X_i(x_3) \quad (3.30)$$

where $\tilde{\mathbf{u}}^i$ are displacement modes defining the kinematics and X_i are the kinematic unknowns. The displacement modes $\tilde{\mathbf{u}}^i$ are defined on the 2D cross-section of the beam. The displacement modes $\tilde{\mathbf{u}}^i$ are an input of the beam model, allowing the reduction of 3D kinematic unknowns for the 3D model into 1D kinematic unknowns. The 3D displacement is therefore decomposed into a "2D+1D" expression. The kinematic unknowns are computed by the resolution of the global equilibrium equation which is expressed by the formulation of the beam element. The formulation of the reduced element is obtained by expressing the principle of virtual work:

$$\mathcal{W}(\mathbf{u}, \hat{\mathbf{u}}) = \int_{\Omega} \boldsymbol{\varepsilon}[\mathbf{u}] : \mathbf{C} : \boldsymbol{\varepsilon}[\hat{\mathbf{u}}] d\Omega - \int_{\Omega} \mathbf{f} \cdot \hat{\mathbf{u}} - \int_{\partial\Omega_t} \mathbf{t} \cdot \hat{\mathbf{u}} dS = 0, \quad \forall \hat{\mathbf{u}} \in C(\mathcal{S}^\pm, \mathbf{0}). \quad (3.31)$$

The strain $\boldsymbol{\varepsilon}$ is expressed by applying the compatibility relation to the equation (3.30):

$$\boldsymbol{\varepsilon}(\mathbf{x}) = \sum_i \left(\mathbf{M}_1^i(x_\alpha) X_i(x_3) + \mathbf{M}_2^i(x_\alpha) X_{i,3}(x_3) \right). \quad (3.32)$$

3.3. From a 3D model to a higher order beam model

where \mathbf{M}_1^i and \mathbf{M}_2^i are the following matrices:

$$\mathbf{M}_1^i = \frac{1}{2} \begin{bmatrix} 2\tilde{u}_{1,1}^i & \tilde{u}_{1,2}^i + \tilde{u}_{2,1}^i & \tilde{u}_{3,1}^i \\ \tilde{u}_{1,2}^i + \tilde{u}_{2,1}^i & 2\tilde{u}_{2,2}^i & \tilde{u}_{3,2}^i \\ \tilde{u}_{3,1}^i & \tilde{u}_{3,2}^i & 0 \end{bmatrix}, \quad \mathbf{M}_2^i = \frac{1}{2} \begin{bmatrix} 0 & 0 & \tilde{u}_1^i \\ 0 & 0 & \tilde{u}_2^i \\ \tilde{u}_1^i & \tilde{u}_2^i & 2\tilde{u}_3^i \end{bmatrix} \quad (3.33)$$

The virtual displacement $\hat{\mathbf{u}} \in C(\mathcal{S}^\pm, \mathbf{0})$ is expressed according to equation (3.30) on the basis of modes $\tilde{\mathbf{u}}^i$ with kinematics unknowns \hat{X}_i . Injecting equation (3.32) into equation (3.31) then leads to an expression of \mathcal{W} in terms of the 1D kinematic unknowns X_i and \hat{X}_i . The factorization of $\mathcal{W}(X_i, \hat{X}_i)$ by \hat{X}_i gives the 1D global equilibrium equation. Its resolution yields the kinematic unknowns X_i . The total displacement can then be computed thanks to equation (3.30).

3.3.2 The higher-order beam model

The beam model introduced in the previous section is completely defined by the choice of the modes $\tilde{\mathbf{u}}^i$. The kinematics can be arbitrarily assumed like in the Euler-Bernoulli's or the Timoshenko's beam models. They can also be established by means of an automated procedure, independent of the section, which is the choice made in this paper.

3.3.2.1 The Asymptotic Expansion Load Decomposition beam model

This paper is based on the higher-order elastic beam model developed in [Ferradi et al., 2016] and extended in [Corre et al., 2017a]. This model based on the asymptotic expansion method enables the development of a systematic procedure in order to extend the kinematics of the model. The kinematic unknowns are associated to displacement modes computed on the cross-section of the beam. In [Ferradi et al., 2016], the kinematics is composed of two kinds of modes. The first collection of modes are the modes of the *Saint-Venant's* solution. The collection of modes they form is denoted by $\mathbb{B}^{\text{S-V}}$. These modes are specific to the geometry of the cross-section. The second collection of modes comprises modes also specific to the load applied on the structure. For a given force \mathbf{f} applied on the structure, the model presented by Ferradi and al. enriches the kinematics with additional modes specific to \mathbf{f} . These modes enable the model to describe the participation of the load into the global response. This additional basis of force modes is denoted by $\mathbb{B}^{\mathbf{f}}$ and represented by the action of the operator $\mathcal{B}^{\mathbf{f}}$ on the load \mathbf{f} :

$$\mathbb{B}^{\mathbf{f}} = \mathcal{B}^{\mathbf{f}}(\mathbf{f}) \quad (3.34)$$

The computation of the displacement modes is now explained in more details. For the computation of the kinematics, we consider the beam to be purely linear elastic. The equations

of the boundary value problem (BVP) are therefore:

$$P : \begin{cases} \operatorname{div}_x \boldsymbol{\sigma} + \mathbf{b} = 0 & \text{on } \Omega \\ \boldsymbol{\sigma} = \mathbf{C} : \boldsymbol{\varepsilon} & \text{on } \Omega \\ \boldsymbol{\varepsilon} = \nabla_x^s \mathbf{u} & \text{on } \Omega \times [0, T], \\ \boldsymbol{\sigma} \cdot \mathbf{n} = \mathbf{t} & \text{on } \partial\Omega_t \\ \mathbf{u} = 0 & \text{on } \mathcal{S}^\pm \end{cases} \quad (3.35)$$

Noticing that the ratio $\eta = \frac{h}{L}$ is small for the geometry of a beam, a change of coordinates is operated as follows:

$$(x_1, x_2, x_3) = (hy_1, hy_2, Ly_3) \quad (3.36)$$

The scaled section is denoted \mathcal{S}^0 , and $\partial\mathcal{S}^0$ is its boundary. Then, the method is based on two main assumptions. The loads applied on the structure are first decomposed as products of a cross-sectional function and a longitudinal function:

$$\begin{aligned} b_\alpha &= \frac{1}{h} \eta^2 \tilde{b}_\alpha(y_\alpha) F(y_3), & b_3 &= \frac{1}{h} \eta \tilde{b}_3(y_\alpha) F(y_3), \\ t_\alpha &= \eta^2 \tilde{t}_\alpha(y_\alpha) F(y_3), & t_3 &= \eta \tilde{t}_3(y_\alpha) F(y_3). \end{aligned} \quad (3.37)$$

The variables are then expressed as power series of the scaling ratio η (asymptotic expansion):

$$\begin{aligned} \mathbf{u} &= L \left(\mathbf{u}^0 + \eta \mathbf{u}^1 + \eta^2 \mathbf{u}^2 + \dots \right), \\ \boldsymbol{\varepsilon} &= \boldsymbol{\varepsilon}^0 + \eta \boldsymbol{\varepsilon}^1 + \eta^2 \boldsymbol{\varepsilon}^2 + \dots, \\ \boldsymbol{\sigma} &= \boldsymbol{\sigma}^0 + \eta \boldsymbol{\sigma}^1 + \eta^2 \boldsymbol{\sigma}^2 + \dots, \end{aligned} \quad (3.38)$$

and introduced in the equations of the BVP (3.35). The powers p of η are then identified: for each power $p \in \mathbb{N}$, each compatibility equations, boundary conditions and constitutive equations for p and equilibrium equations for $p - 1$ yield an auxiliary problem on the cross-section which splits in two uncoupled boundary value problems.

Transverse displacement First, the in-section displacement problems (transverse mode) \mathcal{T} are gathered for $p \geq 0$:

$$\mathcal{T}^{p+1} : \begin{cases} \sigma_{\alpha\beta,\beta}^p + \sigma_{\alpha 3,3}^{p-1} + \delta_{p2} \tilde{b}_\alpha F = 0 & \text{on } \mathcal{S}^0 \\ \sigma_{\alpha\beta}^p = 2\mu \varepsilon_{\alpha\beta}^p + \lambda \varepsilon_{kk}^p \delta_{\alpha\beta}, \quad \sigma_{33}^p = 2\mu \varepsilon_{33}^p + \lambda \varepsilon_{kk}^p & \text{on } \mathcal{S}^0 \\ 2\varepsilon_{\alpha\beta}^p = u_{\alpha,\beta}^{p+1} + u_{\beta,\alpha}^{p+1}, \quad \varepsilon_{33}^p = u_{3,3}^p & \text{on } \mathcal{S}^0 \\ \sigma_{\alpha\beta}^p n_\beta = \delta_{p2} \tilde{t}_\alpha F & \text{on } \partial\mathcal{S}^0 \end{cases} \quad (3.39)$$

where $\sigma^{-1} = 0$ and $\delta_{p2} = 1$ if $p = 2$ and $\delta_{p2} = 0$ else. For a simply connected cross-section, this BVP on the displacement u_α^{p+1} is well-posed if the applied load is globally self-equilibrating for in-section translations and rotation:

$$\left\langle \sigma_{\alpha 3,3}^{p-1} \right\rangle = 0, \quad \left\langle y_\beta \varepsilon_{\beta\alpha} \sigma_{\alpha 3,3}^{p-1} \right\rangle = 0 \quad (3.40)$$

3.3. From a 3D model to a higher order beam model

where $\epsilon_{11} = \epsilon_{22} = 0$, $\epsilon_{12} = +1$, $\epsilon_{21} = -1$. The solution is thus defined up to a rigid motion of the section in its plane.

Longitudinal displacement Second, the longitudinal displacement problems (warping mode) \mathcal{W}^p are obtained for $p \geq 0$:

$$\mathcal{W}^{p+1} : \begin{cases} \sigma_{3\alpha,\alpha}^p + \sigma_{33,3}^{p-1} + \delta_{1p} \tilde{b}_3 F = 0 & \text{on } \mathcal{S}^0 \\ \sigma_{\alpha 3}^p = 2\mu \varepsilon_{\alpha 3}^p + \lambda \varepsilon_{kk}^p \delta_{\alpha 3} & \text{on } \mathcal{S}^0 \\ 2\varepsilon_{\alpha 3}^p = u_{3,\alpha}^{p+1} + u_{\alpha,3}^p & \text{on } \mathcal{S}^0 \\ \sigma_{\alpha 3}^p n_\alpha = 0 & \text{on } \partial \mathcal{S}^0 \end{cases} \quad (3.41)$$

Again, for a simply connected cross-section, this BVP on the displacement u_3^{p+1} is well-posed if the load applied is globally self-equilibrating for the longitudinal translation:

$$\left\langle \sigma_{33}^{p-1} \right\rangle = 0 \quad (3.42)$$

The solution is defined up to a longitudinal displacement.

The successive resolutions of \mathcal{T}^{p+1} and \mathcal{W}^{p+1} for each p such that $0 \leq p \leq n_{AE}$ yields a collection of displacement modes $(\tilde{\mathbf{u}}^i)_{0 \leq i \leq n_{AE}}$ where n_{AE} is the order of the asymptotic expansion. Once orthonormalized thanks to a Gram-Schmidt procedure, these modes form the kinematics of the model. The modes are orthonormalized according to the L_2 -norm defined as follows:

$$\|\tilde{\mathbf{u}}^i\| = \left(\int_S \sum_{j=1}^3 (\tilde{\mathbf{u}}_j^i)^2 dS \right)^{1/2} \quad (3.43)$$

The computation of the modes is only made possible by assuming variable separation: they are decomposed and expressed as the product of a function of the cross-sectional coordinates and a function of the longitudinal coordinate. Therefore this model is here named the Asymptotic Expansion Load Decomposition beam model (AELD-beam model).

3.3.2.2 The AELD extended to the case of eigenstrains

This higher-order beam model has been extended in [Corre et al., 2017a] to the case of eigenstrain. Based on a situation where eigenstrains are applied on the structure, new modes specific to eigenstrains are computed thanks to the same systematic procedure and are added to the kinematics of the model. This enables the model to deal with various situations such as creep, thermal loads or prestressed loads. The applied eigenstrain is also expressed as the

product of a function of the cross-sectional coordinates and a function of the longitudinal coordinate. Considering an applied eigenstrain $\boldsymbol{\varepsilon}^*$, the basis of modes specific to $\boldsymbol{\varepsilon}^*$ is denoted by $\mathbb{B}^{\boldsymbol{\varepsilon}^*}$ and represented as the action of the operator $\mathcal{B}^{\boldsymbol{\varepsilon}}$ on $\boldsymbol{\varepsilon}^*$:

$$\mathbb{B}^{\boldsymbol{\varepsilon}^*} = \mathcal{B}^{\boldsymbol{\varepsilon}}(\boldsymbol{\varepsilon}^*) \quad (3.44)$$

The computation of the displacement modes of a beam submitted to eigenstrain is now presented. The beam is still considered with a purely elastic behavior. The equations of the BVP are in this case:

$$P : \begin{cases} \operatorname{div}_x \boldsymbol{\sigma} = 0 & \text{on } \Omega \\ \boldsymbol{\sigma} = \mathbf{C} : (\boldsymbol{\varepsilon} - \boldsymbol{\varepsilon}^*) & \text{on } \Omega \\ \boldsymbol{\varepsilon} = \nabla_x^s \mathbf{u} & \text{on } \Omega \\ \boldsymbol{\sigma} \cdot \mathbf{n} = 0 & \text{on } \partial\Omega_t \\ \mathbf{u} = 0 & \text{on } \mathcal{S}^\pm \end{cases} \times [0, T], \quad (3.45)$$

The assumptions are the same as the ones described for the computation of modes for a beam submitted to internal or external forces. We first operate a change of coordinate. The eigenstrain is then expressed as the product of a cross-sectional function and a longitudinal function:

$$\boldsymbol{\varepsilon}_{ij}^* = \eta \tilde{d}_{ij}(y_\alpha) T(y_3) \quad (3.46)$$

The variables are then expressed as power series of η and introduced into the equations of the BVP (3.45), yielding a series of auxiliary problems which split into two uncoupled boundary value problems.

Transverse displacement The in-section displacement problems \mathcal{T} are expressed for $p \geq 0$:

$$\mathcal{T}^{p+1} : \begin{cases} \sigma_{\alpha\beta,\beta}^p + \sigma_{\alpha 3,3}^{p-1} = 0 & \text{on } \mathcal{S}^0 \\ \sigma_{\alpha\beta}^p = 2\mu \left(\varepsilon_{\alpha\beta}^p - \delta_{p1} \tilde{d}_{\alpha\beta} T \right) + \lambda \left(\varepsilon_{kk}^p - \delta_{p1} \tilde{d}_{kk} T \right) \delta_{\alpha\beta} & \text{on } \mathcal{S}^0 \\ \sigma_{33}^p = 2\mu \left(\varepsilon_{33}^p - \delta_{p1} \tilde{d}_{33} T \right) + \lambda \left(\varepsilon_{kk}^p - \delta_{p1} \tilde{d}_{kk} T \right) & \text{on } \mathcal{S}^0 \\ 2\varepsilon_{\alpha\beta}^p = u_{\alpha,\beta}^{p+1} + u_{\beta,\alpha}^{p+1}, \quad \varepsilon_{33}^p = u_{3,3}^p & \text{on } \mathcal{S}^0 \\ \sigma_{\alpha\beta}^p n_\beta = 0 & \text{on } \partial\mathcal{S}^0 \end{cases} \quad (3.47)$$

where $\boldsymbol{\sigma}^{-1} = 0$. For a simply connected section, this BVP on the displacement u_α^{p+1} is well-posed if the applied load is globally self-equilibrating for in-section translations and rotation:

$$\left\langle \sigma_{\alpha 3,3}^{p-1} \right\rangle = 0 \quad \text{and} \quad \left\langle y_\beta \varepsilon_{\beta\alpha} \sigma_{\alpha 3,3}^{p-1} \right\rangle = 0 \quad (3.48)$$

The solution is defined up to a rigid motion of the setion in its plane.

3.4. The elastoplastic beam model

Longitudinal displacement The longitudinal displacement problems \mathcal{W}^{p+1} are obtained for $p \geq 0$:

$$\mathcal{W}^{p+1} : \begin{cases} \sigma_{3\alpha,\alpha}^p + \sigma_{33,3}^{p-1} = 0 & \text{on } \mathcal{S}^0 \\ \sigma_{\alpha 3}^p = 2\mu \left(\varepsilon_{\alpha 3}^p - \delta_{p1} \tilde{d}_{\alpha 3} T \right) & \text{on } \mathcal{S}^0 \\ 2\varepsilon_{\alpha 3}^p = u_{3,\alpha}^{p+1} + u_{\alpha,3}^p & \text{on } \mathcal{S}^0 \\ \sigma_{\alpha 3}^p n_\alpha = 0 & \text{on } \partial\mathcal{S}^0 \end{cases} \quad (3.49)$$

For a simply connected section, this BVP on the displacement u_3^{p+1} is well-posed if the applied load is globally self-equilibrating for the longitudinal translation:

$$\left\langle \sigma_{33,3}^{p-1} \right\rangle = 0 \quad (3.50)$$

The solution is defined up to a uniform longitudinal displacement.

The higher-order elasto-plastic beam model developed in this paper is based on the *AELD*-beam model and its extension to the case of eigenstrains.

3.4 The elastoplastic beam model

This section introduces a new higher-order elastoplastic beam element. Based on the higher-order elastic beam element presented in **Chapter II**, the elastoplastic beam element is derived within the framework of standard plasticity previously set. The three dimensional volume of the beam element must discretized in order to locally integrate the local elastoplastic equilibrium equations. The beam element is then formulated and the elastoplastic algorithm of the beam model is presented.

3.4.1 Adaptation of the *AELD*-beam model to the elasto-plastic behavior

The *AELD*-beam model introduced in the previous section has proven its efficiency for elastic materials. The model is now adapted to the elasto-plastic behavior. Based on this higher-order model, we must establish the right collection of displacement modes in order to describe faithfully the behavior of an elasto-plastic structure.

We consider the elasto-plastic boundary value problem expressed in equation (3.3). The first collection of modes to consider is the basis \mathbb{B}^{S-V} described previously. This basis of modes is specific to the cross-section of the beam. The surface traction \mathbf{t} applied on the beam then generates a collection of force modes computed thanks to the operator \mathcal{B}^f :

$$\mathbb{B}^t = \mathcal{B}^f(\mathbf{t}) \quad (3.51)$$

The introduction of degrees of freedom related to the plastic state of the beam is necessary to correctly describe the effect of plasticity in the global response. Therefore, the plastic strain computed at a given iteration of the global algorithm is considered as an eigenstrain imposed on the structure in the next iteration. Based on the model presented in [Corre et al., 2017a], additional modes of displacement are computed according to this eigenstrain. These new *plastic modes* are computed added to the kinematics on the fly. The basis of modes specific to a plastic strain $\boldsymbol{\varepsilon}^p$ is denoted by $\mathbb{B}^{\varepsilon^p}$ as expressed in equation (3.44).

This operation is repeated at each iteration. The model takes the effect of plasticity into account through these plastic modes. The kinematics of the model is the union of the basis \mathbb{B}^{S-V} , \mathbb{B}^f and $\mathbb{B}^{\varepsilon^p}$. This union of basis is orthogonalized thanks to a *Gram-Schmidt* orthogonalization to form the total basis, and the total number of modes n_{mod} used in the kinematics is the number of modes in the total basis. An increment of displacement at a given iteration can be written as follows:

$$\Delta \mathbf{u}(\mathbf{x}) = \sum_{i=1}^{n_{\text{mod}}} \tilde{\mathbf{u}}^i(x_\alpha) \sum_{j=1}^m N_j(x_3) \Delta \tilde{U}^{i,j} \quad (3.52)$$

where n_{mod} is the number of modes in the basis used for this iteration, m is the number of longitudinal interpolation functions and $\Delta \tilde{U}^{i,j}$ are the increments the generalized displacement. We define the generalized displacement vector $\Delta \tilde{\mathbf{U}}$ by:

$$\Delta \tilde{\mathbf{U}} = \left(\Delta \tilde{U}^{i,j} \right)_{\substack{1 \leq i \leq n_{\text{mod}} \\ 1 \leq j \leq m}} \quad (3.53)$$

The total number of degrees of freedom is therefore equals to $n_{\text{dof}} = n_{\text{mode}} \times m$. The definition of the interpolation functions N_j and the computation of the plastic strain required for the computation of $\mathbb{B}^{\varepsilon^p}$ is described in the next section.

3.4.2 Numerical approximation of the higher order beam model

3.4.2.1 Longitudinal discretization

A longitudinal discretization of the beam must be defined for the computation of the longitudinal interpolation functions introduced in equation (3.30). As in [Corre et al., 2017a], we choose to use NURBS basis functions to interpolate the beam element. The number of NURBS interpolation functions m is defined by the relation:

$$m = n_{\text{knot}} + n_{\text{order}} - 1 \quad (3.54)$$

where n_{knot} is the number of knots used for the definition of the NURBS and n_{order} is the interpolation order of the NURBS. A set of longitudinal integration points are needed for the integration of the interpolation functions. Plasticity can appear anywhere in the structure, and

3.4. The elastoplastic beam model

its detection is only made possible by the application of the local radial return algorithm in the volume Ω . A 3D discretization of the beam volume is therefore necessary. The simplest way is to define a set of positions along the longitudinal axis and to run the radial return algorithm on the cross-sections placed at these positions. Assuming a 3D displacement increment $\Delta \mathbf{u}$, the strain increment $\Delta \boldsymbol{\varepsilon}$ is computed on each cross-section. The plastic strain potentially detected in these sections is then used for the computation of the plastic modes. The beam is therefore decomposed into sections where the local equations of equilibrium are integrated and the state variables are computed. We naturally choose to place these sections at the positions of the longitudinal integration points of the interpolation functions. This set of $N_s > m$ longitudinal positions is denoted $\{s_1, \dots, s_{N_s}\}$.

3.4.2.2 Cross-sectional discretization

The discretization of the section of the beam used for the computation of the modes is the same as the one used in [Corre et al., 2017a]: the modes are computed by using finite elements, the elements being triangles and the interpolation being quadratic. The number of elements in the section is denoted N_e and the number of Gauss points by element is denoted G . $N_g = N_e \times G$ is therefore the total number of Gauss points in the section.

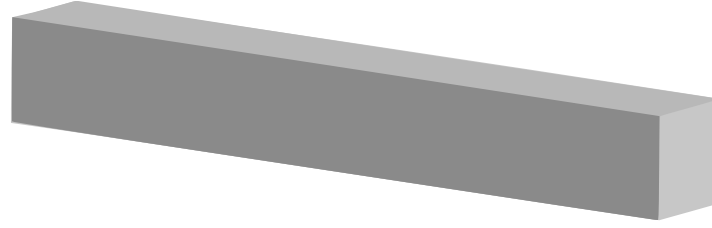
As exposed in the previous section, $\Delta \boldsymbol{\varepsilon}$, $\Delta \boldsymbol{\varepsilon}^p$ and $\Delta \boldsymbol{\sigma}$ are computed in the N_s sections defined by their longitudinal position, at the Gauss points of the mesh of each section. For simplicity the sectional discretization of each section is similar to the one defined for the computation of the modes. Therefore, the total number of Gauss points where the state variables are computed is $N_{Gtot} = N_s \times N_e \times G$.

An illustration of a square beam discretization is presented on Figure 3.2: the beam is longitudinally discretized with $N_s = 10$ points (which is also the number of integration points of the beam), and each section is meshed with 712 triangle elements. The NURBS discretization scheme is not recalled here.

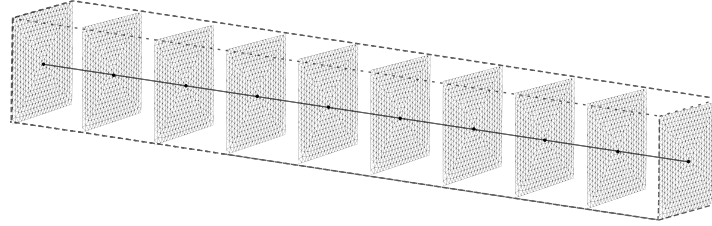
3.4.3 Formulation of the beam element

Injecting equation (3.32) into equation (3.31) leads to the expression of the residual $\mathcal{R}(\Delta \tilde{\mathbf{U}}_n^{(k)}, \hat{\mathbf{U}})$ expressed in terms of the 1D increment of generalized displacement $\Delta \tilde{\mathbf{U}}_n^{(k)}$ and the 1D virtual generalized displacement $\hat{\mathbf{U}}$. We use the Newton-Raphson procedure in order to cancel this residual and get the following equation:

$$\mathcal{R}(\Delta \tilde{\mathbf{U}}_n^{(k)}, \hat{\mathbf{U}}) + \left\langle \mathcal{R}'(\Delta \tilde{\mathbf{U}}_n^{(k)}, \hat{\mathbf{U}}), \delta \tilde{\mathbf{U}}_n^{(k)} \right\rangle = 0 \quad (3.55)$$



(a) 3D view of the beam



(b) Discretization of the beam with $N_e = 712$ and $N_s = 10$

Figure 3.2 – Discretization of a square beam

which is the 1D counterpart of equation (3.23). The discretization of equation (3.55) leads to the following 1D-equilibrium equation:

$$[\mathbf{K}^{\text{ep}}] \{ \delta \tilde{\mathbf{U}}_n^{(k)} \} = \{ \mathbf{R} \} . \quad (3.56)$$

$[\mathbf{K}^{\text{ep}}] \in \mathbb{R}^{n_{\text{dof}} \times n_{\text{dof}}}$ is the global stiffness matrix of the beam element, computed with the local elasto-plastic tangent moduli $\mathbf{C}_{n+1}^{\text{ep}}$. $\{ \mathbf{R}_n^{(k)} \} \in \mathbb{R}^{n_{\text{dof}}}$ is the 1D residual vector. The reduction of the 3D model to a beam model has been exposed, and its numerical approximation described. The elasto-plastic algorithm associated to this higher-order beam model is detailed in the next section.

3.4.4 The elasto-plastic algorithm

The combination of the standard plasticity presented in section 3.2 and the reduced model defined in Section 3.4 yields a new higher-order elasto-plastic beam model, characterized by a the plasticity algorithm defined hereafter.

There is no change in the local integration of the constitutive equations and since the reduced model has been discretized in Section 3.4 for the computation of local 3D variables, the local algorithm remains defined by Algorithm 1. Major changes are made at the global level of the algorithm.

3.4. The elastoplastic beam model

3.4.4.1 $t = t_n$, first iteration: initialization of the increment

We consider the time step $t = t_{n+1}$ and assume that the structure remains purely elastic until t_n ($\boldsymbol{\varepsilon}_n^p = 0$). If $n = 0$, the first iteration starts with the computation of the basis of modes, $\mathbb{B}_1^{(0)}$ as described in [Ferradi et al., 2016]. The asymptotic expansion is carried out up to the order n_{AEM} . The basis of modes is built by adding the basis composed of the modes of the *Saint-Venant* solution $\mathbb{B}^{\text{S-V}}$, and the basis composed of the modes associated to the applied load \boldsymbol{t}_1 : $\mathbb{B}^{t_1} = \mathcal{B}^f(\boldsymbol{t}_1)$. The union of this two basis is then orthonormalized thanks to a *Gram-Schmidt* procedure to form a linearly independent family:

$$\mathbb{B}_1^{(0)} = \left(\mathbb{B}^{\text{S-V}} \cup \mathbb{B}^{t_1} \right)_{\perp} \quad (3.57)$$

where $(\bullet)_{\perp}$ means that the basis is orthonormalized.

Since we consider monotonically incremental loads, $\mathbb{B}^{t_n} = \mathbb{B}^{t_1}$ and the basis $\mathbb{B}_{n+1}^{(0)}$ do not need to be computed again for $n \geq 1$. We have the relation:

$$\mathbb{B}_{n+1}^{(0)} = \mathbb{B}_1^{(0)} \quad (3.58)$$

The total number of modes is $n_{\text{mod}}^{(0)} = \text{card}(\mathbb{B}_{n+1}^{(0)})$. The displacement $\boldsymbol{u}(\boldsymbol{x})$ is decomposed on $\mathbb{B}_{n+1}^{(0)}$, as defined in equation (3.52). The numerical approximation has been described in Section 3.4.2. The basis $\mathbb{B}_{n+1}^{(0)}$ is used to express the beam formulation presented in Section 3.4.3:

$$[\boldsymbol{K}]_{\mathbb{B}_{n+1}^{(0)}} \{ \delta \tilde{\boldsymbol{U}} \}_{\mathbb{B}_{n+1}^{(0)}} = \{ \boldsymbol{R} \}_{\mathbb{B}_{n+1}^{(0)}} \quad (3.59)$$

In what follows, global matrices expressed on a basis \mathbb{B} are denoted with the notation $[\bullet]_{\mathbb{B}}$, and global vectors expressed on a basis \mathbb{B} are denoted with the notation $\{ \bullet \}_{\mathbb{B}}$. The norm of the residual is saved in the scalar r^{ref} . Equation (3.59) is solved, yielding the first displacement increment $\{ \Delta \tilde{\boldsymbol{U}} \}_{\mathbb{B}_{n+1}^{(0)}} = \{ \delta \tilde{\boldsymbol{U}} \}_{\mathbb{B}_{n+1}^{(0)}}$. We assume that this increment generates plasticity in the structure, meaning that the yield criterion has been violated at least once. The sections where a plastic strain has been computed are gathered in \mathbb{P}_s :

$$\mathbb{P}_s = \{ q \in \{1, \dots, N_s\} / \exists g \in \{1, \dots, N_g\}, \Delta \boldsymbol{\varepsilon}^p(x_\alpha^g, s_q) \neq 0 \} \quad (3.60)$$

where x_α^g denotes the transverse coordinates of the g^{th} Gauss point of the section. It is recalled that the same transverse discretization is used for the N_s sections (see Section 3.4.2). The residual $\{ \boldsymbol{R} \}_{\mathbb{B}_{n+1}^{(0)}}$ is computed and we assume that it is found larger than the tolerance, meaning that convergence is not reached. Hence the algorithm leads to the second iteration.

3.4.4.2 $t = t_n$, subsequent iterations: computation of plastic modes

Subsequent iterations must bring corrections to the initial displacement. These corrections take plastic flow into account by generating additional plastic modes. For each section $q \in \mathbb{P}_s$ where

plasticity has been detected, *plastic modes* are computed from the eigenstrain $\boldsymbol{\varepsilon}_{n+1}^{\text{p}(k)}(x_\alpha^g, s_q)$. The asymptotic expansion is performed up to the order n_{AEM} introduced earlier. The plastic basis computed at each plastic section are added to the basis of the previous iteration $\mathbb{B}_{n+1}^{(k-1)}$ to form the single orthonormalized basis $\mathbb{B}_{n+1}^{(k)}$:

$$\mathbb{B}_{n+1}^{(k)} = \left(\mathbb{B}_{n+1}^{(k-1)} \cup \left(\bigcup_{q \in \mathbb{P}_s} \mathbb{B}_q^{\varepsilon_{n+1}^{\text{p}(k)}} \right) \right)_\perp \quad (3.61)$$

where $\mathbb{B}_q^{\varepsilon_{n+1}^{\text{p}(k)}} = \mathcal{B}^\varepsilon \left(\boldsymbol{\varepsilon}_{n+1}^{\text{p}(k)} \right)$ denotes the family of plastic modes computed for the q^{th} plastic section. The new number of modes is $n_{\text{mod}}^{(k)} = \text{card} \left(\mathbb{B}_{n+1}^{(k)} \right)$. The kinematics of the model may have changed and the number of degrees of freedom $n_{\text{dof}}^{(k)}$ may be modified. Therefore the residual previously computed on $\mathbb{B}_{n+1}^{(k-1)}$ might need to be computed again on $\mathbb{B}_{n+1}^{(k)}$. Since $\mathbb{B}_{n+1}^{(k-1)} \subset \mathbb{B}_{n+1}^{(k)}$, the update of the residual on the new basis is limited to the addition of the values of the new degrees of freedom. The tangent global stiffness is built on the updated basis, and the new correction $\{\delta \tilde{\mathbf{U}}\}_{\mathbb{B}_{n+1}^{(k)}}$ is computed.

The addition of the increment of displacement between the increments n and $n + 1$ is only possible if this increment of displacement is independent from the basis on which it has been computed. Using the fact that the number of interpolation functions m is constant, we form at each iteration the displacement δU^j which only depends on the beam interpolation functions:

$$\delta U^j(x_\alpha) = \sum_{i=1}^{n_{\text{mod}}^{(k)}} \tilde{\mathbf{u}}^i(x_\alpha) \delta \tilde{\mathbf{U}}^{i,j}, \quad \text{with } 1 \leq j \leq m. \quad (3.62)$$

The increment of displacement is updated:

$$\Delta U^j = \Delta U^j + \delta U^j. \quad (3.63)$$

The strain increment $\Delta \boldsymbol{\varepsilon}$ is then computed on the integration sections and the radial return yields the stress increment. The state variables are updated from the converged value of the previous iteration:

$$\begin{cases} \{\boldsymbol{\sigma}_{n+1}^{(k)}\} = \{\boldsymbol{\sigma}_n\} + \{\Delta \boldsymbol{\sigma}_n\}, \\ \{\boldsymbol{\varepsilon}_{n+1}^{\text{p}(k)}\} = \{\boldsymbol{\varepsilon}_n^{\text{p}}\} + \{\Delta \boldsymbol{\varepsilon}_n^{\text{p}}\}, \\ \{p_{n+1}^{(k+1)}\} = \{p_n\} + \{\Delta p_n\}. \end{cases} \quad (3.64)$$

The residual is assembled and the iterations are continued until convergence is reached. The total displacement is updated at the end of the increment n :

$$\mathbf{u}_{n+1}(\mathbf{x}) = \mathbf{u}_n(\mathbf{x}) + \sum_{j=1}^m \Delta U^j(x_\alpha) N_j(x_3) \quad (3.65)$$

3.5. Application to a cantilever beam

3.4.4.3 Optimization and description of the algorithm

It has been noticed from experience that plastic modes computed at different iterations of a same increment were very similar. Therefore the orthonormalization of plastic modes computed at an iteration $k + 1$ with respect to the basis of iteration k yields modes of a lower significance. Computing again plastic modes within an increment increases the computational time for a very weak gain in the local description of state variables. Without loss of accuracy, it is more efficient to compute the plastic modes only at the first iteration. Thus, the basis of modes remains constant during the increment and consequent gain in CPU time can be obtained in the computation of the stiffness matrix and the force residual. This choice remains valid as long as the load increments are not too important.

The global process is presented in algorithms 8 and 5. Algorithms 2 and 3 were expressed in terms of the 3D kinematic unknown $\Delta \mathbf{u}$, while Algorithms 8 and 5 are expressed in terms of the 1D kinematic unknown $\Delta \tilde{U}$. The main differences between Algorithm 2 and Algorithm 8 lie in the computation and the update of the kinematics of the beam model. The basis of modes is updated as soon as plasticity occurs. This implies that the generalized external forces \mathbf{F}^{ext} must be computed at each plastic iteration and that the generalized internal forces \mathbf{F}^{int} must be computed at both the end of an iteration and at the beginning of the next one. Algorithm 3 and Algorithm 5 are different by their inputs: the first one deals with 3D increments of displacement on every element of the 3D mesh, while the second one deals with 1D increments of displacement on each one of the N_s integration sections of the beam. The 1D inputs of Algorithm 5 are converted into 3D variables before applying the radial return algorithm.

3.5 Application to a cantilever beam

This section first briefly investigates different Newton-Raphson's incremental algorithms: the quasi-Newton-Raphson method and the modified-Newton-Raphson method are successively compared to the classic Newton-Raphson method. The section then shows an application of the elastoplastic beam element to a cantilever I-beam asymmetrically loaded at its end. The case study is computed with a volumic reference solution and compared to the results provided by the beam solution. Parametric studies are then carried out in order to assess the parametric sensitivity of the model.

3.5.1 Study of alternative Newton-Raphson's methods

Before exposing the performance of the beam model on a I-beam, we first investigate on the possible alternatives to the classic Newton-Raphson's method. The most time-consuming step of the algorithm 8 is the assembly of the consistent elasto-plastic stiffness matrix. It is

Algorithm 4 Beam global algorithm

```

1: Initialize state variables:  $\mathbf{S}_0 = \{\mathbf{u}_0, \boldsymbol{\varepsilon}_0, \boldsymbol{\varepsilon}_0^p, \boldsymbol{\sigma}_0, p_0\}$ 
2: Compute the invariant base of modes  $\mathbb{B}^{\text{S-V}}$ 
3: for  $n = 0$  to  $M - 1$  do
4:   Initialize  $\mathbf{S}_{n+1} = \mathbf{S}_n$ 
5:    $\{\Delta\tilde{\mathbf{U}}\}_{\mathbb{B}_{n+1}^{(k)}} = \{\mathbf{0}\}$ 
6:   if  $n = 0$  then
7:     Compute the basis of force modes  $\mathbb{B}^{\mathbf{f}_1} = \mathcal{B}^{\mathbf{f}}(\mathbf{f}_1) \leftarrow$  see [Ferradi et al., 2016] and
     Section 3.3.2.1
8:     Assemble the initial basis of modes  $\mathbb{B}_1^{(0)} = (\mathbb{B}^{\text{S-V}} \cup \mathbb{B}^{\mathbf{f}_1})_{\perp}$ 
9:   else
10:     $\mathbb{B}_{n+1}^{(0)} = \mathbb{B}_1^{(0)}$ 
11:   end if
12:    $k = 1$ 
13:    $cmd = 0$ 
14:   while  $cmd = 0$  do
15:     if  $\boldsymbol{\varepsilon}_n^p \neq \mathbf{0}$  and  $k = 1$  then
16:       Compute the basis of plasticity modes  $\mathbb{B}^{\boldsymbol{\varepsilon}_n^p} = \mathcal{B}^{\boldsymbol{\varepsilon}}(\boldsymbol{\varepsilon}_n^p) \leftarrow$  see [Corre et al.,
       2017a] and Section 3.3.2.2
17:       Assemble the new basis  $\mathbb{B}_{n+1} = (\mathbb{B}_{n+1}^{(0)} \cup \mathbb{B}^{\boldsymbol{\varepsilon}_n^p})_{\perp}$ 
18:       Compute  $\{\mathbf{F}^{\text{ext}}\}_{\mathbb{B}_{n+1}}$  and  $\{\mathbf{F}^{\text{int}}\}_{\mathbb{B}_{n+1}}$ 
19:     end if
20:     Compute  $\{\mathbf{R}\}_{\mathbb{B}_{n+1}} = \{\mathbf{F}^{\text{ext}}\}_{\mathbb{B}_{n+1}} - \{\mathbf{F}^{\text{int}}\}_{\mathbb{B}_{n+1}}$ 
21:     if  $k = 1$  then
22:        $r^{\text{ref}} = \|\{\mathbf{R}\}_{\mathbb{B}_{n+1}}\|$ 
23:     end if
24:     Assemble the consistent elasto-plastic stiffness matrix  $[\mathbf{K}^{\text{ep}}]_{\mathbb{B}_{n+1}}$ 
25:     Solve  $[\mathbf{K}^{\text{ep}}]_{\mathbb{B}_{n+1}} \{\delta\tilde{\mathbf{U}}\}_{\mathbb{B}_{n+1}} = \{\mathbf{R}\}_{\mathbb{B}_{n+1}}$  and assemble  $\{\Delta\mathbf{U}\} = \{\Delta\mathbf{U}\} + \{\delta\mathbf{U}\}$ 
26:     Compute  $\{\boldsymbol{\sigma}_{n+1}\}, \{\boldsymbol{\varepsilon}_{n+1}^p\}$  and  $\mathbf{C}^{\text{ep}} \leftarrow$  Algorithm 5
27:     Compute  $\{\mathbf{F}\}_{\mathbb{B}_{n+1}}^{\text{int}}$ 
28:     Update  $\{\mathbf{R}\}_{\mathbb{B}_{n+1}}, r = \|\{\mathbf{R}\}_{\mathbb{B}_{n+1}}\|$ 
29:     if  $r < \epsilon r^{\text{ref}}$  then
30:        $cmd = 1$ 
31:     end if
32:      $k = k + 1$ 
33:   end while
34:   Update 3D total displacement  $\mathbf{u}_{n+1} = \mathbf{u}_n + \sum \Delta U^j N_j$ 
35: end for

```

3.5. Application to a cantilever beam

Algorithm 5 Beam global subalgorithm

Require: $\{\Delta U_n\}, S_n$
Ensure: $\{\sigma_{n+1}^{(k)}\}, \{\epsilon_{n+1}^{p(k)}\}, \{p_{n+1}^{(k)}\}, C^{ep}(\mathbf{x})$

- 1: **for** $s = 1$ to N_s **do**
- 2: **for** $e = 1$ to N_e **do**
- 3: **for** $g = 1$ to G **do**
- 4: Compute $\Delta \epsilon_n(\mathbf{x}^g)$ from ΔU and $\mathbb{B}_{n+1}^{(k)}$
- 5: Update $\epsilon_n(\mathbf{x}^g)$
- 6: Update $\epsilon_n^p(\mathbf{x}^g), \sigma_n(\mathbf{x}^g), p_n(\mathbf{x}^g)$ and $C^{ep}(\mathbf{x}^g) \leftarrow$ **algorithh 1**
- 7: **end for**
- 8: **end for**
- 9: **end for**

assembled by an integration operated both cross-sectionally and longitudinally. The update of the basis of modes and the update of the consistent elasto-plastic moduli C^{ep} imply a new computation of the stiffness matrix in the classic Newton-Raphson's method.

A simplified method commonly used in standard 3D plasticity consists in approximating at each iteration the consistent elasto-plastic stiffness matrix by the elastic stiffness matrix. This method, called the modified Newton-Raphson's method [Zienkiewicz, 1977], naturally implies more iterations within a load increment, but each iteration is computed faster since it avoids the update of the stiffness matrix. For the present higher-order beam model, it means that we always consider the elastic moduli C instead of the consistent elasto-plastic moduli C^{ep} for the assembly of the global stiffness. However the stiffness matrix must still be computed each time the basis of modes changes.

A third solution can be formulated in between the Newton-Raphson's and the modified Newton-Raphson's method. The elastic moduli is updated at the first iteration of each increment, but is kept constant during the whole increment. The update is therefore operated only once. This method, called the quasi Newton-Raphson's method, should provide time performances in between the performances of two first methods.

In order to compare the numerical performances of the three methods, we consider a simple case of study. A cantilever beam of length $L = 10$ m with a square section of $A = 1$ m² is loaded at its end by a vertical force $F = 8MN$, as represented on Figure 3.3.

The material characteristics considered are:

$$E = 210 \text{ GPa}, \quad \mu = 0.3, \quad H = 0.1E, \quad \sigma_0 = 235 \text{ MPa} \quad (3.66)$$

The maximal plastic moment of a square beam is $M_{pl} = \sigma_0 Ah/4$. With the values considered here, $M_{pl} = 58,75$ MN.m. The ratio between the moment applied and the maximal plastic

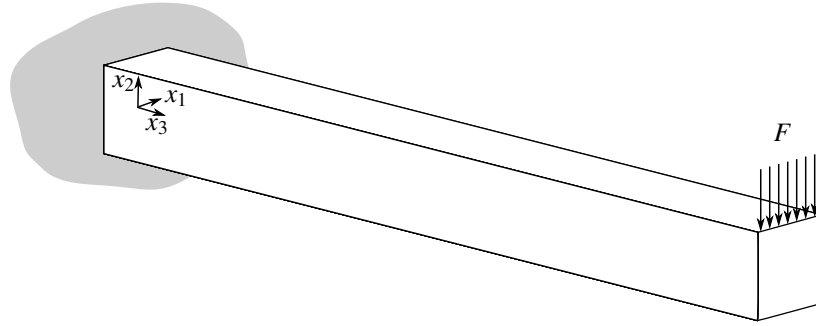


Figure 3.3 – 10 m cantilever beam loaded at its end by a force F

moment is $FL/M_{pl} = 1,36$. Plasticity is expected to occur close to the clamped extremity which should therefore be completely plastified. The longitudinal discretization of the beam is therefore refined close to $x_3 = 0$. The longitudinal mesh is composed of $N_s = 29$ points and represented in Figure 3.4. The cross-sectional mesh is composed of 898 quadratic triangles. The influence of the mesh refinement is not investigated in this example and will be studied in the next section.

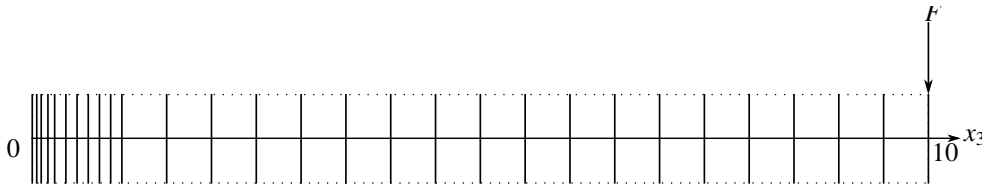


Figure 3.4 – Longitudinal mesh of the beam, composed of 29 points represented by their respective section

The problem is divided into 10 time steps. The force applied is uniformly divided, with $f_0 = 0$ and $f_{10} = F$. The Newton-Raphson's method ($N-R$), the quasi Newton-Raphson's method ($qN-R$) and the modified Newton-Raphson's method ($mN-R$) are computed. The average vertical displacements computed at $x_3 = L$ by the three solutions are compared to a 3D reference solution. The mesh of the 3D solution is defined by extruding longitudinally a 2D section mesh with triangles. The number of triangles used is the same as the number of triangles in the section of the beam model and the longitudinal partition of the 3D mesh is the same as the longitudinal mesh of the beam model. The 3D model is composed of 25424 prismatic elements, each prism being quadratic in interpolation. The 3D solution uses a classic Newton-Raphson algorithm. The average vertical displacement at the free extremity is defined by:

$$\langle u_2 \rangle = \frac{1}{A} \left| \int_S u_2(x_\alpha, L) dS \right| \quad (3.67)$$

The value of $\langle u_2 \rangle$ is computed for each solution at each time step. Results are presented in Figure 3.5.

3.5. Application to a cantilever beam

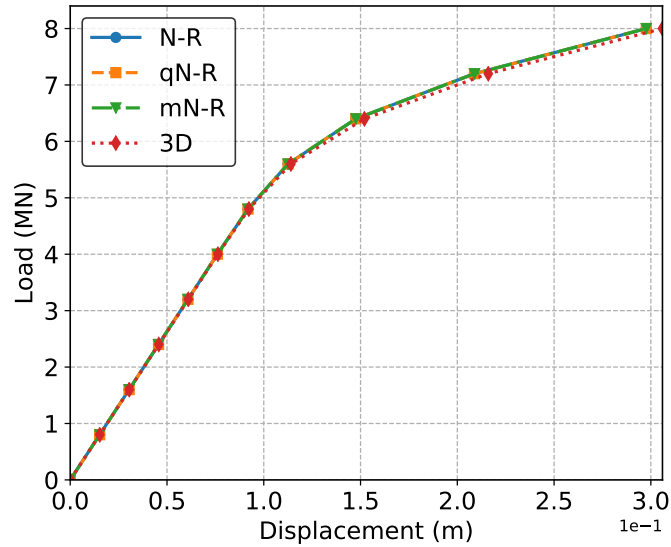


Figure 3.5 – Vertical average displacement at $x_3 = L$

increment	1	2	3	4	5	6	7	8	9	10	total time	avg time/iteration
<i>N-R</i>	1	1	1	1	3	4	4	4	4	4	82 s	3.03 s
<i>qN-R</i>	1	1	1	1	6	14	21	23	19	17	201 s	1.93 s
<i>mN-R</i>	1	1	1	1	6	14	35	78	126	148	726 s	1.77 s
3D	1	1	1	3	4	4	5	5	4	5	8030 s	243 s

Table 3.1 – Comparison of the time performances of the *N-R*, *qN-R* and *mN-R* methods

The three methods converge on the same values. The average displacement computed for each solution matches well with the 3D solution. The maximum relative distance between the beam curves and the 3D solution on Figure 3.5 is 3,3% for time step 9. The results provided by the beam model are satisfactory. The comparison of the time performances of the three methods are compared in Table 3.1.

Consequently to this investigation, computations are operated with the *N-R* method in all what follows.

3.5.2 Cantilever beam loaded at its free extremity

3.5.2.1 Case study

To illustrate the efficiency of the model presented, we consider a steel beam clamped at one end and loaded on its free end. The beam chosen is a wide flange beam HE600M. This section is in class 1 in Eurocode 3, meaning that the beam reaches its limit of elasticity with no risk of

buckling. The geometry of a HE600M beam is detailed in Figure 3.6.

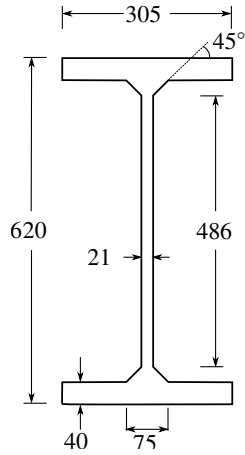


Figure 3.6 – Dimensions in mm of a HE600M cross-section

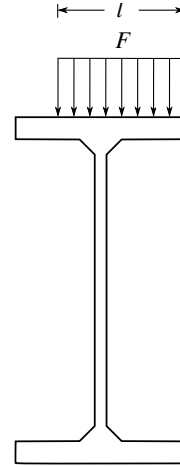


Figure 3.7 – Application of the load F on the free end section

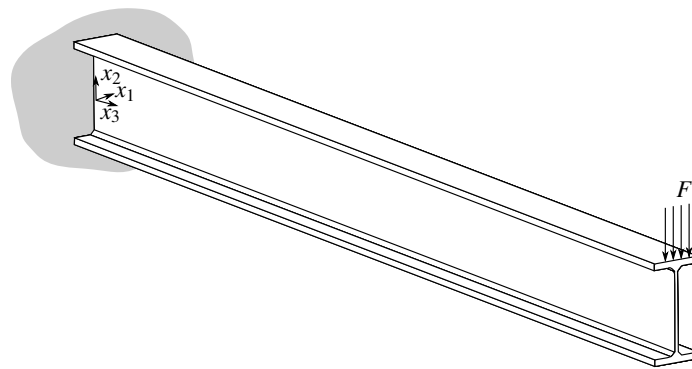


Figure 3.8 – 3D representation of the HE600M cantilever beam loaded at its end

The beam considered has a length $L = 6$ m. A load is applied with eccentricity on top edge of the free end of the beam, as represented on Figures 3.7 and 3.8. The force F is applied on the length $l = 230$ mm. The study is decomposed into 10 times steps, and the load is incrementally increased of 0.25 MN at each step until it reaches its final value 2.5 MN.

We consider the following values of the Young's modulus and the Poisson's ratio:

$$E = 210 \text{ GPa}, \quad \mu = 0.3, \quad H = 0.02E, \quad \sigma_0 = 235 \text{ MPa} \quad (3.68)$$

3.5.2.2 Reference solution

A 3D reference solution is computed on the finite element software *Code_Aster*. The beam is modeled by extruding along the longitudinal axis a cross-section meshed with triangles,

3.5. Application to a cantilever beam

forming 3D prismatic elements. The longitudinal extrusion is discretized such that shorter 3D elements are used close to the clamped extremity. This choice of modeling allows an easy comparison between the 3D model and the beam model in terms of mesh refinement. A cross-section is meshed with 430 triangles and the longitudinal axis is discretized with 19 sections, forming 7740 prismatic elements in total. The prismatic elements are interpolated with quadratic functions. The longitudinal discretization is more refined close to the clamped extremity since this is where plasticity is expected to occur.

All the computations presented in this paper are processed on a processor i7-4510U (2 cores at 2.00 GHz).

3.5.2.3 Higher-order beam solution S_0

Parameters of the solution S_0 The method presented in the present paper is first computed with a set of parameters chosen with an educated guess. This solution is called S_0 . Some sensitivity studies are carried out later in the paper. The section of the solution S_0 is meshed with 399 triangle elements, as shown on Figure 3.9. The triangle elements are quadratic and the mesh is composed of 399 triangles.

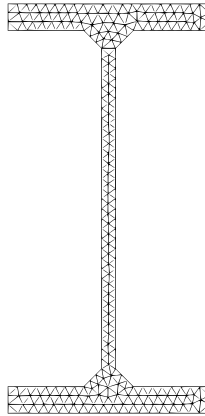


Figure 3.9 – Cross-section meshed with 399 triangles

The NURBS basis functions which are the interpolation shape functions of the element are defined by the following knot vector : $V_{\text{NURBS}} = \{0, 0.125, 0.25, 0.5, 1, 2, 3, 4, 5, 6\}$. The total number of interpolation functions is defined by the relation $N = n_{\text{knot}} + n_{\text{order}} - 1$. We consider second-order NURBS and therefore get 11 NURBS basis functions. As explained in Section 3.4.2, the integration points used for the longitudinal integration of the interpolation functions are also the points where we place the integration sections. These integration sections are the sections where the local radial algorithm is computed. Using the Simpson's integration, the total number of integration points is generally defined by the relation:

$$n_{\text{integ}} = 1 + 2 \times E \left(\frac{n_{\text{order}} + 1}{2} \right) \times (n_{\text{knot}} - 1) \quad (3.69)$$

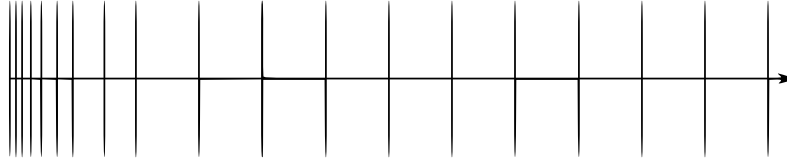


Figure 3.10 – Longitudinal mesh composed of 19 integration sections

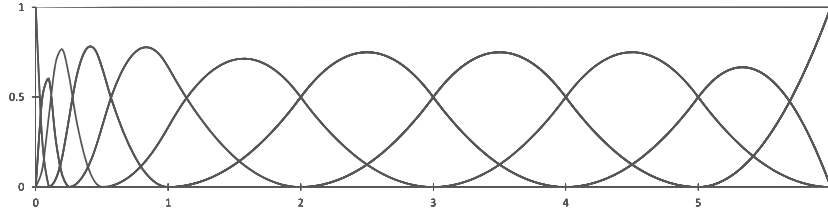


Figure 3.11 – Second-order NURBS basis functions used for the longitudinal interpolation of the element

Second-order NURBS basis functions require the addition of one integration point in each interval of the knot vector. The longitudinal axis is therefore meshed with 19 integration points by refining V_{NURBS} with the add of an integration point in the middle of each interval. The 19 corresponding integration sections are represented on Figure 3.10. The mesh is refined close to the clamped extremity since the plasticity is expected to mainly occur in this location. This longitudinal discretization is the same as the one defining the mesh of the reference solution. The NURBS defined by V_{NURBS} are represented on Figure 3.11.

All sections where a plastic strain occurs are not used for the computation of the plastic modes. Indeed, it will drastically increase the computation time while close sections create very similar plastic modes. Consequently, only the plastic strain of the 5th section is used for the computation of the plastic modes. This section is called *plastic mode section*. The choice of one or multiple plastic mode sections is arbitrary at this time but it should be then automated.

Force modes are computed up to the 4th order of the asymptotic expansion (this choice is based on experience), and plastic modes are computed up to the 3rd order of the asymptotic expansion. Both expansion orders can indeed be different since force modes and plastic modes are computed independently.

During the computation, the maximum number of modes in the basis is 22. The number of interpolation shape functions being 11, the maximum number of degrees of freedom during the computation is therefore $n_{\text{dof}} = 242$. This number could be reduced by associating the plastic modes only to the interpolation functions with non-zero values where plasticity has been detected. But at this time, the modes of the basis are considered all along the beam element.

3.5. Application to a cantilever beam

	Solution S_{ref}	Solution S_0
type of elements	15-nodes prisms	6-nodes triangle + 19 longitudinal nodes
number of elements	7740	399 + 1
CPU computation time	818 s	11 s

Table 3.2 – Main features of the 3D solution and solution S_0

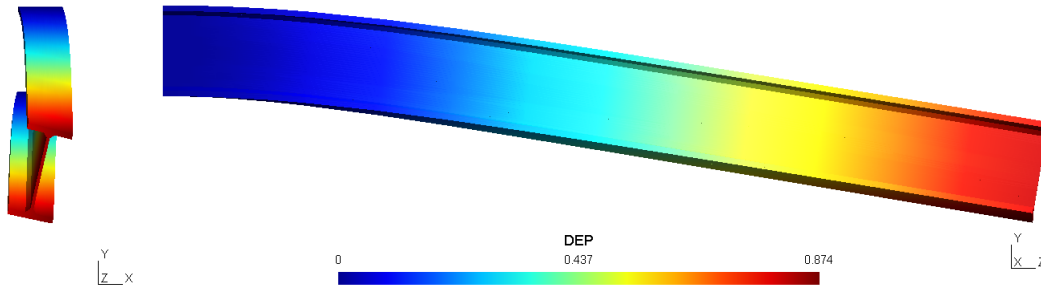


Figure 3.12 – Deformed shape of the beam after the 10 load increments (solution S_0)

Comparison with the 3D solution The main features of the 3D solution and solution S_0 are presented in Table 3.2.

The deformed structure obtained with the solution S_0 is presented on Figure 3.12. The torque due to the eccentricity of the load induces a longitudinal rotation of the cross-section, and the transverse part of the load induces a bending of the beam.

In order to compare the two solutions, we compute the absolute displacement at the point A placed on the free section of the beam ($x_3 = L$) as represented on Figure ???. The absolute displacements computed by both solutions during the 10 time steps of the study are shown on Figure 3.13.

In view of the force-displacement curves shown on Figure 3.13, the results obtained with the beam solution S_0 are consistent with the reference solution. The beam solution satisfactorily captures the plastic branch despite a low kinematic hardening ($H = 0.02E$). The curve of S_0 is slightly above the curve of S_{ref} meaning that the force obtained with S_0 for a given displacement at point A is higher than the force obtained with S_{ref} . For $u_A = 0.8$ m, solution S_0 associates a force higher than the force obtained by S_{ref} of 2,42%. In order to assess the accuracy of the beam solution when compared to the reference solution the six components of the plastic strain computed by the solution S_0 and by the reference solution at $x_3 = 0,5$ m for the given displacement of point A $u_A = 0.8$ m are presented on Figure 3.14. All the variables presented for a given displacement of point A are obtained by linear interpolations between the increments defined in Section 3.5.2 and represented by dots on Figure 3.13.

We also define the following L_2 -estimator to compare the beam model and the reference model

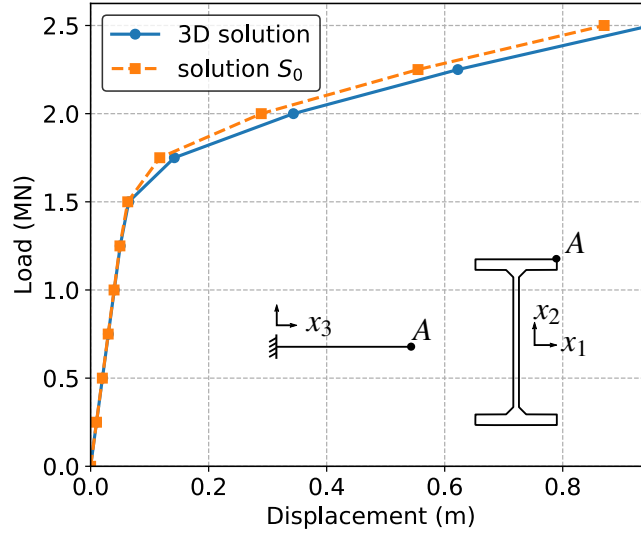


Figure 3.13 – Absolute displacement at point A

on a cross-section S:

$$e_{L_2}(\varepsilon_{ij}^p) = \left[\frac{\int_S (\varepsilon_{ij}^{p,3D} - \varepsilon_{ij}^p)^2 dS}{\int_S (\varepsilon_{ij}^{p,3D})^2 dS} \right]^{1/2} \quad (3.70)$$

where $\varepsilon_{ij}^{p,3D}$ is the plastic strain computed by the reference solution.

The axial plastic strain presented on Figures 3.14a to 3.14c shows that nearly all parts of the section have reached the elastic limit. As expected, the eccentricity of the load on the free extremity of the beam creates a slightly uneven progression of plasticity in the section. Therefore the highest values of the plastic strain components are observed on the top left and the bottom left of the section where the absolute values of the stresses are the most important. The plastic strain computed by S_0 is slightly lower than the plastic strain computed by S_{ref} for each component. A late detection of plasticity due to the longitudinal refinement could originate this "plastic delay". The influence of the longitudinal mesh refinement is investigated in the next section. The values of the L_2 -estimator defined previously are for the axial strains $e_{L_2}(\varepsilon_{11}^p) = 3.92\%$, $e_{L_2}(\varepsilon_{22}^p) = 3.46\%$ and $e_{L_2}(\varepsilon_{33}^p) = 3.90\%$

The non-axial components presented on Figures 3.14d to 3.14f seem less satisfying but this should be qualified as their amplitude is about 10 times lower than the axial components. Thus, the beam solution presented here shows satisfying results with a good compliance with the 3D solution. The solution S_0 has been defined with a set of parameters: mesh refinement, NURBS order, expansion order, etc. The following sections investigate the influence of these parameters on the results and show the possible ways to get more accurate results.

3.5. Application to a cantilever beam

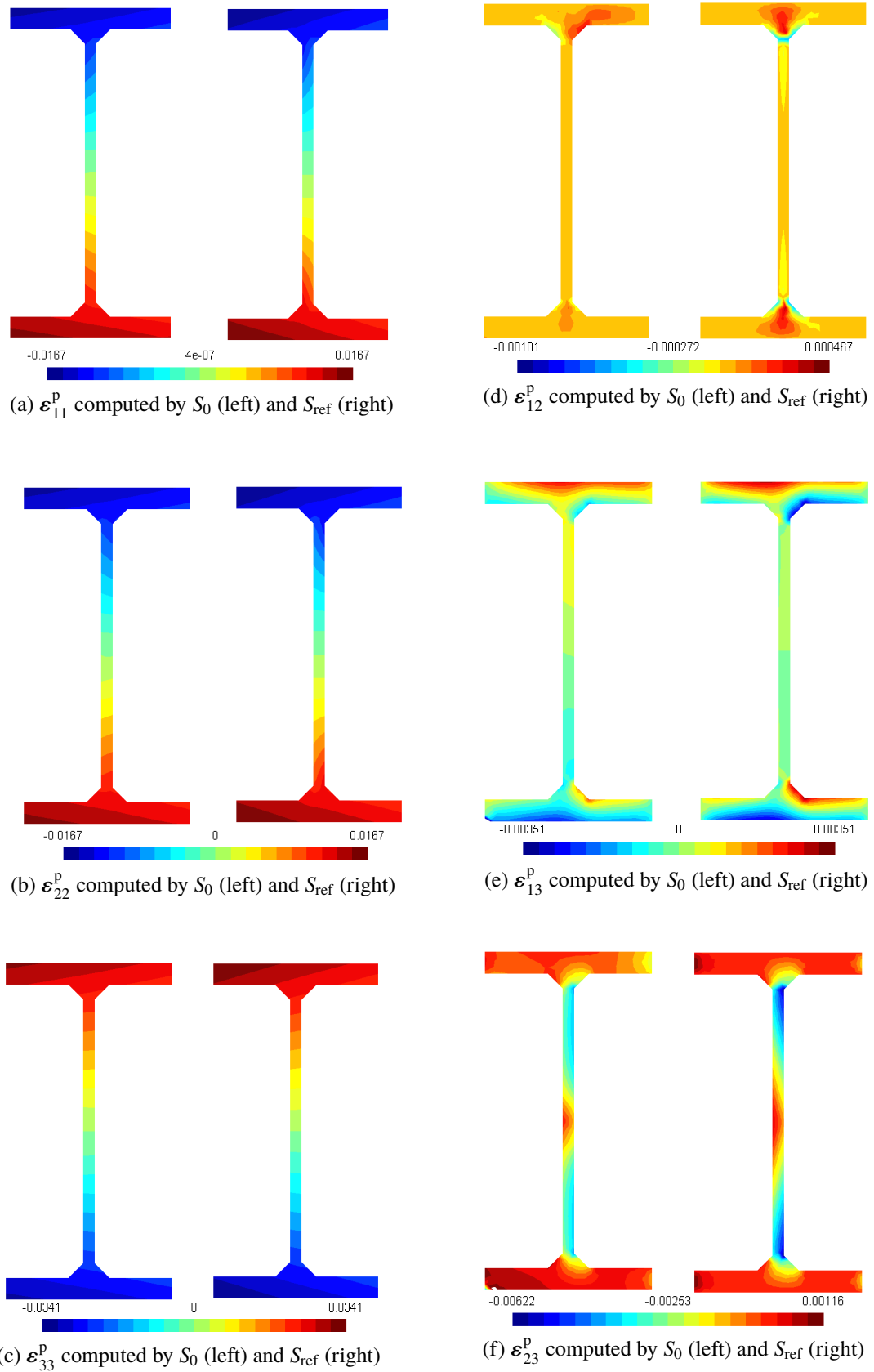


Figure 3.14 – Plastic strain computed by S_0 and S_{ref} close to the clamped extremity at $x_3 = 0.5$ m for $u_A = 0.8$ m

3.5.3 Parametric studies

3.5.3.1 Mesh refinement

Solution S_0 shows satisfying results in terms of displacement. Its longitudinal mesh has been chosen arbitrarily and it is now interesting to investigate on the influence of the refinement of the longitudinal mesh on the results. All solutions considered here are interpolated with second-order NURBS, meshes can therefore be characterized by the knot vector used for the definition of the NURBS, as explained in Section 3.5.2.3. A reference mesh m_0 is characterized by the following knot vector: $\{0, 1, 2, 3, 4, 5, 6\}$. More refined meshes are defined by adding new knots in the interval $[0, 1]$. These additional knots are placed at the position $x_3 = 1/2^n$. Thus, the knot vector of the mesh $m_n, n \in \mathbb{N}$ is $\left\{0, \frac{1}{2^n}, \frac{1}{2^{n-1}}, \dots, \frac{1}{2}, 1, 2, 3, 4, 5, 6\right\}$. The same case study is computed for different longitudinal meshes. The main parameters of the six solutions studied in this section are gathered in Table 3.3.

Solution	S^{m0}	S^{m1}	S^{m2}	S_0	S^{m4}	S^{m5}
plastic modes AE order	3	3	3	3	3	3
force modes AE order	4	4	4	4	4	4
NURBS order	2	2	2	2	2	2
knots	7	8	9	10	11	12
integration sections	13	15	17	19	21	23

Table 3.3 – Main parameters of solutions S^{m0} to S^{m5}

The absolute displacement computed for each mesh is presented on Figure 3.15.

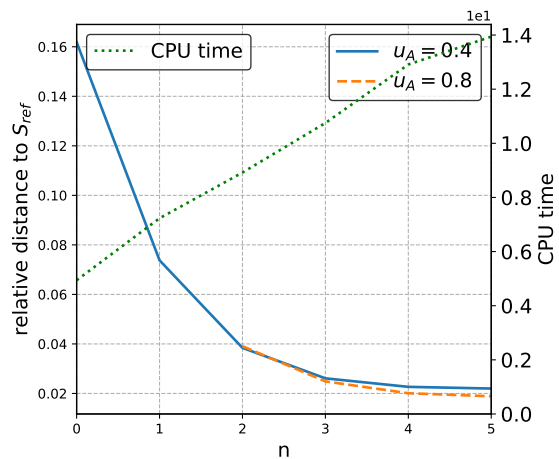
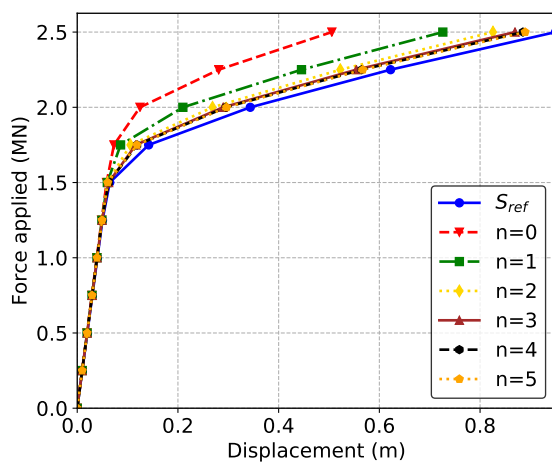


Figure 3.15 – Force-displacement curve for solutions S^{m0} to S^{m5}

Figure 3.16 – $e_A(0.4)$ and $e_A(0.8)$ and CPU time for solutions S^{m0} to S^{m5}

3.5. Application to a cantilever beam

The refinement of the longitudinal mesh close to the clamped end means an improvement of the results. We define the relative distance between the reference solution and solution S^{m_n} for a given u_A by:

$$e_A^{(n)}(u_A) = \left| \frac{F_{S^{m_n}}(u_A) - F_{S_{\text{ref}}}(u_A)}{F_{S_{\text{ref}}}(u_A)} \right| \quad (3.71)$$

The relative distance $e_A^{(n)}$ is computed for each mesh m_n for $u_A = 0.4$ m and $u_A = 0.8$ m. The results are presented on Figure 3.16 with the CPU time needed by the computation of each solution S^{m_n} . $e_A(u_A = 0.8)$ can not be computed for $i \leq 1$ since the computed displacement does not reach this value (see on Figure 3.15). The two curves associated to $e_A(u_A = 0.4)$ and $e_A(u_A = 0.8)$ confirms the results of Figure 3.15: the more the mesh is refined, the more the results are accurate. Solutions S^{m_4} and S^{m_5} reach relative distances of 2% for $u_A = 0.4$ m and $u_A = 0.8$ m. The improvement of the results naturally comes with a cost in CPU time. When the less refined solution S^{m_0} takes only 10.5 s, the most refined solution S^{m_5} needs 14s of computation.

Better results can therefore be obtained with a better refinement of the mesh. The choice of the refinement is a compromise between the accuracy of a solution and its computational time.

3.5.3.2 Interpolation functions

The interpolation functions have a role in the quality of the results. The functions used in the present paper are NURBS as described in [Corre et al., 2017a]. The degree of interpolation of the NURBS has an incidence on the model: the higher is the degree of interpolation, the more numerous are the functions of interpolation and the longer is their support. The parameters used for the 4 solutions studied in this section are the same as the ones for solution S_0 and the interpolation degree of NURBS takes values from 1 to 4. The main parameters of the 4 solutions studied here are gathered in Table 3.4.

Solution	S^{p1}	S_0	S^{p3}	S^{p4}	S^{p5}
plastic modes AE order	3	3	3	3	3
force modes AE order	4	4	4	4	4
NURBS order	1	2	3	4	5
knots	10	10	10	10	10
integration sections	19	19	37	37	55

Table 3.4 – Main parameters of solutions S^{p1} to S^{p5}

The absolute displacement at point A computed for each solution is presented on Figure 3.17. The relative distances $e_A(u_A = 0.4)$ and $e_A(u_A = 0.8)$ and the CPU time required by solution are presented on Figure 3.18.

Solution S^{p1} is notably less satisfying than the other solutions: the relative distance $e_A(u_A =$

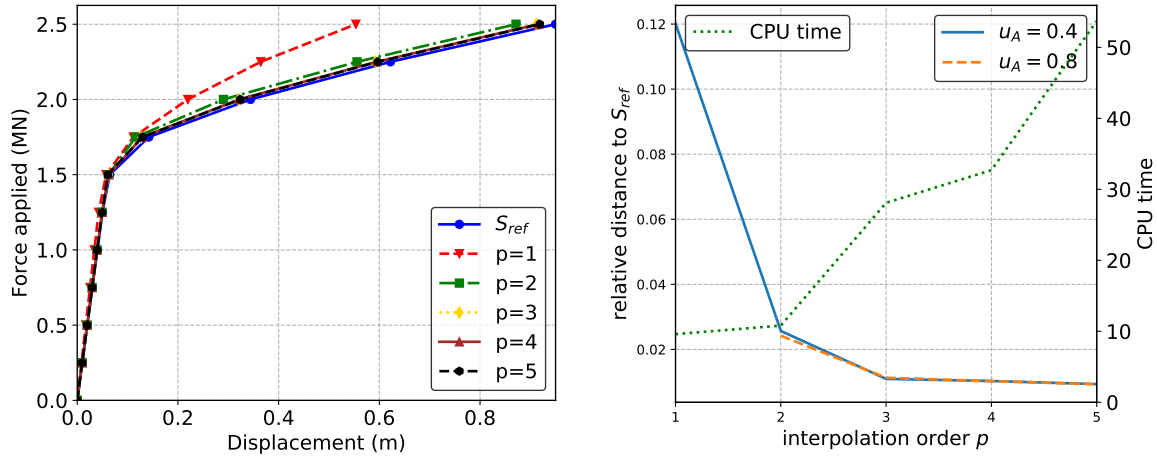


Figure 3.17 – Displacement at point A for solutions S^{p1} , S_0 to S^{p5} – Figure 3.18 – e_A and computational cost for solutions S^{p1} to S^{p5}

0.4) is important (12%) and the force-displacement curve does not reach $u_A = 0.8$ m. These poor results were expected since locking occurs in the element for this interpolation order. The increase of the order of the interpolation functions comes with an improvement in the results: while $e_A(0.4) = 2.56\%$ and $e_A(0.8) = 2.42\%$ for S_0 , the relative distance is improved in S^{p3} with $e_A(0.4) = 1.09\%$ and $e_A(0.8) = 1.13\%$. Best values are reached with S^{p5} : $e_A(0.4) = 0.93\%$ and $e_A(0.8) = 0.93\%$.

The computational cost of the solutions increases with the interpolation order. This is mainly due to the increase of the number of degrees of freedom and of the integration sections induced by a higher interpolation order. The CPU time curve presented in Figure 3.18 shows levels of computation time: S^{p1} and S_0 need approximately the same CPU time, and so do S^{p3} and S^{p4} . This is explained by the increase of the number of integration sections: this number is determined by equation (3.69) and is the same for the interpolation order $2p + 1$ and $2p + 2$. The small increase of CPU time between $p = 1$ and $p = 2$ and between $p = 3$ and $p = 4$ is only due to the increase of degrees of freedom. In view of the results, solutions S^{p3} and S^{p4} can be an alternative to S_0 : the increase of the computational cost is notable but the improvement of the results is significant.

3.5.3.3 Asymptotic expansion order for the computation of the plastic modes

The asymptotic expansion order used for the computation of the plastic modes in solution S_0 has been set to $n_{AE} = 3$. In this section, we investigate on the impact of n_{AE} on the results. The higher is n_{AE} , the richer should be the kinematics and the better should be the solution. Based on solution S_0 , ($n_{AE} = 3$), 4 new solutions are studied with n_{AE} taking values from 0 to 4. The main parameters of these solutions are gathered in Table 3.5 .

3.5. Application to a cantilever beam

Solution	S^{n0}	S^{n1}	S^{n2}	S_0	S^{n4}
plastic modes AE order	0	1	2	3	4
force modes AE order	4	4	4	4	4
NURBS order	2	2	2	2	2
knots	10	10	10	10	10
integration sections	19	19	19	19	19

Table 3.5 – Main parameters of solutions S^{n0} to S^{n4}

The relative distance e_A for $u_A = 0.8$ m computed by each solution and the relative total time of each solution are presented on Figure 3.19. The force-displacement curves at point A are not shown here since they are too close to afford a good comparison of the solutions.

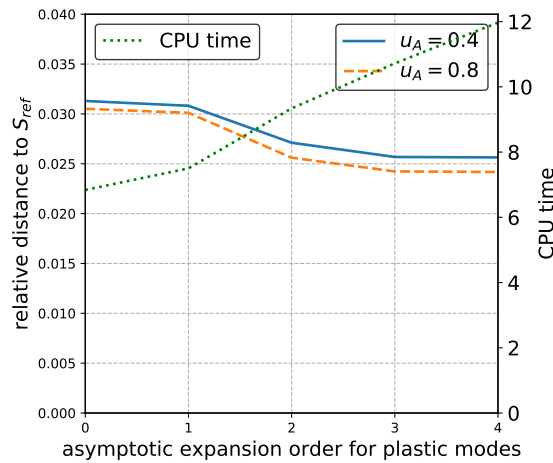


Figure 3.19 – e_A and computational cost for solutions S_0^{n0} to S_0^{n4}

As expected, the highest distance from the reference solution is obtained with the solution without plastic modes: $e_A(u_A = 0.4) = 3.13\%$ and $e_A(U_a = 0.8) = 3.05\%$. Its computational cost is the smallest since no time is spent on extending the kinematics with plastic modes. The increase of n_{AE} brings a reduction of the distance from the reference solution, and comes with an increase of the computational cost. S_0^{n4} is not better than S_0^{n3} (respectively 2.56% versus 2.57% for $u_A = 0.4$ m and 2.42% for both solutions for $u_A = 0.8$ m). This means that the plastic modes computed at the fourth expansion order do not bring information (in a spectral meaning) when compared to the basis computed at the third order. However, it is interesting to note that the solution without plastic modes quickly converges and yield satisfying results. This is explained by the fact that the displacements induced by the plastic strain are already well described by the modes of the Saint-Venant's solution and the force modes in this particular case study.

Based on Figure 3.19, the value $n_{AE} = 3$ seems relevant in the present case.

3.6 Conclusion

A new higher-order elasto-plastic beam model has been presented. The model is based on an enrichment of its kinematics on the fly during the incremental-iterative process. The kinematics of the model, represented by 2D-displacement modes, is updated at each increment according to the plastic state of the beam.

The model is based on the elastic beam model recently presented in [Ferradi et al., 2016; Correat al., 2017a]. This higher-order elastic beam model does not need any *a priori* knowledge on the solution of the problem to extend its kinematics. All the modes of the model are computed thanks to the formal asymptotic expansion which is a systematic method. In the elasto-plastic beam model presented in this paper, the plastic strain is considered as an eigenstrain loading the structure and additional modes specific to the plastic state of the beam are added to the kinematics of the model. The plastic strain is computed on integration sections defined by their longitudinal position. The plastic strains computed on some chosen integration sections are then used to compute 2D displacement plastic modes which extend the basis of modes forming the kinematics of the element.

Locally, the model uses a classic radial return algorithm. 3D state variables are computed on integration section where the local equilibrium equations are then integrated. This model therefore yields local 3D results. The global algorithm is based on a standard global plastic algorithm: the global equilibrium is expressed thanks to the principle of virtual works and is reached with a Newton-Raphson's convergence procedure. The algorithm is adapted to the fact that the kinematics of the model is not fixed during the incremental-iterative process. Thus, internal and external forces must be computed again every time the basis of modes changes.

The model shows satisfying results with reduced time of computation when compared to 3D computation. The method has been applied to the case of a cantilever beam loaded at its free extremity by a force applied with eccentricity. The beam model required a computation time about 100 times shorter than the computation time of the reference 3D solution computed on *Code_Aster*. Since the kinematics of the element is adapted to the forces applied and to the plastic state of the structure, this beam model is a general plastic model able to capture all the deformations induced by the load considered: bending, torsion or shear forces. The numerical differences between the beam solution and the reference solution for the example presented are low, but we think they can still be lowered. Indeed, the computation of the displacement modes do not take the boundary conditions into account. The clamped extremity of the cantilever beam has a strong local influence on the values of the stress. The model could therefore be improved if displacement modes specific to the boundary conditions were computed and added to the kinematics of the model. Moreover, the model already presents very interesting gains in computation time, but it could be even more time-efficient by considering parallelization process, in particular for the computation of the stiffness matrix.

3.6. Conclusion

The elasto-plastic beam model has been presented with isotropic material with a J_2 yield criterion. Its adaption to different yield criteria is easy. The extension of the model to anisotropic material or to more complex material like reinforced concrete could be the next step of the development of this elasto-plastic beam element.

* *

 *

Chapter 4

Higher-order elastoplastic beam model for reinforced concrete

Abstract: *This chapter defines a new beam model for reinforced concrete. The model is defined in three steps. First the constitutive behavior of concrete is described and the kinematic connection between steel and concrete is presented. Then the beam element based on the elastoplastic beam element of Chapter 3 is introduced. The model is finally validated by a multi-step procedure and illustrated by a study case.*

Contents

4.1	Introduction	124
4.2	Definition of an elastoplastic reinforced concrete model	127
4.2.1	General framework and methodology	127
4.2.2	A new model for concrete materials	130
4.2.3	Modeling of steel rebars	135
4.2.4	Kinematic relation between rebars and concrete	137
4.3	Definition of a beam element	140
4.3.1	The AELD beam model	140
4.3.2	Description of the beam kinematics	141
4.3.3	Numerical approximation	142
4.3.4	Local integration of the equilibrium equations	142
4.4	Validation of the model	142
4.4.1	Reinforced T-beam in elasticity	143
4.4.2	Reinforced T-beam in elastoplasticity	148
4.4.3	Reinforced beam with the new concrete model	154
4.4.4	Validity of the elastoplastic model	158
4.4.5	Mesh sensitivity	161
4.5	Conclusion	165

4.1 Introduction

The development of a beam model for reinforced concrete is a complex process involving three main issues. The first difficulty arises in the definition of the materials behavior. Many models of various complexity have been proposed to describe the global and local behavior of concrete whereas theory of plasticity is almost always used for the material definition of steel. The second difficulty lies in the definition of the kinematics and formulation of the beam model. The beam element considered here should account for axial, shear and bending responses and for their interactions. Finally, the structural connection between steel and concrete must be numerically expressed.

The first important feature is the definition of the concrete constitutive behavior. High stresses lead to the apparitions of cracks in both tension and compression and has an impact on the strain-stress behavior. First, we observe softening which is comparable to a negative hardening. Second it causes damage [Lubliner et al., 1988]. Three types of concrete models can be distinguished: damage models, plastic models using the plasticity theory and plastic-damage models combining both damage and plasticity. Damage models efficiently capture the stiffness degradation in the structure but they cannot represent the irreversible deformations. [Govindjee et al., 1995; Mazars, 1986; Oller and Barbat, 2005]. By contrast, plastic models cannot capture the effect of microcracks on the Young modulus but they are suitable for the description of the irreversible deformations they cause [Chen, 2007; Feenstra and Borst, 1996; Grassl et al., 2002]. The majority of models therefore consider both damage and plasticity. Most of them are developed with isotropic damage law [Salari et al., 2004; Grassl and Jirásek, 2006]. Anisotropic damage models have been developed but their numerical applications is much more complex [Meschke et al., 1998]. Numerical applicability of concrete models quickly suffers from complex constitutive behaviors. Without regularization techniques, the softening phase in the strain-stress response leads to mesh-dependent solutions. Moreover, in the case of softening, both damage and plastic models can lead to multiple discontinuous solutions.

The approach adopted in this paper to overcome this difficulty is the theory of plasticity without softening in order to provide a simple and robust concrete model. The Rankine yield criterion is chosen for both tension and compression because of its simplicity and its usage in the engineering community [ICAB, 2005; ACI, 2014]. The aim of the present model is obviously not to provide a representation of the microcracks in concrete, but to yield accurate kinematic descriptions of loaded reinforced concrete structures. Assuming that the degradation of the stiffness in compression is not very important and that concrete strength in tension is very low, the use of a damage parameter may be neglected. Based on the previous remarks on softening, the choice is made not to consider negative hardening. The main limitation of this approach is the infinite energy it can dissipate without restriction. Consequently the present model adopts a fracture energy approach in order to limit the energy dissipation in tension. Given the high strength of concrete in compression, the energy dissipation in compression will

4.1. Introduction

not be an issue in most cases. In order to develop a simple and efficient reinforced concrete model, we combine the simplicity of this concrete definition to the numerical efficiency of a beam model. It is important to mention that a more complex constitutive behavior for concrete could be considered and a damage law could be coupled in a second step to the plastic model presented in this paper.

The second important aspect of this paper is the definition of a kinematically accurate beam model. The most natural way to define elastoplastic beam models is to use global scale approach based on 1D stress-resultants. The nonlinear behavior of the structure is expressed in terms of generalized stress integrated on the cross-section. It requires a preliminary analysis for the computation of the linear and non-linear diagrams of stress-resultants: axial and shear forces, bending moment and torque. If several stress-resultants are considered, their linear and non-linear interactions should therefore be also considered. By solving the nonlinear problem in terms of 1D generalized stress at each longitudinal integration points, this approach prevents costly local integrations and provides fast computations [Ibrahimbegović and Frey, 1993]. Stress-resultant models are frequently used to study the ultimate load of frames [Pham et al., 2012] but has also been used for other slender structures such as bridges [Oller and Barbat, 2005]. However the computation of the stress-resultants interactions can turn out to be tough. Bui and al. [Bui et al., 2014] choose not to explicitly consider the interaction between shear and bending in their beam element but to represent it through the assembly of two elements. The main limitation of these models is their poor local accuracy since they are limited by the beam theory assumptions and use 1D plastic or damage description.

The common way to improve local accuracy is to use multi-fibers beam models. The beam cross-section is discretized in layers for 2D-beams or in fibers for 3D-beams. Each layer or fiber is associated with a local beam kinematics. One of the first mention of the multi-fibers model can be found in the book of Owen and Hinton [Owen and Hinton, 1980]. The model have since widely been used for linear and nonlinear analysis of beam structures. Thanks to its cross-sectional discretization, a multi-fibers model is suitable for describing non-homogeneous structures such as reinforced concrete beam: some fibers are associated with the concrete properties while others are associated with steel properties thus representing longitudinal rebars. Cross-sectional rebars cannot properly be represented with multi-fibers model. However concrete can be given a modified constitutive law considering the effect of confinement. This model is an intermediate solution between the macroscopic approach of a single beam element and the microscopic approach of a 3D finite element solution. Indeed it provides a microscopic description of the cross-sectional behavior of the structure while benefiting from the simple kinematic assumption of each beam fiber. The 3D global response of the beam submitted to external loads is recovered by integrating the fibers behavior through the cross-section.

The simplest kinematics to associate with the fibers is the Euler-Bernoulli kinematics [Spacone et al., 1996; Spacone and Limkatanyu, 2000; Moulin, 2010] where each cross-section remains plane and normal to the deformed longitudinal axis. It provides an efficient and fast-computing

element that accounts for axial and bending effects but the simple assumptions of the Euler-Bernoulli beam model fails in taking shear effects into account. This model is therefore not relevant as soon as shear effects are significant.

For this reason, many developments have been made using the Timoshenko beam model that considers the cross-section not necessarily normal to the deformed longitudinal axis. It consequently introduces a uniform shear force through the beam cross-section. Mazars et al. used this kinematics to develop a multi-fibers beam element accounting for shear and torsion for two damage models [Mazars et al., 2006]. As a result, the inclusion of shear effects in the fibers kinematics provides far more accurate damage fields. By considering shear effects, the Timoshenko kinematics leads to new failure mechanisms. This approach has therefore been used to study reinforced concrete frames for shear failure analysis [Bui et al., 2014; Pham et al., 2012; Jukić et al., 2014] or cyclic loading [Marini and Spacone, 2006]. However the uniform shear stress introduced by the Timoshenko kinematics cannot satisfy the free boundary conditions on the cross-section.

In order to further improve local accuracy of the element and to get a better description of macroscopic forces, the approach adopted in the present paper is to use a higher-order elastoplastic beam element. First developed in elasticity by [Ferradi et al., 2016], it has been extended to eigenstrains [Corre et al., 2017a] before being adapted to the case of elastoplasticity [Corre et al., 2017b]. The kinematics is enriched thanks to a systematic method with displacement modes computed on the 2D cross-section of the structure. These modes bring local accuracy and can easily describe higher-order shear effects as well as bending or torsion.

The third issue in the definition of a reinforced concrete beam model is the description of the connection between steel and concrete. In most reinforced concrete beam models, the description of the rebars is closely linked to the definition of the beam model like in the multi-fibers models described previously. In the present model, one single higher-order beam element is used and only the concrete matrix is represented by this element. Steel rebars are therefore added as embedded elements and considered as 1D bars into the concrete volume. They are meshed independently from concrete. This method affords a wide range of reinforcement layouts.

The organization of the chapter is based on the three important steps first introduced. The general definition of a material in multisplasticity and the global resolution of the reinforced concrete structure are first given in Section 4.2. Based on this framework, Section 4.2.2 is dedicated to the definition of the concrete material: constitutive behavior, yield criterion and local projection algorithm on the yield surface are presented. Steel is then similarly defined in Section 4.2.3. Both materials being characterized, the kinematic connection between concrete and steel rebars is presented in Section 4.2.4. Section 4.3 provides a brief description of the beam model. A validation procedure of the present model is then carried out and the fracture-based approach defining the domain of validity of the computed strain-stress curves is introduced. A mesh sensibility is finally processed.

4.2. Definition of an elastoplastic reinforced concrete model

4.2 Definition of an elastoplastic reinforced concrete model

This section presents and characterizes an elastoplastic beam element for reinforced concrete. The procedure considered for the definition of the model is first set. A concrete model based on the Rankine's yield criterion is presented and the local integration of the elastoplastic equilibrium equations are formulated in a closed-form solution based on this criterion. The steel rebars are introduced in the model as one dimensional bar elements embedded into the concrete volume. The structural connection between concrete and rebars is numerically expressed through kinematic relations.

4.2.1 General framework and methodology

4.2.1.1 Definition of the elastoplastic behavior

We consider an elastoplastic material in multisurface plasticity (see [Simo, 1985] and [Godio et al., 2016]). In order to determine if the material is locally elastic or plastic, we first define the space of plastically admissible states \mathbb{E}_σ . Considering the stress σ and a plastic variable p , \mathbb{E}_σ is defined in stress-space by:

$$\mathbb{E}_\sigma = \{(\sigma, p) \in \mathbb{S} \times \mathbb{R}_+ \mid f_i(\sigma, p) \leq 0, \forall i \in [1, \dots, m]\}, \quad (4.1)$$

where \mathbb{S} is the space of statically compatible stresses defined by m yield criterion functions $f_i : \mathbb{S} \times \mathbb{R}_+ \rightarrow \mathbb{R}$. The definition of the functions f_i fully characterizes \mathbb{E}_σ . The yield criterion of concrete is defined in Section 4.2.2.2.

The total strain splits into an elastic part and a plastic part:

$$\varepsilon = \varepsilon^e + \varepsilon^p. \quad (4.2)$$

An elastoplastic constitutive law must then be defined. The constitutive law locally links the stress to the elastic strain thanks to the stiffness matrix respectively denoted by \mathbf{C} :

$$\sigma = \mathbf{C} : (\varepsilon - \varepsilon^p). \quad (4.3)$$

The plastic strain ε^p involved in Equation (4.3) is computed thanks to the definition of the flow rule. The present flow rule is associative and therefore links ε^p to the yield criterion functions f_i :

$$\dot{\varepsilon}^p = \sum_{i=1}^m \dot{\gamma}_i \frac{\partial f_i}{\partial \sigma}, \quad (4.4)$$

where γ_i are nonnegative scalars called consistency parameters. They follow the Kuhn-Tucker complementary conditions:

$$\gamma_i \geq 0, \quad f_i(\boldsymbol{\sigma}, p) \leq 0, \quad \gamma_i f_i(\boldsymbol{\sigma}, p) = 0, \quad (4.5)$$

and the consistency requirement:

$$\gamma_i \dot{f}_i(\boldsymbol{\sigma}, p) = 0 \quad (4.6)$$

Equations (4.5) and (4.6) condition the evolutions of $\boldsymbol{\sigma}$ in \mathbb{E}_σ .

4.2.1.2 Numerical formulation

We consider a 3D concrete structure defined by the domain Ω . The structure is loaded by the volumic forces \mathbf{b} and by the surfacic force \mathbf{t} on \mathcal{S}_t and displacements are imposed on \mathcal{S}_u . Let $[0, T] \subset \mathbb{R}^+$ be the time interval of interest of the problem. The displacements are defined by the functions:

$$\mathbf{u} : \Omega \times [0, T] \rightarrow \mathbb{R}^3 \quad (4.7)$$

All the variables are functions of space position \mathbf{x} and time t .

The elastoplastic boundary value problem to consider is expressed as follows:

$$\left. \begin{array}{ll} \operatorname{div}_x \boldsymbol{\sigma} + \mathbf{b} = 0 & \text{on } \Omega \\ \boldsymbol{\sigma} = \mathbf{C} : (\boldsymbol{\varepsilon} - \boldsymbol{\varepsilon}^p) & \text{on } \Omega \\ \boldsymbol{\varepsilon} = \nabla_x^s \mathbf{u} & \text{on } \Omega \\ \dot{\boldsymbol{\varepsilon}}^p = \sum \gamma_i \frac{\partial f_i}{\partial \boldsymbol{\sigma}} & \text{on } \Omega \\ \gamma_i \geq 0, f_i \leq 0, \gamma_i f_i = 0 & \text{on } \Omega \\ \gamma_i \dot{f}_i = 0 & \text{on } \Omega \\ \boldsymbol{\sigma} \cdot \mathbf{n} = \mathbf{t} & \text{on } \mathcal{S}_t \\ \mathbf{u} = 0 & \text{on } \mathcal{S}_u \end{array} \right\} \times [0, T] \quad (4.8)$$

For the resolution Equation (4.8), the time interval is divided into time increments. The numerical resolution consists in finding the state $\mathcal{S}_{n+1} = (\mathbf{u}_{n+1}, \boldsymbol{\sigma}_{n+1}, \dots)$ at time t_{n+1} with the knowledge of the previous state \mathcal{S}_n . The local integration of Equation (4.8) ensures that the stresses are plastically admissible, meaning that $(\boldsymbol{\sigma}, p) \in \mathbb{E}_\sigma$. The equilibrium equations are verified globally, ensuring the static admissibility of the stresses. If the evolution is plastic, both conditions are not reached simultaneously, motivating an iterative procedure. The local algorithm used in this article is a return map algorithm defined in Section 4.2.1.3, and the global procedure is a *Newton-Raphson* algorithm.

4.2.1.3 Local integration of the elastoplastic behavior

We assume that the state \mathcal{S}_n is fully known. Strain increments $\Delta \boldsymbol{\varepsilon}$ is applied on \mathcal{S}_n between t_n and t_{n+1} . The total strain at time t_{n+1} is then $\boldsymbol{\varepsilon}_{n+1} = \boldsymbol{\varepsilon}_n + \Delta \boldsymbol{\varepsilon}$. Because of the nonlinear relation

4.2. Definition of an elastoplastic reinforced concrete model

between stresses and plastic strains (Equations (4.3) and (4.5)) they cannot be computed simultaneously. Therefore we first assume that the evolutions are elastic and we form the trial stress $\boldsymbol{\sigma}_{n+1}^{\text{trial}}$:

$$\boldsymbol{\sigma}_{n+1}^{\text{trial}} = \boldsymbol{\sigma}_n + \mathbf{C} : \Delta \boldsymbol{\varepsilon} \quad (4.9)$$

If $f_i(\boldsymbol{\sigma}_{n+1}^{\text{trial}}) \leq 0$ for all the yield functions f_i , then the assumption is correct and the evolution is elastic and $\boldsymbol{\sigma}_{n+1} = \boldsymbol{\sigma}_{n+1}^{\text{trial}}$. Otherwise, then the trial stress needs to be projected on the surface of the yield criterion. The local projection of the trial stress is defined in Section 4.2.2.3.

Once the projection has yielded the plastically admissible state $(\boldsymbol{\sigma}_{n+1}, p_{n+1})$, the plastic strain increment $\Delta \boldsymbol{\varepsilon}_{n+1}^p$ can be computed.

4.2.1.4 Global resolution of the structure

The *Newton-Raphson* algorithm implies the use of the tangent stiffness matrix for the global resolution of the structure. We iteratively solve the following equation to reach the global equilibrium:

$$[\mathbf{K}^{\text{ep}}] \{\delta \tilde{\mathbf{u}}\} = \{\mathbf{R}\}, \quad (4.10)$$

where $\{\delta \tilde{\mathbf{u}}\}$ is the increment of generalized displacements, $\{\mathbf{R}\}$ is the force residual and $[\mathbf{K}^{\text{ep}}]$ is the global tangent stiffness matrix.

Since we aim to define a reinforced concrete model and anticipating the integration of the rebars, the global tangent stiffness matrix can be defined as the sum of the global tangent stiffness matrix of concrete and the global tangent stiffness matrix of the rebars:

$$[\mathbf{K}^{\text{ep}}] = [\mathbf{K}^{\text{ep,c}}] + [\mathbf{K}^{\text{ep,st}}], \quad (4.11)$$

where $[\mathbf{K}^{\text{ep,c}}]$ is the tangent stiffness of concrete and $[\mathbf{K}^{\text{ep,st}}]$ is the tangent stiffness of steel. The modeling of steel rebars and their definition as 1D elastoplastic material are presented in Section 4.2.3. Their connection with the concrete material is described in Section 4.2.4. In all the article, variables referring to concrete are denoted with no superscript and variables referring to steel are denoted with the superscript \bullet^{st} .

For a time step t_{n+1} , the global tangent stiffness matrix of concrete is defined by the following relation:

$$\int_{\Omega} \boldsymbol{\varepsilon} [\delta \mathbf{u}] : \mathbf{C}_{n+1}^{\text{ep,c}} : \boldsymbol{\varepsilon} [\mathbf{w}^c] d\Omega = \{\delta \tilde{\mathbf{u}}\} [\mathbf{K}^{\text{ep,c}}] \{\tilde{\mathbf{u}}^c\}, \quad \forall \mathbf{w}^c \in C(\mathcal{S}_u, \mathbf{0}), \quad (4.12)$$

where $\mathbf{C}_{n+1}^{\text{ep,c}}$ is the local elastoplastic tangent moduli of concrete at time step t_{n+1} . $C(\mathcal{S}_u, \mathbf{0})$ is the space of displacements kinematically admissible for a zero displacement on \mathcal{S}_u , and $\{\tilde{\mathbf{u}}^c\}$ is the general displacement vector associated to the displacement \mathbf{w}^c .

Similarly, the global tangent stiffness matrix of steel rebars is defined by:

$$\int_{\Omega^{\text{st}}} \boldsymbol{\varepsilon}^{\text{st}} [\delta \mathbf{u}^{\text{st}}] : \mathbf{C}_{n+1}^{\text{ep,st}} : \boldsymbol{\varepsilon}^{\text{st}} [\mathbf{w}^{\text{st}}] d\Omega = \{\tilde{\mathbf{u}}^{\text{st}}\} [\mathbf{K}^{\text{ep,st}}] \{\delta \tilde{\mathbf{u}}\}, \quad \forall \mathbf{w}^{\text{st}}, \quad (4.13)$$

where $\mathbf{C}_{n+1}^{\text{ep,st}}$ is the local elastoplastic tangent moduli of steel rebars at time step t_{n+1} . The definition of the local elastoplastic tangent moduli are given in Section 4.2.2.4 for concrete and in Section 4.2.3.3 for steel reinforcement.

The next section is dedicated to the description of the concrete material: the yield criterion, the local integration algorithm and the computation of the elastoplastic tangent moduli are exposed. The definition of the rebars is likewise given in Section 4.2.3 and Section 4.2.4 is dedicated to their kinematic integration.

4.2.2 A new model for concrete materials

4.2.2.1 Concrete as an elastoplastic material

Despite its heterogeneous local properties, concrete can reasonably be considered as an isotropic homogeneous material for its numerical modeling. The present model is developed in order to study reinforced concrete structures submitted to moderate strains. The approach adopted is to consider concrete as an elastoplastic material as represented on Figure 4.1. An isotropic hardening with a very low isotropic hardening modulus H is considered. This choice avoids potential strain localisation problems that can occur in perfect plasticity. Plasticity is relevant for the representation of the behavior of concrete in compression. Despite concrete has a brittle behavior in tension, the simplicity of the theory of plasticity is here preferred as explained in the introduction.

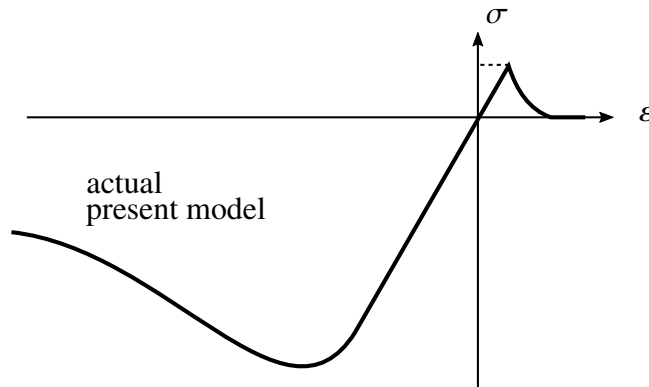


Figure 4.1 – Elastoplastic model used for the concrete

4.2. Definition of an elastoplastic reinforced concrete model

4.2.2.2 The Rankine's yield criterion

Investigating the shape of \mathbb{E}_σ for concrete materials, Kupfer carried out a series of biaxial tests [Kupfer et al., 1969]. This way, he identified the shape of the admissible space states for $(\sigma_I, \sigma_{II}, \sigma_{III} = 0)$ in principal stresses. While the limit of compression of concrete was identified to a certain value in uniaxial stress, its limit was about 16% higher in bi-compression, giving $\mathbb{E}_\sigma(\sigma_I, \sigma_{II}, \sigma_{III} = 0)$ the shape of a square rounded in the bi-compression zone. This experimental results are considered as a reference in civil engineering. However, civil engineers are more likely to use a yield criterion were the compression and tension limits of concrete are constant in uniaxial, bi-axial, or tri-axial compression. This assumption brings simplicity in the analysis of the numerical results, particularly for the identification of the inelastic zones. This criterion is defined in principal stress by:

$$-f_c \leq \sigma_I, \sigma_{II}, \sigma_{III} \leq f_t \quad (4.14)$$

where $f_c, f_t \geq 0$ are respectively the compression and tension resistances of the material. The criterion is known as the Rankine criterion, dating from 1876, and is represented by a cube in principal stress. Since concrete is considered with an isotropic hardening, the usual Rankine criterion defined in Equation (4.14) is modified as follows to account for the hardening:

$$-f_c - Hp \leq \sigma_I, \sigma_{II}, \sigma_{III} \leq f_t + Hp \quad (4.15)$$

where H is the plastic modulus. \mathbb{E}_σ is therefore constructed with the 6 following functions:

$$\begin{aligned} f_1 = \sigma_I - f_t - Hp \leq 0, \quad f_2 = \sigma_{II} - f_t - Hp \leq 0, \quad f_3 = \sigma_{III} - f_t - Hp \leq 0 \\ f_4 = -\sigma_I - f_c - Hp \leq 0, \quad f_5 = -\sigma_{II} - f_c - Hp \leq 0, \quad f_6 = -\sigma_{III} - f_c - Hp \leq 0 \end{aligned} \quad (4.16)$$

\mathbb{E}_σ being defined with 6 criteria, 6 consistency parameters γ_i are considered. Thanks to the simple expression of this yield criterion in principal stress, the local projection of a trial state $(\sigma_{n+1}^{\text{trial}}, p_n) \notin \mathbb{E}_\sigma$ can be easily conducted as it will be shown in Section 4.2.2.3.

4.2.2.3 Local projection on the criterion

Equation (4.8) is locally integrated. The method used for the local integrations is a classic return map algorithm as explained in Section 4.2.1.3: given a strain increment $\Delta\boldsymbol{\varepsilon}$, an elastic trial stress $\sigma_{n+1}^{\text{trial}}$ is formulated. If $(\sigma_{n+1}^{\text{trial}}, p_n) \in \mathbb{E}_\sigma$, meaning that the yield criterion is satisfied, the stress is plastically admissible and $(\sigma_{n+1}, p_{n+1}) = (\sigma_{n+1}^{\text{trial}}, p_n)$. If $(\sigma_{n+1}^{\text{trial}}, p_n) \notin \mathbb{E}_\sigma$, σ_{n+1} is the closest point projection (see [Simo and Hughes, 1998]) of $\sigma_{n+1}^{\text{trial}}$ onto the boundary $\partial\mathbb{E}_\sigma$ in the norm induced by the metric \boldsymbol{G} defined by:

$$\boldsymbol{G} = \begin{pmatrix} \boldsymbol{C}^{-1} & 0 \\ 0 & 1/H \end{pmatrix}, \quad (4.17)$$

where \mathbf{C}^{-1} is the compliance matrix. Thus, $(\boldsymbol{\sigma}_{n+1}, p_{n+1})$ is the state which satisfies the following minimum principle:

$$(\boldsymbol{\sigma}_{n+1}, p_{n+1}) = \text{ARG} \left[\underset{(\boldsymbol{\sigma}, p) \in \mathbb{E}_\sigma}{\text{MIN}} \left\{ \frac{1}{2} \|\boldsymbol{\sigma}_{n+1}^{\text{trial}} - \boldsymbol{\sigma}\|_{\mathbf{C}^{-1}}^2 + \frac{1}{2} H(p_n - p)^2 \right\} \right], \quad (4.18)$$

where $\|\boldsymbol{\sigma}\|_{\mathbf{C}^{-1}} = \sqrt{\boldsymbol{\sigma} : \mathbf{C}^{-1} : \boldsymbol{\sigma}}$. The Lagrangian associated with this linearly constrained problem is expressed:

$$\mathcal{L}(\boldsymbol{\sigma}, p, \gamma) = \frac{1}{2} \|\boldsymbol{\sigma}_{n+1}^{\text{trial}} - \boldsymbol{\sigma}_{n+1}\|_{\mathbf{C}^{-1}}^2 + \frac{1}{2} H(p_n - p)^2 + \sum_{i=1}^6 \Delta\gamma_i f_i(\boldsymbol{\sigma}, p), \quad (4.19)$$

and the corresponding *Kuhn-Tucker* optimality conditions are:

$$\left. \frac{\partial \mathcal{L}}{\partial \boldsymbol{\sigma}} \right|_{n+1} = \mathbf{C}^{-1} : \left(-\boldsymbol{\sigma}_{n+1}^{\text{trial}} + \boldsymbol{\sigma}_{n+1} \right) + \sum_{i=1}^6 \Delta\gamma_i \left. \frac{\partial f_i}{\partial \boldsymbol{\sigma}} \right|_{n+1} = \mathbf{0}, \quad (4.20)$$

$$\left. \frac{\partial \mathcal{L}}{\partial p} \right|_{n+1} = \Delta p - \sum_{i=1}^6 \Delta\gamma_i = 0, \quad (4.21)$$

$$f_i(\boldsymbol{\sigma}_{n+1}, p_{n+1}), \quad \Delta\gamma_i \geq 0, \quad \Delta\gamma_i f_i(\boldsymbol{\sigma}_{n+1}, p_{n+1}) = 0. \quad (4.22)$$

Equation (4.22) is actually the expression of the *Kuhn-Tucker* complementary conditions. According to Equations (4.21) and (4.22), $\Delta p \geq 0$ which is consistent with the definition of $p \in \mathbb{R}^+$. Given that \mathbf{C}^{-1} is isotropic, it can be shown that solving Equation (4.20) is equivalent to solving its counterpart equation in principal stress, that is:

$$\mathbf{C}^{-1} : \left(-\boldsymbol{\Sigma}_{n+1}^{\text{trial}} + \boldsymbol{\Sigma}_{n+1} \right) + \sum_{i=1}^6 \Delta\gamma_i \left. \frac{\partial f_i}{\partial \boldsymbol{\Sigma}} \right|_{n+1} = \mathbf{0} \quad (4.23)$$

where $\boldsymbol{\Sigma}$ is the stress tensor expressed in the principal stress space and the derivatives of the second term are defined by:

$$\left(\frac{\partial f_i}{\partial \boldsymbol{\Sigma}} \right)_{ij} = \frac{\partial f_i}{\partial \sigma_{l(j)}}, \quad \text{with } l(1) = I, \quad l(2) = II \text{ and } l(3) = III. \quad (4.24)$$

The *Kuhn-Tucker* optimality conditions defined by Equations (4.21), (4.22) and (4.23) are now considered. Assuming that $\boldsymbol{\Sigma}_{n+1}^{\text{tr}} \notin \mathbb{E}_\sigma$, 26 situations can be distinguished: $\boldsymbol{\Sigma}_{n+1}$ is on one of the 6 plans of the criterion, $\boldsymbol{\Sigma}_{n+1}$ is on one of the 12 edges of the criterion or $\boldsymbol{\Sigma}_{n+1}$ is on one of the 8 corners of the criterion.

4.2. Definition of an elastoplastic reinforced concrete model

The 26 local minimum values of Σ_{n+1} and their associated consistency parameters $\Delta\gamma_i$ are given in closed form solutions. The solution of Equation (4.18) is therefore the minimum of these 26 values. A simple change of basis yields the expression σ_{n+1} .

The 2D interpretation of the projection of $\Sigma_{n+1}^{\text{trial}}$ onto \mathbb{E}_σ is shown on Figure 4.2. Two cases are represented: in the first case, the trial stress is in front of a plane and Σ is projected on this plane; in the second case the trial stress is in front of a corner and Σ is projected on this corner. The orthogonality represented on Figure 4.2 must be considered in the norm induced by the metric \mathbf{G} defined in Equation (4.17). This 2D representation can be easily extrapolated to the 3D case.

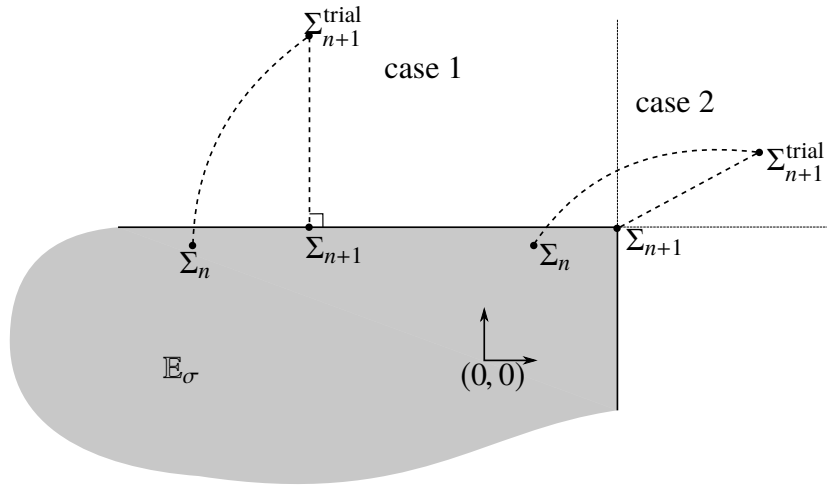


Figure 4.2 – Orthogonal projection of the trial elastic stress on the yield surface

Once the projected state σ_{n+1}, p_{n+1} is obtained, the plastic strain increment $\Delta\epsilon^p$ can be computed. It is directly computed from the trial stress and its projection. Indeed, the trial stress is expressed:

$$\sigma_{n+1}^{\text{trial}} = \sigma_n + \mathbf{C} : \Delta\epsilon \quad (4.25)$$

therefore the projected stress σ_{n+1} can be written:

$$\sigma_{n+1} = \sigma_n + \mathbf{C} : (\Delta\epsilon - \Delta\epsilon^p) = \sigma_{n+1}^{\text{trial}} - \mathbf{C} : \Delta\epsilon^p \quad (4.26)$$

leading to the expression of the increment of plastic strain:

$$\Delta\epsilon^p = \mathbf{C}^{-1} : (\sigma_{n+1}^{\text{trial}} - \sigma_{n+1}) \quad (4.27)$$

The local algorithm for concrete is presented in Algorithm 6.

Algorithm 6 Concrete local algorithm

- 1: Compute the strain increment $\Delta \boldsymbol{\varepsilon}$ from the generalized displacement increment $\Delta \tilde{\boldsymbol{u}}$
 - 2: Form the trial stress $\boldsymbol{\sigma}_{n+1}^{\text{trial}}$
 - 3: Compute $f_{n+1}^{\text{trial}} = f(\boldsymbol{\sigma}_{n+1}, p_n)$
 - 4: **if then** $f_{n+1}^{\text{trial}} > 0$ **then**
 - 5: Compute $(\boldsymbol{\sigma}_{n+1}, p_{n+1})$ and $\Delta \gamma_i$ according to Section 4.2.2.3
 - 6: $\boldsymbol{\varepsilon}_{n+1}^p = \boldsymbol{\varepsilon}_n^p + \mathbf{C}^{-1} : (\boldsymbol{\sigma}_{n+1}^{\text{tr}} - \boldsymbol{\sigma}_{n+1})$
 - 7: **else**
 - 8: $\boldsymbol{\sigma}_{n+1} = \boldsymbol{\sigma}_{n+1}^{\text{trial}}, \boldsymbol{\varepsilon}_{n+1}^p = \boldsymbol{\varepsilon}_n^p, p_{n+1} = p_n$
 - 9: **end if**
 - 10: Compute the tangent stiffness matrix $\mathbf{C}_{n+1}^{\text{ep,c}} \leftarrow$ see Section 4.2.2.4
-

4.2.2.4 Computation of the algorithmic elastoplastic tangent moduli

We denote by \mathbb{C}_{act} the array containing the indices of the saturated constraints, that is the constraints for which $f_i(\boldsymbol{\sigma}_{n+1}, p_{n+1}) = 0$. Then, according to [Simo and Hughes, 1998], the algorithmic tangent moduli in the case of multisurface plasticity is expressed by:

$$\mathbf{C}^{\text{ep}} = \mathbf{D}_{n+1} - \sum_{i \in \mathbb{C}_{\text{act}}} \sum_{j \in \mathbb{C}_{\text{act}}} \frac{\mathbf{D}_{n+1} : \partial_{\sigma} f_{i,n+1} \otimes \mathbf{D}_{n+1} : \partial_{\sigma} f_{j,n+1}}{\partial_{\sigma} f_{i,n+1} : \mathbf{D}_{n+1} : \partial_{\sigma} f_{j,n+1}} \quad (4.28)$$

where \mathbf{D}_{n+1} is defined by:

$$\mathbf{D}_{n+1} = \left[\mathbf{C}_{n+1}^{-1} + \sum_{i \in \mathbb{C}_{\text{act}}} \Delta \gamma_i \partial_{\sigma\sigma}^2 f_{i,n+1} \right]^{-1} \quad (4.29)$$

The derivatives $\partial_{\sigma} f_{i,n+1}$ and $\partial_{\sigma\sigma}^2 f_{i,n+1}$ are necessary for the computation of the tangent stiffness moduli. The criterion is expressed in the principal stress space, and its derivatives according to the general stress are required. The chain rule yields the following expression:

$$\frac{\partial f_i}{\partial \boldsymbol{\sigma}} = \frac{\partial f_i}{\partial \boldsymbol{\Sigma}} : \frac{\partial \boldsymbol{\Sigma}}{\partial \boldsymbol{\sigma}} \quad (4.30)$$

It can be shown that the second derivative has the following expression:

$$\frac{\partial^2 f_i}{\partial \boldsymbol{\sigma}^2} = \frac{\partial \boldsymbol{\Sigma}}{\partial \boldsymbol{\sigma}} : \frac{\partial^2 f_i}{\partial \boldsymbol{\Sigma}^2} : \frac{\partial \boldsymbol{\Sigma}}{\partial \boldsymbol{\sigma}} + \frac{\partial f_i}{\partial \boldsymbol{\Sigma}} : \frac{\partial^2 \boldsymbol{\Sigma}}{\partial \boldsymbol{\sigma}^2} \quad (4.31)$$

The first and second derivatives $\partial_{\Sigma} f_i$ and $\partial_{\Sigma\Sigma}^2 f_i$ are easy to obtain since the yield surface is analytically expressed in the principal stress. In particular, $\partial_{\Sigma\Sigma}^2 f_i = 0$ for plans, leading to the new relation:

$$\frac{\partial^2 f_i}{\partial \boldsymbol{\sigma}^2} = \frac{\partial f_i}{\partial \boldsymbol{\Sigma}} : \frac{\partial^2 \boldsymbol{\Sigma}}{\partial \boldsymbol{\sigma}^2} \quad (4.32)$$

4.2. Definition of an elastoplastic reinforced concrete model

We denote by σ_1 , σ_2 and σ_3 the 3 eigenvalues of σ , and by \mathbf{n}_1 , \mathbf{n}_2 and \mathbf{n}_3 their respective eigenvector. The term $\partial_\sigma \Sigma$ is then expressed:

$$(\partial_\sigma \Sigma)_{lpqr} = \begin{cases} \frac{\partial \sigma_l}{\partial \sigma_{qr}} & \text{if } l = p \\ 0 & \text{otherwise} \end{cases}, \quad \text{where} \quad \frac{\partial \sigma_l}{\partial \sigma_{qr}} = (\mathbf{n}_l \otimes \mathbf{n}_l)_{qr} \quad (4.33)$$

and

$$\frac{\partial \mathbf{n}_l}{\partial \sigma_{qr}} = \sum_{p=1, p \neq l}^3 \frac{\mathbf{n}_l \otimes \mathbf{n}_p + \mathbf{n}_p \otimes \mathbf{n}_l}{\sigma_l - \sigma_p} \cdot \mathbf{n}_l \quad (4.34)$$

Equation (4.34) leads to the expression of $\partial_{\sigma\sigma} \Sigma$. The demonstration of Equation (4.33) can be found for example in [Silhavy, 2013]. The derivatives $\partial_\sigma f_i$ and $\partial_{\sigma\sigma}^2 f_i$ is computed with Equations (4.32) to (4.34).

4.2.3 Modeling of steel rebars

Concrete has been fully described as an elastoplastic material in Section 4.2.2. The same procedure is now adopted for the definition of the steel rebars.

4.2.3.1 Kinematic modeling of the steel rebars

The steel rebars are often modeled in reinforced concrete models by using homogenization methods. Benefiting from the thin cross-sectional dimensions of a rebar compared to the dimensions of a concrete beam and from the higher Young modulus of steel compared to concrete, we can reasonably consider the rebars as 1D bar elements. All variables related to steel are thus expressed in scalar forms in the own coordinate system of a rebar: the stress σ^{st} , the total strain ε^{st} , the plastic strain ε^{pst} and the displacement v^{st} .

Denoting by s the local axis of a rebar, its elastoplastic boundary value problem can be expressed as follows:

$$\left. \begin{aligned} \frac{d\sigma^{\text{st}}}{ds} + b^{\text{st}} &= 0 \\ \sigma^{\text{st}} &= E^{\text{st}}(\varepsilon^{\text{st}} - \varepsilon^{\text{pst}}) \\ \varepsilon^{\text{st}} &= \frac{dv^{\text{st}}}{ds} \\ \varepsilon^{\text{p}} &= \gamma \text{sign}(\sigma) \\ \gamma &\geq 0, f^{\text{st}} \leq 0, \gamma^{\text{st}} f^{\text{st}} = 0 \\ \gamma \dot{f}^{\text{st}} &= 0 \end{aligned} \right\} \text{on } \Omega^{\text{st}} \times [0, T], \quad (4.35)$$

where Ω^{st} is the domain occupied by steel and f^{st} is the 1D yield criterion. The young modulus of the rebars is E^{st} and the elastoplastic tangent moduli is denoted by E^{epst} .

4.2.3.2 Elastoplastic behavior and yield criterion of the steel reinforcement

The steel rebars are considered to be elastoplastic material with an isotropic hardening. Although it would be easy to distinguish different steel properties in our model, we choose here to consider that all the rebars share the same material properties in order to avoid cumbersome notations. Thus, the isotropic hardening modulus of the rebars is denoted by H^{st} , and their yield limit f_y^{st} . The strain-stress curve of the steel rebars is shown on Figure 4.3.

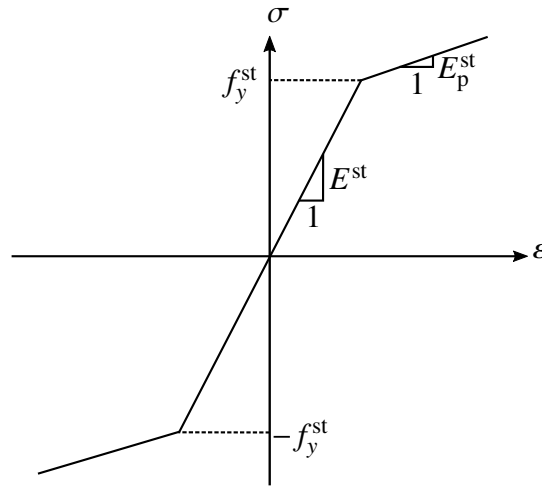


Figure 4.3 – Elastoplastic model used for the steel rebars

The Von-Mises criterion with isotropic hardening is expressed in 1D as follows:

$$f^{st}(\sigma^{st}, p^{st}) = |\sigma^{st}| - f_y^{st} - H^{st} p^{st} \quad (4.36)$$

with $H^{st} = \frac{E^{st} E_p^{st}}{E^{st} + E_p^{st}}$, E_p^{st} being defined on Figure 4.3.

4.2.3.3 Local integration of the equilibrium equations

The local integration of Equation (4.35) yields to the 1D return mapping algorithm presented in Algorithm 7.

4.2. Definition of an elastoplastic reinforced concrete model

Algorithm 7 Local 1D return-mapping algorithm for steel rebars

- 1: Compute the strain increment $\Delta \varepsilon^{\text{st}}$ from the displacement increment v^{st}
 - 2: Form the trial stress $\sigma_{n+1}^{\text{trial,st}} = \sigma_n^{\text{st}} + E^{\text{st}} \Delta \varepsilon^{\text{st}}$
 - 3: Compute $f_{n+1}^{\text{trial,st}} = f^{\text{st}}(\sigma_{n+1}^{\text{trial,st}})$
 - 4: **if** $f_{n+1}^{\text{trial,st}} > 0$ **then**
 - 5: $\Delta \gamma^{\text{st}} = \frac{f_{n+1}^{\text{st,trial}}}{E^{\text{st}} + H^{\text{st}}}$
 - 6: $\sigma_{n+1}^{\text{st}} = \left[1 - \frac{\Delta \gamma^{\text{st}}}{|\sigma_{n+1}^{\text{trial,st}}|} \right] \sigma_{n+1}^{\text{trial,st}}$
 - 7: $\varepsilon_{n+1}^{p^{\text{st}}} = \varepsilon_n^{p^{\text{st}}} + \Delta \gamma^{\text{st}} \text{sign}(\sigma_{n+1}^{\text{trial,st}})$
 - 8: $p_{n+1}^{\text{st}} = p_n^{\text{st}} + \Delta \gamma^{\text{st}}$
 - 9: **else**
 - 10: $\sigma_{n+1}^{\text{st}} = \sigma_{n+1}^{\text{trial,st}}, \varepsilon_{n+1}^{p^{\text{st}}} = \varepsilon_n^{p^{\text{st}}}, p_{n+1}^{\text{st}} = p_n^{\text{st}}$
 - 11: **end if**
 - 12: Compute the tangent moduli $E^{\text{ep,st}}$
-

The tangent moduli is given by:

$$E^{\text{ep,st}} = \frac{\Delta \sigma_{n+1}^{\text{st}}}{\Delta \varepsilon_{n+1}^{\text{st}}} \quad (4.37)$$

4.2.4 Kinematic relation between rebars and concrete

Concrete and steel have been assigned an elastoplastic behavior. We now need to describe the kinematic relation between the two materials.

4.2.4.1 Procedure adopted

The choice adopted in the present paper is to connect steel to concrete by expressing explicitly the degrees of freedom of the rebars in terms of the degrees of freedom of concrete. In other words, the steel rebars are driven by the degrees of freedom of concrete and both global tangent stiffness matrices $[\mathbf{K}^{\text{ep,c}}]$ and $[\mathbf{K}^{\text{ep,st}}]$ of Equation (4.11) are expressed according to this kinematics.

As it will be described in Section 4.2.4.2, this method enables the description of rebars with any orientation in the 3D global axis system. Therefore, very complex reinforcements can be described by the model. Moreover, since the kinematics adopted for the model is the kinematics of concrete, we avoid unwanted bond-slip issues. It describes correctly the cohesion between rebars and concrete aggregates, assuming that any cracking or debonding

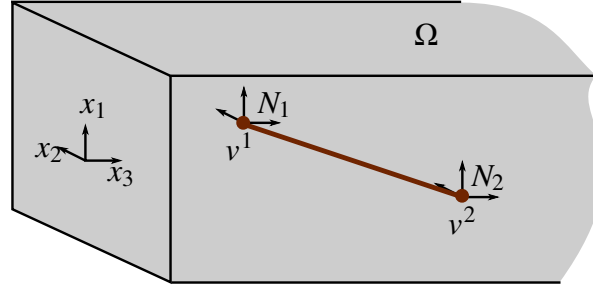


Figure 4.4 – Modeling of a steel rebar for its integration in the stiffness of the beam element

occur.

The computation of the global elastoplastic tangent stiffness matrix $[\mathbf{K}^{\text{ep}}]$ is given in Section 4.2.4.2, then the discretization of the rebars is described in Section 4.2.4.3.

4.2.4.2 Computation of the global tangent stiffness matrix

We consider a single bar defined by two nodes N_1 and N_2 into a concrete structure represented by its domain Ω as shown on Figure 4.4. The respective positions of the nodes are $\mathbf{x}^1 = (x_1^1, x_2^1, x_3^1)$ and $\mathbf{x}^2 = (x_1^2, x_2^2, x_3^2)$. Their respective displacement in the 3D space are $\mathbf{u}^1 = (u_1^1, u_2^1, u_3^1)$ and $\mathbf{u}^2 = (u_1^2, u_2^2, u_3^2)$, while their scalar displacement in the local coordinate system of the bar are v^1 and v^2 . The local tangent stiffness of the bar is:

$$\mathbf{k}^{\text{ep,st}} = \frac{E^{\text{ep,st}} S^{\text{st}}}{l_0^{\text{st}}} \begin{pmatrix} 1 & -1 \\ -1 & 1 \end{pmatrix} \quad (4.38)$$

where $E^{\text{ep,st}}$ is defined in Equation (4.37), and S^{st} is the section of the bar.

We need to define the kinematics of concrete in order to express the stiffness of the bar according to the degrees of freedom of concrete. We assume that a 3D displacement \mathbf{u} can be expressed in terms of the generalized displacement $\tilde{\mathbf{u}}$ as follows:

$$\mathbf{u}^1 = \mathbf{T}^1 \tilde{\mathbf{u}}, \text{ and } \mathbf{u}^2 = \mathbf{T}^2 \tilde{\mathbf{u}} \quad (4.39)$$

If n_{dof} is the number of degrees of freedom of the model, then the matrices $\mathbf{T}^1, \mathbf{T}^2 \in \mathbb{R}^{3 \times n_{\text{dof}}}$. \mathbf{T}^1 and \mathbf{T}^2 are the interpolation matrices at the respective positions \mathbf{x}^1 and \mathbf{x}^2 linking the 3D displacements of the nodes to the degrees of freedom of concrete.

The angles between the bar and the three axis of the global coordinate system are denoted by θ_1, θ_2 and θ_3 . Denoting $c^i = \cos \theta_i$, and $\boldsymbol{\theta} = (c^1, c^2, c^3)$, the scalar local displacements v^1 and v^2 can be expressed $v^1 = \boldsymbol{\theta} \mathbf{u}^1$ and $v^2 = \boldsymbol{\theta} \mathbf{u}^2$. Consequently, the tangent stiffness matrix of the rebar is:

$$[\mathbf{K}^{\text{ep,st}}] = {}^t \mathbf{A} \mathbf{k}^{\text{ep,st}} \mathbf{A}, \quad \text{with } \mathbf{A} = \begin{pmatrix} \boldsymbol{\theta} \mathbf{T}^1 \\ \boldsymbol{\theta} \mathbf{T}^2 \end{pmatrix} \quad (4.40)$$

4.2. Definition of an elastoplastic reinforced concrete model

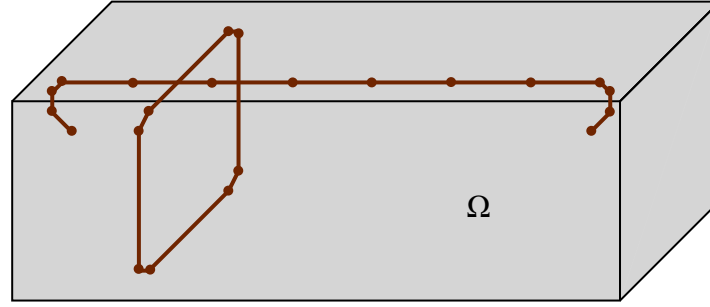


Figure 4.5 – Discretization of a longitudinal rebar and a transversal frame

Equation (4.40) is actually the application of Equation (4.13) on the 1D bar element.

4.2.4.3 Discretization of the rebars

The rebar are discretized in bar elements. This discretization is especially necessary for non straight rebars. The nodes numerically represent the structural embedding of steel in concrete. The total number of nodes of the rebar i is denoted by $n_{\text{node}}(i)$ where $i \in [1, n_{\text{rebar}}]$ and n_{rebar} is the total number of rebars. The rebar s_i is decomposed into $n_{\text{elem}}(i)$ bar elements. $n_{\text{elem}}(i)$ depends on the shape of the rebar:

$$n_{\text{elem}}(i) = \begin{cases} n_{\text{rebar}}(i) & \text{if the rebar is closed} \\ n_{\text{rebar}}(i) - 1 & \text{else} \end{cases} \quad (4.41)$$

This discretization is illustrated on Figure 4.5: a longitudinal rebar is discretized with $n_{\text{node}}(1) = 14$ nodes, forming 13 bar elements, and a transversal frame is discretized with $n_{\text{node}}(2) = 8$ nodes, forming 8 bar elements. The local integration presented in Algorithm 7 is computed on each bar element of each rebar.

According to the computation of the tangent stiffness matrix of steel described in Section 4.2.4.2, the global tangent stiffness matrix of Equation (4.11) can be decomposed on each bar element of each rebar:

$$[\mathbf{K}^{\text{ep}}] = [\mathbf{K}^{\text{ep,c}}] + \sum_{i=1}^{n_{\text{rebar}}} \sum_{j=1}^{n_{\text{elem}}(i)} [\mathbf{K}^{\text{ep,st}}]^{i,j} \quad (4.42)$$

It is important to note that the discretization of the rebars is totally independent from the discretization of the concrete volume. The local integrations of equilibrium equations of concrete and steel can therefore be processed in any order. A mesh sensitivity study is carried out in Section 4.4.5.

4.2.4.4 Global algorithm for the reinforced concrete model

The global algorithm of the present elastoplastic reinforced concrete model is presented in Algorithm 8.

Algorithm 8 Global algorithm for the elastoplastic reinforced concrete model

- 1: Initialize the state variables $S_0 = \{\mathbf{u}_0, \mathbf{u}_0^{\text{st}}, \boldsymbol{\varepsilon}_0, \boldsymbol{\varepsilon}_0^{\text{st}}, \dots\}$
 - 2: Initialize $\{\mathbf{F}^{\text{int}}\} = \mathbf{0}$
 - 3: **for** $n = 0$ to $M - 1$ **do**
 - 4: Initialize $\{\Delta\tilde{\mathbf{u}}\} = \{\mathbf{0}\}$
 - 5: Compute generalized residual force vector $\{\mathbf{R}\} = \{\mathbf{F}_{n+1}^{\text{int}}\} + \{\mathbf{F}_{n+1}^{\text{ext}}\}$
 - 6: $r^{\text{ref}} = \|\{\mathbf{R}\}\|$
 - 7: **while** $r > \epsilon r^{\text{ref}}$ **do**
 - 8: Compute the stiffness matrix $[\mathbf{K}^{\text{ep}}] = [\mathbf{K}^{\text{ep,c}}] + [\mathbf{K}^{\text{ep,st}}]$
 - 9: Solve $[\mathbf{K}^{\text{ep}}] \{\delta\tilde{\mathbf{u}}\} = \{\mathbf{R}\}$
 - 10: Update $\{\Delta\tilde{\mathbf{u}}\} = \{\Delta\tilde{\mathbf{u}}\} + \{\delta\tilde{\mathbf{u}}\}$
 - 11: Compute locally $\{\boldsymbol{\sigma}_{n+1}\}, \{\boldsymbol{\varepsilon}_{n+1}^{\text{p}}\}, \{p_{n+1}\}$ and $\mathbf{C}^{\text{ep}} \leftarrow$ **Algorithm 6**
 - 12: Compute locally $\{\boldsymbol{\sigma}_{n+1}^{\text{st}}\}, \{\boldsymbol{\varepsilon}_{n+1}^{\text{p,st}}\}, \{p_{n+1}^{\text{st}}\}$ and $\mathbf{C}^{\text{ep,st}} \leftarrow$ **Algorithm 7**
 - 13: Compute $\{\mathbf{F}^{\text{int}}\} = \{\mathbf{F}^{\text{int,c}}\} + \{\mathbf{F}^{\text{int,st}}\}$
 - 14: Update $\{\mathbf{R}\}$ and $r = \|\{\mathbf{R}\}\|$
 - 15: **end while**
 - 16: Update the 3D total displacement $\mathbf{u}_{n+1} = \mathbf{u}_n + \Delta\mathbf{u}$
 - 17: **end for**
-

4.3 Definition of a beam element

This section is a short reminder of the elastoplastic beam model introduced in **Chapter III**. The definition of the reinforced concrete model as defined in the previous section could actually be combined with any reduced or volumic model.

4.3.1 The AELD beam model

The present elastoplastic model for reinforced concrete has been presented for any kinematics or 3D finite elements. The kinematics is the link between the general displacement vector $\{\tilde{\mathbf{u}}\}$ and the 3D displacement vectors $\{\mathbf{u}\}$ and $\{\mathbf{u}^{\text{st}}\}$. So far, this relation has only been represented by the matrix \mathbf{T} in Equation (4.39). This section is dedicated to the short presentation of the kinematic model used for the case studies of Section 4.4.

This paper is based on the elastoplastic beam model developed by [Corre et al., 2017b] called

4.3. Definition of a beam element

the Asymptotic Expansion Load Decomposition (AELD) beam model. The elastic kinematics of the element is based on a higher-order elastic beam model using the asymptotic expansion method to extend its kinematics [Ferradi et al., 2016]. This model introduces new degrees of freedom associated to arbitrary loads as well as eigenstrains applied to the beam [Corre et al., 2017a]. In order to capture the effect of plasticity on the structure, this elastoplastic model considers the plastic strain as an eigenstrain imposed on the structure and new degrees of freedom are added on the fly into the kinematics during the incremental-iterative process.

This higher-order elastoplastic beam model has been initially developed with J_2 -plasticity. Its adaptation to the elastoplastic behaviors presented in Section 4.2.2 and 4.2.3 is straightforward. The main elements of this model are briefly recalled.

4.3.2 Description of the beam kinematics

The beam element represents the concrete matrix of the structure and the concrete kinematics drives the steel rebars. Therefore the elastoplastic boundary value problem and the elastoplastic framework considered here are those of concrete presented in Section 4.2.

We consider a beam occupying the prismatic domain Ω . Considering a point $(x_1, x_2, x_3) \in \Omega$, its 3D displacement \mathbf{u} can be expressed with the following expression:

$$\mathbf{u}(x_1, x_2, x_3) = \sum_i^n \hat{\mathbf{u}}^i(x_1, x_2) \sum_j^m N_j(x_3) \tilde{u}^{i,j} \quad (4.43)$$

where $\hat{\mathbf{u}}^i$ are displacement modes defining the kinematics, N_j are the longitudinal interpolation functions and $\tilde{u}^{i,j}$ are the generalized displacements. n and m are respectively the number of displacement modes and the number of interpolation functions.

The displacement modes $\hat{\mathbf{u}}^i$ are defined on the 2D cross-section of the beam. As described in Section 4.3.1, the displacement modes belong to 3 different categories of modes. Some modes only depends on the geometry of the cross-section. The participation of the loads applied on the structure is captured by other modes, specific to the forces or the eigenstrains considered. At last, some other modes capture the displacements due to the apparition of plasticity in the beam.

The computation of the modes specific to the geometry and to the forces applied is presented in [Ferradi et al., 2016]. [Corre et al., 2017a] presents the modes specific to eigenstrains while the computation of modes for plasticity are developed in [Corre et al., 2017b]. For boundary conditions different from clamped extremities (including linear or surfacic supports) additional modes specific to the boundary conditions considered are also added in the collection of modes. The boundary conditions are imposed by considering the supports as external forces imposed on the structure. New degrees of freedom associated to the supports are introduced. The

method is presented in [STRAINS, 2016].

4.3.3 Numerical approximation

The modes are computed on a transversal mesh of the cross-section \mathcal{S} . The discretization used is the same as the one used in [Corre et al., 2017a] and [Corre et al., 2017b]: the modes are computed by using finite elements. The finite elements chosen are triangles, their interpolation is quadratic. Strain and stress are computed and integrated at the 3 Gauss points of each triangle element, and the modes of displacement are computed on the nodes of the transversal mesh. We use NURBS basis functions for the longitudinal interpolations. The reasons motivating this choice are explained in [Corre et al., 2017a]. We also define a set of N_s longitudinal integration points for the integration of these interpolation functions.

4.3.4 Local integration of the equilibrium equations

Equation (4.8) must be integrated over the 3D volume of the structure. A 3D discretization of the structure is therefore necessary. This 3D discretization is based on the transversal and longitudinal meshes already defined: the local equations are integrated on a set of cross-sections all transversally discretized with the cross-sectional mesh described previously and placed at the longitudinal positions of the N_s longitudinal integration points. Assuming a generalized displacement increment $\Delta\tilde{u}$, the corresponding 3D strain increment $\Delta\boldsymbol{\varepsilon}$ is computed on the Gauss points of each one of the N_s cross-sections. This way, the beam is decomposed into sections where the local equations are integrated and the states variables are computed. We naturally choose to place these sections at the positions of the longitudinal integration points of the interpolation functions. We ensure that N_s is greater than m .

4.4 Validation of the model

This section suggests a procedure in order to validate the reinforced concrete beam model presented in the two previous sections. A reinforced T-beam is first submitted to a load case in elasticity in order to validate the connection between concrete and rebars. The model is then submitted to an elastoplastic load case, a classic Von-Mises criterion being considered. The results provided by the beam solutions are compared to a volumic reference solution in both cases. This second step validates the elastoplastic beam algorithm. Finally, the yield criterion designed in Section 4.2 is implemented and results are commented.

The model has been described in the previous sections with a new model for concrete. The Rankine's criterion being not implemented in 3D in classic finite softwares (*Code_Aster*, *Abaqus*), a comparison of a solution using the present model with a reference solution using a

4.4. Validation of the model

different yield criterion would not be relevant. Therefore we suggest to validate and evaluate our model with a step-by-step procedure. First, the model is tested on a case study in elasticity and evaluated by a comparison with a reference solution. This first step validates the inclusion of the rebars in the model presented in Section 4.2.4. Then, the global elastoplastic element is validated by using a Von-Mises criterion for both concrete and steel. This widely used criterion affords an easy comparison with a solution computed on another finite element software. The local integration algorithm used is the classic radial return algorithm. Finally, the Von-Mises criterion and the radial return algorithm are replaced by the Rankine criterion and the local algorithm respectively defined in Sections 4.2.2.2 and 4.2.2.3.

4.4.1 Reinforced T-beam in elasticity

In order to validate the integration of rebars in the elastoplastic model, a first case study is conducted in linear elasticity. The results are compared with a 3D reference model computed on the finite element software *Code_Aster*.

4.4.1.1 Description of the case study

We consider a 10 m-long T-beam simply supported at each end. The section of the T-beam studied is presented on Figure 4.6. The load is applied over the entire width of the table, between the longitudinal positions $x_3 = 4.5$ m and $x_3 = 5.5$ m as shown on Figure 4.7.

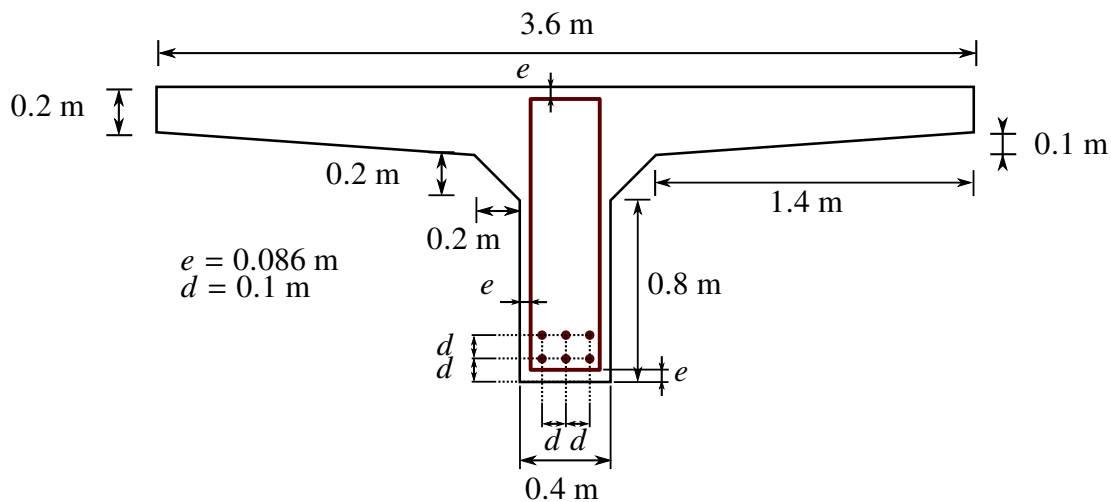


Figure 4.6 – Geometry of the T-beam section

The beam is reinforced with steel rebars. The cross-sectional reinforcement is presented on Figure ???. The beam is reinforced with 2×3 longitudinal rebars and 11 frames between $x_3 = 0$ and $x_3 = L$. The boundary conditions and the longitudinal reinforcement are shown on Figure 4.9. The left support is applied on the entire width of the cross-section and between

Higher-order elastoplastic beam model for reinforced concrete

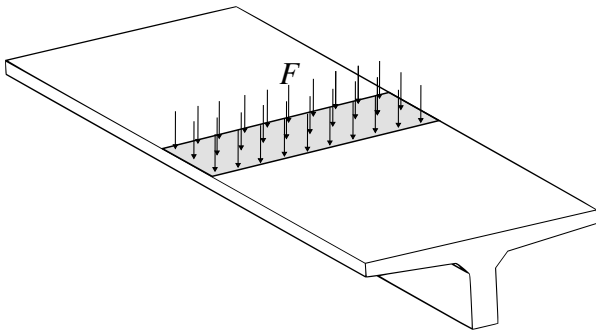


Figure 4.7 – 3D description of the beam and its load

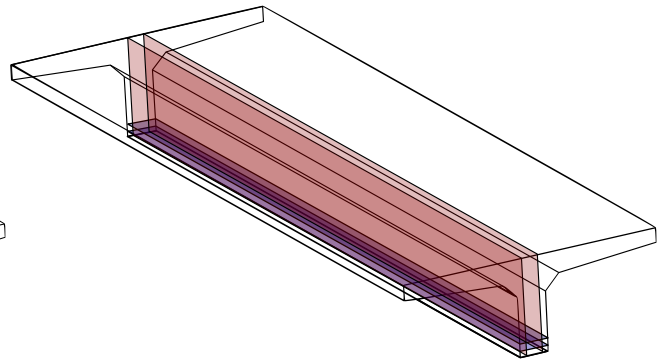


Figure 4.8 – Surfaces modeling the rebars in the reference solution

$x_3 = 0$ m and $x_3 = 0.1$ m where it freezes the three translations. The right support is applied on the entire width of the cross-section between $x_3 = 9.9$ m and $x_3 = 10$ m where it freezes the cross-sectional translations.

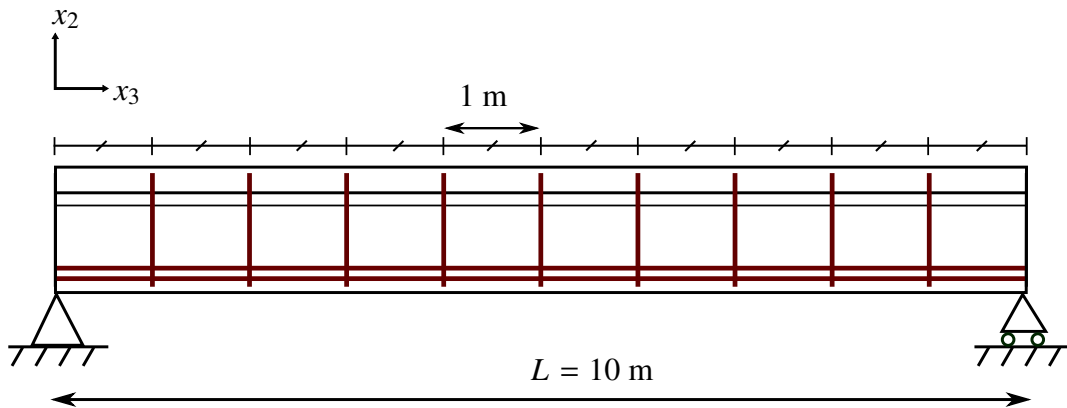


Figure 4.9 – Boundary conditions and longitudinal reinforcement

	Young modulus	Poisson's ratio
concrete	20 GPa	0.2
steel	200 GPa	-

Table 4.1 – Material properties of the T-beam

The materials property of the beam are gathered in Table 4.1. The diameters of the longitudinal rebars and the frames are respectively 16 mm and 10 mm. All the distances indicated on Figure 4.6 are given according to the central axis of the rebars.

The beam is loaded by a force $F = S \times P$ with $S = 3.6$ m² and $P = 50$ kN. The load is described on Figure 4.7.

4.4. Validation of the model

4.4.1.2 Reference solution

The reference solution is computed with the finite element software *Code_Aster*. The concrete is modeled with 3D elements. The elements used here are tetrahedron with quadratic interpolation and 10 Gauss points (TETRA10).

The rebars are represented as uniaxial grid, and modeled with anisotropic membrane elements [De Soza, 2015]. The membranes are defined by surfaces based on the 3D mesh and are consequently meshed with triangles. The 2D interpolation of the triangles is also quadratic (T6 elements). Gauss points are added in the triangles for the integration of the steel behavior. The considered surfaces are defined on Figure 4.31.

The longitudinal rebars are modeled with two horizontal membranes represented in blue on Figure 4.31 and the frames are modeled with two vertical membranes represented in red. Each membrane is characterized by a section per unit length (in m^2/m) and by the orientation of the rebars.

The mesh characteristics for the reference solution are presented in Table 4.2.

	concrete	longitudinal rebars	frames
Reference solution	146067 TETRA10	2136 T6	8908 T6
Beam solution	477 T6 \times 81	21 1D bars	12 1D bars

Table 4.2 – Mesh characteristics for the reference solution

4.4.1.3 The beam solution

One only cross-sectional mesh is used in the beam model as explained in Section 4.2.4.3. For the present case study, the cross-section of the T-beam is meshed with 477 quadratic triangles. The mesh is shown on Figure 4.10.

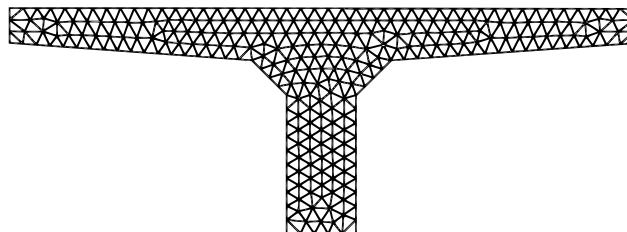


Figure 4.10 – Cross-sectional mesh of the T-beam for the beam solution

The longitudinal interpolation functions are third-order NURBS and are defined by 21 knots evenly distributed along the longitudinal axis of the beam. The element is locally integrated on 81 integration section also evenly distributed along its axis. The kinematics of the element

is composed of 28 displacement modes: 12 specific to the geometry, 6 modes specific to the load applied and 10 modes specific to the boundary conditions.

The longitudinal rebars and the frames are respectively discretized with 21 and 12 bars.

4.4.1.4 Results

Once the problem solved, the 3D displacement of the beam solution can be easily assembled according to Equation 4.43. The norm of the 3D displacement computed by the beam solution and the reference solution are compared on Figure 4.11 (the same scale is adopted for both deformed structures and the magnification factor is 500).

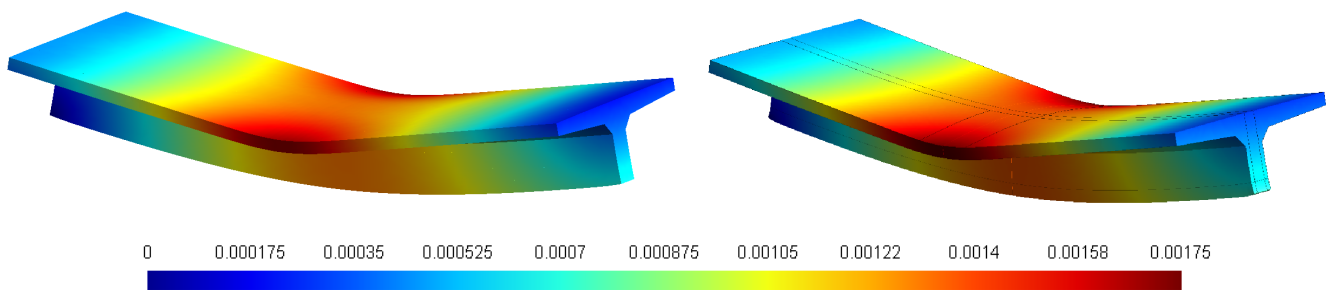


Figure 4.11 – Deformed shape computed by the beam solution (left) and by the reference solution (right) in elasticity

Beyond the consistency of the two solutions, the ability of the beam solution to capture cross-sectional displacements can be here underlined. Indeed, the lowering of the wings of the T-beam is well described by the beam model thanks to its higher-order kinematics.

An interesting asset of the solution adopted for the modelling of the rebars in the beam element is that it yields a 3D viewing of the rebar displacements as shown on Figure 4.12

In order to better estimate the validity of the beam solution, the displacement and stress of the rebars computed by each solution are compared on Figures 4.13 and 4.14. The rebars being not individually modeled in the 3D model, we use results computed by the reference solution at the positions corresponding to the rebars defined in Figures 4.6 and 4.9.

On Figure 4.13, the vertical displacement of two rebars (denominated by ST_0 and ST_1) are presented according to the longitudinal position. The beam solution shows consistent results when compared to the reference solution. The values computed by the beam solution are slightly higher in absolute value: a maximum relative distance of 2.1% and 2.2% is respectively observed for ST_0 and ST_1. This gap could be reduced by a finer discretization of the rebars.

4.4. Validation of the model

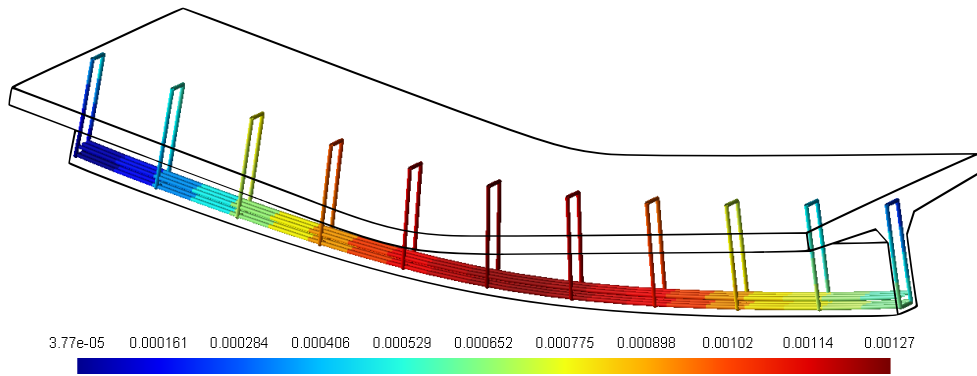


Figure 4.12 – 3D viewing of the displacement of the rebars (absolute displacement in meters)

The axial stress of ST_0 and ST_1 are presented on Figure 4.14. The beam solution matches with the reference solution: the relative distance between the two solutions at mid-span of the beam ($x_3 = 5$ m) are respectively 1.7% and 1.6% for ST_0 and ST_1. The stress computed by the reference solutions shows oscillations close to the supports. These numerical effects are regularized by the beam model.

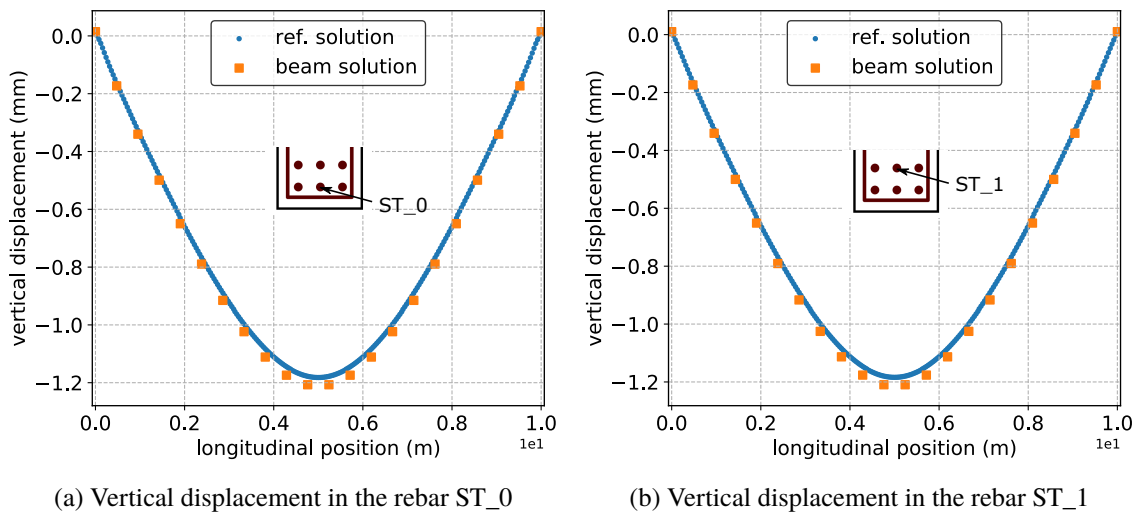


Figure 4.13 – Vertical displacement computed by the beam model in the rebars ST_0 and ST_1 and by the reference model at the corresponding positions

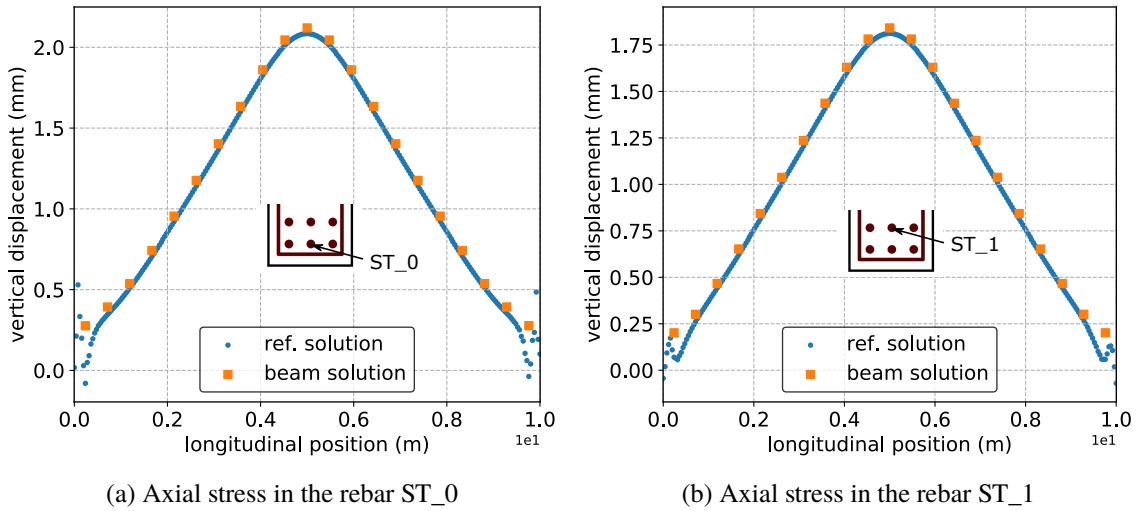


Figure 4.14 – Axial stress computed by the beam model in the rebars ST_0 and ST_1 and by the reference model at the corresponding positions

Finally, the components of the concrete stress computed by the two solutions at mid-span of the beam ($x_3 = 5$ m) are compared. Only the axial components and σ_{12} are presented in Figure 4.15, the shear stresses σ_{13} and σ_{23} being zero by symmetry.

4.4.2 Reinforced T-beam in elastoplasticity

Section 4.4.1 has proven the validity of the present reinforced concrete model in elasticity. Following the procedure defined previously, the model is now studied in elastoplasticity with a Von-Mises criterion for both concrete and steel.

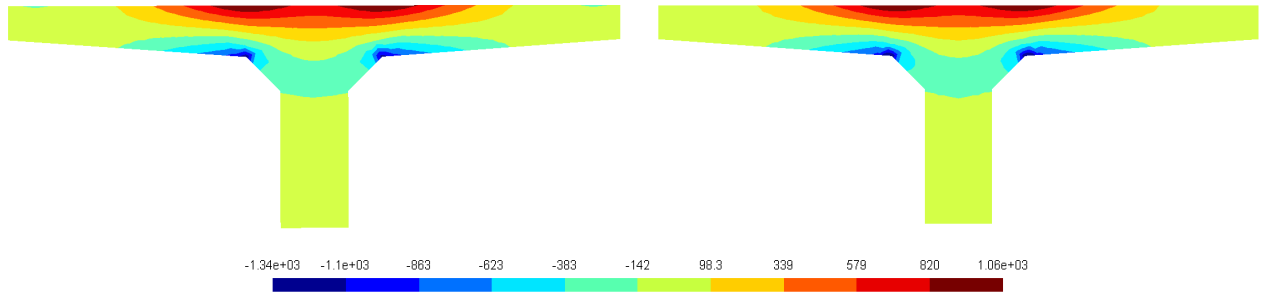
4.4.2.1 Description of the case study

The case study is the same as the one described in Section 4.4.1.1. Only the material properties are changed and presented in Table 4.3. A Von-Mises criterion and an isotropic hardening is adopted for both steel and concrete. The dimensions of the rebars are unchanged.

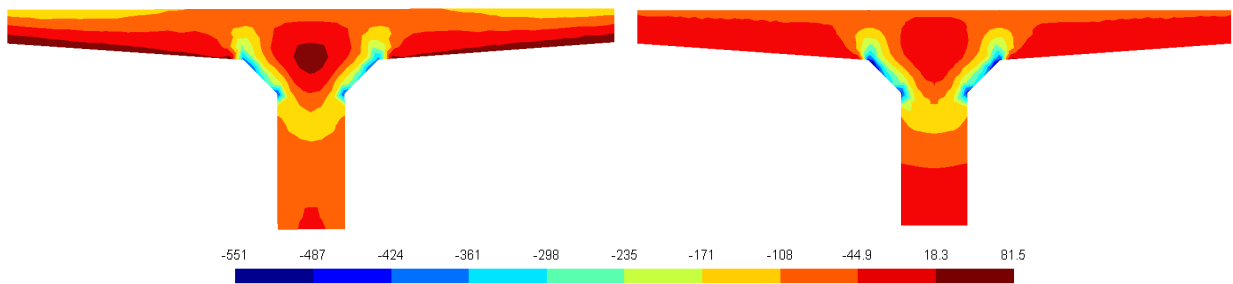
	Young Modulus	Poisson's ratio	Yield stress	Plastic modulus
concrete	20 GPa	0.2	10 MPa	2 GPa
steel	200 GPa	-	300 MPa	20 GPa

Table 4.3 – Material properties of the elastoplastic T-beam

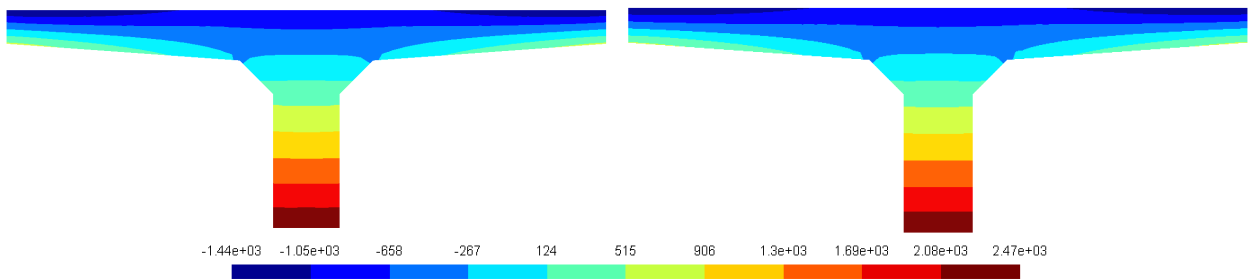
4.4. Validation of the model



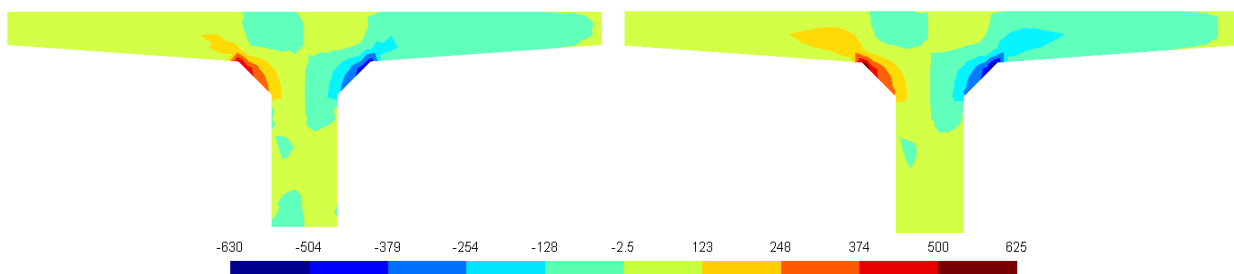
(a) σ_{11} computed by the beam solution (left) and by the reference solution (right) in kPa



(b) σ_{22} computed by the beam solution (left) and by the reference solution (right) in kPa



(c) σ_{33} computed by the beam solution (left) and by the reference solution (right) in kPa



(d) σ_{12} computed by the beam solution (left) and by the reference solution (right) in kPa

Figure 4.15 – Stress computed at mid-span of the beam ($x_3 = 5$ m) by the beam solution and the reference solution

The beam is loaded by a force $F(t) = S \times P(t)$ with $S = 3.6 \text{ m}^2$. P takes values between 0 and 700 kPa. The load is discretized into 5 increments between 0 and 500 kPa and into 10 increments between 500 kPa and 700 kPa.

4.4.2.2 Results

During this case study, the yield stress of concrete and the yield stress of the rebars are successively reached. This test provides therefore a good assessment of the accuracy of the elastoplastic beam element presented here. The deformed shapes computed by the two solutions are first compared on Figure 4.16 (the magnification ratio is 20). As for the elastic case the beam solution describes correctly the lowering of the wings of the T-beam.

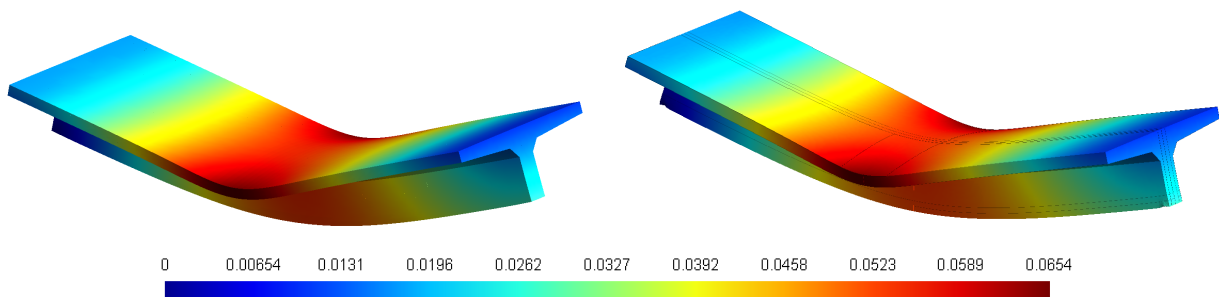


Figure 4.16 – Deformed shape computed by the beam solution (left) and by the reference solution (right) in Von-Mises elastoplasticity (in meters)

In order to best evaluate the elastoplastic response of the structure computed by the beam solution, the vertical displacement of the rebars ST_0 and ST_1 are presented on Figure 4.13. The response of both rebars matches very well with the reference solution. A maximum relative distance of $7.5 \cdot 10^{-3}$ and $7.1 \cdot 10^{-3}$ is respectively observed for ST_0 and ST_1 between the two solutions.

The maximum vertical displacement at mid-span of the beam is represented according to the load applied on Figure 4.18. This displacement corresponds to the point located at the middle bottom of the section. As shown on the figure, the nonlinearity of the elastoplastic behavior is well captured by the beam element. The yield stress of concrete is reached after the second increment while the yield stress of steel is reached after the fourth. At the last increment, the beam solution shows a displacement 1.83% larger than the reference solution. This is consistent with the fact that the beam element appears to be slightly less stiff than the reference solution (see Figures 4.13 and 4.17). We would normally have expected a stiffer response of the beam solution. The explanation must be found in the modelling adopted for the rebars since the modellings of the reference and beam solutions are neither fully satisfactory nor equivalent.

The stress in rebar ST_0 at $x_3 = 5 \text{ m}$ is shown on Figure 4.19. Three stages are easily

4.4. Validation of the model

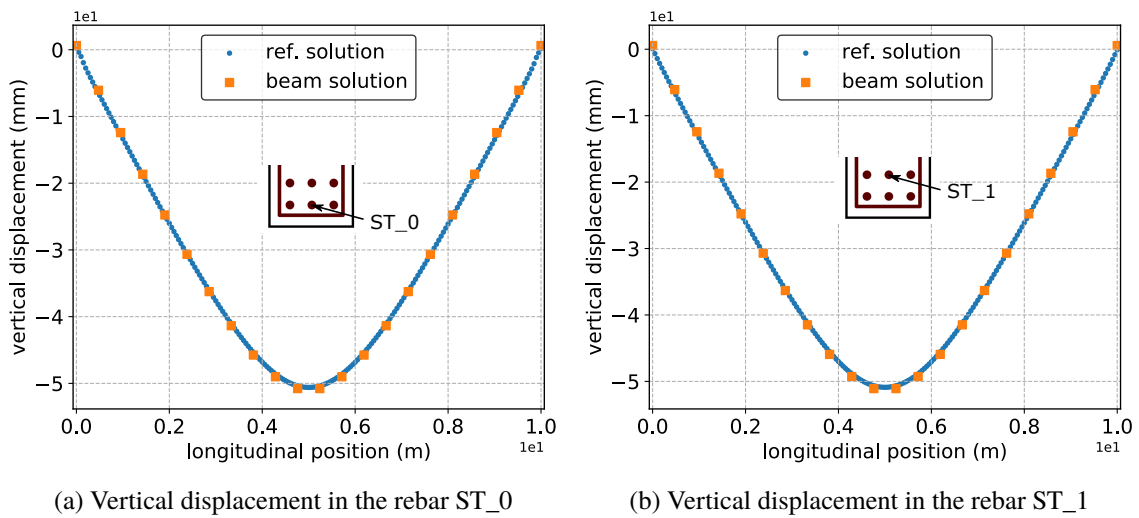


Figure 4.17 – Vertical displacement computed by the beam model in the rebars ST_0 and ST_1 and by the reference model at the corresponding positions at the last increment

identifiable. The two materials are first elastic and the stress progresses linearly in the rebar. Once concrete has reached plastification, the stress increases faster until the yield stress of steel is reached. The stress then progressed beyond the yield stress according to the plastic modulus. Since the ratio between the Young modulus of steel and concrete is 10 and the concrete yield stress is 10 MPa, the concrete yield stress is reached when the stress is 100 MPa in steel. The yield stress of each material is numerically reached between two increments as shown on Figure 4.19. A better time discretization should make the three different stages even more distinct.

As long as the rebars are elastic, the relative distance between the two solutions is about 10^{-2} . Once the steel yield stress is reached a relative distance of $2.5 \cdot 10^{-2}$ is observed. This gap could be reduced by a finer discretization of the rebars.

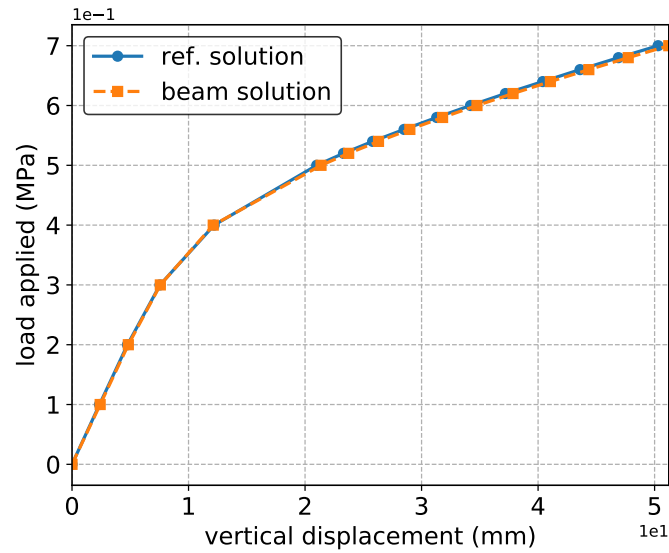


Figure 4.18 – Maximum vertical displacement at mid-span of the beam ($x_3 = 5$ m)

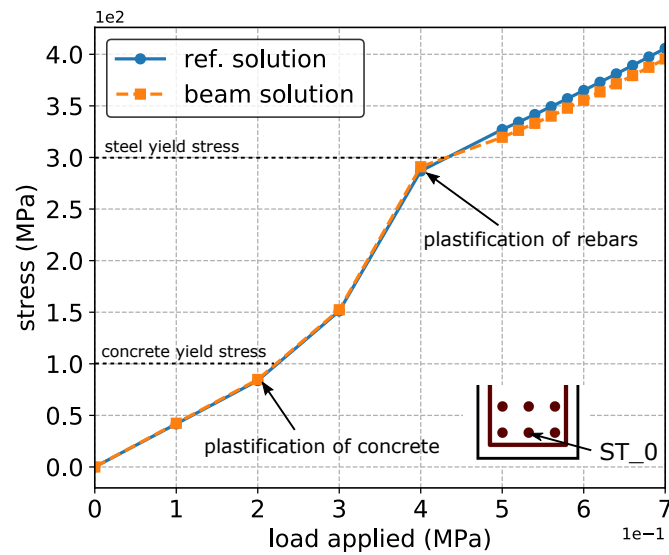
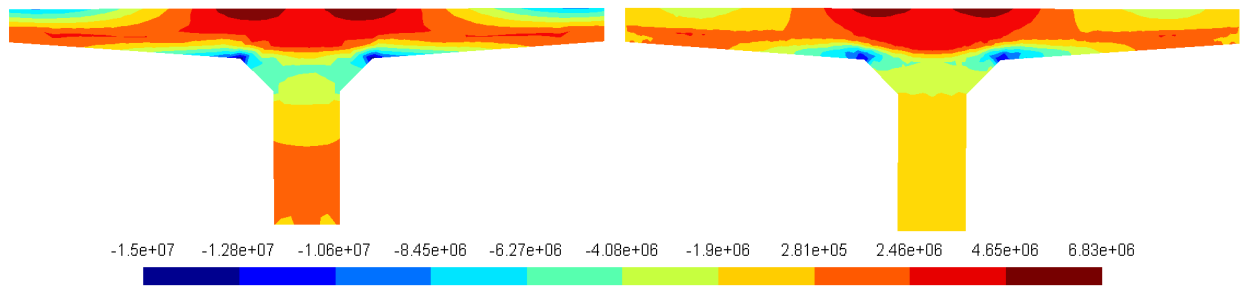
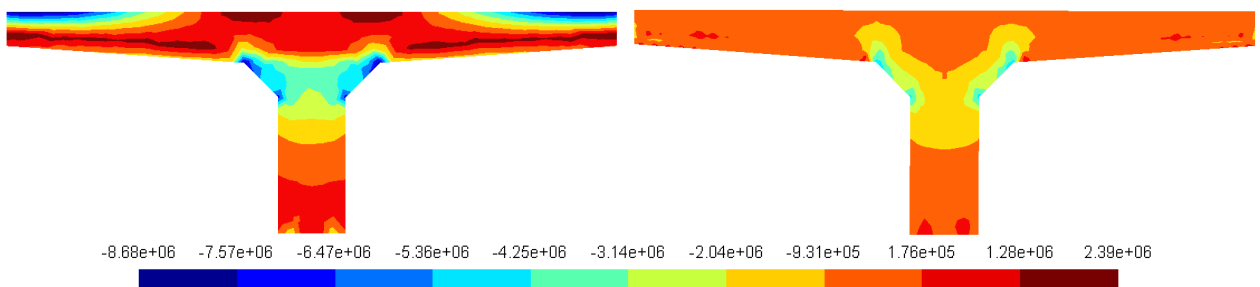


Figure 4.19 – Stress in ST_0 at $x_3 = 5$ m according to the load applied

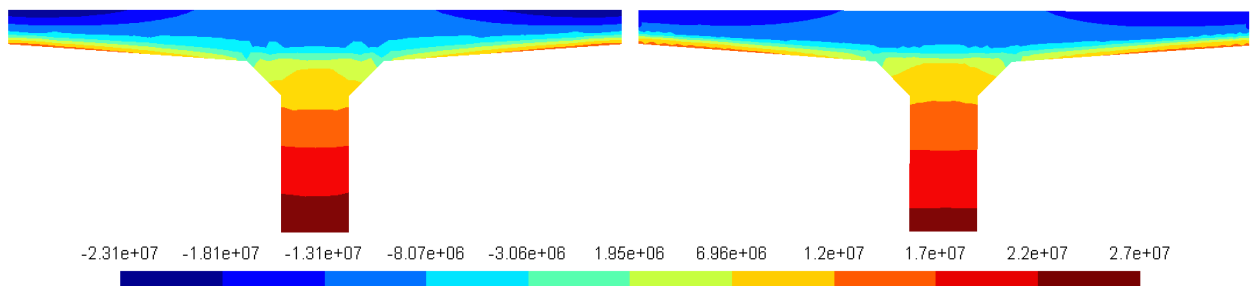
4.4. Validation of the model



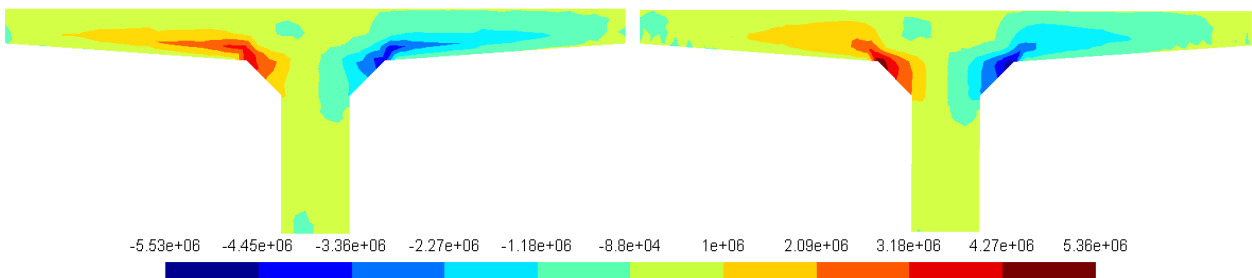
(a) σ_{11} computed by the beam solution (left) and by the reference solution (right) in Pa



(b) σ_{22} computed by the beam solution (left) and by the reference solution (right) in Pa



(c) σ_{33} computed by the beam solution (left) and by the reference solution (right) in Pa



(d) σ_{12} computed by the beam solution (left) and by the reference solution (right) in Pa

Figure 4.20 – Stress computed at mid-span of the beam ($x_3 = 5$ m) by the beam solution and the reference solution

Finally, the stresses at mid-span of the beam are presented in Figure 4.20 at the last increment. The normal stress σ_{33} is the highest stress in value and the best described by the beam solution when compared to the 3D model. The axial stress σ_{22} is the less satisfactory, but it is consistent with the observation made in elasticity in Figure 4.15.

4.4.3 Reinforced beam with the new concrete model

The numerical behavior of the present reinforced concrete elastoplastic beam element has been validated by the two previous sections. The new concrete model presented in Section 4.2.2 is now used instead of the Von-Mises criterion. The local radial return algorithm is therefore replaced by the local projection algorithm described in Section 4.2.

4.4.3.1 Description of the case study

We consider a rectangular beam for the present case study: the cross-section of the beam is a rectangle of dimensions $0.4 \text{ m} \times 1.3 \text{ m}$. The beam is still 10 m long but is now clamped at both ends. As a consequence the reinforcement is modified. The cross-sectional reinforcement of the section is presented on Figure 4.21: 3 longitudinal rebars are placed at the bottom of the section along the complete length of the beam while 3 rebars are placed at the top of the section between $x_3 = 0 \text{ m}$ and $x_3 = 3.5 \text{ m}$ and their symmetric counterparts are placed between $x_3 = 6.5 \text{ m}$ and $x_3 = 10 \text{ m}$. This reinforcement is motivated by the sign shift of the bending moment. The longitudinal description of the reinforcement and the load applied on the structure are shown on Figure 4.22.

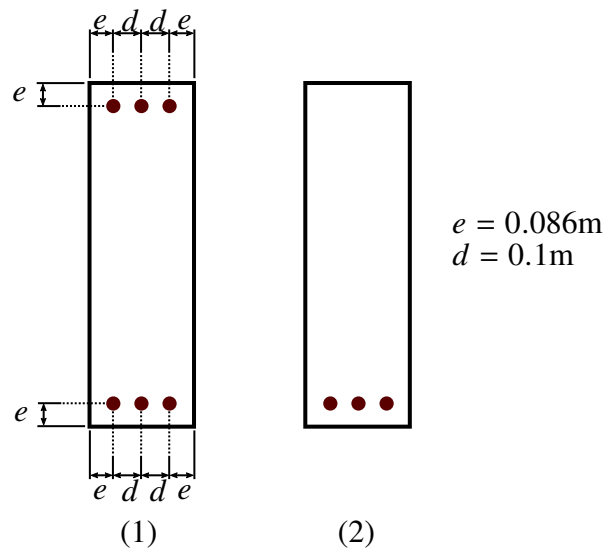


Figure 4.21 – Cross-sectional reinforcement for $x_3 \in [0, 3.5] \cup [6.5, 10]$ (1) and $x_3 \in [3.5, 6.5]$ (2)

4.4. Validation of the model

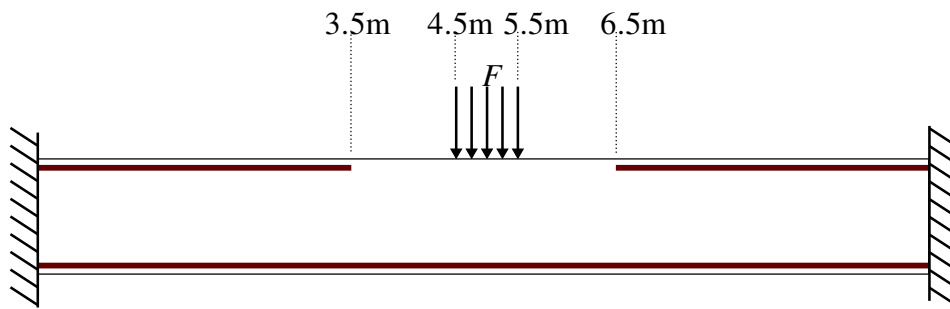


Figure 4.22 – Longitudinal reinforcement and boundary conditions

The material properties of the reinforced beam are presented in Table 4.4.

	Young Modulus	Poisson's ratio	Plastic modulus
concrete	20 GPa	0.2	2 Pa
steel	200 GPa	-	2 GPa

Table 4.4 – Material properties of the rectangular beam

The plastic modulus of concrete is intentionally very low. The plastic modulus of steel has been chosen lower than actual values in order to emphasize the nonlinearity of the global response of the structure. As explained in Section 4.2.2, an isotropic hardening is used only to avoid potential localization problems. The tension strength of concrete is $f_t = 2\text{MPa}$ and its compression resistance is $f_c = 40\text{MPa}$. The rebars still follow a Von-Mises criterion with an isotropic hardening and their yield stress is 300 MPa.

The load is decomposed into 30 equivalent increments of $F_t = 0.1\text{MPa}$. The final load is therefore $F_{30} = 3\text{MPa}$.

4.4.3.2 The beam solution

The cross-section is meshed with 102 quadratic triangular elements. As for the previous case study, the interpolation functions are third-order NURBS defined by 21 knots evenly distributed along the beam axis. The local integration is processed on 81 integration sections also evenly distributed along the longitudinal axis. The kinematics is composed of 18 displacement modes: 12 modes specific to the geometry and 6 modes specific to the load applied.

4.4.3.3 Results

The maximum vertical displacement (corresponding to the point located at the middle bottom of the mid-span section) is presented on Figure 4.23. The successive plastification of concrete

and steel are identified during the computation and indicated on the figure. Three stages can be distinguished:

1. Concrete and steel are elastic
2. Concrete is plastic and steel is elastic
3. Concrete and steel are plastic

The stage before the plastification of concrete is short but can be identified on the figure. Once concrete has reached f_t , the loads are transmitted to the clamped end mainly by the rebars. The global stiffness of the structure is reduced and the displacement increases faster. This increase is then amplified by the plastification of the rebars.

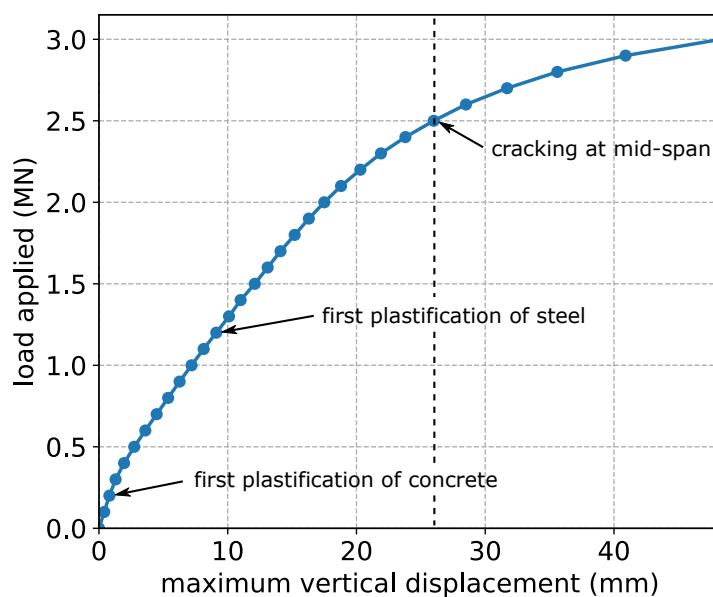


Figure 4.23 – Maximum vertical displacement computed by the beam model

On Figure 4.24 is shown the stress computed in the rebar ST_3 (defined on the figure) as function of the load applied on the beam. The stress represented is computed close to the clamped end ($x_3 = 0.25$ m) where plastification first occurs. The three stages listed above are clearly illustrated. Both materials are elastic until the yield stress of concrete is reached. Since the ratio between the respective Young modulus of steel and concrete is 10 and because the traction resistance of concrete is 2 GPa, stress in steel is 20 GPa when f_t is reached in concrete. Once concrete has plastified, the rebar remains elastic but concrete no longer participates in the load transmission, leading to a new linear stage with a more important increase of the steel stress. Eventually the stress in the rebar reaches the yield stress (300 MPa). The evolution of the stress is then limited due to the low plastic modulus adopted.

Figure 4.24 shows a satisfactory local reponse of the element. The global reponse of the structure to the load applied is illustrated on Figures 4.25 and 4.26. The principal stress of

4.4. Validation of the model

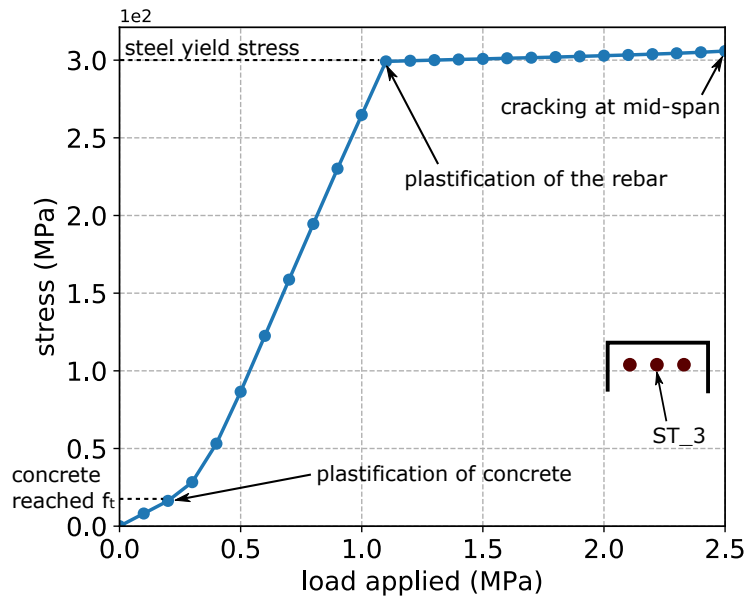


Figure 4.24 – Stress in the rebar ST_3 closed to the clamped extremity ($x_3 = 0.25$ m)

concrete are computed in the whole element, and the compression eigenvalue (the lowest eigenvalue) is represented on Figure 4.25 and the traction eigenvalue (the highest eigenvalue) is represented on Figure 4.26. Both figures show the same sidewall of the beam at the 6 successive time steps $\{t_5, t_{10}, t_{15}, t_{20}, t_{25}, t_{30}\}$.

The minimum eigenvalues of the 6 time steps take values between -41 MPa and 1 MPa, describing the distribution of compression stresses in the structure. The chosen lower bound is smaller than the compression resistance f_c because of the small isotropic hardening adopted. The principal stresses are obtained by post-processing the general stress. This step can lead to positive compression eigenvalues, explaining the higher bound of 1 MPa. The 6 successive time steps describe clearly the development of two struts in the structure from the load application to the extremities. The compression limit is first reached at the clamped end at t_{15} and then at the load application area at t_{20} . The compression plastified area (in blue) then expands and the compression increases in the two struts.

This load transmission was expected and highlights the ability of the present beam model to represent 3D phenomenon out of its longitudinal axis.

The maximum eigenvalues take values between -0.2 MPa and 2.2 MPa, describing the distribution of tensile stresses in the structure. The scale is slightly extended in traction and compression for the reasons mentioned above. The traction limit f_t is reached as of time step t_5 . This is consistent with Figures 4.23 and 4.24 where the plastification of concrete seems to occur at t_2 . The three expected areas in traction are distinctly described. These traction

eigenvalues are complementary and consistent with compression eigenvalues observed on Figure 4.25. The empty areas are due to eigenvalues out of scale. Finally the normal stress

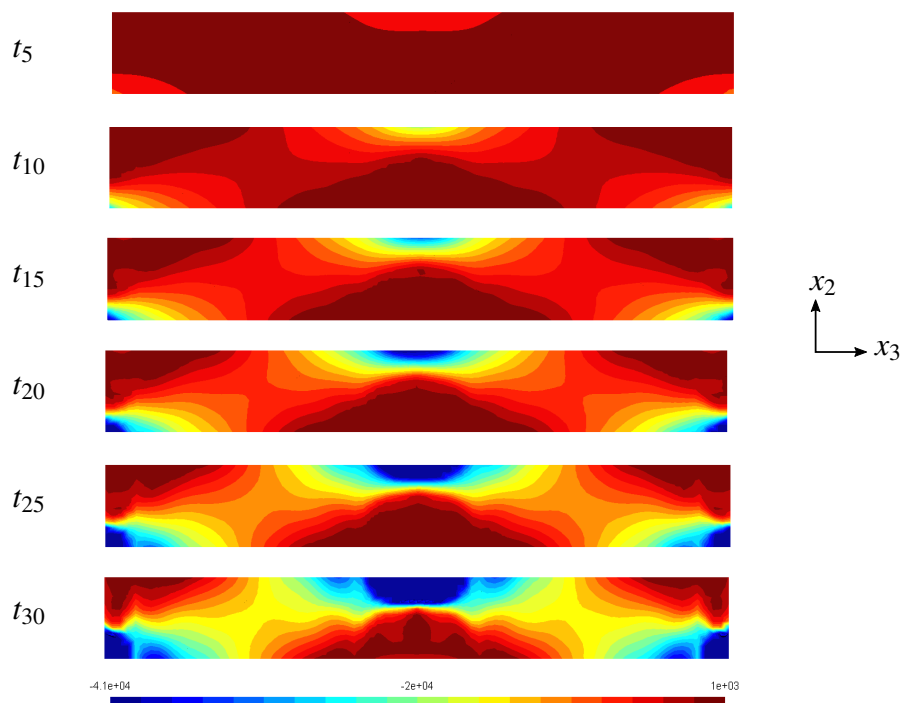


Figure 4.25 – Evolution of the minimum eigenvalues in the beam (in kPa)

computed at mid-span of the beam ($x_3 = 5$ m) is presented on Figure 4.27. The same 6 time steps are considered. The scale is $[-42$ MPa, 2.2 MPa]. On this figure, the equilibrium between traction and compression is progressively setting up. The lower half of the section reaches traction limit as of time step t_5 . Compression then gradually expands in the upper half until the equilibrium is reached at t_{30} .

By showing the expected reponse of the structure, this case study has confirmed the efficiency of the present reinforced concrete elastoplastic beam model. Figures 4.25 and 4.26 demonstrate that the introduction of our new concrete model leads to a relevant 3D global response of the beam. Moreover, it shows the great ability of this beam element to describe 3D phenomenon such as the formation of the struts exhibited here.

4.4.4 Validity of the elastoplastic model

The main disadvantage of an elastoplastic approach is the infinite energy it can dissipate after yield stress has been reached. Concrete is known to be a brittle material in tension and it

4.4. Validation of the model

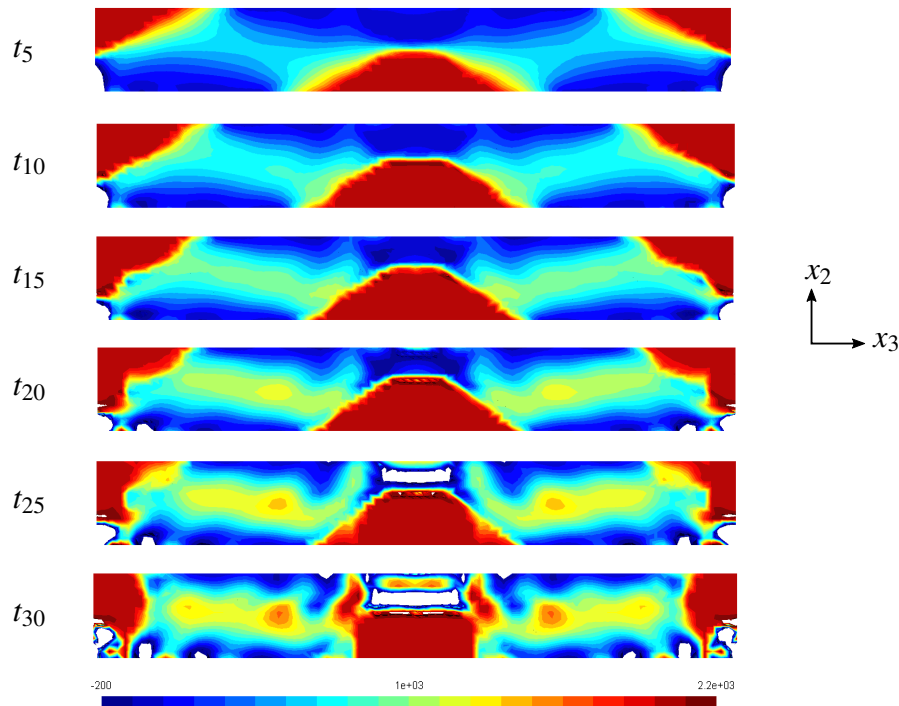


Figure 4.26 – Evolution of the maximum eigenvalues in the beam (in kPa)

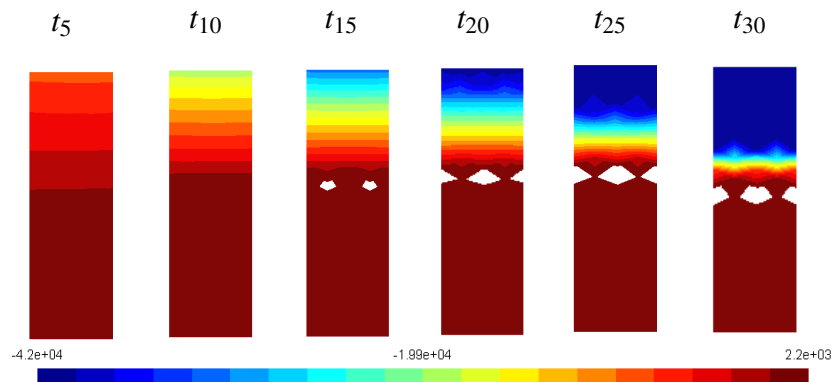


Figure 4.27 – Evolution of the normal stress σ_{33} in the mid-span cross-section ($x_3 = 5$ m)

cannot sustain high strains. Based on the results presented in the previous section, we suggest a fracture mechanics approach. Considering the traction eigenvalues presented on Figure 4.26, we identify on Figure 4.28 the concrete volume V_{crack} in traction under the load application as the area most likely to suffer from cracking. The energy needed to open a vertical crack in the middle of this area is compared to the energy dissipated in V_{crack} .

Based on Figure 4.27, we consider a crack opening of width $b = 0.4$ m and height $h = 0.8$ m (approximately 60% of the height of the cross-section). The energy needed to open this crack

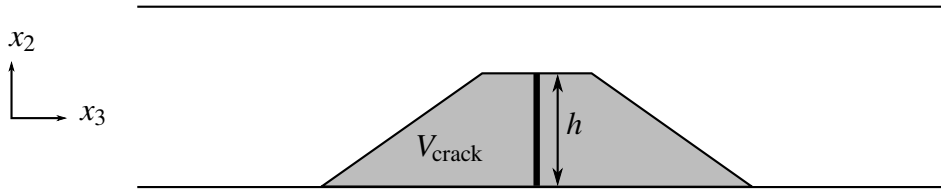


Figure 4.28 – Definition of the potential cracked area

is thus:

$$E_{\text{crack}} = G_f \times b \times h \quad (4.44)$$

where G_f is the fracture energy. According to the norm CEB-FIP [Comité Euro International du Béton, 1993], G_f is defined as follows:

$$G_f = G_{f_0} \left(\frac{f_c}{10} \right)^{0.7} . \quad (4.45)$$

G_{f_0} is a reference fracture energy based on the size of the aggregates in concrete. Considering an average size of 20 mm, $G_{f_0} = 36 \text{ N.m/m}^2$ and Equation (4.44) yields:

$$E_{\text{crack}} = 30.4 \text{ N.m} \quad (4.46)$$

This energy must be compared to the energy dissipated in V_{crack} defined by:

$$E_{\text{diss}}(t) = \int_0^t \int_{V_{\text{crack}}} \boldsymbol{\sigma}(\tau) : \dot{\boldsymbol{\varepsilon}}^P(\tau) dV d\tau \quad (4.47)$$

The time-discretization of Equation 4.47 then yields:

$$E_{\text{diss}}(t_n) = \sum_{k=1}^n \left[\int_{V_{\text{crack}}} \boldsymbol{\sigma}_n : \Delta \boldsymbol{\varepsilon}_n^P dV \right] . \quad (4.48)$$

The computed dissipated energy is presented on Figure 4.29. As long as concrete is elastic, no energy is dissipated since $\boldsymbol{\varepsilon}^P = 0$. Once concrete stress reaches f_i , the energy increases linearly, reflecting a linear evolution of the plastic strain increments (by neglecting the hardening of concrete, the stress can be considered as constant). The energy drastically increases as soon as plastification in the rebars is too important. The energy needed to open the crack is reached at t_{25} .

4.4. Validation of the model

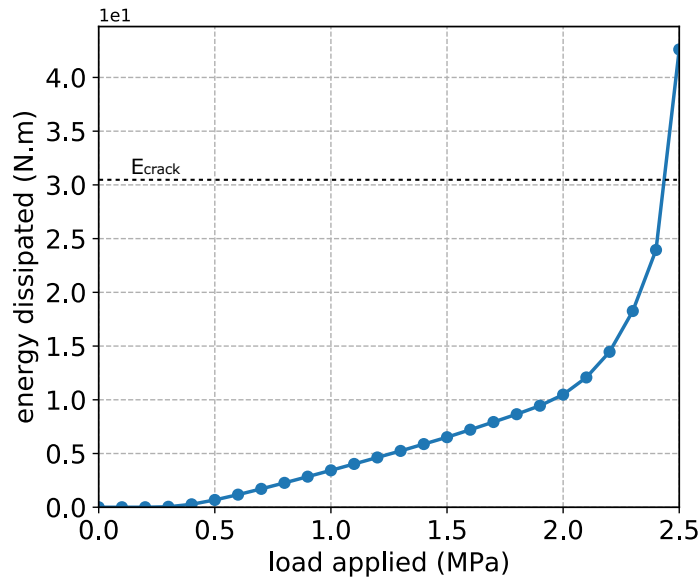


Figure 4.29 – Energy dissipated in V_{crack} according to the load applied

Time step t_{25} corresponding to the crack opening at mid-span of the beam has been indicated on Figures 4.23 and 4.24. All the time steps subsequent to t_{25} can therefore be considered not valid. This fracture mechanics approach has notably been used in [Radfar, 2013] for the study of peeling off in a reinforced concrete beam submitted to three points bending.

4.4.5 Mesh sensitivity

4.4.5.1 Case study

The beam element and the rebars have different and independent meshes, as mentioned in Section 4.2.4.3. This section is dedicated to the study of its mesh sensitivity. To this purpose, we consider the beam represented on Figure 4.30 with the I-section presented on Figure 4.31. This example is taken from the validation document [Flejou, 2011] of the documentation of the finite element software *Code_Aster*.

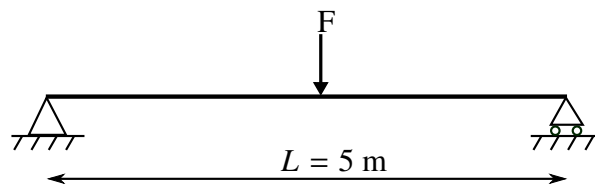


Figure 4.30 – 5 m beam loaded at mid-span

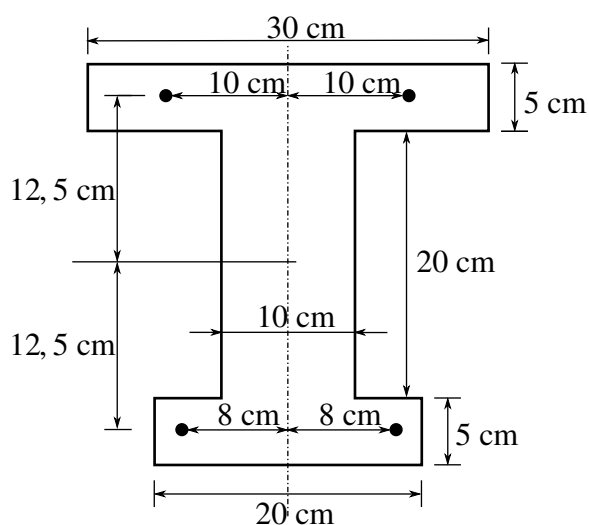


Figure 4.31 – Geometry of the I-section

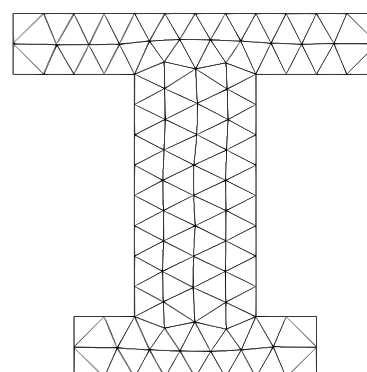


Figure 4.32 – Transversal mesh of the I-section

Since we study the mesh sensitivity of the model, the beam is supposed to be purely elastic. The mechanical properties of the beam are summarized in Table 4.5. The total sections of the upper and lower rebars are respectively $3 \cdot 10^{-4} \text{ m}^2$ and $4 \cdot 10^{-4} \text{ m}^2$. The applied load is $F = 10 \text{ kN}$.

	Young modulus	Poisson's ratio
concrete	$E = 21 \text{ GPa}$	$\nu = 0.2$
steel	$E^{\text{st}} = 210 \text{ GPa}$	-

Table 4.5 – Material properties

4.4.5.2 The AELD beam element

The beam is modeled with 1 AELD beam element. The kinematics of the beam element is composed of 23 displacement modes.

The transversal mesh is composed of 144 quadratic triangles, as shown on Figure 4.32. The transversal mesh sensitivity is not studied here.

The longitudinal mesh sensitivity of the beam element is investigated by changing the number of knots defining the interpolation functions. As mentioned in Section 4.3.3, the element is interpolated with NURBS functions. The polynomial order of the NURBS is 3. The number of knots n_{knot} takes different values from 2 to 40.

The rebars mesh sensitivity is studied with different discretizations: the rebars are successively

4.4. Validation of the model

meshed with $n_{\text{node}} = 3$ to $n_{\text{node}} = 15$ (the total number of bar elements defined in Section 4.2.4.3 is $n_{\text{rebar}} = 4 \times n_{\text{node}}$).

The data observed is the maximum vertical displacement u_m at mid-span of the beam. The results are presented on Figure 4.33.

4.4.5.3 Results

The maximum vertical displacement $u_m(n_{\text{knot}}, n_{\text{node}})$ is computed for 4 different number of longitudinal knots: 5, 10, 20 and 40. The 4 corresponding curves are displayed on Figure 4.33. For each curve, the number of nodes in each one of the rebars takes values from 3 to 15. The Euler solution is also represented and corresponds to the following value of u_m^{Euler} :

$$u_m^{\text{Euler}} = \frac{FL^3}{48(EI)^{\text{tot}}}, \quad (4.49)$$

where $(EI)^{\text{tot}} = EI + E^{\text{st}}I^{\text{st}}$. The numerical value is $u_m^{\text{Euler}} = 2.2735 \cdot 10^{-3}$ m. Because of the enriched kinematics of the AELD beam model, the beam element considered here is less stiff than the Euler solution. Consequently the 4 curves are placed above the Euler solution.

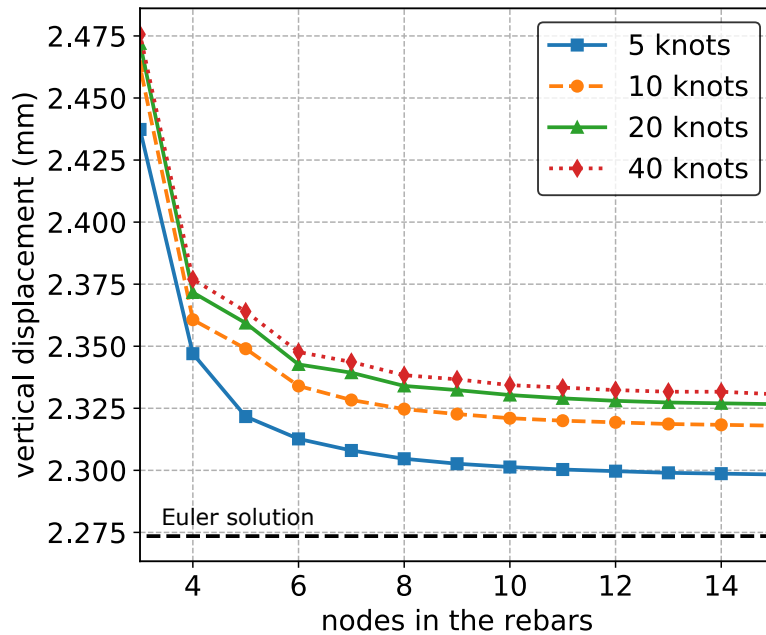


Figure 4.33 – Maximum vertical displacement for different meshes refinements

As expected, the more numerous the knots are, the less stiff the element is. Thus, for a given value of n_{node} , the values of u_m monotonically increase from $n_{\text{knot}} = 5$ to $n_{\text{knot}} = 40$. On the

Higher-order elastoplastic beam model for reinforced concrete

opposite, the more numerous the nodes are, the stiffer the element is. Thus, for a given value of n_{knot} , each curve monotonically decreases from $n_{\text{node}} = 3$ to $n_{\text{node}} = 15$. The increase of the number of nodes in each rebar increases the connectivities between the degrees of freedom of the beam element, and consequently makes it stiffer.

Considering the value $u_m(n_{\text{knot}} = 40, n_{\text{node}} = 15)$ as the converged value, we define the relative error of each curve to the converged value by:

$$e_1(n_{\text{knot}}) = \left| \frac{u_m(n_{\text{knot}}, 15) - u_m(40, 15)}{u_m(40, 15)} \right| \quad (4.50)$$

The values of e_1 for each curve are presented in Table 4.6.

n_{knot}	5	10	20
e_1	$1.39 \cdot 10^{-2}$	$5.43 \cdot 10^{-3}$	$1.72 \cdot 10^{-3}$

Table 4.6 – relative error to the converged value $u_m(40, 15)$

The relative error to the converged value is lower than 1% for $n_{\text{knot}} = 10$.

In order to determine the minimum number of nodes in each rebar, the following relative error is defined:

$$e_2(n_{\text{knot}}, n_{\text{node}}) = \left| \frac{u_m(n_{\text{knot}}, n_{\text{node}}) - u_m(n_{\text{knot}}, 15)}{u_m(n_{\text{knot}}, 15)} \right| \quad (4.51)$$

where $u_m(n_{\text{knot}}, 15)$ is considered as the reference for a given value of n_{knot} . The results are gathered in Table 4.7.

n_{node}	4	6	8	10	12	14
$e_2(5, n_{\text{node}})$	$2.12 \cdot 10^{-2}$	$6.24 \cdot 10^{-3}$	$2.76 \cdot 10^{-3}$	$1.31 \cdot 10^{-3}$	$5.80 \cdot 10^{-4}$	$1.45 \cdot 10^{-4}$
$e_2(10, n_{\text{node}})$	$1.84 \cdot 10^{-2}$	$6.90 \cdot 10^{-3}$	$2.88 \cdot 10^{-3}$	$1.29 \cdot 10^{-3}$	$5.75 \cdot 10^{-4}$	$1.44 \cdot 10^{-4}$
$e_2(20, n_{\text{node}})$	$1.93 \cdot 10^{-2}$	$6.88 \cdot 10^{-3}$	$3.15 \cdot 10^{-3}$	$1.58 \cdot 10^{-3}$	$5.73 \cdot 10^{-4}$	$1.43 \cdot 10^{-4}$
$e_2(40, n_{\text{node}})$	$1.99 \cdot 10^{-2}$	$7.29 \cdot 10^{-3}$	$3.29 \cdot 10^{-3}$	$1.57 \cdot 10^{-3}$	$7.15 \cdot 10^{-4}$	$4.29 \cdot 10^{-4}$

Table 4.7 – relative error of each curve for its own converged value

The number of nodes corresponding to the first value of e_2 lower than 1% is $n_{\text{node}} = 6$ for each curve. For the present study it can therefore be considered as a sufficient discretization of the rebars. This reference case study for mesh sensitivity is a good predictor for the refinement to adopt, even though a similar study should be carried out in plasticity to be completely exhaustive.

* *
*

4.5 Conclusion

This work introduces a new elastoplastic beam element for reinforced concrete. Both concrete and steel are considered as elastoplastic materials. Concrete is associated with a Rankine criterion and steel with a 1D Von-Mises criterion. The two materials are described and their local integration in the global elastoplastic algorithm is presented. The structural connection between concrete and steel rebars is then numerically characterized. The model is finally validated through a step-by-step procedure where the relevance of the elastoplastic model is justified. The beam element is based on the elastic beam formulation first developed by [Ferradi et al., 2016], extended to eigenstrains in [Corre et al., 2017a] and adapted to the elastoplastic case in [Corre et al., 2017b]. There is no limitation in the choice of the constitutive behavior of concrete. A more complex model with damage and softening could be considered. The coupling of damage to plasticity would require some modifications in the definition of the beam model which model should be adapted in consequence.

The general definition of a material in multisurface plasticity is first given. In this framework we define a concrete material with the multisurface Rankine criterion. During the local integration of the equilibrium equations, the stress is first assumed elastic before being projected on the criterion if actually plastic. Thanks to the closed form expression of the criterion in principal stress space, the projection step can be analytically solved. The elastoplastic steel rebars are then characterized. They are independently meshed into the 3D structure with one dimensional bar elements. This method has the great advantage to enable the definition of various shape and layout of the rebars in the concrete volume. Complex reinforcement can be represented. In this instance, this model offers more possibilities than the multifibers model which are limited to longitudinal reinforcement. A classic 1D yield criterion is therefore used and the radial return algorithm is processed for the local integration of the elastoplastic equilibrium equations.

Rebars are fully embedded in the concrete matrix. Their structural connection is expressed through the connection of their kinematics to the kinematics of concrete. Indeed, the displacement of each node of the rebars is expressed in terms of the degrees of freedom of the concrete beam element. Consequently the kinematics defined for concrete is imposed to the rebars. Without additional kinematic enrichment, this method avoids unwanted bond-slip effects. The tangent stiffness matrix used to solve the global element is the sum of the stiffness of concrete and the stiffness of rebars, both expressed on the kinematics preliminarily defined for the concrete beam element.

To our knowledge, the 3D Rankine criterion is not implemented in finite element softwares. In

Higher-order elastoplastic beam model for reinforced concrete

order to validate the present model, the following step-by-step procedure is therefore adopted. The integration of the rebars is first validated by proceeding to an elastic computation on a reinforced concrete structure. The results are then compared to a 3D reference solution computed on the finite element software *Code_Aster*. The elastoplastic global algorithm is then validated by processing the previous case study in elastoplasticity with a 3D Von-Mises criterion for concrete and the 1D yield criterion for steel. The results are again compared to a 3D reference solution. These two steps show very satisfactory consistency between the beam solution and the reference solution. The rebar integration and the elastoplastic algorithm being validated, the yield criterion is finally replaced by the Rankine criterion and the local projection defined in the present paper. The example considered highlights the strength of the present beam model to represent complex 3D phenomena. This ability is provided by the enriched kinematics of the higher-order model considered.

The actual failure of the beam is estimated by a fracture mechanics approach. Based on the stress distribution in the structure, the areas the more likely to crack are identified. The energy dissipated in these areas are compared to the fracture energy of concrete. Once the fracture energy is reached, the subsequent computations are considered not significant. This method is a post processing and needs a local knowledge of the stress. It could therefore be improved by implementing a systematic detection of the fracture mechanisms.

* *
 *
 *

Conclusion and outlook

Conclusion

In order to provide new tools for the structural analysis of bridges and slender structures, a new beam model has been derived and adapted to a wide range of material properties and load cases in this work. The result is the development of a new time efficient and numerically accurate finite element.

Chapter 1 first sets the industrial context of this work. After outlining the historical context that led to the current methods in structural engineering, we insisted on the need for change observed by the company STRAINS. The former paradigm, based on linear elastic analysis and conservative computations must now move to more explicit methods based on material savings and on the accurate expertise of the structural reliability of existing structures. The development of the software *Qantara* dedicated to the analysis of bridges is the industrial framework of the present work which also benefits from the support of the Laboratoire Navier. We introduced the successive beam models, from the Euler-Bernoulli theory to the more recent reduced model techniques. Based on very simple assumptions, the first beam models are very time efficient and suitable for simple computations but may quickly prove insufficient. Thus, each new beam model aimed at mitigating the weakness of the previous model. This incremental improvement of the beam theories has led to a progressive extension of the beam kinematics. Among recent beam models, we specifically presented models using the asymptotic expansion method. Based on a rescaling of the beam geometry, this method provides a systematic extension of the kinematics of the model thus producing accurate beam elements able to capture a wide range of deformations.

The next section dealt with elastoplastic beam models. A clear distinction between two categories of models was operated: models based on a yield criterion expressed in terms of the stress-resultants and models using a yield criterion expressed in terms of the stress-components. The first are obviously more time-efficient since they are based on a 1D elastoplastic constitutive behavior. But two main drawbacks were underlined: first it requires a preliminary computations of the yield surface potentially complex in case of multiple stress-resultants; second, it cannot accurately describe the local behavior of the structure. On the other hand, we described the local accuracy provided by the models based on a local yield criterion, but expressed the fact that these models are naturally more demanding.

In the last part of **Chapter 1**, a quick overview of the beam model for reinforced concrete was depicted. The definition of a beam model for reinforced concrete was focused on three major issues: the description of the materials behavior, the definition of the beam model and the kinematic connection between steel rebars and concrete. In this section, we exposed the complexity of models involving damage laws or softening behaviors and insisted on the potential numerical difficulties to implement such models.

In **Chapter 2** a higher-order beam element submitted to eigenstrains called the AELD beam

model is derived. This element answered to the need to describe many inelastic phenomena in civil engineering applications. We first introduced the 3D problem and exposed the asymptotic expansion method. Based on a scaling of the beam geometry, we showed how this method leads to a series of cross-sectional auxiliary problems and how their successive resolution yield displacement modes. Among these modes, some are specific to the strains applied to the structure. The strength of this model is that it does not require any *a priori* knowledge on the solution of the problem to extend its kinematics. The user can arbitrarily enrich the kinematics until a given order n .

Two applications of the previous model were then given. First, a thermal load case highlighted the ability of the model to capture faithfully the discontinuities of the strain applied. The local variables proved to be satisfactorily described thanks to the additional displacement modes specific to the eigenstrains. Furthermore, these results were obtained with a reduced number of displacement modes. A prestressed cantilever beam was studied in a second time. We showed the ability of the model to describe the local punching effect of the steel cable on the beam. We considered that these two examples were good illustrations of performance of this beam element. In both cases, fields close to the clamped end were more difficult to compute. In order to better describe the mechanical response close to the boundary conditions, the computation of additional displacement modes can be considered. These modes have actually already been implemented in the code of *Qantara* but were not presented in this work.

Chapter 3 was dedicated to the extension of the AELD beam model to the framework of the theory of plasticity. The standard 3D plasticity context was first established. We studied the case of J_2 flow theory with isotropic hardening. The classic radial return algorithm was considered for the local integration of the equilibrium equations and a Newton-Raphson procedure was used for the global incremental algorithm. These classical tools of plasticity theory enabled us to focus on the reduced model formulation. We briefly described the methodology to reduce a 3D problem into a beam problem, and we recalled the definition of the elastic beam model developed in the previous section.

The next section was dedicated to the formulation of the elastoplastic beam model. Considering the plastic strains of the previous iteration as eigenstrains imposed to the structure, we used the elastic beam element previously formulated to solve each iteration. Additional modes specific to the plastic strains were consequently computed. These new modes enable the model to capture the displacement due to the yielding of the structure. The discretization of the volume of the beam is an essential point. Indeed, the first detection of a plastic strain is highly depending on the position of the sections on which the local equilibrium equations are integrated. This point is still manual and it is necessary to implement an automatic procedure in the future.

The model was illustrated with a cantilever I-beam loaded at its end. We intentionally chose to asymmetrically load the beam in order to create torsion. Through the comparison of the beam solution with the volumic reference solution, it highlights the ability of the model to capture 3D effects. Parametric studies were then conducted in order to assess the parametric sensitivity of the model. As mentioned before, the definition of the longitudinal mesh appeared to be an important feature of the model. This model has been presented with J_2 flow rule

4.5. Conclusion

and with an isotropic hardening, but its extension to new yield criteria and hardening laws is straightforward.

As an extension of the previous chapter, we developed a higher-order elastoplastic beam model for reinforced concrete in **Chapter 4**. Following the three main steps identified in Section 1.4 for the definition of a model for reinforced concrete, Section 4.2 was dedicated to the description of the model without consideration of the reduced model. Considering that the added value of this chapter was not the beam element but the elastoplastic model for reinforced concrete, we focused on the definition of the material properties and the kinematic description of the connection between steel and concrete. We aimed at developing an efficient and simple model for the analysis of reinforced concrete structures. We therefore considered the theory of plasticity for the description of the concrete behavior. The steel rebars were considered as 1D bar elements embedded into the concrete volume. The connection between steel and concrete was ensured by expressing the displacements of the rebars in terms of the degrees of freedom of concrete. Without specific measures, this method avoids unwanted numerical bond-slip effect between rebars and concrete. The reinforced concrete model were then combined to the AELD beam model in Section 4.3.

To our knowledge, the 3D Rankine's yield criterion is not implemented in commercial codes. The direct comparison of our model to a reference solution was consequently not possible. Therefore we suggested a multistep procedure to validate our new model for reinforced concrete. First, the connection between steel and concrete has been validated by the computation of an elastic load case. The elastoplastic algorithm has then been verified by the computation of an elastoplastic load case, a Von-Mises criterion being considered for both steel and concrete. We compared the beam solution to volumic reference solutions computed on *Code_Aster* for these first two steps. For the last step we replaced the yield criterion of concrete by the Rankine's criterion designed previously. A load case was then computed and analyzed. The validity of the elastoplastic computation was finally assessed by an energy-based approach.

Outlook

The possibilities offered by the AELD beam model are important, and this work is a first step towards the development of a high-performance beam element for the study of bridges. Some improvements can already be identified, some of which have been mentioned previously.

Improvements for the current AELD beam model

The extension of the kinematics thanks to the asymptotic expansion method provides very accurate local results that could not be observed with other beam models. However, the displacements are computed for a cross-section far from the boundary conditions. The displacements close to the extremities and in particular close to clamped ends are therefore more difficult to describe. To address this issue, the computation of additional displacement modes specific to the boundary conditions have been implemented into STRAINS's software. The boundary conditions are modeled by springs and their stiffness is added into the local equilibrium equation. Then using the asymptotic expansion method, new auxiliary problems are formulated and solved, thus yielding additional modes specific to the conditions considered. These modes proved their efficiency in capturing the displacements originated by the kinematic frustration of the boundary conditions. Moreover, this method can be similarly applied to deal with stiffeners placed along the axis of the beam since additional modes can be computed likewise. An area for improvement is the longitudinal mesh of the element, both for elastic or elastoplastic computations. In elasticity, we could consider a first computation with an homogeneous longitudinal mesh. An automatic remeshing could then be operated in a second time according to the results obtained, thus refining the areas close to the boundary conditions and close to the load application area. This remeshing could be processed according to the elastic energy or to the L_2 -norm of the elastic strain. An automatic remshing could be processed similarly for elastoplastic computations, the main difference being that remeshing would occur directly from one iteration to following, the same iteration being not computed twice. We expect the mesh to be finer close to the boundary conditions, the load application areas and the plastified areas. A minimum size of mesh should be considered in order to avoid a too important increase of the computation time.

The selection of the cross-sections on which are computed the displacement modes specific to the plastic strains is still manual for elastoplastic computations. An educated guess is necessary in order to anticipate the first or more significant plastification area. An automatic procedure could be implemented in order to select these cross-section. Relevant criteria should be defined in order to the number of cross-sections which could evolve during the computations, and especially their positions. The automatic procedure could be taken to a higher level by automating the choice of the asymptotic expansion order and therefore the number of displacement modes. However such a procedure should not involve additional iterations or increments that could increase the total computation cost.

4.5. Conclusion

Extension of the model

The AELD beam model was first defined in a linear elastic case, then extended in this work to the case of eigenstrains, to the theory of plasticity and finally used for the definition a model for reinforced concrete. Other extension are already considered by STRAINS for the AELD beam model.

The AELD beam model has been naturally developed for prismatic bar element. But actual bridges are rarely fully prismatic and exhibit more complex features, including skewed cross-sections and curved longitudinal axis. That's why an extension of the AELD beam model to the case of non prismatic geometries has already been implemented into *Qantara*. This extension of the element enables for example the user to carry out structural analysis on a curved bridge by using one single beam element and still expect the local accuracy and time efficiency of the model developed for prismatic bars. The next step is now to adapt this geometrically non-linear beam element to the case of plasticity. The same methodology previously developed for prismatic elements should be here re-used.

In order to enlarge the scope of our beam element, we intend to extend it to the case of large displacements. An extension to large displacements would encompass a large scope of possible applications in the analysis of bridges like the study of geometrical instabilities of decks, stiffeners or bridge piers, or the modeling of large span stay-cables.

Furthermore, we think that this beam element could be used for the modeling of pipe structures. Indeed, the deformation of a pipe is characterized by special displacement patterns like ovalization of the cross-section. Such displacements cannot be described with classical beam models but are easily captured by the additional displacement modes composing the kinematics of the AELD beam model. Simple tests on pipes submitted to transversal compressive loads have confirmed our insight that such an application would be relevant for this beam element.

Connection with volumic finite elements

The objective of *Qantara* is not to provide only a stand-alone beam element for the analysis of bridges but to provide a software for the modeling of the entire structure, from decks to concrete abutments. The AELD model is not appropriate for the modeling of all the structural elements. Indeed, it is not relevant to model massive piers or superstructures with beam elements. Consequently we need to implement the connection of this beam element to volumic elements. This work is currently processed by STRAINS and is developed within a European project in a partnership with the french engineering company EGIS INDUSTRIES and the Edinburgh Parallel Computing Centre. An important objective of this collaborative project is to process complex computations with an High Performance Computing (HPC) infrastructure.

Improvement of the numerical performance of the model

One of the strength of the model is its reduced beam formulation providing time efficient computations. However the computational performance of the model could still be largely

Higher-order elastoplastic beam model for reinforced concrete

improved. Indeed, the computation of the stiffness matrix or the local integration of the elastoplastic equilibrium equations are stages of the model which could be processed with parallelization procedures. As mentioned before, this improvement of the numerical performance of the STRAINS's software programs is a major area of interest for STRAINS and is currently handled via the collaborative European project Fortissimo.

* *
*
*

Appendix A

Proof of the symmetry of the beam constitutive equation

In this section, the symmetry of the constitutive equation (2.29) is briefly sketched for $S_\eta = S_\eta^*$.

Recall that:

$$S_\eta = \langle \tilde{\sigma}_{33}^{\chi_\eta} \rangle \quad \text{and} \quad S_\eta^* = \langle x_\eta \tilde{\sigma}_{33}^{e_3} \rangle. \quad (\text{A.1})$$

The boundary value problem 2.22 being linear, each localization field $\tilde{u}^A, \tilde{\sigma}^A$ satisfies the equations for a unit value of the macroscopic field A and vanishing the other macroscopic fields. From the longitudinal constitutive equation (2.22c):

$$S_\eta = \langle C_{33\alpha\beta} \tilde{u}_{\alpha,\beta}^{\chi_\eta} + C_{3333} x_\eta \rangle \quad \text{and} \quad S_\eta^* = \langle x_\eta (C_{33\alpha\beta} \tilde{u}_{\alpha,\beta}^{e_3} + C_{3333}) \rangle, \quad (\text{A.2})$$

and the transverse constitutive equation (2.22b):

$$S_\eta = \left\langle \left(\tilde{\sigma}_{\alpha\beta}^{e_3} - C_{\alpha\beta\gamma\delta} \tilde{u}_{\delta,\gamma}^{e_3} \right) \tilde{u}_{\alpha,\beta}^{\chi_\eta} + C_{3333} x_\eta \right\rangle \quad \text{and} \quad S_\eta^* = \left\langle \left(\tilde{\sigma}_{\alpha\beta}^{\chi_\eta} - C_{\alpha\beta\gamma\delta} \tilde{u}_{\delta,\gamma}^{\chi_\eta} \right) \tilde{u}_{\alpha,\beta}^{e_3} + x_\eta C_{3333} \right\rangle \quad (\text{A.3})$$

Because the in-plane stress must satisfy equilibrium equation (2.22a) as well as free boundary conditions (2.22e) we have:

$$\left\langle \tilde{\sigma}_{\alpha\beta}^{e_3} \tilde{u}_{\alpha,\beta}^{\chi_\eta} \right\rangle = - \left\langle \tilde{\sigma}_{\alpha\beta,\beta}^{e_3} \tilde{u}_\alpha^{\chi_\eta} \right\rangle = 0 \quad \text{and} \quad \left\langle \tilde{\sigma}_{\alpha\beta}^{\chi_\eta} \tilde{u}_{\alpha,\beta}^{e_3} \right\rangle = - \left\langle \tilde{\sigma}_{\alpha\beta,\beta}^{\chi_\eta} \tilde{u}_\alpha^{e_3} \right\rangle = 0 \quad (\text{A.4})$$

From this and equation (A.3) it appears that $S_\eta = S_\eta^*$. Similar arguments ensure $D_{12}^* = D_{12}$.

Bibliography

- Abambres, M., Camotim, D., Silvestre, N., and Rasmussen, K. J. (2014). Gbt-based structural analysis of elastic–plastic thin-walled members. *Computers & Structures*, 136:1 – 23. 34
- ACI (2014). *Building Code Requirements for Structural Concrete and Commentary*. 124
- Actis, R. L., Szabo, B. A., and Schwab, C. (1999). Hierarchic models for laminated plates and shells. *Comput. Methods Appl. Mech. Eng.*, 172(1-4):79–107. 50
- Al-Rub, R. K. A. and Voyiadjis, G. Z. (2004). Analytical and experimental determination of the material intrinsic length scale of strain gradient plasticity theory from micro- and nano-indentation experiments. *International Journal of Plasticity*, 20(6):1139 – 1182. Recent Advances in Multiscale Modeling of Plasticity. 41
- Amrouche, C., Ciarlet, P. G., Gratie, L., and Kesavan, S. (2006). On the characterizations of matrix fields as linearized strain tensor fields. *Journal de Mathématiques Pures et Appliquées*, 86(2):116–132. 54
- Anthoine, A., Guedes, J., and Pegon, P. (1997). Non-linear behaviour of reinforced concrete beams: From 3d continuum to 1d member modelling. *Computers & Structures*, 65(6):949 – 963. 42
- Argyris, J., Boni, B., Hindenlang, U., and Kleiber, M. (1982). Finite element analysis of two- and three-dimensional elasto-plastic frames—the natural approach. *Computer Methods in Applied Mechanics and Engineering*, 35(2):221 – 248. 85
- Baba, S. and Kajita, T. (1982). Plastic analysis of torsion of a prismatic beam. *International Journal for Numerical Methods in Engineering*, 18(6):927–944. 35, 86
- Bathe, K.-J. and Chaudhary, A. (1982). On the displacement formulation of torsion of shafts with rectangular cross-sections. *International Journal for Numerical Methods in Engineering*, 18(10):1565–1568. 33, 35, 85
- Bathe, K.-J. and Wiener, P. M. (1983). On elastic-plastic analysis of i-beams in bending and torsion. *Computers and Structures*, 17(5):711 – 718. 86
- Benscoter, S. (1954). A theory of torsion bending for multicell beams. 20, 49, 50, 62
- Bigoni, D. and Piccolroaz, A. (2004). Yield criteria for quasibrittle and frictional materials. *International Journal of Solids and Structures*, 41(11):2855 – 2878. 41

- Bleyer, J. (2015). Méthodes numériques pour le calcul à la rupture des structures de génie civil. 7
- Bleyer, J. and de Buhan, P. (2013). Yield surface approximation for lower and upper bound yield design of 3d composite frame structures. *Computers and Structures*, 129:86 – 98. 30, 85
- Bognet, B., Bordeu, F., Chinesta, F., Leygue, A., and Poitou, A. (2012). Advanced simulation of models defined in plate geometries: 3D solutions with 2D computational complexity. *Comput. Methods Appl. Mech. Eng.*, 201-204(null):1–12. 84
- Boulton, N. (1962). Plastic twisting and bending of an i-beam in which the warp is restricted. *International Journal of Mechanical Sciences*, 4(6):491 – 502. 85
- Brüning, M. and Ricci, S. (2005). Nonlocal continuum theory of anisotropically damaged metals. *International Journal of Plasticity*, 21(7):1346 – 1382. 41
- Buannic, N. and Cartraud, P. (2001a). Higher-order effective modeling of periodic heterogeneous beams. I. Asymptotic expansion method. *Int. J. Solids Struct.*, 38(40-41):7139–7161. 49, 53
- Buannic, N. and Cartraud, P. (2001b). Higher-order effective modeling of periodic heterogeneous beams. II. Derivation of the proper boundary conditions for the interior asymptotic solution. *Int. J. Solids Struct.*, 38(40-41):7163–7180. 49
- Bui, N. N., Ngo, M., Nikolic, M., Brancherie, D., and Ibrahimbegovic, A. (2014). Enriched timoshenko beam finite element for modeling bending and shear failure of reinforced concrete frames. *Computers and Structures*. 42, 43, 125, 126
- Carol, I., Rizzi, E., and Willam, K. (2001). On the formulation of anisotropic elastic degradation.: Ii. generalized pseudo-rankine model for tensile damage. *International Journal of Solids and Structures*, 38(4):519 – 546. 41
- Carrera, E. and Giunta, G. (2010). Refined beam theories based on a unified formulation. *International Journal of Applied Mechanics*, (1):117–143. 34
- Carrera, E., Giunta, G., and Petrolo, M. (2011). *Beam Structures*. John Wiley & Sons, Ltd, Chichester, UK. 48, 86
- Ceresa, P., Petrini, L., and Pinho, R. (2007). Flexure-shear fiber beam-column elements for modeling frame structures under seismic loading — state of the art. *Journal of Earthquake Engineering*, 11(sup1):46–88. 44
- Chatterjee, A. (2000). An introduction to the proper orthogonal decomposition. *Current Science*, 78(7):808–817. 34

Bibliography

- Chen, W. (2007). *Plasticity in Reinforced Concrete*. J. Ross Publishing Classics. J. Ross Pub. 124
- Chinesta, F., Lavevèze, P., and Cueto, E. (2011). A short review in model order reduction based on proper generalized decomposition. *Archives of computational methods in engineering*, 18(4):395 – 404. 36, 84
- Christopherson, D. (1940). A theoretical investigation of plastic torsion in an i-beam. *Journal of Applied Mechanics*, 7:1–4. 29, 85
- Ciarlet, P. G. and Ciarlet, P. (2004). Another approach to linearized elasticity and Korn's inequality. *Comptes Rendus Mathématique*, 339(4):307–312. 54
- Cicekli, U., Voyiadjis, G. Z., and Al-Rub, R. K. A. (2007). A plasticity and anisotropic damage model for plain concrete. *International Journal of Plasticity*, 23(10):1874 – 1900. In honor of Professor Dusan Krajcinovic. 41
- Corre, G., Lebée, A., Sab, K., Ferradi, M. K., and Cespedes, X. (2017a). Higher-order beam model with eigenstrains. *submitted*. 84, 86, 95, 97, 100, 101, 106, 117, 120, 126, 141, 142, 165
- Corre, G., Lebée, A., Sab, K., Ferradi, M. K., and Cespedes, X. (2017b). Higher-order elastoplastic beam model. *submitted*. 126, 140, 141, 142, 165
- de Saint Venant, A. J. C. B. (1855). *De la torsion des prismes: avec des considérations sur leur flexion ainsi que sur l'équilibre des solides élastiques en flexion*. Imprimerie Imperiale, Paris. 15, 16, 17, 48
- de Sciarra, F. M. (2012). Hardening plasticity with nonlocal strain damage. *International Journal of Plasticity*, 34:114 – 138. 41
- De Soza, T. (2015). *Eléments MEMBRANE et GRILLE_MEMBRANE, R3.08.07*. Code_Aster. 145
- de Vree, J., Brekelmans, W., and van Gils, M. (1995). Comparison of nonlocal approaches in continuum damage mechanics. *Computers & Structures*, 55(4):581 – 588. 40
- Du, X., Lu, D., Gong, Q., and Zhao, M. (2010). Nonlinear unified strength criterion for concrete under three-dimensional stress states. *Journal of Engineering Mechanics*. 40
- Echter, R. and Bischoff, M. (2010). Numerical efficiency, locking and unlocking of {NURBS} finite elements. *Computer Methods in Applied Mechanics and Engineering*, 199(5-8):374 – 382. Computational Geometry and Analysis. 65
- El Fatmi, R. (2016). A refined 1D beam theory built on 3D Saint-Venant's solution to compute homogeneous and composite beams. *J. Mech. Mater. Struct.*, 11(4):345–378. 50, 62

- Feenstra, P. H. and Borst, R. D. (1996). A composite plasticity model for concrete. *International Journal of Solids and Structures*, 33(5):707 – 730. 124
- Ferradi, M. K. and Cespedes, X. (2014). A new beam element with transversal and warping eigenmodes. *Comput. & Struct.*, 131:12–33. 7
- Ferradi, M. K., Cespedes, X., and Arquier, M. (2013). A higher order beam finite element with warping eigenmodes. *Eng. Struct.*, 46:748–762. 7
- Ferradi, M. K., Lebée, A., Fliscounakis, A., Cespedes, X., and Sab, K. (2016). A model reduction technique for beam analysis with the asymptotic expansion method. *Comput. Struct.*, 172:11–28. i, 1, 7, 8, 47, 50, 51, 52, 62, 65, 79, 84, 86, 95, 103, 106, 120, 126, 141, 165
- Flejou, J. (2011). *Réponse statique d'une poutre béton armé (section en T) à comportement linéaire, V3.01.111*. Code_Aster. 161
- Gendy, A. and Saleeb, A. (1993). Generalized yield surface representations in the elastoplastic three-dimensional analysis of frames. *Computers and Structures*, 49(2):351 – 362. 32, 85
- Giunta, G., De Pietro, G., Nasser, H., Belouettar, S., Carrera, E., and Petrolo, M. (2016). A thermal stress finite element analysis of beam structures by hierarchical modelling. *Composites Part B: Engineering*, 95:179–195. 48
- Godio, M., Stefanou, I., Sab, K., and Sulem, J. (2016). Multisurface plasticity for cossear materials: Plate element implementation and validation. *International Journal for Numerical Methods in Engineering*. 127
- Gonçalves, R., Ritto-Corrêa, M., and Camotim, D. (2010). A new approach to the calculation of cross-section deformation modes in the framework of generalized beam theory. *Computational Mechanics*, 46(5):759–781. 34
- Govindjee, S., Kay, G. J., and Simo, J. C. (1995). Anisotropic modelling and numerical simulation of brittle damage in concrete. *International Journal for Numerical Methods in Engineering*, 38(21):3611–3633. 40, 124
- Grassl, P. and Jirásek, M. (2006). Damage-plastic model for concrete failure. *International Journal of Solids and Structures*, 43(22):7166 – 7196. 41, 124
- Grassl, P., Lundgren, K., and Gylltoft, K. (2002). Concrete in compression: a plasticity theory with a novel hardening law. *International Journal of Solids and Structures*, 39(20):5205 – 5223. 41, 124
- Hansen, E., Willam, K., and Carol, I. (2000). A two-surface anisotropic damage/plasticity model for plain concrete. Technical report. 41

Bibliography

- Hill, R. and Siebel, M. (1951). Lxxiii. on combined bending and twisting of thin tubes in the plastic range. *The London, Edinburgh, and Dublin Philosophical Magazine and Journal of Science*, 42(330):722–733. 29
- Hill, R. and Siebel, M. P. (1953). On the plastic distortion of solid bars by combined bending and twisting. *Journal of the Mechanics and Physics of Solids*, 1(3):207–214. 29, 85
- Hodges, D. H. (2006). *Nonlinear Composite Beam Theory*. American Institute of Aeronautics and Astronautics, Reston ,VA. 49
- Hsieh, S., Ting, E., and Chen, W. (1988). Applications of a plastic-fracture model to concrete structures. *Computers & Structures*, 28(3):373 – 393. 40
- Hughes, T. J. and Taylor, R. L. (1978). Unconditionally stable algorithms for quasi-static elasto/visco-plastic finite element analysis. *Computers & Structures*, 8(2):169 – 173. 90
- Ibrahimbegović, A. and Frey, F. (1993). An efficient implementation of stress resultant plasticity in analysis of Reissner-Mindlin plates. *Int. J. Numer. Methods Eng.*, 36(2):303–320. 125
- ICAB (2005). *Calcul des structures en béton*. 124
- Iesan, D. (1976). Saint-Venant’s problem for inhomogeneous and anisotropic elastic bodies. *J. Elast.*, 6(3):277–294. 22, 49, 50, 62
- Jouravskii, D. I. (1856). *Remarques sur la résistance d’un corps prismatique et d’une pièce composée en bois ou en tôle de fer à une force perpendiculaire à leur longueur*, volume 12. 12, 60
- Jukić, M., Boštjan, B., and Ibrahimbegovic, A. (2014). Failure analysis of reinforced concrete frames by beam finite element that combines damage, plasticity and embedded discontinuity. *Engineering Structures*. 43, 126
- Kim, J. S., Cho, M., and Smith, E. C. (2008). An asymptotic analysis of composite beams with kinematically corrected end effects. *Int. J. Solids Struct.*, 45(7-8):1954–1977. 49
- Kim, J.-S. and Wang, K. (2011). On the asymptotic boundary conditions of an anisotropic beam via virtual work principle. *Int. J. Solids Struct.*, 48(16-17):2422–2431. 49
- Kolpakov, A. G. (1993). Problem of the theory of beams with initial stresses. *Journal of Applied Mechanics and Technical Physics*, 33(6):897–902. 50
- Kolpakov, A. G. (1998). Application of homogenization method to justification of 1-D model for beam of periodic structure having initial stresses. *International Journal of Solids and Structures*, 35(22):2847–2859. 50

- Kolpakov, A. G. (2012). *Stressed Composite Structures: Homogenized Models for Thin-Walled Nonhomogeneous Structures with Initial Stresses*. Foundations of Engineering Mechanics. Springer Berlin Heidelberg. 50
- Krieg, R. and Key, S. (1976). Implementation of a time dependent plasticity theory into structural computer programs. *Constitutive equations in viscoplasticity: Computational and engineering aspects*, pages 125–137. 90
- Kupfer, H., Hilsdorf, H. K., and Rusch, H. (1969). Behavior of concrete under biaxial stresses. In *ACI Journal Proceedings*, volume 66, pages 656–666. ACI. 38, 39, 41, 131
- La Borderie, C. (1991). Phénomènes unilatéraux dans un matériau endommageable: Modélisation et application à l'analyse des structures en béton. 40
- Ladeveze, P. (1999). *Nonlinear Computational Structural Mechanics - new approaches and non-incremental methods of calculation*. Mechanical Engineering Series, Springer New York. 36, 84
- Lahmar, M., Naccache, F., and El Fatmi, R. (2017). Thermo-mechanical analysis of composite beams. *Compos. Struct.*, 162(November):388–400. 50
- Leroux (2012). Modèle multiaxial d'endommagement anisotrope: gestion numérique de la rupture et application à la ruine de structures en béton armé sous impacts. 40
- Lions, J. L. (1973). Perturbations singulières dans les problèmes aux limites et en contrôle optimal. *Lecture Notes in Mathematics*. 23
- Lublinter, J., Oliver, J., Oller, S., and Oñate, E. (1988). A plastic-damage model for concrete. *International Journal of Solids and Structures*, 25:299–326. 124
- Marini, A. and Spacone, E. (2006). Analysis of reinforced concrete elements including shear effects. *ACI Structural Journal*, 103:645–655. 126
- Mazars, J. (1986). A description of micro- and macroscale damage of concrete structures. *Engineering Fracture Mechanics*, 25(5):729 – 737. 40, 124
- Mazars, J., Kotronis, P., Ragueneau, F., and Casaux, G. (2006). Using multifiber beams to account for shear and torsion. applications to concrete structural elements. *Computational Mechanics Applied to Mechanical Engineering*, 195:7264–7281. 43, 86, 126
- Meschke, G., Lackner, R., and Mang, A. (1998). An anisotropic elastoplastic-damage model for plain concrete. *International Journal for Numerical Methods in Engineering*, 42:703–727. 124
- Miara, B. and Trabucho, L. (1992). A Galerkin spectral approximation in linearized beam theory. *Math. Model. Numer. Anal.*, 26(3):425–446. 24, 50, 52, 62, 84

Bibliography

- Michel, J. and Suquet, P. (2003). Nonuniform transformation field analysis. *Int. J. Solids Struct.*, 40(25):6937–6955. 34, 86
- Michel, J. and Suquet, P. (2004). Computational analysis of nonlinear composite structures using the nonuniform transformation field analysis. *Computer Methods in Applied Mechanics and Engineering*, 193(48):5477 – 5502. Advances in Computational Plasticity. 86
- Miled, B., Ryckelynck, D., and Cantournet, S. (2013). A priori hyper-reduction method for coupled viscoelastic–viscoplastic composites. *Computers and Structures*, 119:95 – 103. 84
- Mises, R. v. (1913). Mechanik der festen körper im plastisch- deformablen zustand. *Nachrichten von der Gesellschaft der Wissenschaften zu Göttingen, Mathematisch-Physikalische Klasse*, 1913:582–592. 89
- Moulin, S. (2010). *Elément de poutre multifibre (droite)*, R3.08.08. Code_Aster. 125
- Nadai, A. (1923). Der beginn des fließvorganges in einem tordierten stab. *Zeitschrift für angewandte Mathematik und Mechanik*. 29
- Nadai, A. (1931). *Plasticity*. McGraw-Hill. 29, 85
- Oller, S. and Barbat, A. H. (2005). Moment-curvature damage model for bridges subjected to seismic loads. *Computational Methods Applied to Mechanical Engineering*. 124, 125
- Olsen, P. C. (1999). Rigid plastic analysis of plane frame structures. *Computer Methods in Applied Mechanics and Engineering*, 179(1):19 – 30. 85
- Ottosen, N. S. (1977). A failure criterion for concrete. *American Society of Civil Engineers. Engineering Mechanics Division. Journal*, 103(4):527–535. 40
- Owen, D. R. and Hinton, E. (1980). *Finite elements in plasticity*, volume 271. Swansea: Pineridge Press. 26, 125
- Papadrakakis, M. and Papadopoulos, V. (1995). A computationally efficient method for the limit elasto plastic analysis of space frames. *Computational Mechanics*, 16(2):132–141. 85
- Park, H. and Kim, J.-Y. (2005). Plasticity model using multiple failure criteria for concrete in compression. *International Journal of Solids and Structures*, 42(8):2303 – 2322. 41
- Pham, B. H., Brancherie, D., Davenne, L., and Ibrahimbegovic, A. (2012). Stress-resultant models for ultimate load design of reinforced concrete frames and multi-scale parameter estimates. *Computational Mechanics*. 42, 125, 126
- Poltronieri, F., Piccolroaz, A., Bigoni, D., and Baivier, S. R. (2014). A simple and robust elastoplastic constitutive model for concrete. *Engineering Structures*, 60:81 – 84. 41

- Prandtl, L. (1903). Zur torsion von prismatischen stäben. *Physikalische Zeitschrift*, 4:758,759. 29
- Radfar, S. (2013). Modélisation d'éléments de structure en béton armé renforcées par collage de PRF: application à la rupture de type peeling-off. 161
- Roussette, S., Michel, J., and Suquet, P. (2009). Nonuniform transformation field analysis of elastic–viscoplastic composites. *Composites Science and Technology*, 69(1):22 – 27. *Mechanical Response of Fibre Reinforced Composites*. 34, 86
- Sadowsky, M. A. (1941). An extension of the sand-heap analogy in plastic torsion applicable to cross sections having one or more holes. *Journal of Applied Mechanics*, 8:166–168. 29
- Saeed, M. M. (1962). Torsion, shear and bending in reinforced concrete beams. 16
- Salari, M. R., Saeb, S., Willam, K. J., Patchet, S. J., and Carrasco, R. C. (2004). A coupled elastoplastic damage model for geomaterials. *Computer Methods in Applied Mechanics and Engineering*, 193(27):2625 – 2643. *Computational Failure Mechanics for Geomaterials*. 41, 124
- Sanchez-Palencia, E. (1980). *Non-Homogeneous Media and Vibration Theory*, volume 127 of *Lecture Notes in Physics*. Springer Berlin Heidelberg, Berlin, Heidelberg. 53
- Shaw, F. S. (1944). The torsion of solid and hollow prisms in the elastic and plastic range by relaxation methods. *Australian council for Aeronautics*. 29
- Silhavy, M. (2013). *The Mechanics and Thermodynamics of Continuous Media*. Theoretical and Mathematical Physics. Springer Berlin Heidelberg. 135
- Simo, J. (1985). A finite strain beam formulation. The three-dimensional dynamic problem. Part I. *Comput. Methods Appl. Mech. Eng.*, 49(1):55–70. 127
- Simo, J. and Hughes, T. (1998). *Computational Inelasticity*. Interdisciplinary applied mathematics. Springer. 131, 134
- Simo, J. and Taylor, R. (1985). Consistent tangent operators for rate-independent elastoplasticity. *Computer Methods in Applied Mechanics and Engineering*, 48(1):101 – 118. 90
- Smith, J. and Sidebottom, O. (1965). *Inelastic behaviour of load-carrying members*. Wiley. 29, 35, 85
- Sokolovsky, W. (1946). *Theory of plasticity*. 29, 85
- Spacone, E., Filippou, F. C., and Taucer, F. F. (1996). Fibre beam-column model for non-linear analysis of r/c frames: Part i. formulation. *Earthquake Engineering and Structural Dynamics*, 25:711–725. 43, 125

Bibliography

- Spacone, E. and Limkatanyu, S. (2000). Response of rc members including bond-slip effects. *ACI Structural Journal*. 43, 125
- STRAINS (2016). Note interne. 142
- Comité Euro International du Béton (1993). *CEB-FIP model code 90*. *CEB Bulletins*. 160
- Timoshenko, S. (1922). On the transverse vibrations of bars of uniform cross-section. *Philos. Mag. Ser. 6*, 43(253):125–131. 13, 48
- Štok, B. and Halilović, M. (2009). Analytical solutions in elasto-plastic bending of beams with rectangular cross section. *Applied Mathematical Modelling*, 33(3):1749 – 1760. 85
- Trabucho, L. and Viaño, J. (1987). Derivation of generalized models for linear elastic beams by asymptotic expansion methods. *Applications of multiple scaling in mechanics, Proc. Int. Conf., Paris 1986, Rech. Math. Appl. 4*, 302-315 (1987). 24
- Trabucho, L. and Viaño, J. (1990). A new approach of timoshenko's BEAM theory by asymptotic expansion method. *Math. Model. Numer. Anal.*, 24(5):651–680. 24
- Trabucho, L. and Viaño, J. (1996). Mathematical modelling of rods. In Ciarlet, P. G. and Lions, J. L., editors, *Handb. Numer. Anal.*, volume 4, pages 487–974. 49, 50, 53
- Trabucho, L. and Viano, J. M. (1988). A derivation of generalized saint venant's torsion theory from three dimensional elasticity by asymptotic expansion methods. *Journal of Applicable Analysis*, 31:129–148. 24
- Trabucho, L. and Viano, J. M. (1989). Existence and characterization of higher-order terms in an asymptotic expansion method for linearized elastic beams. *Asymptotic Analysis*, 2:223–255. 24
- Tsiatas, G. C. and Babouskos, N. G. (2017). Elastic-plastic analysis of functionally graded bars under torsional loading. *Composite Structures*, 176:254 – 267. 86
- Vidal, P., Gallimard, L., and Polit, O. (2012). Composite beam finite element based on the proper generalized decomposition. *Computers & Structures*, 102-103:76 – 86. 36
- Vlasov, V. Z. (1961). *Thin-walled elastic beams*. National Science Foundation and Department of Commerce. 18, 49
- Vogelius, M. and Babuska, I. (1981a). On a Dimensional Reduction Method I. The Optimal Selection of Basis Functions. *Math. Comput.*, 37(155):31. 50
- Vogelius, M. and Babuska, I. (1981b). On a Dimensional Reduction Method II. Some Approximation-Theoretic Results. *Math. Comput.*, 37(155):47. 50
- Wilkins, M. L. (1964). *Methods in Computational Physics*, chapter Calculation of Elastic-Plastic Flow, pages pp. 211–263. Academic Press. 90

- Willam, K. and Warnke, E. (1974). Constitutive model for the triaxial behavior of concrete. In for Bridge, I. A. and Engineering, S., editors, *Proceedings seminar on concrete structures subjected to triaxial stresses*. 40
- Wu, J. Y., Li, J., and Faria, R. (2006). An energy release rate-based plastic-damage model for concrete. *International Journal of Solids and Structures*, 43(3):583 – 612. 41
- Yu, W. and Hodges, D. H. (2004). Elasticity Solutions Versus Asymptotic Sectional Analysis of Homogeneous, Isotropic, Prismatic Beams. *J. Appl. Mech.*, 71(January):15–23. 49
- Yu, W., Hodges, D. H., and Ho, J. C. (2012). Variational asymptotic beam sectional analysis - An updated version. *Int. J. Eng. Sci.*, 59:40–64. 49
- Yu, W., Volovoi, V. V., Hodges, D. H., and Hong, X. (2002). Validation of the Variational Asymptotic Beam Sectional Analysis. *AIAA J.*, 40(10):2105–2112. 49
- Zhao, Q., Cartraud, P., and Kotronis, P. (2015). Justification of the asymptotic expansion method for homogeneous isotropic beams by comparison with the Saint-Venant solution. *J. Elast.* 53, 56
- Zienkiewicz, O. C. (1977). *The finite element method*. McGraw-Hill London ; New York, 3d expanded and rev. ed. edition. 107